Harvesting Time-Frequency-Space Diversity with Coded Modulation for Underwater Acoustic Communications

by

Konstantinos Pelekanakis

Submitted to the Department of Mechanical Engineering
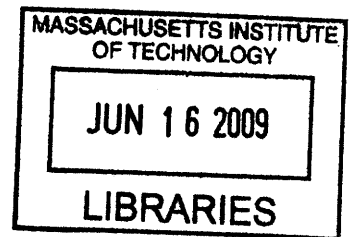in partial fulfillment of the requirements for the degree of

Doctor of Philosophy in Mechanical and Ocean Engineering

at the

MASSACHUSETTS INSTITUTE OF TECHNOLOGY

June 2009

© Konstantinos Pelekanakis. All rights reserved.

Signature of Author . . . .
Department of Mechanical Engineering
May 21st, 2009

Certified by . . . .
Arthur B. Baggeroer
Ford Professor of Engineering
Secretary of the Navy - Chief of Naval Operations - Chair for Ocean Sciences
Depts. of Mechanical and Electrical Engineering & Computer Science, MIT
Thesis Supervisor

Accepted by . . . .
David E. Hardt
Chairman, Department Committee on Graduate Students

Harvesting Time-Frequency-Space Diversity with Coded Modulation for Underwater Acoustic Communications

by

Konstantinos Pelekanakis

Submitted to the Department of Mechanical Engineering
on May 21st, 2009, in partial fulfillment of the
requirements for the degree of
Doctor of Philosophy in Mechanical and Ocean Engineering

Abstract

The goal of this thesis is to design a low-complexity, high data-rate acoustic communications system with robust performance under various channel conditions. The need for robust performance emerges because underwater acoustic (UWA) channels have time-varying statistics, thus a coded modulation scheme optimally designed for a specific channel model will be suboptimal when the channel statistics change.

A robust approach should use a coded modulation scheme that provides good performance in both additive white Gaussian noise (AWGN) and Rayleigh fading channels (and, consequently in the Rice fading channel, an intermediate channel model between the latter two). Hence, high data-rate coded modulation schemes should exhibit both large free Euclidean and Hamming distances. In addition, coded modulation is regarded as a way to achieve time diversity over interleaved flat fading channels. UWA channels offer additional diversity gains in both frequency and space; therefore a system that exploits diversity in all three domains is highly desirable.

Two systems with the same bit-rate and complexity but different free Euclidean and Hamming distances are designed and compared. The first system combines Trellis Coded Modulation (TCM) based on an 8-PSK signal set, symbol interleaving and orthogonal frequency-division multiplexing (OFDM). The second system combines bit-interleaved coded modulation (BICM), based on a convolutional code and a 16-QAM signal set, with OFDM. Both systems are combined with specific space-time block codes (STBC) when two or three transmit antennas are used. Moreover, pilot-symbol-aided channel estimation is performed by using a robust 2-D Wiener filter, which copes with channel model mismatch by employing appropriate time and frequency correlation functions.

The following result was obtained by testing the aforementioned systems using both simulated and experimental data from RACE '08: the BICM scheme performs better when the UWA channel exhibits limited spatial diversity. This result implies that coded modulation schemes emphasizing higher Hamming distances are preferred when there is no option for many receive/transmit hydrophones. The TCM scheme, on the other hand, becomes a better choice when the UWA channel demonstrates a high spatial diversity order. This result implies that coded modulation schemes emphasizing higher free Euclidean distances are preferred when multiple receive/transmit hydrophones are deployed.

Thesis Supervisor: Arthur B. Baggeroer
Title: Ford Professor of Engineering
Secretary of the Navy - Chief of Naval Operations - Chair for Ocean Sciences
Depts. of Mechanical and Electrical Engineering & Computer Science, MIT

Contents

List of Figures

8

List of Tables

Notation

Lower-case boldface letters indicate vector quantities. Capital boldface letters symbolize matrix quantities. Some commonly used symbols and letters throughout the thesis are:

B_c	channel coherence bandwidth
B_d	channel Doppler spread
D	# of diversity branches
K	Rician factor
L	# of taps of channel impulse response
N_c	# of OFDM sub-carriers
N_t	# of transmit hydrophones
N_r	# of receive hydrophones
T_c	channel coherence time
T_s	channel symbol duration
T_{cp}	cyclic prefix duration
T_d	channel delay spread
W	signal bandwidth
c	speed of sound in water (1500 m/sec)
d_E	minimum Euclidean distance of a signal set
d_H	Hamming distance of a code
λ	acoustic wavelength
$\delta(\cdot)$	Dirac function
$\tilde{x}(t)$	low-pass equivalent of the passband signal $x(t)$
$\text{Re}[x]$	real part of complex number x
$\text{Im}[x]$	imaginary part of complex number x
$\dagger$	complex conjugate transpose for vectors or matrices
$\top$	transpose for vectors or matrices
$*$	complex conjugate of a complex scalar quantity

13

Abbreviations

Some commonly used abbreviations throughout the thesis are:

AWGN	additive white Gaussian noise
AoA	angle of arrival
AoD	angle of departure
BER	bit-error-rate
BICM	bit-interleaved coded modulation
CSI	channel state information
DFE	decision feedback equalization
FFT	fast Fourier transform
IFFT	inverse fast Fourier transform
ISI	intersymbol interference
ICI	intercarrier interference
MIMO	multiple-input multiple-output
ML	maximum likelihood
MLSE	maximum likelihood sequence estimation
MRC	maximum-ratio combining
OFDM	orthogonal frequency division multiplexing
PEP	pairwise error probability
PSK	phase shift keying
QAM	quadrature phase shift keying
SNR	signal-to-noise ratio
SISO	single-input single-output
TCM	trellis coded modulation
UWA	underwater acoustic
WSS	wide sense stationary

ACKNOWLEDGEMENTS

Travayakis.

My non-Greek friends in Boston: Anna Custo, Andrew Poulsen, Hyun Joe Kim, Harish Mukundan, Sleiman Itani, Ethem Sozer.

The "M" company: Andrea Adamo, Luigi Adamo and his wife Jen Baltz, Maria Nikolinakou, Areti Kiara, and Aristeidis Karalis. Thank you for the fantastic memories. The best are yet to come...

My amazing roommates: Daniel Phung, Panayotis Lemonidis, and "my little brother" Ghassan Fayad.

Tal! You showed unparalleled patience during my thesis defence. Just for this, I will be eternally grateful to you.

My friends in Chania: Stelaras, Michelas, Xigos, Kobitsos, Androulis, Frank, Papidaki, Agapi, Papados, Theofilos. Thank you so much for your friendship and support despite the 5000 mile distance separating us.

My beloved cousins: Renata, Christos and his wife Marianna, Evdoras, Chryssa, Giannis, Emi, Vlassia.

My brother and my parents ... sas xrwstaw to einai mou. Sas agapw oso tipota allo sto kosmo afto.

To God who created everything ...

Chapter 1

Intoduction

Underwater acoustic (UWA) communications, namely, the idea of sending and receiving messages below water, started evolving during World War II. A characteristic analog communications application was the Gertrude, an underwater phone which allowed communications between military submarines [43]. In the early 1980's, the confluence of high-capability, low-power digital signal processors (DSPs) and advances in acoustic channel modeling and communication theory allowed commercial and scientific applications to emerge. Today, a reliable, high-rate acoustic link is of great importance for transmission of time-critical sea data from deep moored sensors, real-time underwater video transmission for ocean exploration, undersea automated surveillance, communication between manned/unmanned underwater vehicles, remote control signals for deep submersibles, to name a few. The current vision is the development of an underwater sensor network, namely a collection of bottom-mounted instruments and tetherless moving platforms (e.g., AUVs, gliders) in which different kinds of oceanographic data will be exchanged among the members of the network in real time.

Early digital acoustic communication systems relied on incoherent frequency shift keying (FSK) modulation [53] to cope with the time and frequency spreading of the received signal. The pursuit for higher data rates motivated research towards applying phase-coherent modulation techniques and during the 90's, a plethora of coherent systems were developed and deployed in various shallow and deep water environments [32]. Although significant advances in the development of phase-coherent UWA communications have been accomplished, the objective of achieving low bit-error-rate (BER), high-speed communication link still remains a challenging

goal due to five main reasons:

1. The operational bandwidth is **severely limited**, and thus system's throughput is also limited. This limitation is due to high-frequency signal absorption by sea water and low-frequency signal contamination by ambient noise. The typical bandwidth for long-range communications (10 - 100 km) is on the order of a kilohertz. For medium-range communications (5 - 10 km), the bandwidth is on the order a few kilohertz while for small-range communications (1 - 5 km) the bandwidth is on the order of tens of kilohertz.

2. The channel time-varying impulse response is **not always tractable** using conventional pilot symbol techniques. This can been seen by examining the channel spread factor[1]. For example, in shallow water channels, sound scattering off the physical boundaries results in a multipath spread T_d on the order of 10 msec for short-ranges while it could reach hundreds of milliseconds for long-ranges. In addition, the induced Doppler spread could be on the order of 10 Hz. Consequently, the undespread condition $(T_d B_d \ll 1)$ for reliable channel estimation is often violated implying that an adaptive equalizer will not be able to track the time fluctuations of the channel. Channel equalization may be avoided by choosing the symbol duration T_s such that $T_s \gg T_d$. This is the case, for example, in multi-carrier or spread-spectrum techniques. Consider the typical case of $T_d = 10$ msec. If one chooses $T_s = 100$ msec and $B_d = 10$ Hz, the normalized Doppler bandwidth $B_d T_s$ equals 1 so the channel varies appreciably during one symbol duration, therefore channel estimation techniques based on insertion of known pilot symbols within the data symbols at a regular rate is impossible. To achieve reliable coherent tracking, $B_d T_s$ must be less than 10^{-2} [28]. One way to communicate over fast varying (not underspread) UWA channels using coherent receivers is to simultaneously transmit the pilot and the data symbols using orthogonal waveforms [30].

3. UWA channels exhibit **extended intersymbol interference** (ISI) when high data rates are required. Either in deep water or shallow water channels, the ISI often is on the order of 100 symbol intervals, thus immediately yielding the optimum maximum likelihood

---

[1] As we will explain later, the channel spread factor is defined as the product of the delay spread and the Doppler spread.

sequence estimation (MLSE) receiver prohibitively complex since its complexity grows exponentially with the ISI span [55]. But even if suboptimal adaptive equalizers are employed, their computational load often surpass the capabilities of the DSP chip [70],[43]. Reducing receiver complexity while maintaining a satisfactory system performance has been an active research topic.

4. Mobile UWA channels need explicit **synchronization**. The small speed of sound (~1500 m/sec) relative to a moving platform (2-3 m/sec is a typical velocity in the water) results to Mach numbers on the order of 10^{-3} as opposed to 10^{-6}, which is a typical value for mobile radio communications. This is one major difference between mobile radio and mobile UWA communications since in the latter case the Doppler spreading of the received signal cannot be neglected. Synchronization algorithms which estimate the Mach number of a single path arrival have been proposed [51], however when the channel exhibits more than one strong path arrivals with different Mach numbers, the problem of estimating each path Mach number becomes quite involved and has not been addressed in the UWA communications literature.

5. UWA channels exhibit **non-stationary statistics**. This weakness comes from the fact that channel statistics depend on the receiver/transmitter location and the environmental conditions (e.g. calm/rough seas), hence channel statistics are not stationary in time. If the codewords are relatively short (and thus, not capacity achieving), the channel statistical model has a major impact on the design of the coded modulation scheme. This implies that a coded modulation scheme optimally designed for specific fading statistics (e.g., Rayleigh fading) will be suboptimal when the channel model changes. The use of relatively short codes, which fully exploit the channel's inherent diversity, has not been given yet the attention it deserves in UWA communications.

1.1 Exploiting diversity in underwater acoustic communications: past and current work

Diversity has been playing a center role towards improving the reliability of UWA communications. Time/frequency diversity techniques may be classified as either *explicit*, where the message is intentionally transmitted through different uncorrelated parts of the signal space, or *implicit*, where the message occupies the entire signal spectrum and the receiver tries to identify it by compensating for the channel distortion. For instance, explicit frequency diversity is obtained by employing coded modulation across uncorrelated bands of the signal spectrum while implicit diversity reception includes linear/non-linear equalization. In this section we identify the literature in the context of diversity exploitation. For a broader review of the UWA communications field, the reader is directed to [12] for a review of UWA communications prior to 1983 and to [32],[53] for a review on modeling, adaptive equalization, coded modulation and networks as applied to UWA channels prior to 1998.

Explicit time/frequency diversity has been used since the early days of digital UWA telemetry (modems). In the 80's, a representative system was the Digital Acoustic Telemetry System (DATS), which has been tested successfully over 1 km range, shallow water channel [13]. The DATS transmitted (8,4) Hamming codewords via 8-FSK modulation in the 45-55 kHz band. Frequency diversity was achieved because the transmitted codeword used eight different tones separated by 2 kHz, which was much larger that the channel coherent bandwidth. This separation was enough to take 600 Hz Doppler spread into account. To overcome the ISI, the transmitter employed beamforming to reduce multipath and frequency hopping to a new set of tones at every codeword period. In a seminal paper by Proakis [16], the concept of coded modulation was introduced in the underwater communication community, however not experimental results were reported. In particular, he showed that in Rayleigh fading, the maximum diversity order of an FSK (incoherent) modem using channel coding (either linear block codes or convolutional codes) is equal to the minimum Hamming distance of the code. This result motivated the choice of powerful concatenated codes since these codes are designed to maximize their minimum Hamming distance. In [22], a coded modulation scheme based on a convolutional encoder followed by bit interleaver and binary FSK modulation was used. The bit interleaver

ensured that the coded bits were transmitted across different coherent bands of the channel. To account for ISI, the system used a guard interval bigger that the channel delay spread before transmission of data. The achieved rate was 250 bps and the reported BER was on the order of 10^{-3} over nine different short-range, shallow water channels. The need to operate at higher data rates using low-complexity receivers led the community to pursuit coherent, multi-carrier modulation methods. Orthogonal frequency division multiplexing (OFDM) modulation, which has been extensively used in wired and wireless radio systems [29], became an attractive modulation technique for UWA communications. Probably the first coded OFDM system for UWA communications was introduced by [34], however only simulation results were given. A convolutional code followed by bit-interleaving was used before symbol mapping to PSK constellation. Then, the coded symbols were spread in frequency using direct-sequence spread-spectrum techniques. Consequently, frequency diversity as well as low-probability of intercept was achieved. Another system exploiting time/frequency diversity by transmitting the same bit (repetition coding) across different OFDM sub-bands was suggested by [52]. The system demonstrated satisfactory performance over various long-range, shallow water channels in the Baltic sea, the Indian and the Pacific ocean. A notable characteristic of the system was the simultaneous transmission of data and pilot symbols by spreading both across different m-sequencies. Consequently, the system could cope with fast varying (overspread) channels at very low SNR. In [78], a coded OFDM was experimentally demonstrated over a 350 m range, 15 m depth channel dominated by strong currents and snapping shrimp noise. Two serially concatenated convolutional encoders via two bit interleavers were used to encode the data, while differential phase shift keying (DPSK) modulation was used to modulate each sub-carrier. The interleavers ensure to break the burst errors caused by fading and impulsive noise before decoding. The system managed to achieve approximately 10^{-4} bit-error-rate (BER) at 5.3 kbps. A similar OFDM system which used a turbo product code (TPC) and DPSK modulation per sub-carrier was tested in real channels [85]. In one of the test trials, 10^{-6} BER at 10 kbps was measured over a highly underspread, 1700 m range, shallow water channel.

Implicit frequency diversity over horizontal links was initially demonstrated by [24]. The essential element of the receiver structure was the combination of a fractionally spaced adaptive decision feedback equalization (DFE) with a second order phase locked loop (PLL). The

22

DFE-PLL structure was jointly adapted using the RLS algorithm. The PLL compensates for the rapidly varying common phase rotation (when it exists) of the delay-spread function taps alleviating the equalizer to track the slowly varying impulse response. Excellent performance at 10 kbps using QPSK signaling over a short-range, shallow water channel was achieved. The authors also reported excellent performance at rates up to 1000 bps using uncoded QPSK/8PSK signals over long-range, deep and shallow water channels. The last 15 years, a plethora of systems based on the DFE-PLL receiver structure have been developed. A representative example is the DSP implementation of the WHOI Acoustic Modem originally developed for use on small AUVs in shallow water [80]. The data rate is variable and depends on the propagation conditions. In adverse conditions, transmission of frequency-hopping FSK signals yields 80 bps data rates while in better channel conditions PSK signals can yield up to 5000 bps. A common remedy to increase the reliability of the link without sacrificing bandwidth is by means of trellis coded modulation (TCM). In [39], TCM codes designed for Rayleigh fading channels were introduced in the underwater communications community. TCM codes in conjuction with symbol interleaving and an adaptive DFE-PLL structure using the LMS algorithm were also proposed by [60]. Excellent results at rates up to 30 kbps from a carefully designed (less than 40 m) vertical, shallow water link were obtained.

In addition to time/frequency diversity, the spatial variability of the ocean offers space diversity provided that the hydrophones are sufficiently far apart. Spatial diversity at the receiver (receive diversity) has been relative mature subject over the last 15 years. The authors in [17] used square law combining for FSK signaling where they manage to reduce the BER from 0.03 (one hydrophone) to 0.0006 (two hydrophones). The optimum structure for multipath channels with receive diversity was introduced by [21]. This structure is a multi-channel coherent combiner or equivalently a bank of matched filters, each of which is matched to the channel response as seen by the corresponding sensor followed by a single channel MLSE. The prohibitive computational complexity of the optimum receiver led the authors to implement an MMSE-adaptive multi-channel DFE with carrier phase synchronization. Error free rates were demonstrated using uncoded QPSK/8PSK signaling over several shallow and deep water channels. One drawback of the multi-channel DFE is that its computational complexity and the convergent rate is dramatically affected by the number of the receive sensors. Furthermore,

the gain from adding more sensors may be compensated by noise enhancement, always present in sparse channel equalization. These problems motivated the same authors in [32] to propose a receiver which jointly adapts a beamformer and a reduced multi-channel DFE under a single MMSE criterion. In this case, the number of the feedforward filters needed equals to the number of physical paths rather than the number of sensors, which is often a larger number. Contrary to the "classical" beamforming receivers which treat multipath as an unwanted interference [23], the aforementioned structure takes advantage of multipath propagation, thus exploiting also frequency diversity. A different space-time processing approach was investigated by [54], [75] motivated by the lack of the tracking capability of the DFE when the channel becomes overspread. The authors suggested a low-complexity structure consisting of two separately adjusted entities: an adaptive beamformer followed by a linear adaptive multichannel equalizer. The beamformer decomposes the UWA channel into multiple coherent orthogonal paths using the SVD approach and retains only the paths with higher energy (eigenvalues). The "effective" channel seen by the equalizer has a smaller spread factor, hence the equalization process becomes robust and computationally efficient. Driven by the requirement of low complexity receivers, a group or researchers at Scripps [82] exploited receive diversity using passive time reversal (or passive phase conjugation) initially introduced by Dowling [25].

Employing multiple projectors has been recently become notable at-sea experiments. The authors in [71] were the first to experimentally demonstrate that multiple-input multiple-output (MIMO) UWA channels offer spatial degrees of freedom yielding higher data rates as opposed to the single projector counterparts. The result was achieved by using transmit beamforming based on the singular value decomposition (SVD) of the known (previously measured) channel transfer function matrix and computing the post-equalization SNR of each data stream. However, measured BER and achieved data rates were not reported. In [90], two independently coded data streams were transmitted via two antennas using OFDM modulation over a 9 m depth, 500-2000 m range channel. Although this scheme does not exploit transmit diversity, error-free performance at 12 kbps was accomplished due to the strong error correction capability of the LDPC code. Increased reliability by using two different transmit diversity techniques, i.e., space-time trellis codes (STTC) [40] and turbo coded, layered space-time codes (LSTC) [33], was demonstrated by [89]. To account for ISI and co-channel interference, the authors extended

the canonical multi-channel DFE-PLL receiver of [21] to a MIMO-DFE receiver with iterative equalization and decoding. Multi-band transmissions were used to compromise between equalization complexity and tracking ability of the receiver. When the turbo-coded LSTC system was used, error-free data rate of 23 kbps (accounting for all transmission bands) was achieved over a 2 km range, shallow water channel. However, when STTC system was used, error rates on the order of 10^{-2} were experienced. This indicates that full space-time-frequency diversity was not exploited by the latter method. Potentially higher diversity gains would be achieved if coding across the different multi-band transmissions was employed.

1.2 Thesis approach

The aim of this work is to design a low-complexity, high-data-rate acoustic telemetry system. This translates to designing an attractive channel-coding and modulation scheme for which, a number of competing factors (e.g., data throughput, acceptable bit-error-rate, decoding delay, implementation complexity) must be taken into account. Real-time applications, such as real-time underwater video transmission, impose a strict decoding delay constraint, and thus applying powerful "capacity achieving" codes (e.g. turbo codes, LDPC codes) is not suitable. In this thesis, codes with relatively short block lengths (and therefore not capacity achieving) are considered so that their decoding delay lies within the delay limits real-time applications pose. In this case, the channel model has a significant impact on the choice of the coded modulation scheme. Unfortunately, UWA channels demonstrate time-varying statistics due to highly dynamic environmental fluctuations (surface waves, underwater currents) and platform motion. Consequently, a coded modulation scheme matched to a specific fading channel model performs poorly for a substantial fraction of time during which communication takes place.

A robust approach assumes a coded modulation scheme that provides good performance in both AWGN and Rayleigh fading channels (and, consequently in Rice fading channels, which is an intermediate channel model between the latter two). In AWGN, efficient design of coded modulation focuses on maximizing the minimum Euclidean distance between any pair of codewords (free Euclidean distance). Furthermore, in Rayleigh fading channels, maximizing the minimum Hamming distance (number of bits/symbols for which two codewords differ) of any

pair of codewords is essential in order to achieve good performance. Consequently, coded modulation schemes should exhibit both large free Euclidean and Hamming distances to ensure robust performance over a variety of channel conditions. There are two approaches widely found in the communications literature that apply these design concepts is practice; either coupling channel coding with modulation in a single entity or treating channel coding and modulation independently [50]. If coding and modulation are combined into a single entity, the most widely applicable approach is trellis coded modulation (TCM) [26]. In fading channels, TCM is combined with symbol interleaving for improved performance. If coding and modulation are considered as two separate entities, then bit-interleaved coded modulation (BICM) [42] offers an increase in both the Hamming and the free Euclidean distance by using a bit-wise interleaver at the encoder output prior to modulation.

Diversity is a power-efficient method to combat channel fading and it refers to the capability of having multiple, uncorrelated replicas of the transmitted information bearing signal. These replicas may be acquired over different frequencies (frequency diversity) and/or different time periods (time diversity) and/or spatially separated sensors (space diversity). Coded modulation is regarded as a way to achieve time diversity over interleaved flat fading channels[2]. UWA channels offer additional diversity gains in both frequency and space.

A low-complexity solution for obtaining frequency diversity is to combine channel coding, interleaving, and OFDM modulation. OFDM splits the fast-rate symbol stream into parallel slow-rate sub-streams and each-substream modulates a different sub-carrier. The symbol duration of each sub-stream is much larger than the delay spread of the channel, hence each sub-stream undergoes flat fading, i.e., one tap equalization per sub-carrier is needed. When channel coding across the sub-streams is introduced, OFDM signals exploit frequency and time diversity.

Spatial diversity is leveraged when sufficiently separated multiple transmit/receive transducers are employed. Receive diversity is easily obtained by having multiple receive hydrophones and by using maximal ratio combining (MRC), i.e., a bank of matched filters each of which is matched to the corresponding channel of each hydrophone. On the other hand, transmit

---

[2]For this reason, the Hamming distance is also referred to as the code diversity of the coded modulation scheme.

diversity is harder to obtain because the channel in unknown at the transmitter, therefore sophisticated space-time signaling methods are required. As of today, the most promising methods stem from the family of the space-time trellis codes (STTC) [40] and the family of space-time block codes (STBC) [48]. Although STTC perform better than STBC, in this thesis, STBC are employed because they are easy to design for any number of transmit antennas and simple to decode by retaining a maximum likelihood decoder based on linear combining of the received signals.

A code modulation scheme that exploits space-time-frequency diversity must distribute the coded data across all transmit transducers and coherent bands [65]. Towards this end, we propose to concatenate TCM/BICM (as an outer code) with STBC (as an inner code) before applying OFDM modulation. The first system combines TCM based on an 8-PSK signal set, symbol interleaving, STBC, and OFDM. The second system combines BICM, based on a convolutional code and a 16-QAM signal set, STBC, and OFDM. Pilot-symbol-aided channel estimation is performed by using a 2-D Wiener filter, which can cope with channel model mismatch by employing appropriate time and frequency correlation functions. Although both systems achieve the same data rate and require the same decoding complexity, their interaction with different channels will reveal interesting conclusions based on their different coding (free Euclidean distance) and diversity (Hamming distance) gains.

1.3   Thesis outline

The rest of this thesis is organized in five chapters. Chapter 2 develops a model for SISO and MIMO UWA channels respectively, based on the channel's physical properties for the frequencies at which communications take place. Chapter 3 describes SISO and MIMO UWA channels as diversity systems, and an upper bound on the number of their diversity branches is given based on the channel-signal space interaction. In addition, time, frequency and space diversity techniques are discussed. In chapter 4, SISO- and MIMO-OFDM systems based on TCM and BICM are designed. A robust channel estimation method is discussed for the proposed OFDM systems. Moreover, BER performance results based on simulating various types of fading channels are also given. Chapter 5 evaluates the proposed systems using field

data from Rescheduled Acoustic Communications Experiment (RACE' 08). Finally, the thesis is concluded in Chapter 6 where future research directions are also suggested.

Chapter 2

Underwater Acoustic Communications Channels and Models

Traditional point-to-point UWA communications are based on single-input single-output (SISO) architectures, where a single projector transmits signals over the channel to a single hydrophone. Recent results in information theory have shown that systems with multiple transmit and receive antennas using space-time methods can provide a tremendous increase in data rate and/or reliability as opposed to conventional single antenna systems, provided that the channel exhibits rich scattering [68]. It is valid to claim that the rich scattering environment of shallow water channels provides sufficient spatial degrees of freedom to be exploited by multiple input multiple-output (MIMO) architectures, where closely located projectors concurrently transmit different signals over the channel to closely located hydrophones. Indeed, recent work has shown that the use of MIMO system with space-time methods is a promising way towards achieving higher data rates and/or improved error performance [54],[71],[89],[90]. This incredible increase in system performance motivates us to consider MIMO structures in this thesis.

Chapter summary: Our concern in this chapter is to characterize the channel behavior at the frequencies of interest and to develop a realistic channel model, which can accurately and efficiently predict the performance of either SISO or MIMO UWA communication systems.

We begin by considering the mechanisms of sound propagation in the ocean; the influence of the spatially-varying sound speed on sound propagation is emphasized. Then, we identify the principal factors that determine the average received SNR at a given distance from the transmitter and we explicitly demonstrate that UWA communications are severely bandlimited. We also explain that time-varying multipath propagation leads to time, frequency and angle spreading of the transmitted signal. Fortunately for us, these physical characteristics of the UWA channel are also found in the mobile radio channel, so borrowing concepts from radio communications is a plausible way to start our channel modeling. Towards this end, we first use a systems theory approach to develop a physical model for SISO UWA channels and then we draw concepts from the array processing literature to extend the SISO physical model to a MIMO one. Finally, based on the channel-signal interaction, we classify the fading channel as *fast* or *slow* and as *flat* or *frequency selective*. In addition, key channel physical parameters such as *coherence time/Doppler spread, coherence bandwidth/delay spread, and coherence space/angle spread* are explained. These parameters play a center role in the design of our systems.

2.1   Sound propagation in the ocean

Sound propagation at the frequencies of interest (> 5 kHz) can be well described as propagating along paths or rays through the ocean. A rule of thumb for the validity of ray theory is when the spatial scale of the environment is large compared to the wavelength. Since the nominal speed of sound in the ocean is 1500 m/sec, the wavelengths of interest are less than 0.3 m so ray theory is well justified. Normal mode theory is a more accurate way to describe the sound field but becomes computationally complex when the number of modes required to estimate the sound field increases in proportion to the acoustic frequency [56]. Reflection, scattering, and refraction (the last being the most important) are the three basic mechanisms which impact sound propagation in the ocean. These mechanisms are briefly explained next.

Reflection occurs when sound impinges upon surfaces which have very large dimension compared to the acoustic wavelength. For instance, reflection occurs when a sound wave impinges on the sea bottom or the sea surface.

Scattering occurs when a propagating ray interacts with rough surfaces or small (compared

(a) incidence wave   scattering wave

                                      specular

(b) incidence wave   scattering wave

                                      rough

(c)   incidence wave   scattering wave

                                      very rough
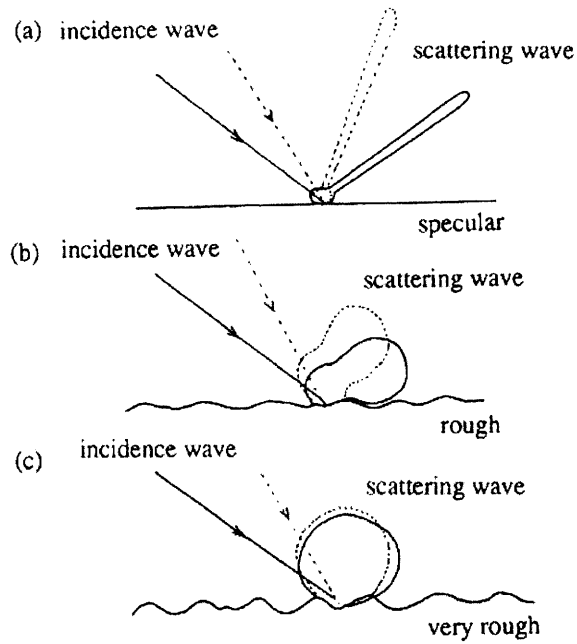
Figure 2-1: Surface scattering pattern with different surface roughness.

to the acoustic wavelength) objects. In the case of a smooth surface, as shown in Figure 2-1(a), there will be a specular reflection with a symmetric angle to the incident angle. Figure 2-1(b) illustrates that as the surface roughness increases, the returned sound wave separates into a coherent field (specular reflection) and an incoherent field (the scattering component or reverberation), which can act as interference for a coherent receiver. As surface roughness continues to increase, only diffuse components will remain without any component of specular reflection, as seen in Figure 2-1(c).

Refraction plays the most fundamental role in understanding sound propagation at sea. It occurs when a propagating ray does not travel along straight paths but bends (according to Snell's law) due to the spatially-varying sound speed in the ocean. An expression of the speed of sound c as a function of temperature, salinity and static pressure (function of depth) is given
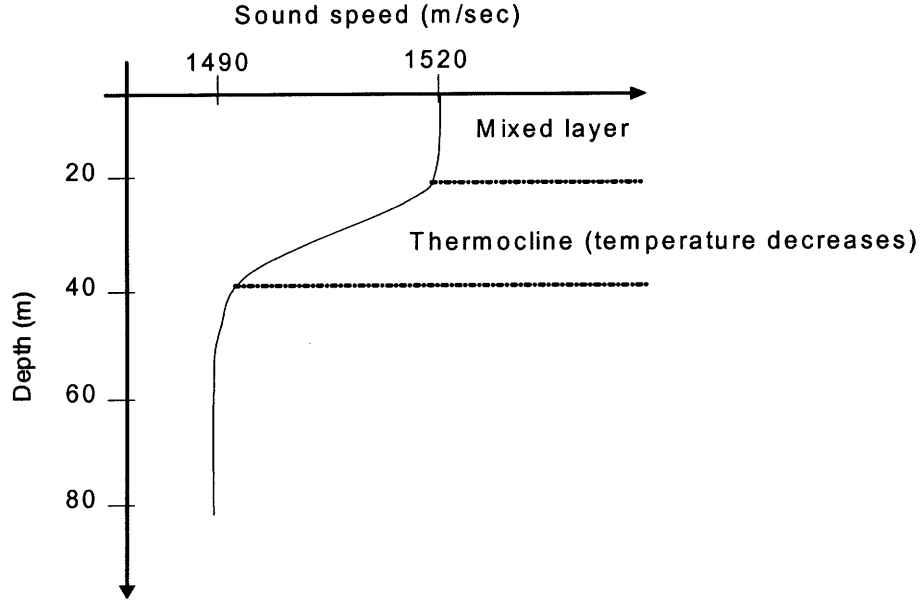
Figure 2-2: Typical shallow water sound speed profile during summer.

by [7]:

$$\begin{aligned}
c(T, S, z) &= 1448.96 + 4.591T - 0.05304T^2 + 0.00024T^3 \\
&\quad + 1.340(S - 35) + 0.0163z + 1.675 \times 10^{-7}z^2 \\
&\quad - 0.01025T(S - 35) - 7.139 \times 10^{-13}Tz^3
\end{aligned} \quad (2.1)$$

where T is the water temperature in °C, S is the salinity in parts per thousand and z is the depth in meters. This expression is accurate for $0 \leq T \leq 30$, $30 \leq S \leq 40$ and $0 \leq z \leq 8000$. Note that the sound speed increases as the temperature and depth increases. Since the sound speed depends on the environmental conditions, different environments will yield different sound speed profiles. We now describe two typical sound speed profiles, which are often encountered in shallow and deep water environments.

The typical shallow-water environment is a continental shelf with depth up to 200 m. The sound speed profile tends to be irregular and unpredictable due to the local meteorological and environmental conditions. During the winter, especially after the passage of storms, the water column is well mixed resulting in an almost constant sound speed with depth. On the other
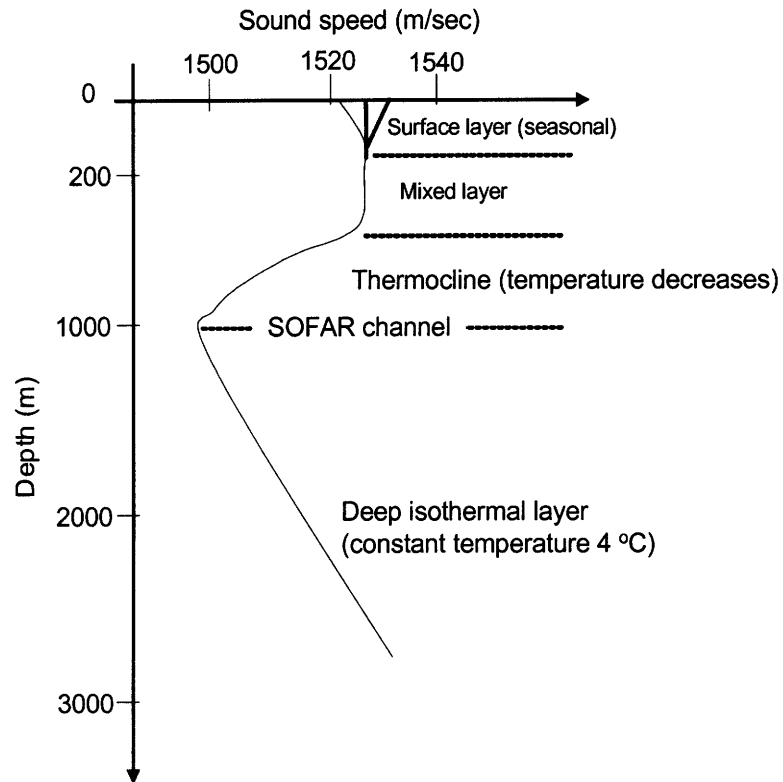
Figure 2-3: Typical deep water sound speed profile for mid-latitude.

hand, solar heating during the summer, makes the water near the surface warmer, therefore the speed of sound is higher towards the sea surface. Figure 2-2 shows a typical sound speed profile encountered during the summer [56]. The layer of water at the sea-surface has the highest sound speed and is called the *mixed layer*. Below the mixed layer is the *thermocline*, which is characterized by a negative sound speed gradient due to temperature decrease. For the rest of the water column, the sound speed remains constant. When this sound speed profile is experienced, sound propagation experiences extensive bottom interaction because sound refracts towards the region of minimum sound speed. This kind of propagation limits the coverage area of transmitter because bottom scattering losses are high. In general, shallow-water waveguides are characterized by extensive signal interaction with the physical boundaries yielding significant time variation in the received signal power.

In mid-latitudes deep water, the sound speed profile is different than the shallow water

profile. A representative sound speed profile for this region is illustrated in Figure 2-3 [10],[56]. The surface layer depends on the seasonal environmental conditions (heating, cooling, waves). It can be either isothermal or upward refracting. In the latter case a natural waveguide is formed because sound turns towards the surface (*surface ducting*). In the thermocline layer, the temperature decreases with depth, therefore the sound speed decreases as well. Below the thermocline, there is the *deep isothermal layer* where the temperature remains constant at 4 °C (property of sea water at high pressure) but the sound speed increases towards larger depths due to the pressure gradient effect. Note that there is always a depth located between the the thermocline and the deep isothermal layer at which the sound speed obtains a minimum value. At this depth, a natural waveguide is formed called the *SOFAR channel* or *deep channel* sound channel axis, within which rays are trapped. It has been experimentally shown that low-frequency sound can travel for thousands of kilometers in the SOFAR channel.

The mechanisms of reflection/scattering and refraction yield multiple sound paths between a transmitter and a receiver. Multipath formation depends on transmitter/receiver position, sea depth and the current environmental conditions (i.e., sound speed profile, surface waves, bottom geoacoustic properties). In shallow water, sound propagates from transmitter to receiver through repeated surface and bottom reflections, where the latter suffer much higher loss. A radiating shallow source in deep water, will form *convergence zones*. These high intensity zones are formed by superposition of two types of rays: (1) rays trapped in the mixed layer; (2) rays escaped from the mixed layer, intersected the deep isothermal layer and refracted upwards until they reach the surface layer. Convergence zones usually appears at intervals of 50-70 km with zone widths (the distance over which there is significant enhancement of the signal) of about 10% of the convergence zone range.

Even when there is no platform motion, multipath formation is time-varying due to environmental fluctuations. Slow-time variations are due to changes of large-scale spatial features of the environment (e.g., changes in sound speed profile due to daily heating and cooling). Fast-time variations are due to rapid, small-scale environmental fluctuations (e.g., changes in the roughness of sea surface due to increasing wind speed). The distinction between small- and large-scale fluctuations is based on how these spatial fluctuations are compared with the nominal wavelength of the source. Although ray theory can predict the slowly-varying multipath formation,

a stochastic description of multipath propagation is necessary to account for the unpredictable, rapid changes in the medium. Flatte [11] proposed a theory on how internal waves impact sound propagation in deep water. This theory decomposes multipath into a quasi-deterministic component (*macro-multipath*) and a rapidly-varying stochastic component (*micro-multipath*) and as the authors in [43] indicated, it can be readily applied in UWA communications. For example, consider a signal transmitted in a shallow water channel, as it is displayed in Fig. 2-4. The solid black lines represent the nominal rays (macro-multipath) whose formation depend on the transmitter/receiver location and the large-scale changes of the sea bottom and/or sea surface of the waveguide. The gray regions represent the ray tubes (micro-multipath) whose radius depend on the small-scale fluctuations of the roughness of the sea surface and/or sea bottom. Signals do not necessarily propagate along the black lines but may split into one or more micro-rays within the ray tubes. The received signal corresponding to one ray tube is the sum of all signals which propagate along the micro-multipaths within the tube. In general, different ray tubes have little overlap and small correlation. If the ray tube is *unsaturated* (spatial scale of environmental fluctuations is much greater than the carrier wavelength leading to a single perturbed path within the ray tube), the tube will show high correlation at different sensor locations. This implies that unsaturated tubes do not aid spatial diversity techniques for fading suppression. On the contrary, if the tube is *saturated* (spatial scale of fluctuations is much smaller than the carrier wavelength leading to independently varying micro-rays), the tube will show small correlation at different sensor locations. Hence, saturated tubes aid the efficiency of spatial diversity techniques.

Although transmitting sound underwater has its limitations, it is much more efficient than employing electromagnetic waves. For example, at 30 kHz, radio waves are attenuated 1 dB in 0.3 m while higher frequencies waves (light and gamma rays) are attenuated even more rapidly. In comparison with other available means, the use of sound waves is the best way to achieve underwater communications for ranges of more than 100 m [10].
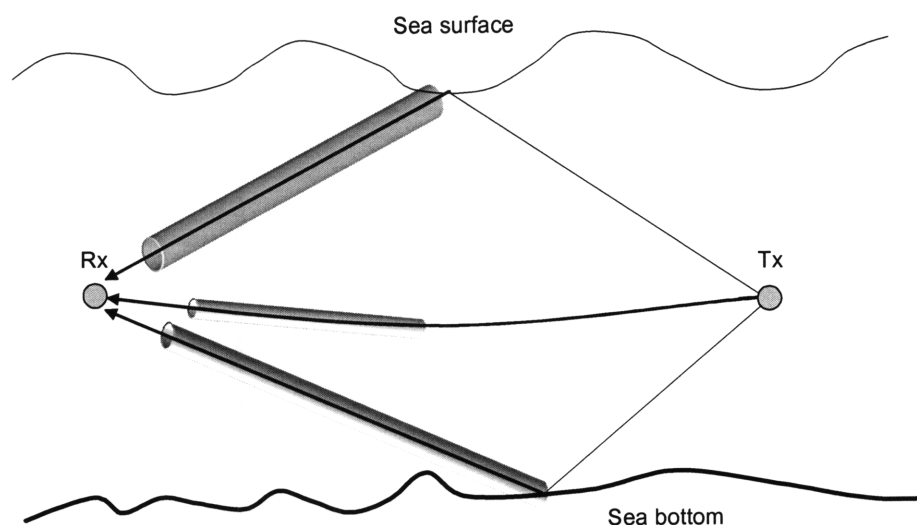
Figure 2-4: Ray tubes model for mutlipath propagation.

2.2 Signal losses and ambient noise

The power attenuation an acoustic signal experiences as it propagates through the ocean is known as signal loss. Signal loss can predict the mean signal power for large transmitter-receiver distances (also referred to as *large-scale* loss) and is useful to estimate the coverage area of a transmitter. This loss is divided into four categories: geometrical spreading loss, absorption loss, reflection loss, and scattering loss.

Geometrical spreading loss is further divided into two types: spherical spreading loss and cylindrical spreading loss. If r is the range from the source, when the waves haven't reached the boundaries of the waveguide, the total power radiated through a sphere centered at the source must remain fixed so the power per meter squared decays as r^{-2}. When the sound is trapped within the boundaries of the waveguide the power per meter is inversely proportional to the surface of a cylinder so it decays as r^{-1}. Geometrical spreading loss is independent of the signal frequency.

Absorption is the effect of the transformation of acoustic energy into heat during the sound propagation over the ocean and depends on the source frequency. At low frequencies (< 1 kHz), the dominant process of sound absorption is the chemical relaxation of boric acid $B(OH)_3$. At

mid-range frequencies (1 kHz - 100 kHz), sound absorption is due to relaxation of magnesium sulfate MgSO$_4$. At high frequencies (> 100 kHz), shear and volume viscosity are the main mechanisms which contribute to sound absorption. At frequencies above a few hundred Hz, plane wave absorption is approximately described by Thorp's empirical formula [9]:

$$\alpha(f) = \frac{0.11f^2}{1+f^2} + \frac{44f^2}{4100+f^2} + 0.000275f^2 + 0.003 \quad (\text{dB/km}) \tag{2.2}$$

where f is the frequency of the plane wave in kHz. Observe that absorption increases with frequency, thus limiting the maximum operational frequency. For example, $a(f) \simeq 1$ dB/km at 9 kHz.

Reflection loss occurs when a sound wave impinges the boundary of two fluid layers. The amount of loss depends on the properties of the layer (density, sound speed) and angle of incidence of the sound wave with the boundary. The *critical angle* plays an important role in understanding how sound propagates in a waveguide, especially in shallow water. If we consider a homogeneous water column with sound speed c_1 overlying a homogeneous fluid bottom with speed c_2, then the critical angle is given by [56]

$$\theta_c = \arccos\left(\frac{c_1}{c_2}\right). \tag{2.3}$$

No reflection loss occurs if the incident angles of the propagating ray are smaller than θ_c. In shallow water waveguides, the critical angle defines a cone near the horizontal axis of source (typically -17° to 17°) where transmitted power suffers much smaller loss within the cone than outside the cone since less power is trapped inside the sea bottom.

For communication frequencies, acoustic wavelengths are usually much smaller than the spatial variability of the sea surface and the sea bottom. Hence, these boundaries are often modeled as rough surfaces. The effect of sound scattering off a rough surface results in additional attenuation of the specular coherent field due to the generation of the scattered incoherent field. The reflection coefficient of a rough surface is often described in the following form [56]

$$R'(\theta) = R(\theta)e^{-0.5\Gamma^2} \tag{2.4}$$
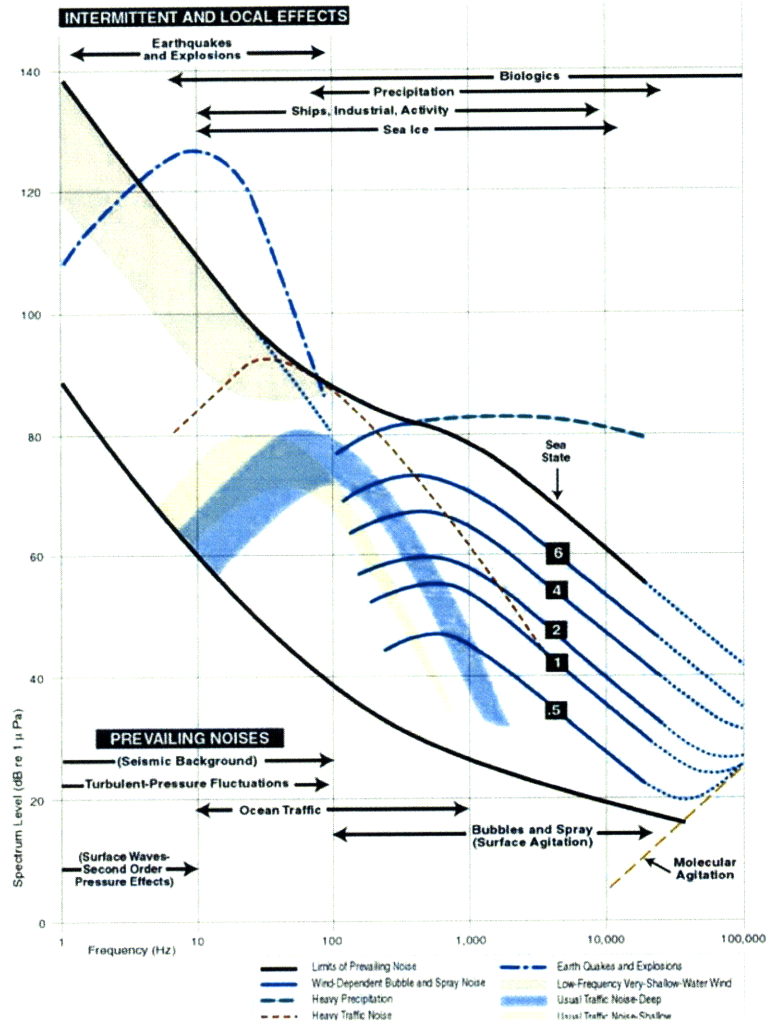
Figure 2-5: Collection of ambient noise spectra (figure is taken from [56])

where $R(\theta)$ in the reflection coefficient of the surface when there is no roughness, θ is the angle of incidence and Γ is the Rayleigh roughness parameter. For sea-air interface $R(\theta)$ becomes -1 while at the sea-bottom interface $|R(\theta)| \leq 1$. The Rayleigh roughness parameter is defined as follows:

$$\Gamma = 4\pi \frac{f}{c} \sigma \sin(\theta) = 4\pi \frac{\sigma}{\lambda} \sin(\theta) \qquad (2.5)$$

where σ is the rms roughness of the surface f and λ are, respectively, the frequency and the wavelength of the source. Observe that the loss due to scattering increases as the frequency increases.

38
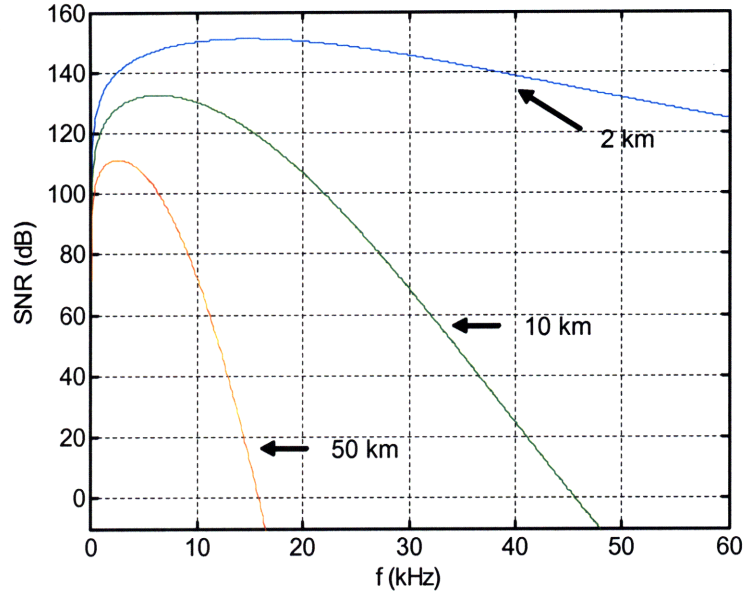
Figure 2-6: Large-scale SNR for a lossless waveguide. The source is at 100 m while the total depth is 200 m.

In addition to signal losses, received signals are contaminated with ambient noise, limiting the received SNR. Often, ambient noise is directional. There are many sources of ambient noise such as passing ships, marine life, breaking waves, rain, and seismic events. Due to the large number of sources, the total level of the ambient noise can vary significantly. Noise levels could typically range from 90 dB to 120 dB [31]. In general, ambient noise exhibits a continuous power density spectrum with Gaussian statistics [83]. A collection of ambient noise spectra is displayed in Figure 2-5. Observe that, in the absence of intermittent and local phenomena, the ambient noise spectra decrease approximately as 20 dB/decade at frequencies less than 100 kHz.

The preceding discussion helps us to compute the average received SNR for a given transmitter-receiver separation distance. This is very useful for estimating the coverage area of a wireless communication link. Toward this end, we compute an estimate of the received SNR when a tone of frequency f_o is transmitted in a shallow water (flat bottom, flat surface) waveguide. Suppose we have a $P = 20$ Watts omnidirectional source (source level 184 dB re 1μPa at 1 m) that is located at $d = 0.1$ km below the sea surface. The total depth of the waveguide is

$h = 0.2$ km. In addition, any reflection/scattering losses are neglected. The received SNR (in dB), parameterized by frequency f_o (Hz), range r (km) and depth d (km), is captured by the following formula [84]:

$$SNR(f_o, r, d) \simeq 171 + 10\log_{10}(P) - \alpha(10^{-3}f_o)r - k\log_{10}r - 10\log_{10}\left(\int\limits_{f_o-\Delta f/2}^{f_o+\Delta f/2} N(f_o)df \right) \quad (2.6)$$

In Eq. 2.6, the first two terms account for the source level, the third term describes the absorption loss, the fourth term represents the geometrical spreading loss and the final term approximates the ambient noise power $N(f_o)\Delta f$, where Δf is a very small band around the source frequency f_o. The spreading factor k dictates the type of geometrical spreading loss (e.g., $k = 1$ corresponds to cylindrical spreading, $k = 2$ corresponds to spherical spreading, and $k = 1.5$ is the value for practical spreading). The noise power spectral density is approximated as $N(f) = 10^{10}f^{-2}$ Watts/Hz re 1μPa (decay rate of 20 dB/decade) based on the Figure 2-5. Figure 2-6 illustrates a collection of SNR vs. frequency curves for several ranges. Note that the longer the range, the less the operational bandwidth. For long ranges (> 50 km), the bandwidth is limited to few kilohertz while for small ranges ($\simeq$ 2 km) is unlikely to be more than 50 kHz. In addition, an optimum carrier frequency exists for a given channel geometry which decays with range and is comparable to the operational bandwidth. The latter fact renders UWA channels inherently wideband.

2.3 Time-varying multipath effects

Multipath propagation dramatically affects the performance of underwater acoustic modems because it induces severe signal distortion. This type of propagation results in multiple replicas of the same transmitted signal, which arrives at any point in space at various delays and orientations with different amplitudes and phases. The destructive and constructive combination of each multipath component gives a resultant signal that experiences rapid amplitude fluctuations, known as *fading*. Maintaining good communications becomes challenging because the received signal power may decay by as much as 30 to 40 dB while the receiver only moves by a fraction of a wavelength. Even when there is no platform motion, the motion of boundaries

40

(e.g., sea surface, internal waves) cause time-varying fading.

One of the major effects of multipath propagation is that the transmitted signal experiences *delay spread* (or time spread). If the signaling interval is much smaller than the channel delay spread then ISI occurs, namely, the delayed replicas of the previously transmitted symbols interfere with the decision of the current symbol. In medium-range, shallow-water channels, a typical delay spread is 10 msec causing the ISI to span 100 symbols for a 10 kilosymbols/sec (ksps) signaling rate (symbol duration is $T_s = 10^{-4}$ sec). In long range, deep water channels, formation of convergence zones results in typical delay spreads of 50 msec. The amount of ISI could reach 50 symbols if 1 ksps signaling rate is used. In both cases, the order of ISI length makes the optimum MLSE receiver prohibitively complex (since its complexity increases exponentially with the ISI span [55]) unless sparse channel modeling is used.

Another implication of multipath propagation is that the transmitted signal arrives at different angles at the receiver. If an array of sensors is employed, a large *angle spread* will cause the multipath components to add up in a random fashion at different sensor locations giving rise to space diversity exploitation. To ensure uncorrelated amplitude fluctuations between the sensors, their spatial separation, which depends on the waveguide spatial characteristics and the carrier frequency, must be sufficiently large. Significant spatial coherence of 30 wavelengths was reported for a shallow water channel (20 m depth, 200 m range) using the 11.5-17.5 kHz band [43]. In general, spatial coherence is decreased when the range of the link and/or the carrier frequency of the signal are increased.

In addition to delay and angle spread, the transmitted signal undergoes frequency spreading (or *Doppler spread*) due to translation of the reflection point of a moving boundary. For example, consider the tone reflection off a smooth surface wave (ignoring scattering effects). If both the transmitter and the receiver are at a depth much greater than the surface wave amplitude, a transmitted tone at carrier frequency f_c is received as a phase modulated (PM) signal[1], namely:

$$\cos\left(2\pi f_c\left(t - \tau_0 - \frac{2s(t)\cos(\theta)}{c}\right)\right) \tag{2.7}$$

where τ_0 is the time of arrival of the beginning edge of the tone, $s(t)$ is the wave amplitude and

---

[1]This result is inspired by the work in [32].

41

θ is the incident angle. Assuming wind generated surface waves following a Pierson-Moskowitz wave amplitude spectrum, the surface wave modal frequency is determined by [76]:

$$f_w = 0.877\frac{g}{2\pi u_{19.5}} \qquad (2.8)$$

where g is the gravitational acceleration (m/sec^2) and $u_{19.5}$ is the wind speed (m/sec) at height 19.5 m above the sea surface. The *significant amplitude* of the waves at that frequency is given by:

$$h = 0.21\frac{u_{19.5}^2}{2g} \qquad (2.9)$$

If the sea surface elevation is approximated as $s(t) = h\sin(2\pi f_w t)$, then the received signal is not appeared as a single tone any more but exhibits a frequency spread (*Doppler spread*) which is approximated by using Carson's rule [64]:

$$B_d = 2f_w\left(1 + \frac{2\pi f_c 2h\cos(\theta)}{c}\right) = 0.877\frac{g}{\pi u_{19.5}} + 0.368\frac{\cos(\theta)f_c u_{19.5}}{c}. \qquad (2.10)$$

If a wind speed of $u_{19.5} = 7$ m/sec (sea state 3) is assumed, then it follows that $f_w = 0.2$ Hz and $h = 0.5$ m from Eq. (2.8) and (2.9), respectively. Assuming $f_c = 10$ kHz, $c = 1500$ m/sec, and $\theta = \pi/4$, Eq. (2.10) results in 12.5 Hz Doppler spread.

Apart from any channel fluctuations, platform motion also gives rise to Doppler spread. Let us consider the transmission of a signal $\mathrm{Re}\left[\tilde{x}(t)e^{j2\pi f_c t}\right]$ that occupies a frequency band centered around carrier frequency f_c. If the signal path between the transmitter and the receiver is decreased at a rate of u m/sec, then the non-faded, noiseless received signal is expressed as:

$$\mathrm{Re}\left[\tilde{x}\left(t(1 + \frac{u}{c}) - \tau_o\right)e^{j2\pi f_c t(1+u/c)-j2\pi f_c \tau_o}\right], \qquad (2.11)$$

where τ_0 is the arrival time of the beginning edge of the signal. Obviously, the time axis of the received signal is compressed by $1 + u/c$, therefore the bandwidth of the received signal is expanded by $1 + u/c$ as well. In addition to the generated Doppler spread, platform motion induces a *Doppler shift*; namely, the frequency content of the signal is translated by $f_d = f_c u/c$. A coherent receiver must compensate for the Doppler shift otherwise an adaptive channel estimation algorithm may experience severe tracking problems. In addition, the Mach number

u/c is often on the order of 10^{-3} (in contrast with radio communications which is on the order of 10^{-7}) so the usual assumption $\tilde{x}\left(t(1 + \frac{u}{c}) - \tau_o\right) \simeq \tilde{x}\left(t - \tau_o\right)$ someone invokes in radio communications is not always valid in UWA communications. The relatively high Mach numbers render synchronization algorithms extremely important towards achieving the desired system performance [51].

The Doppler spread of the received signal indicates how fast the channel response varies. The greater the Doppler spread the faster the channel response fluctuation. If the symbol duration T_s is such that $B_d T_s << 1$, then an adaptive receiver will be able to track the time-varying channel on a symbol-to-symbol basis. On the other hand, a small symbol duration induces extended ISI so receiver complexity increases. Clearly, there is a trade-off on the choice of T_s based on the channel's delay and Doppler spread.

2.4 Channel modeling

Our focus here is to incorporate all the physical characteristics and arbitrary effects of UWA channels into a comprehensive mathematical model circumventing the complexities arising from solving the wave equation with arbitrary boundary conditions. Bello [2] introduced a systems theory approach in order to model the time-varying multipath propagation effects of a mobile radio channel. According to this theory, the mobile radio channel is modeled as linear time-varying system and a set of system functions that describe the channel in both time and frequency domain is introduced. Bello's approach has been widely applied in UWA communications [53], however emphasis on the wideband nature of the channel has not been given. Next, we first develop a model for SISO UWA channels and then we extend it to MIMO channels using classical array processing techniques, where both the transmitter and the receiver employ linear arrays.

2.4.1 SISO channels

The UWA channel is modeled as a linear, time-varying system, which is described by the (low-pass equivalent) impulse response $\tilde{h}(\tau, t)$. The variable t (short-time) corresponds to the time variations of the impulse response due to moving platforms and physical boundaries while the

variable τ (fast-time) represents the channel multipath delay for a fixed value of t. A baseband output $\tilde{y}(t)$ is related to the input $\tilde{x}(t)$ via the formula [2]

$$\tilde{y}(t) = \int\limits_{-\infty}^{+\infty} \tilde{h}(\tau, t)\tilde{x}(t - \tau)d\tau + \tilde{w}(t) \tag{2.12}$$

where $\tilde{w}(t)$ models the additive ambient and thermal noise, which is independent from $\tilde{x}(t)$. The above equation may also be interpreted as a system with impulse response $\tilde{h}(\tau, t)$ at time t when an impulse is applied at time $t - \tau$. An equivalent input/output representation of the channel is given by

$$\tilde{y}(t) = \int\limits_{-\infty}^{+\infty} \tilde{H}(f, t)\tilde{X}(f)e^{j2\pi ft}df + \tilde{w}(t). \tag{2.13}$$

where $\tilde{X}(f)$ is the Fourier transform of $\tilde{x}(t)$ and $\tilde{H}(f, t)$ denotes the time-varying frequency response of the channel, which is defined by

$$\tilde{H}(f, t) \triangleq \int\limits_{-\infty}^{+\infty} \tilde{h}(\tau, t)e^{-j2\pi f\tau}d\tau. \tag{2.14}$$

Let us assume the transmission of a wideband signal that occupies the frequency band $[f_c - W/2, f_c + W/2]$ and has total duration T (for example, a sequence of n symbols has total duration of n/W). Furthermore, let the channel consist of L propagation paths connecting the transmitter with the receiver. Each path p induces the following effects on the transmitted (low-pass equivalent) signal[2]:

1. An attenuation (path loss) that incorporates the spreading loss, and the frequency dependent absorption loss. The path loss is expressed as

$$A_p(f) = d_p^k a^{d_p}(f), \tag{2.15}$$

where f denotes the signal frequency, d_p stands for the pth path distance, the spreading factor k varies between 1 (cylindrical spreading) and 2 (spherical spreading), and $a(f)$ is

---

[2]The approach is inspired by the work in [84].

44

the absorption coefficient.

2. A propagation delay τ_p and a carrier-phase shift $e^{-j2\pi f_c \tau_p}$.

3. A carrier-phase offset (or Doppler shift) $\check{f}_p \triangleq f_c u_p / c$, where u_p (m/sec) is the relative transmitter-receiver velocity for the pth path. Any dilation/compression of the received signal is ignored provided that the condition $WT \ll |c/u_p|$ is satisfied.

4. A multiplicative complex gain $b_p(f, t)$ which models the reflection/scattering interaction of the signal with physical boundaries or objects. Note that $b_p(f, t)$ is frequency-dependent (e.g., see the Rayleigh roughness parameter in Eq. (2.5)) and time-varying due to any changes in the reflective characteristics of the pth path (e.g., changes in the sea surface roughness).

Hence, the baseband frequency response of the channel can be expressed as:

$$\tilde{H}(f, t) = \sum_{p=0}^{L-1} \frac{b_p(f, t)}{\sqrt{A_p(f)}} e^{j2\pi \check{f}_p t - j2\pi f_c \tau_p} e^{-j2\pi f \tau_p}. \tag{2.16}$$

In addition, the time-varying impulse response of the channel $\tilde{h}(\tau, t)$ is found by taking the inverse Fourier transform of the above equation with respect to variable f.

Since UWA channels are characterized by several random events, $\tilde{H}(f, t)$ is usually modeled as a random process with respect to the t variable. The random characterization of the channel is addressed in Chapter 3.

2.4.2 MIMO channels

Let us consider a MIMO system with N_T projectors and N_R hydrophones. Denoting the channel response between the nth transmit and the mth receive sensor as $\tilde{H}_{m,n}(f, t)$, the wideband MIMO channel is given by the $N_R \times N_T$ matrix

$$\tilde{\mathbf{H}}(f, t) = \begin{bmatrix} \tilde{H}_{1,1}(f, t) & \tilde{H}_{1,2}(f, t) & \cdots & \tilde{H}_{1,N_T}(f, t) \\ \tilde{H}_{2,1}(f, t) & \tilde{H}_{2,2}(f, t) & \cdots & \tilde{H}_{2,N_T}(f, t) \\ \vdots & \vdots & \ddots & \vdots \\ \tilde{H}_{N_R,1}(f, t) & \tilde{H}_{N_R,2}(f, t) & \cdots & \tilde{H}_{N_R,N_T}(f, t) \end{bmatrix}. \tag{2.17}$$

45
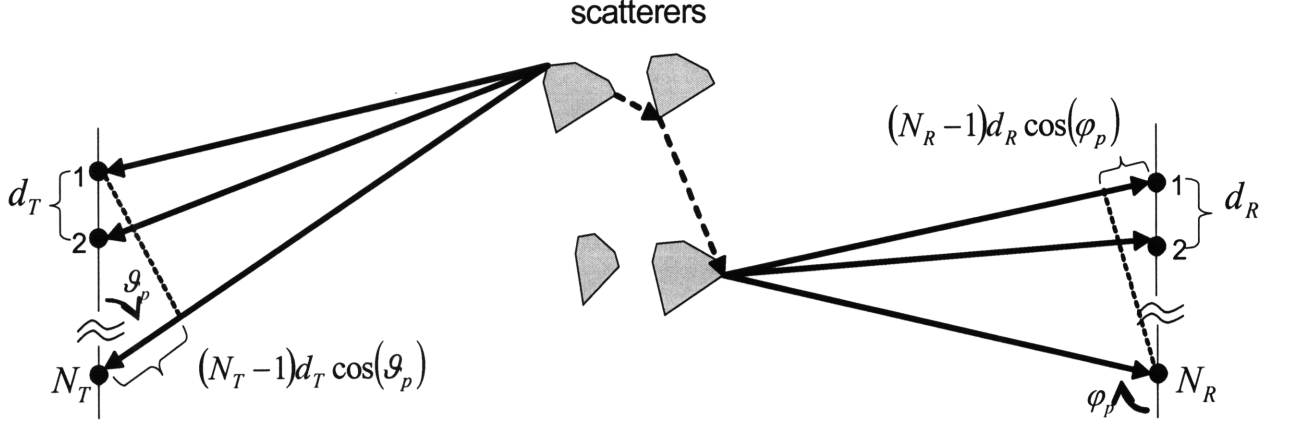
Figure 2-7: MIMO channel with scatterers. Each scattering path is associated with a unique path distance, transmit angle and receive angle.

Note that the above channel description doesn't require any array geometry and no a priori knowledge of spatial signature of signals. Furthermore, if $\tilde{x}_n(t)$ is the signal transmitted from the nth projector, then the signal received in the mth hydrophone can be expressed by

$$\tilde{y}_m(t) = \sum_{n=1}^{N_T} \int_{-\infty}^{+\infty} \tilde{H}_{m,n}(f,t)\tilde{X}_n(f)e^{j2\pi ft}df + \tilde{w}_m(t). \qquad (2.18)$$

Due to the widespread use of linear arrays in UWA communications, it is instructive to develop a MIMO channel model based on signal processing techniques for linear arrays. Information regarding the angle of departure (AoD) and angle of arrival (AoA) of the propagation paths must be incorporated in the channel model. In this thesis, we consider only linear arrays with uniformly spaced sensors.

Let us consider a MIMO channel with N_T projectors and N_R hydrophones as shown in Fig. 2-7. Let d_T be the inter-sensor spacing at the transmitter and d_R at the receiver. We also denote the pth path distance between the first transmit and first receive sensor as d_p and assume that the distance between the scatterers and the receiver/transmitter is much larger than the size of the receiver/transmitter line arrays. Moreover, we denote ϑ_p the AoD of each path p as seen by the transmitter and φ_p the AoA of each path p as seen by the receiver. We emphasize that each path is uniquely associated with an angle pair (ϑ_p, φ_p). Consequently, the pth path distance

between the mth receive sensor and the nth transmit sensor can be approximated as [79]

$$d_{p,m,n} \simeq d_p + (n-1)d_T \cos(\vartheta_p) - (m-1)d_R \cos(\varphi_p). \qquad (2.19)$$

A wideband MIMO channel model which incorporates the knowledge of spatial signatures of multipath components becomes complicated, hence we simplify the channel model by making use of the narrowband assumption for an array of sensors, namely,

$$\max_{n,m} \left[\frac{(n-1)d_T \cos(\vartheta_p) - (m-1)d_R \cos(\varphi_p)}{c} \right] \ll \frac{1}{W}. \qquad (2.20)$$

The above formula implies that the transit time of the signal across the transmit and the receive array is smaller than $1/W$. In addition, we employ the pth path receive *array manifold vector* [67]

$$\mathbf{u}(\varphi_p) = \frac{1}{\sqrt{N_R}} \begin{bmatrix} 1 \\ e^{-j2\pi f_c d_R \cos(\varphi_p)/c} \\ \vdots \\ e^{-j2\pi(N_r-1)f_c d_R \cos(\varphi_p)/c} \end{bmatrix}. \qquad (2.21)$$

The vector $\mathbf{u}(\varphi_p)$ incorporates the spatial characteristics (spatial signature) of the impinging signal as seen by the receive array, namely it includes the phase differences of the signal received at sensors $2,3,\ldots,N_R$ relative to the signal received at the uppermost sensor of the array. Similarly, we use the pth path transmit array manifold vector

$$\mathbf{v}(\vartheta_p) = \frac{1}{\sqrt{N_T}} \begin{bmatrix} 1 \\ e^{-j2\pi f_c d_T \cos(\vartheta_p)/c} \\ \vdots \\ e^{-j2\pi(N_t-1)f_c d_T \cos(\vartheta_p)/c} \end{bmatrix}, \qquad (2.22)$$

which incorporates the spatial characteristics (spatial signature) of the transmitted signal as seen by the transmit array, i.e., it incorporates the phase differences of the signal transmitted from each of the projectors relative to the uppermost projector of the array.

For the narrowband MIMO case, the response of the mth receive sensor due to transmission

from the nth transmit sensor over the pth path can be written as

$$\tilde{C}_{p,m,n}(f,t) = \frac{b_p(f,t)}{\sqrt{A_p(f)}}e^{j2\pi\breve{f}_p t - j2\pi f_c\left(\tau_p + \frac{(n-1)d_T\cos(\vartheta_p)-(m-1)d_R\cos(\varphi_p)}{c}\right)}e^{-j2\pi f\tau_p} \qquad (2.23)$$

where the propagation time delay of the transmitted signal is defined as $\tau_p \triangleq d_p/c$. Hence, the $N_R \times N_T$ channel matrix of the pth physical path as seen by both the transmit and the receive array is

$$\tilde{\mathbf{C}}_p(f,t) = \frac{b_p(f,t)}{\sqrt{A_p(f)}}e^{j2\pi\breve{f}_p t - j2\pi f_c\tau_p - j2\pi f\tau_p}\mathbf{u}(\varphi_p)\mathbf{v}^\dagger(\vartheta_p). \qquad (2.24)$$

Accounting for all the propagation paths, the $N_R \times N_T$ channel matrix becomes

$$\tilde{\mathbf{C}}(f,t) = \sum_{p=0}^{L-1} \frac{b_p(f,t)}{\sqrt{A_p(f)}}e^{j2\pi\breve{f}_p t - j2\pi f_c\tau_p - j2\pi f\tau_p}\mathbf{u}(\varphi_p)\mathbf{v}^\dagger(\vartheta_p). \qquad (2.25)$$

2.5 Channel parameters

A set of parameters is used to quantify the spreading behavior of UWA channels in time, frequency and space. These parameters help us to identify the number of "essential" diversity branches of UWA channels, which is the key to achieving reliable communications (see Sec. 3.2).

2.5.1 Doppler spread and coherence time

The *coherence time* T_c, is a parameter which describes the time scale over which the channel delay spread function $\tilde{H}(f,t)$ changes "significantly" with respect to t variable. T_c is inversely proportional to the Doppler spread B_d, which in turn is the amount of the spectral broadening caused by the change of the UWA channel. An intuitive way to see this inverse relationship is as follows: recall that the channel delay spread function is given by

$$\tilde{H}(f,t) = \sum_{p=0}^{L-1} \frac{b_p(f,t)}{\sqrt{A_p(f)}}e^{j2\pi\breve{f}_p t - j2\pi f_c\tau_p}e^{-j2\pi f\tau_p}. \qquad (2.26)$$

Note that the magnitude of the each path response changes much slower than its phase. Since each path p has an associated Doppler shift $\breve{f}_p = f_c u_p/c = u_p/\lambda$, we note that the phase term

48

changes by $\pi/2$ (significant phase change) when the path length changes by $\lambda/4$. The time required for this phase change is $\lambda/(4u_p) = (4\check{f}_p)^{-1}$, which is inversely proportional to $\check{f}_p$. For instance, assuming $f_c = 15$ kHz, $c = 1500$ m/sec, and relative mobile velocity of 1 m/sec (2 knots), the time required for a $\pi/2$ phase change is 25 msec. A heuristic way to approximate the Doppler spread of the channel is

$$B_d \approx \max_{p,p'} \left| \check{f}_p - \check{f}_{p'} \right| \tag{2.27}$$

counting only the paths with significant energy. Consequently, the differential phase can be approximated by $2\pi B_d t$, so the time required for a $\pi/2$ change is

$$T_c \approx \frac{1}{4B_d}. \tag{2.28}$$

Depending on how fast the channel response changes with respect to the reciprocal of the signal bandwidth, a channel may be classified either as a *fast fading* or a *slow fading* channel. Slow fading may be considered the channel which remains almost static for a few reciprocal bandwidth intervals. This implies that $W \gg B_d$. Fast fading may be considered the channel which varies within $1/W$ sec. This implies that $W \le B_d$.

2.5.2 Delay spread and coherence bandwidth

The *delay spread* T_d is a parameter which describes the amount of time spreading on the received waveform due to the multipath propagation. The delay spread of the channel can be approximately computed as the time different between the latest to earliest arrival (counting only "significant" energy arrivals). In addition, multipath propagation induces *frequency selective fading* to the received signal since some signal frequencies are enhanced (constructive interference of multipath) and some others are attenuated (destructive interference of multi-path). Frequency selective fading is characterized in terms of the *coherence bandwidth B_c*, which is the range of frequencies over which the channel gain is considered almost constant, namely, all the signal frequencies within the coherence bandwidth of the channel experience approximately the same gain and linear phase. The received signal undergoes frequency selective fading when the bandwidth of the transmitted signal is much greater than the coherence bandwidth of the

channel, i.e., $W \gg B_c$. In digital communications, $W \gg B_c$ implies that the symbol duration is smaller than the delay spread of the channel resulting in ISI in the received signal.

T_d and B_c are inversely related and this can be intuitively seen by examining $\tilde{H}(f, t)$. Each path linearly contributes in phase by $2\pi f \tau_p$. Since different paths yield different delays, the differential phase $2\pi f \left(\tau_p - \tau_{p'} \right) \approx 2\pi f T_d$ dictates how fast $H(f, t)$ fluctuates in the f variable. Note that a frequency sweep by $(4T_d)^{-1}$ Hz rotates the phase term by $\pi/2$ therefore it is plausible to say that the coherence bandwidth can be approximated by

$$B_c \approx \frac{1}{4T_d}.$$ (2.29)

Discrete-time, frequncy-selective fading channel model

When dealing with discrete-time signals, the frequency selective channel is modeled as a tapped-delay line filter with time-varying taps. To demonstrate this, we apply the sampling theorem to the complex envelope of the input signal [46], i.e.,

$$\tilde{x}(t) = \sum_n \tilde{x}[n] \operatorname{sinc}(Wt - n)$$ (2.30)

where we define

$$\operatorname{sinc}(x) \triangleq \frac{\sin(\pi x)}{\pi x}$$ (2.31)

and $\tilde{x}(t)$ is bandlimited to $|f| \leq W/2$. Using Eq. (2.12), the response of the channel is expressed as

$$\tilde{y}(t) = \int_{-\infty}^{+\infty} \tilde{h}(\tau, t) \sum_n \tilde{x}[n] \operatorname{sinc}\left(W(t - \tau) - n \right) d\tau + \tilde{w}(t).$$ (2.32)
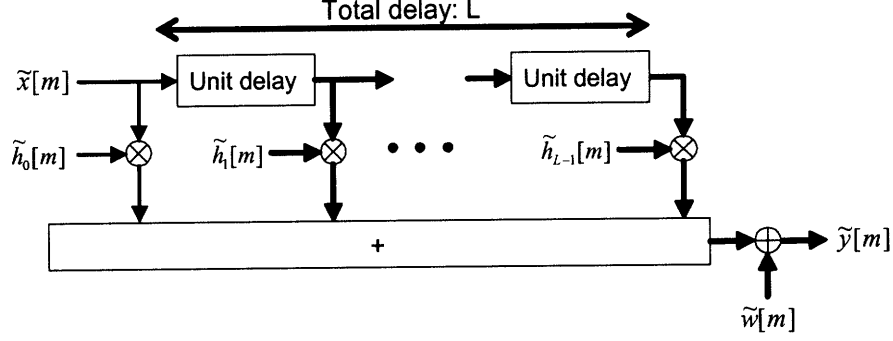
Figure 2-8: Block diagram for discrete-time channel model.

If we assume $W \gg B_d$, we can sample $\tilde{y}(t)$ at multiples of W^{-1}, i.e., $\tilde{y}[m] \triangleq \tilde{y}(m/W)$, so the above equation is written as

$$
\begin{aligned}
\tilde{y}[m] &= \int_{-\infty}^{+\infty} \tilde{h}\left(\tau, \frac{m}{W}\right) \sum_n \tilde{x}[n] \operatorname{sinc}(m - n - W\tau) \, d\tau + \tilde{w}[m] \\
&\stackrel{\ell \triangleq m-n}{=} \sum_\ell \tilde{x}[m - \ell] \underbrace{\int_{-\infty}^{+\infty} \tilde{h}\left(\tau, \frac{m}{W}\right) \operatorname{sinc}(\ell - W\tau) d\tau}_{\tilde{h}_\ell[m]} + \tilde{w}[m] \\
&= \sum_\ell \tilde{x}[m - \ell] \tilde{h}_\ell[m] + \tilde{w}[m]
\end{aligned}
\tag{2.33}
$$

where $\tilde{h}_\ell[m]$ denotes the ℓth (complex) channel tap at discrete time m. Its value is mainly determined by all the rays, whose arrival times (delays) fall in the time window $[\ell/W - 1/2W, \ell/W + 1/2W]$ relative to the first arrival which is considered to occur at time zero. In reality, all UWA channels exhibit a finite T_d so for all practical purposes the above convolution sum can be truncated up to $L \triangleq \lfloor T_d W \rfloor$ terms. Thus, the discrete-time response of the channel is finally written as

$$
\tilde{y}[m] = \sum_{\ell=0}^{L-1} \tilde{x}[m - \ell] \tilde{h}_\ell[m] + \tilde{w}[m].
\tag{2.34}
$$

Figure 2-8 illustrates a block diagram of the discrete-time channel model which is helpful to simulate the wideband characteristics of the UWA channel.

51

Discrete-time, flat-fading channel model

If $W < B_c$ ($\implies T_d W < 1$), the channel is termed as *flat fading* channel, namely all the signal frequencies are weighted by the same channel gain (the received signal preserves the spectral characteristics of the transmitted signal). From Eq. (2.34), we note that the channel at discrete time m can be described by one filter tap, i.e.,

$$\tilde{y}[m] = \tilde{h}_\ell[m]\tilde{x}[m] + \tilde{w}[m]. \tag{2.35}$$

2.5.3 Angle spread and coherence distance

The angle spread at the receiver array Φ, amounts the spread in different AoAs of the arriving paths, while the angle spread at the transmitter array Θ amounts the spread in AoDs of the departing paths. For example at the receiver, the angle spread of the AoAs can be approximately computed as the angle difference between the largest to the smallest polar angle arrival (counting only "significant" energy arrivals), i.e.:

$$\Phi = \max_p \varphi_p - \min_p \varphi_p \tag{2.36}$$

A large Φ causes the multipath components to add constructively or destructively at different parts of the receive array, hence it will lead to *space-selective fading.* Spatial selective fading can be characterized in terms of the *coherence distance* D_c, which is the spatial separation between two receive sensors for which the signal amplitude is almost static. Consequently, two sensors separated by more than the coherence distance tend to experience independent fading. The coherence distance is inversely related to the angle spread, thus environments exhibiting large angle spreads (e.g., small-range, shallow water channels) aid space diversity techniques.

Chapter 3

Exploiting Channel Diversity with Coded Modulation

Although the channel model we described in Chapter 2 encompasses all the key physical characteristics of sound propagation through the ocean, the time variations of each path delay and gain appear to be unpredictable to the system designer. Hence, it is reasonable to characterize the time-varying multipath model statistically. Such a characterization requires a probabilistic model of the channel, which can be obtained by probing the channel and processing statistical measurements. However, as of today, there is no widely accepted statistical model for UWA channels. This is easy to see, for instance, if we try to create a probabilistic model based on the Doppler and multipath spread generated by signal scattering off the moving sea surface. Clearly, different sea states will generate different statistical measurements so claiming a "universal model" which encompasses a wide variety of sea states will be elusive. On the other hand, we need such models to compare different communications systems and to get insight into what types of approaches are worth pursuing.

For the remainder of this thesis, we consider that the channel impulse response $\tilde{h}(\tau, t)$ is a wide-sense stationary (WSS) complex Gaussian process with respect to the t variable, indexed by the τ variable. When there is a need to evaluate the performance of candidate modulation techniques, we assume that $\left|\tilde{h}(\tau, t)\right|$ is either Rician-distributed (existence of line-of-sight path) or Rayleigh-distributed (no line-of-sight path) [53]. Another assumption, which is

justified for the frequencies used in UWA communications, is that processes for different delays are uncorrelated, namely, $\text{cov}\left(\tilde{h}(\tau, t), \tilde{h}(\tau - \Delta\tau, t - \Delta t)\right) = \phi_{\tilde{h}}(\tau, \Delta t)\delta(\Delta t)$. This leads to the ubiquitous wide-sense stationary uncorrelated-scattering channel model (WSS-US) [2],[37]. Based on this model, the channel characterization in terms of delay and Doppler spread can be explained by using the second moments of $\tilde{h}(\tau, t)$ [55].

The WSS-US model must be applied with caution when wideband acoustic signals are transmitted. For instance, the motion-induced Doppler spread of the received signal is not captured by the WSS-US model. A rule of thump to neglect the motion-induced Doppler spread is by restricting the time-bandwidth product of the transmitted waveform as follows [5]:

$$WT \ll \left|\frac{c}{u}\right|. \tag{3.1}$$

If an underwater system experiences motion of $u = 1$ m/sec (2 knots), then c/u is on the order of 10^3. The above condition renders the WSS-US model useful, so when we describe the UWA channel using $\tilde{h}(\tau, t)$, we implicitly assume as short-term stationary channel.

Diversity is an efficient technique that combats channel fading by exploiting the randomness of the channel without increasing the transmitted power. The fact that channel fading dramatically increases the bit-error-rate (BER) of the link can be seen, for example, when one computes the BER of a coherent detection receiver in Rayleigh fading. In this case, the BER is inversely proportional to the SNR [55], where SNR is defined as the ratio of the average signal energy per symbol time to the noise energy per symbol time. In contrast, the error probability of a receiver in the AWGN channel decreases exponentially with the SNR. Hence, at high SNR, the main cause of errors in an acoustic link comes from the channel being in a deep fade.

The Karhunen-Loève expansion theorem [3] lets us deconstruct any received random process in terms of *building blocks* or *diversity branches*, leading to the capability of having multiple, uncorrelated replicas of the transmitted information bearing signal. These replicas may be acquired over different coherent bands (*frequency diversity*) and/or different coherent periods (*time diversity*) and/or spatially separated sensors (*space diversity*). Since the random variables characterizing the received replicas are uncorrelated, the probability of making a bit error by processing all the random variables simultaneously, rather than one, is dramatically reduced. In

practice, UWA channels presents a limited number of diversity branches. Since efficient coded modulation techniques depend on this number, an upper bound of the "essential" diversity branches of the SISO/MIMO channel model is required.

In addition to exploiting the inherent channel diversity, a receiver must mitigate the induced ISI. Towards this end, three approaches are broadly found in the UWA communications literature: single carrier systems with equalization [21], direct-sequence spread spectrum systems [81] and multi-carrier systems [78]. In this thesis, we apply the latter approach. In particular, we employ orthogonal frequency division multiplexing (OFDM) modulation for two reasons: (1) single-carrier and spread spectrum systems can become prohibitively complex since large adaptive equalizers are required to mitigate the long ISI (a typical ISI span is on the order of 100 symbols in medium and long range shallow water channels). For instance, the ubiquitous RLS algorithm has quadratic complexity in the number of taps while linear complexity algorithms are usually required. In contrast, OFDM does not require equalization and uses IFFT/FFT operations for modulation/demodulation.

Chapter summary: We start our discussion by showing that any received signal process can be expanded in an orthogonal series with uncorrelated coefficients by applying the results of the Karhunen-Loeve expansion. Then, we compute an upper bound of the "essential" diversity branches of a SISO/MIMO channel based on its interaction with the signal space. Finally, we describe four diversity methods, which play a key role on the design of the proposed communication systems in Chapter 4. These methods are:

1. Coded modulation and interleaving to achieve time diversity in flat fading channels. The importance of the Hamming distance of the channel code is emphasized.

2. Coupling of coded modulation with OFDM to achieve frequency diversity in frequency selective channels.

3. Maximum-ratio combining (MRC) to achieve receive diversity for systems employing an array of hydrophones at the receiver.

4. Key parameter of space-time signaling techniques to achieve transmit diversity when a system employing an array of transducers at the transmitter.

55

3.1 Karhunen-Loève (K-L) expansion of random processes

In this section, we state the results of the Karhunen-Loeve expansion theorem without proofs, as is applied to random processes. The interested reader is directed to [3],[5] for an extensive discussion of the topic. We denote the channel bandpass input by $x(t)$ and the corresponding channel output by $y(t)$. These signals will be represented by their complex envelopes, e.g., $x(t) \triangleq \mathrm{Re} \left[\sqrt{2} \tilde{x}(t) e^{j2\pi f_c t} \right]$ where $\tilde{x}(t)$ is the complex envelope of $x(t)$ and f_c denotes the nominal carrier frequency in Hz. Also we state that the actual bandpass channel response $h(\tau, t)$ is related to its equivalent complex envelope $\tilde{h}(\tau, t)$ as $h(\tau, t) \triangleq \mathrm{Re} \left[2\tilde{h}(\tau, t) e^{j2\pi f_c (t-\tau)} \right]$.

Recall that the noiseless received signal process is expressed by Eq. (2.12)

$$\tilde{y}(t) = \int \tilde{x}(t - \tau) \tilde{h}(\tau, t) d\tau. \tag{3.2}$$

From the WSS assumption, it follows that $E \left[\tilde{h}(\tau, t_1) \tilde{h}(\tau, t_2) \right] = 0 \ \forall t_1 \neq t_2$. Consequently, the second moment characteristics of $\tilde{y}(t)$ are:

$$R_{\tilde{y}}(t_1, t_2) = E\left[\tilde{y}(t)\tilde{y}^*(t_2) \right] = \int\limits_{-\infty}^{+\infty} \int\limits_{-\infty}^{+\infty} \tilde{x}(t_1 - \tau) E\left[\tilde{h}(\tau, t_1)\tilde{h}^*(v, t_2) \right] \tilde{x}^*(t_2 - v) d\tau dv. \tag{3.3}$$

$$E\left[\tilde{y}(t_1)\tilde{y}(t_2) \right] = 0 \ \forall t_1 \neq t_2. \tag{3.4}$$

The condition in Eq. (3.3) corresponds to a non-stationary process while the condition in Eq. (3.4) enables us to the express the correlation function of $y(t)$ as

$$R_y(t_1, t_2) = \mathrm{Re} \left[R_{\tilde{y}}(t_1, t_2) e^{j2\pi f_c (t_1 - t_2)} \right], \tag{3.5}$$

i.e., we have the desired one-to-one correspondence between the correlation functions of $y(t)$ and $\tilde{y}(t)$.

The Karhunen-Loève (K-L) expansion theorem states that $\tilde{y}(t)$ can be expressed as a linear combination of orthogonal deterministic functions, which each of them is weighted by an

56

uncorrelated coefficient, namely:

$$\tilde{y}(t) = \lim_{K \longrightarrow \infty} \sum_{m=1}^{K} \tilde{y}_m \tilde{\psi}_m(t). \tag{3.6}$$

The above limit converges in the "mean square sense". The functions $\tilde{\psi}_m(t)$ are orthonormal, i.e.

$$\int_{-\infty}^{+\infty} \tilde{\psi}_m(t)\tilde{\psi}_n^*(t)dt = \left\{ \begin{matrix} 0, & m \neq n \\ 1, & m = n \end{matrix} \right\} \tag{3.7}$$

and are also the eigenfunctions, which satisfy the integral equation

$$\lambda_m \tilde{\psi}_m(t) = \int_{-\infty}^{+\infty} R_{\tilde{y}}(t, t')\tilde{\psi}_m(t')dt'. \tag{3.8}$$

λ_m is the mth eigenvalue of the correlation function $R_{\tilde{y}}(t_1, t_2)$. Due to the Hermitian symmetry of $R_{\tilde{y}}(t_1, t_2)$, λ_m are positive real numbers. The coefficients $\tilde{y}_m$ are determined by

$$\tilde{y}_m = \int_{-\infty}^{+\infty} \tilde{y}(t)\tilde{\psi}_m^*(t)dt \tag{3.9}$$

and it can be shown that they are uncorrelated random variables, namely

$$E[\tilde{y}_m \tilde{y}_n^*] = \left\{ \begin{matrix} 0, & m \neq n \\ \lambda_m, & m = n \end{matrix} \right\}. \tag{3.10}$$

There is a simple relationship between the eigenvalues and eigenfunctions of $R_y(t_1, t_2)$ and $R_{\tilde{y}}(t_1, t_2)$ provided that $\tilde{\psi}_m(t)$ are bandlimited and their bandwidth is much smaller than f_c. Precisely stated, if the eigenvalues of $R_{\tilde{y}}(t_1, t_2)$ are $\lambda_1, \lambda_2, \ldots$ and the associated eigenfunctions are $\tilde{\psi}_1(t), \tilde{\psi}_2(t), \ldots$ then

1. the eigenvalues of of $R_y(t_1, t_2)$ are $\lambda_1/2, \lambda_2/2, \ldots$

2. the eigenfunctions associated with each $\lambda_m/2$ are $\text{Re}\left[\sqrt{2}\tilde{\psi}_m(t)e^{j2\pi f_c t}\right]$ and $\text{Im}\left[-\sqrt{2}\tilde{\psi}_m(t)e^{j2\pi f_c t}\right]$ for $m = 1, 2, \ldots$

57

Then, the corresponding bandpass process is given by

$$
\begin{aligned}
y(t) &= \lim_{K \longrightarrow \infty} \sum_{m=1}^{K} \text{Re}[\tilde{y}_m] \, \text{Re}\left[\sqrt{2}\tilde{\psi}_m(t)e^{j2\pi f_c t}\right] + \text{Im}[\tilde{y}_m] \, \text{Im}\left[-\sqrt{2}\tilde{\psi}_m(t)e^{j2\pi f_c t}\right] \\
&= \lim_{K \longrightarrow \infty} \sum_{m=1}^{K} \text{Re}\left[\sqrt{2}\tilde{y}_m\tilde{\psi}_m(t)e^{j2\pi f_c t}\right]
\end{aligned}
\tag{3.11}
$$

The representation in Eq. (3.6) lets us characterize any received process in terms of building blocks or diversity branches, namely each received process can be represented as a linear combination of deterministic orthogonal functions, which are weighted by uncorrelated random variables. Note that each building block can be detected at the receiver via matched filtering, as indicated in Eq. (3.9). Thus, if all the waveforms $\text{Re}\left[\sqrt{2}\tilde{\psi}_m(t)e^{j2\pi f_c t}\right]$ are simultaneously transmitted, they will go through parallel diversity branches (channels), where each diversity branch introduces a random complex gain $\tilde{y}_m$ of mean square value λ_m. The salutary effect of diversity against channel fading is now obvious. Let us assume that P is the probability that the received signal strength falls below some critical value when the signal is transmitted over any diversity branch. If one transmits the same signal across D diversity branches, then P^D is the probability the received signal strength will simultaneously fall below the critical value in all the branches. Obviously, $P^D \ll P$ as D increases, thus the reliability of the link increases dramatically.

It is important to note that the K-L representation of the received process is conditioned upon the knowledge of the transmitted waveform. For a communications system, we need a representation which is valid for all the waveforms which we could potentially transmit. This is a formidable task due to the difficulty of solving the integral equation (3.8).

3.2   Essential number of channel diversity branches

In this section, we tie the K-L representation of the received process with a simplified representation by using the gross properties of the channel (delay spread, Doppler spread, angle spread) and the gross parameters of the transmitted signal (time-bandwidth product). Although a fading channel has an infinite number of eigenvalues (or diversity branches or degrees of freedom), there are only a finite number of them which are large enough to be exploited. In order to find

the "essential" diversity branches we need to understand the interaction between the signal space and the channel. For SISO channels, this interaction happens in two dimensions, namely in time and frequency [3]. For MIMO channels, the interaction happens in four dimensions, namely, time, frequency and the two spatial dimensions at the transmitter and the receiver [63]. We start by decomposing the SISO channel with respect to fixed delay and Doppler bins, which are determined by the bandwidth and duration of the transmitted signal, respectively. This leads to the notion of time and frequency diversity. Then, we decompose the MIMO channel with respect to fixed angle beams, which are determined by the spatial resolution of the transmit and receive arrays. This leads to the notion of transmit and receive (spatial) diversity.

Our aim is to approximate the received signal $\tilde{y}(t)$ by an expression of the form

$$\tilde{y}(t) = \sum_{i=1}^{D} a_i f_i(t) \qquad (3.12)$$

where $f_i(t)$ are deterministic functions, a_i are complex random variables and D depends on the gross properties of the channel and the gross parameters of the transmitted signal. The above equation implies that correlation of the received signal can be written as

$$R_{\tilde{y}}(t_1, t_2) = \sum_{i=1}^{D} \sum_{j=1}^{D} E\left[a_i a_j^*\right] f_i(t_1) f_j^*(t_2) \qquad (3.13)$$

Correlation functions of this form are called *separable kernels* and are known to exhibit at most D positive eigenvalues [3]. Hence, D serves as an upper bound of the number of "essential" diversity branches associated with the channel.

3.2.1 SISO channels

As we explained in Sec. 2.4.1, each arriving multipath component is associated with a unique delay and Doppler shift. Let W denote the signal bandwidth and T symbolize the total signaling duration. Then, a receiver cannot resolve two path delays less than $1/W$, or two path Doppler shifts less than $1/T$. Thus, it is plausible to decompose the channel in terms of the resolvable delays and Doppler shifts. Towards this end, it is instructive to employ the delay-Doppler spread function $\tilde{U}(\tau, v)$, which is related to the time-varying frequency response $\tilde{H}(f, t)$ via a

double Fourier transform [2]

$$\tilde{H}(f,t) = \int\limits_{-\infty}^{+\infty} \int\limits_{-\infty}^{+\infty} \tilde{U}(\tau,v)e^{-2\pi f\tau}e^{j2\pi vt}d\tau dv. \qquad (3.14)$$

The physical interpretation of $\tilde{U}(\tau,v)$ is that of a channel consisting of moving scatterers, each of which is associated with a fixed (complex) gain $\tilde{U}(\tau,v)$, a delay τ and a Doppler shift v.

We assume that $W \gg B_d$, where B_d stands for the maximum Doppler spread B_d of the channel; therefore, any induced spectral broadening on the received signal can be neglected. In addition, we let $T \gg T_d$, where T_d stands for the multipath spread T_d of the channel; hence, any induced time broadening on the received signal is ignored. Applying the sampling theorem to $\tilde{U}(\tau,v)$ with respect to the τ variable we have

$$\tilde{U}(\tau,v) = \sum_m U\left(\frac{m}{W},v\right) \operatorname{sinc}(W\tau - m). \qquad (3.15)$$

Since all physical channels of interest have limited T_d, it is valid to approximate the above infinite sum with a sum of approximately $1 + \lfloor T_d W \rfloor$ terms, therefore the above equation can be approximated as

$$\tilde{U}(\tau,v) \simeq \sum_{m=0}^{\lfloor T_d W \rfloor} \tilde{U}\left(\frac{m}{W},v\right) \operatorname{sinc}(W\tau - m). \qquad (3.16)$$

Similarly, applying the sampling theorem to $\tilde{U}\left(\frac{m}{W},v\right)$ with respect to the v variable we have

$$\tilde{U}(\tau,v) \simeq \sum_{m=0}^{\lfloor T_d W \rfloor} \sum_n \tilde{U}\left(\frac{m}{W},\frac{n}{T}\right) e^{j\pi T\left(v-\frac{n}{T}\right)} \operatorname{sinc}(Tv - n)\operatorname{sinc}(W\tau - m). \qquad (3.17)$$

If the scatterers falling within the mth delay bin $[m/W, m/W + 1/W]$ demonstrate a Doppler spread of $[-B_d(m)/2, B_d(m)/2]$, the above infinite sum can be approximated by a finite sum of approximately $1 + \lfloor TB_d(m) \rfloor$ terms. Thus, the above equation becomes

$$\tilde{U}(\tau,v) \simeq \sum_{m=0}^{\lfloor T_d W \rfloor} \sum_{n=-\lfloor TB_d(m) \rfloor/2}^{\lfloor TB_d(m) \rfloor/2} \tilde{U}\left(\frac{m}{W},\frac{n}{T}\right) e^{j\pi T\left(v-\frac{n}{T}\right)} \operatorname{sinc}(Tv - n)\operatorname{sinc}(W\tau - m). \qquad (3.18)$$

60

Substituting Eq. (3.18) into Eq. (3.14) we have [63]

$$\tilde{H}(f,t) = \sum_{m=0}^{\lfloor T_d W \rfloor} \sum_{n=-\lfloor TB_d(m) \rfloor/2}^{\lfloor TB_d(m) \rfloor/2} \frac{1}{WT} \tilde{U}\left(\frac{m}{W}, \frac{n}{T}\right) e^{-2\pi f \frac{m}{W}} e^{j2\pi t \frac{n}{T}}, \qquad (3.19)$$

where $f \in [-W/2, W/2]$ and $t \in [0, T]$. The above equation is analogous to a double Fourier series expansion [46], thus we can write

$$\tilde{U}\left(\frac{m}{W}, \frac{n}{T}\right) = \int_0^T \int_{-W/2}^{W/2} \tilde{H}(f,t) e^{2\pi f \frac{m}{W}} e^{-j2\pi t \frac{n}{T}} df\, dt. \qquad (3.20)$$

$\tilde{H}(f,t)$ describes the physical channel in Eq. (2.16), rewritten for convenience as:

$$\tilde{H}(f,t) = \sum_{p=0}^{L-1} \frac{b_p(f,t)}{\sqrt{A_p(f)}} e^{j2\pi \check{f}_p t - j2\pi f_c \tau_p} e^{-j2\pi f \tau_p}, \qquad (3.21)$$

we observe that $\tilde{U}\left(\frac{m}{W}, \frac{n}{T}\right)$ is determined by all the rays whose delays and Doppler shift fall within the delay bin $[m/W, m/W + 1/W]$ and the Doppler bin $[n/T - 1/2T, n/T + 1/2T]$ respectively.

Recall that the noiseless received signal can be expressed as:

$$\tilde{y}(t) = \int_{-W/2}^{W/2} \tilde{X}(f)\tilde{H}(f,t) e^{j2\pi ft} df, \qquad (3.22)$$

where $\tilde{X}(f)$ is the Fourier transform of the transmitted signal. Substituting Eq. (3.19) into Eq. (3.22) we have

$$
\begin{aligned}
\tilde{y}(t) &= \sum_{m=0}^{\lfloor T_d W \rfloor} \sum_{n=-\lfloor TB_d(m) \rfloor/2}^{\lfloor TB_d(m) \rfloor/2} \frac{1}{WT} \tilde{U}\left(\frac{m}{W}, \frac{n}{T}\right) e^{j2\pi t \frac{n}{T}} \int_{-W/2}^{W/2} \tilde{X}(f) e^{-2\pi f \frac{m}{W}} e^{j2\pi ft} df \\
&= \sum_{m=0}^{\lfloor T_d W \rfloor} \sum_{n=-\lfloor TB_d(m) \rfloor/2}^{\lfloor TB_d(m) \rfloor/2} \frac{1}{WT} \tilde{U}\left(\frac{m}{W}, \frac{n}{T}\right) e^{j2\pi t \frac{n}{T}} \tilde{x}\left(t - \frac{m}{W}\right). \qquad (3.23)
\end{aligned}
$$

The above expression is analogous to Eq. (3.12), therefore the number of essential diversity branches D is upper bounded by the number of non-zero elements in the above double sum
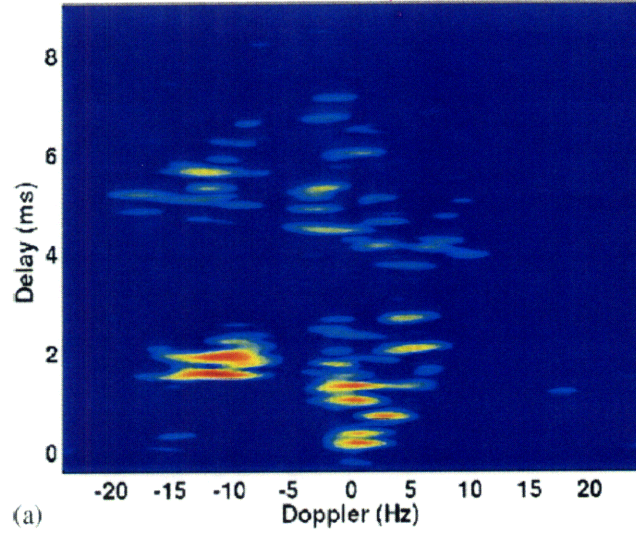
Figure 3-1: Scattering function of a shallow water acoustic channel [77]. The plot is in log scale and the range of the color scale is 16 dB.

([3])

$$D \leq \sum_{m=0}^{\lfloor T_d W \rfloor} \sum_{n=-\lfloor TB_d(m) \rfloor/2}^{\lfloor TB_d(m) \rfloor/2} . \tag{3.24}$$

Note that the upper bound depends on the channel physical properties, i.e., delay and Doppler spread, and the signal properties, i.e., time-bandwidth product. It is instructive to assume a constant Doppler spread for all delay bins. Then, Eq. (3.24) reduces to

$$D \leq \left(1 + \lfloor T_d W \rfloor\right)\left(1 + \lfloor TB_d \rfloor\right), \tag{3.25}$$

which is translated as follows: the number of frequency diversity branches is upper bounded by $1 + \lfloor T_d W \rfloor$ and the number of time diversity branches is upper bounded by $1 + \lfloor TB_d \rfloor$.

The fundamental dependency between delay and Doppler spread is expressed via the channel *scattering function* [2],[5],[55]. The scattering function $S(\tau, v)$ is defined via the correlation function of $\tilde{U}(\tau, v)$, namely,

$$R_U(\tau, \tau + \Delta\tau; v, v + \Delta v) = E\left[U(\tau + \Delta\tau, v + \Delta v)U^*(\tau, v)\right] = S(\tau, v)\delta(\Delta\tau)\delta(\Delta v) \tag{3.26}$$

and describes the average channel power distribution in the delay-Doppler plane. As an example, Fig. 3-1 shows an estimated scattering function of a shallow water channel (16 m depth, 238 m range). Note that the Doppler spread is approximately 20 Hz and the multipath spread is approximately 8 msec. Several researchers have used the scattering function to characterize various UWA channels [37],[77]. Unfortunately, the scattering function is rarely known in practice. One way to estimate it is by using the cross-ambiguity function (see Appendix B).

3.2.2 MIMO channels

We assume a MIMO system with transmit and receive line arrays with uniformly spaced sensors. The receive array has length $L_R = N_R d_R$, where N_R and d_R stand for the number of sensors and the inter-sensor spacing (in meters), respectively. Similarly, the transmit array has length $L_T = N_T d_T$, where N_T and d_T stand for the number of sensors and the inter-sensor spacing (in meters), respectively. Based on the analogy between the finite time resolution of a band-limited system and the finite angular resolution of an array-size limited system, we represent the time-varying frequency response channel matrix $\tilde{C}(f, t)$ (see Eq. (2.25)) using fixed uniformly spaced AoAs and AoDs. The angular domain approach to MIMO narrowband channel modeling with discrete linear arrays was originally developed by Sayeed [63] and is analogous to representing the channel is beamspace, which is a concept widely studied in array processing [67]. The AoA/AoD spacings depend on the affordable resolution of the receive/transmit array. Since the receiver cannot resolve paths with AOAs less than λ/L_R and similarly, the transmitter cannot resolve paths with AoDs less than λ/L_T , this suggests that the angular domain should be sampled at fixed angular spacings of λ/L_R at the receiver and at fixed angular spacings of λ/L_R at the transmitter. Fig. 3-2(a) illustrates the MIMO physical channel modeling, described by $\tilde{C}(f, t)$. Each propagation path is uniquely associated with a delay, Doppler shift, AoA and AoD. Fig. 3-2(b) shows the proposed angular representation of the MIMO channel, which is based on a priori fixed transmit and receive angular bins. The (k, ℓ)th entry of the "angular domain" channel matrix is formed by all the physical paths whose direction falls into the ℓth transmit and kth receive angular bin. To describe the angular domain representation, it is necessary to point out the resolvability associated with a discrete line array.

The spatial signature of a received signal with AoA $\varphi_p \in [-90°, 90°]$ is given by the receive
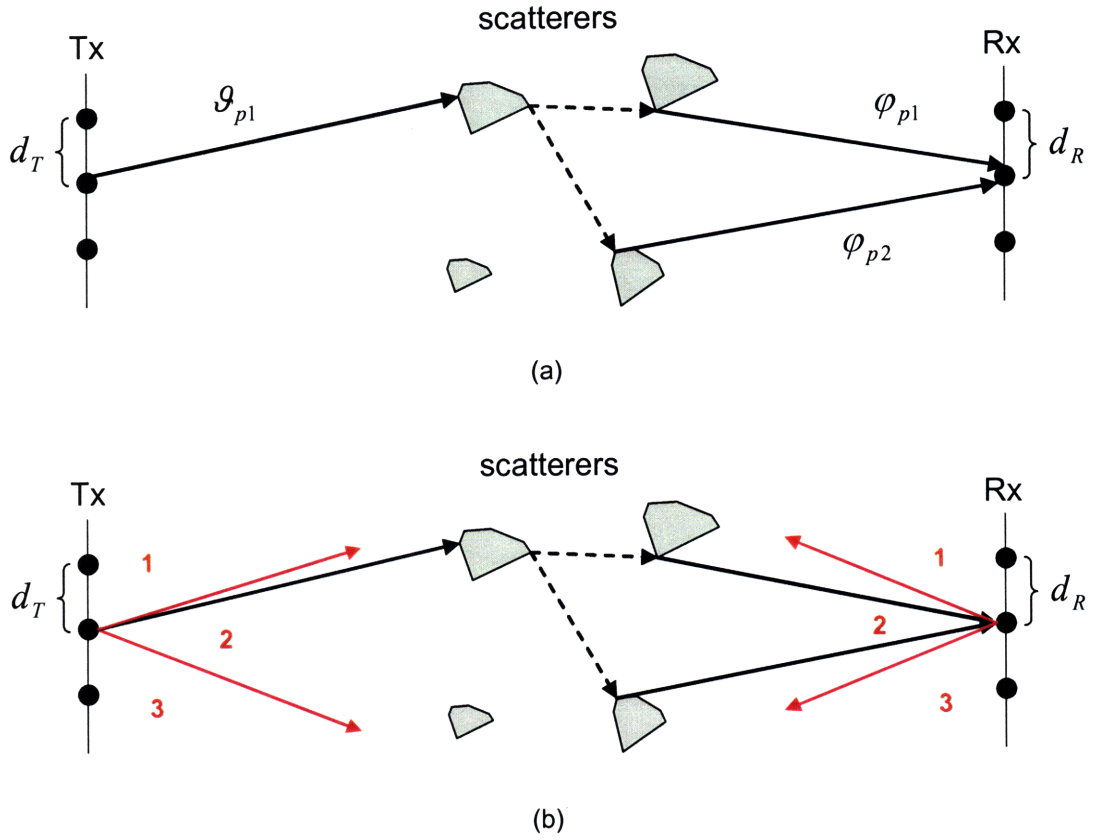
Figure 3-2: Modeling representations of a MIMO channel. (a) Physical modeling. There are two physical paths associated with two angle pairs, i.e., $(\vartheta_{p1}, \varphi_{p1})$ and $(\vartheta_{p1}, \varphi_{p2})$. The 3×3 channel matrix $\mathbf{H}(f, t)$ has two non-zero entries. (b) Angular domain representation. At the transmitter, three sensors partition the angular space into three bins each of which has width λ/L_T. At the receiver the angular width is λ/L_R. Here, the 3x3 channel matrix has only one non-zero entry at position (2,2)

array manifold vector $\mathbf{u}(\varphi_p)$, defined in Eq. (2.21). Let $\Omega_p = \cos(\varphi_p)$ be the directional cosine with respect to the receive array, the array response due to an input narrowband signal with AoA φ_{p2} when the array is steered at φ_{p1} is given by [67],[79]

$$B_R(\Omega_{p1} - \Omega_{p2}) = \mathbf{u}^\dagger(\varphi_{p1})\mathbf{u}(\varphi_{p2}) = \tag{3.27}$$

$$= \frac{1}{N_R}e^{j\pi\frac{d_R}{\lambda}(\Omega_{p1}-\Omega_{p2})(N_R-1)}\frac{\sin\left(\pi\frac{L_R}{\lambda}(\Omega_{p1}-\Omega_{p2})\right)}{\sin\left(\pi\frac{d_R}{\lambda}(\Omega_{p1}-\Omega_{p2})\right)} \tag{3.28}$$

The function $B_R(\Omega_{p1} - \Omega_{p2})$ is well known in the array processing community as the *beam pattern*. Similarly, we can define $B_T(\Omega_{p1}-\Omega_{p2}) = \mathbf{v}^\dagger(\vartheta_{p1})\mathbf{v}(\vartheta_{p2})$. The beam pattern is a periodic function with period λ/d_R, attains its maximum value at $\Omega_{p1} - \Omega_{p2} = \ell\,(\lambda/d_R)$, $k = 0, 1, \ldots$ and has zero crossings at $\Omega_{p1} - \Omega_{p2} = k\,(\lambda/L_R)$, $\ell = 1, \ldots N_R - 1$ [79]. Fig. 3-3(a) pictures the effect of varying d_R for a fixed length array L_R. When $d_R = \lambda$, then there is a main lobe aimed at broadside (90°) and two grating lobes aimed at endfire (0° and 180°). This situation is analogous to aliasing in frequency domain filtering due to undersampling of the spatial field. When $d_R = \lambda/2$, then there is only one main lobe aimed at broadside. This situation is analogous to sampling at the Nyquist frequency. Moreover, the highest side lobe is -13 dB below the main lobe. When $d_R = \lambda/4$, then the beam pattern is exactly the same as in the case where $d_R = \lambda/2$. This situation is analogous to sampling beyond the Nyquist rate. Just as oversampling cannot increase resolvability in time domain, adding more sensors for a fixed L_R cannot increase angular resolvability. This can also be seen by noting that the beam width of the main lobe is equal to $2\lambda/L_R$. Fig. 3-3(b) shows the effect of increasing L_R (we keep d_R fixed and increase the number of sensors). Clearly, just as larger bandwidth increases time resolvability, a larger array size L_R renders thinner the main lobe resulting in finer angular resolution. Now we show how to represent signals in the angular domain.

Since $B(\Omega_{p1} - \Omega_{p2}) = 0$ for $\Omega_{p1} - \Omega_{p2} = k\,(\lambda/L_R)$, $k = 1, \ldots N_R - 1$, the N_R basis (steering) vectors are chosen as follows [79]:

$$\mathbf{U}_R = \left[\mathbf{u}(0) \quad \mathbf{u}\left(\tfrac{\lambda}{L_R}\right) \quad \ldots \quad \mathbf{u}\left((N_R-1)\tfrac{\lambda}{L_R}\right)\right] \tag{3.29}$$

Obviously, $\mathbf{U}_r$ is an orthonormal basis, which provides the angular basis of the received signals

$$L_R = 6, d_R = \lambda \qquad L_R = 6, d_R = \frac{\lambda}{2} \qquad L_R = 6, d_R = \frac{\lambda}{4}$$

(a)

$$L_R = 8, d_R = \frac{\lambda}{2} \qquad L_R = 16, d_R = \frac{\lambda}{2}$$

(b)
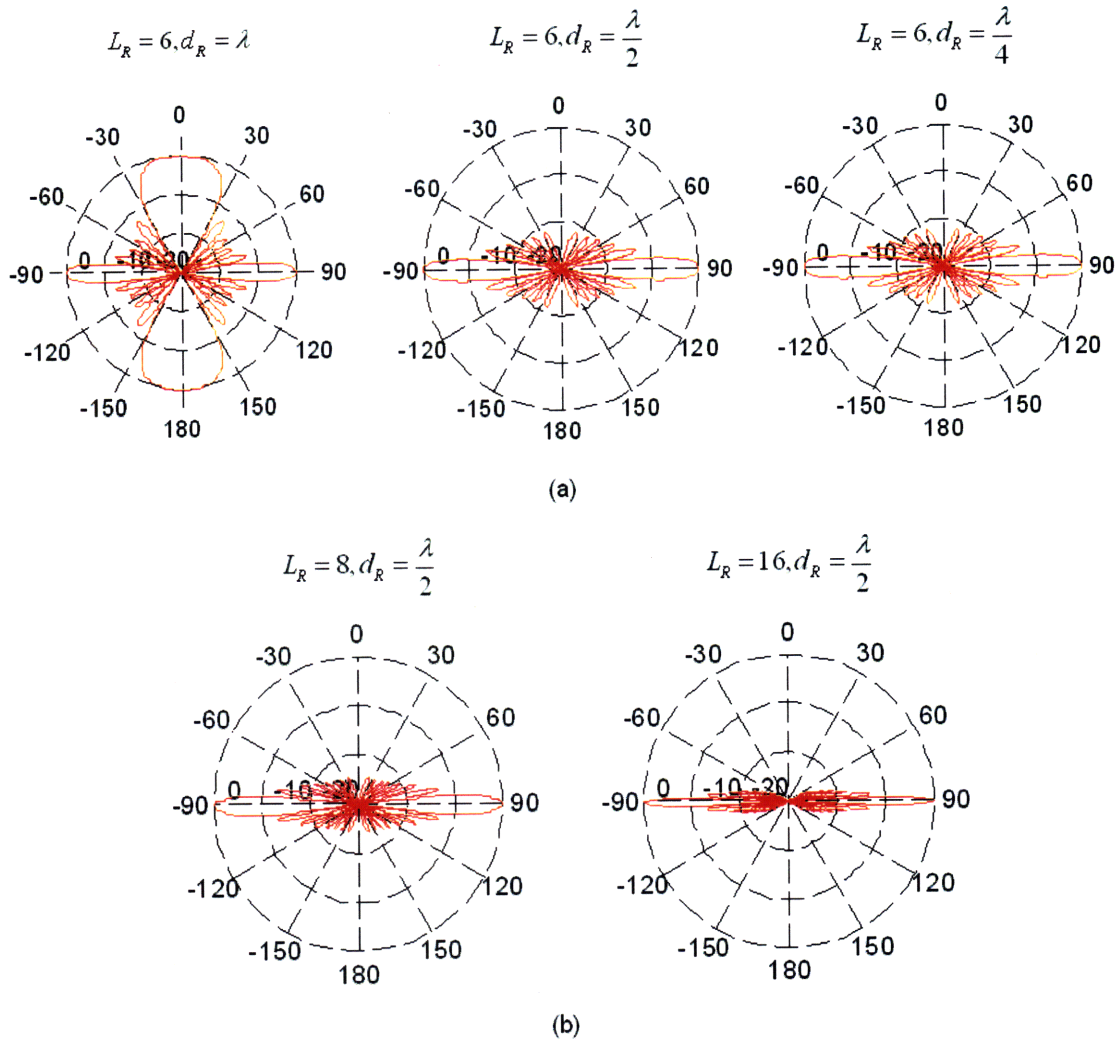
Figure 3-3: Receive beam patterns steered at broadside (90°). The plots are in dB. Note that the beam pattern is always symmetric along the 0°-180° axis so the lobes always appear in pairs. (a) Effect of varying the spacing d_R for a fixed length array L_R. (b) Effect of varying the array length L_R for fixed d_R.

we seek. Any ray impinging the receiver will have most of its energy along one particular $\mathbf{u}\left(k\lambda/L_R\right)$ and very little energy along all the other basis vectors due to the relative small (-13 dB) side lobes. Consequently, the suggested basis provides an (approximate) decomposition of the total received signal into components along different $\mathbf{u}\left(k\lambda/L_R\right)$. Similarly, we choose

$$\mathbf{V}_T = \begin{bmatrix} \mathbf{v}(0) & \mathbf{v}\left(\frac{\lambda}{L_T}\right) & \dots & \mathbf{v}\left((N_T - 1)\frac{\lambda}{L_T}\right) \end{bmatrix} \tag{3.30}$$

as the angular basis of the transmitted signals.

Fig. 3-4 illustrates some examples of different angular bases. Fig. 3-4(a) shows the case when the sensors do not sample the spatial field sufficiently (sparsely spaced). Then, each $\mathbf{u}\left(k/L_R\right)$ is associated with two main lobes inside the visible region due to spatial aliasing. Clearly, this situation is undesired because it leads to a non unique representation of the incoming signal. Fig. 3-4(b) pictures the case of sampling the spatial field at exactly the Nyquist rate. Then, each basis vector $\mathbf{u}\left(k/L_R\right)$ is associated with one main lobe in the direction of k/L_R resulting to the desired unique angular representation of the incoming signal. In Fig. 3-4(c), we note that the basis vectors $\mathbf{u}\left(k/L_R\right)$, $k = L_R + 1, \dots, N_R - L_R$ do not have any main lobes because they do not correspond to any physical directions. Fig. 3-4 leads to the conclusion that unique angular representation of the received (or transmit) signal occurs only when $d_R \leq \lambda/2$ (or $d_T \leq \lambda/2$).

We now apply the angular transformation to the MIMO, narrowband UWA channel described in Eq. (2.25)

$$\tilde{\mathbf{C}}(f,t) = \sum_{p=0}^{L-1} \frac{b_p(f,t)}{\sqrt{A_p(f)}} e^{j2\pi \breve{f}_p t - j2\pi f_c \tau_p - j2\pi f \tau_p} \mathbf{u}(\varphi_p)\mathbf{v}^\dagger(\vartheta_p). \tag{3.31}$$

Since $\mathbf{U}_R$ and $\mathbf{V}_T$ are respectively $N_R \times N_R$ and $N_T \times N_T$ unitary matrices, the angular (coordinate) representation of the channel matrix $\tilde{\mathbf{C}}(f,t)$ is [79]

$$\tilde{\mathbf{C}}^{\mathbf{a}}(f,t) = \mathbf{U}_R^\dagger \tilde{\mathbf{C}}(f,t)\mathbf{V}_T \tag{3.32}$$

(a) $L_R = 3, \dfrac{d_R}{\lambda} = 1$

(b) $L_R = 3, \dfrac{d_R}{\lambda} = 0.5$

(c) $L_R = 3, \dfrac{d_R}{\lambda} = 0.25$
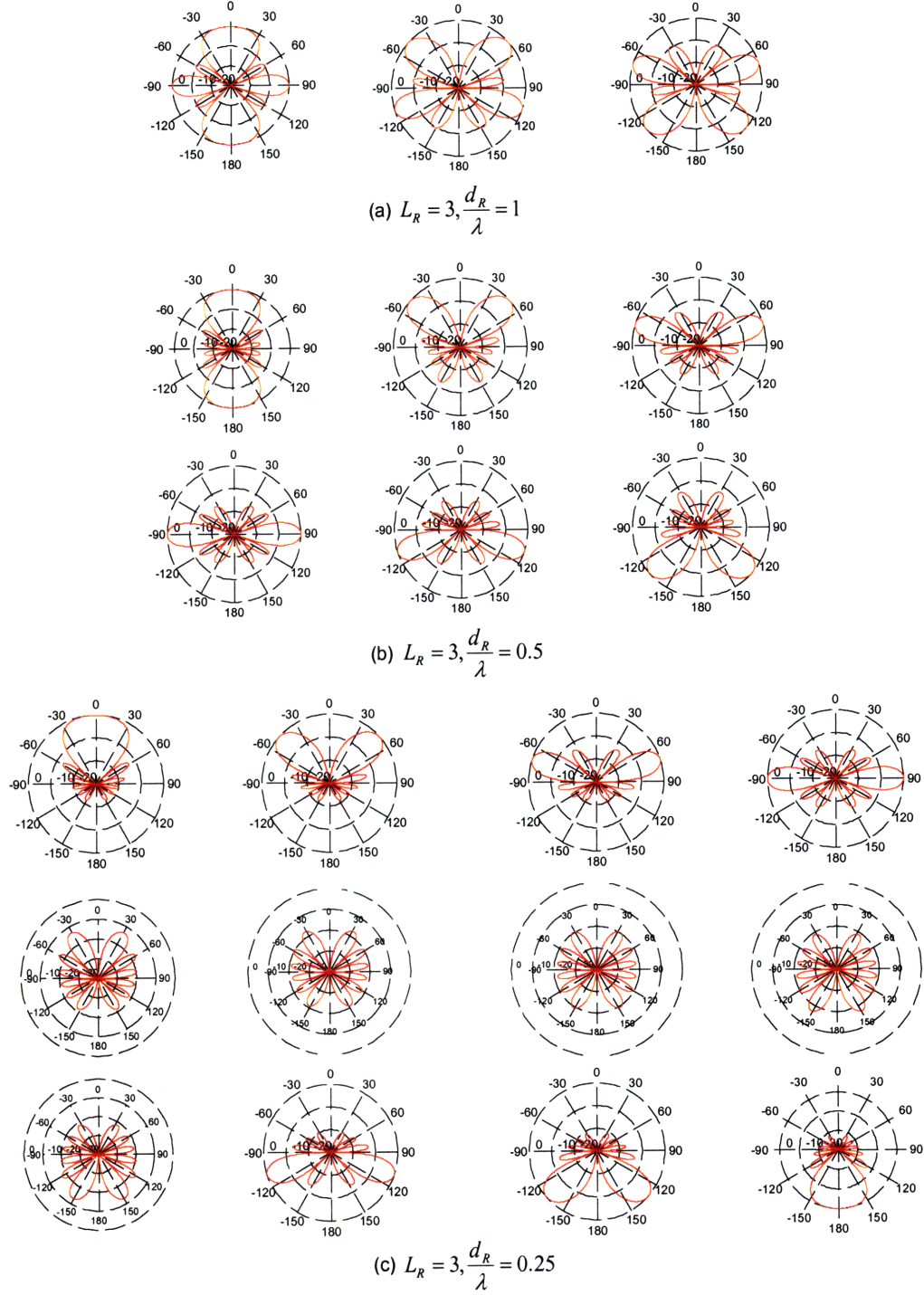
Figure 3-4: Different angular basis represented by their beam patterns. The plots are in dB scale. (a) sensors as sparsely spaced, i.e., $d_R/\lambda > 0.5$. (b) sensors are critically spaced, i.e., $d_R/\lambda = 0.5$. (c) sensors are densely spaced, i.e., $d_R/\lambda < 0.5$.

where each (k, ℓ) entry of $\tilde{\mathbf{C}}^{\mathbf{a}}(f, t)$, $k = 1, \ldots N_R - 1$, $\ell = 1, \ldots N_T - 1$ is given by

$$\tilde{C}^a_{k,\ell}(f, t) = \sum_{p=0}^{L-1} \frac{b_p(f, t)}{\sqrt{A_p(f)}} e^{j2\pi \check{f}_p t - j2\pi f_c \tau_p - j2\pi f \tau_p} \underbrace{\mathbf{u}^\dagger \left(k \frac{\lambda}{L_R} \right) \mathbf{u}(\varphi_p)}_{B_R\left(\frac{k\lambda}{L_R} - \cos(\varphi_p)\right)} \underbrace{\mathbf{v}^\dagger(\vartheta_p) \mathbf{v} \left(\ell \frac{\lambda}{L_T} \right)}_{B_T\left(\cos(\vartheta_p) - \frac{\ell\lambda}{L_T}\right)}. \qquad (3.33)$$

To simplify the notation, we define as

$$B_{k,\ell}(\varphi_p, \vartheta_p) \triangleq B_R \left(k \frac{\lambda}{L_R} - \cos(\varphi_p) \right) B_T \left(\cos(\vartheta_p) - \ell \frac{\lambda}{L_T} \right), \qquad (3.34)$$

so the above equation can be written as

$$\tilde{C}^a_{k,\ell}(f, t) = \sum_{p=0}^{L-1} \frac{b_p(f, t)}{\sqrt{A_p(f)}} B_{k,\ell}(\varphi_p, \vartheta_p) e^{j2\pi \check{f}_p t - j2\pi f_c \tau_p - j2\pi f \tau_p}. \qquad (3.35)$$

Let Φ_k denote the set of all rays p whose angle φ_p falls into the angular window

$$\left| \cos(\varphi_p) - k \frac{\lambda}{L_R} \right| \leq \frac{\lambda}{L_R}. \qquad (3.36)$$

Similarly, let Θ_ℓ denote the set of all rays p whose angle ϑ_p falls into the angular window

$$\left| \cos(\vartheta_p) - \ell \frac{\lambda}{L_T} \right| \leq \frac{\lambda}{L_T}. \qquad (3.37)$$

Then, the value of $\tilde{C}^a_{k,\ell}(f, t)$ is mainly determined by the gains of all the rays that fall within $\Phi_k \cap \Theta_\ell$. Note that the rays in $\Phi_k \cap \Theta_\ell$ are unresolved in the angular domain. Let $\tilde{C}^a_{k,\ell}(f, t)$ be the response of the corresponding SISO channel with some delay spread $T_d^{k,\ell}$ and some Doppler spread $B_d^{k,\ell}$. Obviously, $T_d^{k,\ell} \leq T_d$ (maximum delay spread) and $B_d^{k,\ell} \leq B_d$ (maximum Doppler spread). Following the analysis in Sec. 3.2.1, the number of essential diversity branches for this particular SISO channel is upper bounded by

$$D_{k,\ell} \leq \sum_{m=0}^{\lfloor T_d^{k,\ell} W \rfloor} \sum_{n=-\lfloor T B_d^{k,\ell}(m) \rfloor/2}^{\lfloor T B_d^{k,\ell}(m) \rfloor/2}. \qquad (3.38)$$

Hence, the number of the essential diversity branches of the MIMO channel is upper bounded

by the number of non-zero elements in the following quadruple sum

$$D \le \sum_{k=0}^{N_R-1} \sum_{\ell=0}^{N_T-1} \sum_{m=0}^{\lfloor T_d^{k,\ell} W \rfloor} \sum_{n=-\lfloor TB_d^{k,\ell}(m) \rfloor/2}^{\lfloor TB_d^{k,\ell}(m) \rfloor/2} . \tag{3.39}$$

Observe that D depends on the relationship of the delay and Doppler spread with the angular spread; obviously, larger angular spreads result in larger delay and Doppler spreads.

3.3 Diversity

In this section, coded modulation is employed to exploit diversity in time, frequency, and spatial domain. Before proceeding further, the following terminological convention is used: we denote as $x[m]^1$ the transmitted channel symbol at time m, which is a complex number drawn from a symbol constellation (e.g., PSK) with unit average energy. The minimum Euclidean distance between any two symbols of the constellation is d_E. N_t/N_r stands for the number of projectors/hydrophones of the system. An amplitude scaling factor of $1/\sqrt{N_t}$ is introduced before transmission so that the transmitted average symbol energy is maintained to one when multiple projectors are used. We denote as $w_i[m]$ the additive noise process of the ith diversity branch, which is modeled as an i.i.d. complex Gaussian random variable with zero mean and

$$E\left[|w_i[m]|^2\right] = N_0, \forall i, m. \tag{3.40}$$

We symbolize as $h_i[m]$ the channel fade (or gain) of the ith diversity branch, which is independent for different branches. Moreover, we assume that $h_i[m]$ has unit second moment, i.e.,

$$E\left[|h_i[m]|^2\right] = 1, \forall i, m. \tag{3.41}$$

When $x[m]$ is transmitted over the ith diversity branch, the received symbol at each sensor is modeled as

$$y_i[m] = h_i[m]x[m] + w_i[m] \tag{3.42}$$

---

[1] For the remainder of the thesis, we deal with baseband signals only so we drop the ~ notation.

and the average SNR per symbol duration is

$$SNR_a \triangleq \frac{E\left[|h_i[m]|^2\right] \cdot E\left[|x[m]|^2\right]}{E\left[|w_i[m]|^2\right]} = \frac{1}{N_0}.$$ (3.43)

For our purposes, we suppose that $h_i[m]$ is perfectly known at the receiver. In practice, the channel gains are estimated by sending pilot symbols and the accuracy of the channel estimates depends on how fast the channel varies. The condition to achieve reliable coherent tracking is: $B_d/W < 10^{-2}$ [28]. We further assume that $|h_i[m]|$ is *Rician* distributed with a pdf [26]

$$p_{|h_i|}(a) = 2a(1+K)e^{-(K+a^2(1+K))}I_0\left(2a\sqrt{K(1+K)}\right), \ a \geq 0$$ (3.44)

where $I_0(\cdot)$ is the zero-order modified Bessel function of the first kind[2] and K is the *Rician parameter* defined as the ratio of the energy of the non faded signal component to the energy of the diffused multipath component. Note that when $K = 0$ the above distribution reduces to a Rayleigh distribution.

3.3.1 Time diversity and the impact of Hamming distance

Time diversity is achieved by coupling channel coding with *interleaving*. The choice of a short code should be based on the maximization of the number of distinct symbols (i.e., Hamming distance) between any two codewords [26],[38] rather than the maximization of the minimum Euclidean distance, the latter being the central parameter of good codes for the classical AWGN channel. Fig. 3-5 illustrates an example of time interleaving and its effect on recovering a codeword; when no interleaving is employed, the codeword x_1 cannot be decoded since severe channel fading affects all three symbols. On the contrary, when interleaving is employed, x_1 can be reliably decoded from the other two unfaded symbols.

Let us transmit a codeword $\mathbf{x} = [x_1, \ldots, x_D]^\mathsf{T}$ of D channel symbols. We do not distinguish among linear block codes or convolutional codes or TCM codes. Interleaving ensures that consecutive symbols of the same codeword are transmitted at different coherence time intervals; thus, each transmitted symbol undergoes independent fading. Without loss of generality, we

---

[2]$I_0(x) = \frac{1}{2\pi}\int_0^{2\pi} e^{x\cos t}dt$

71
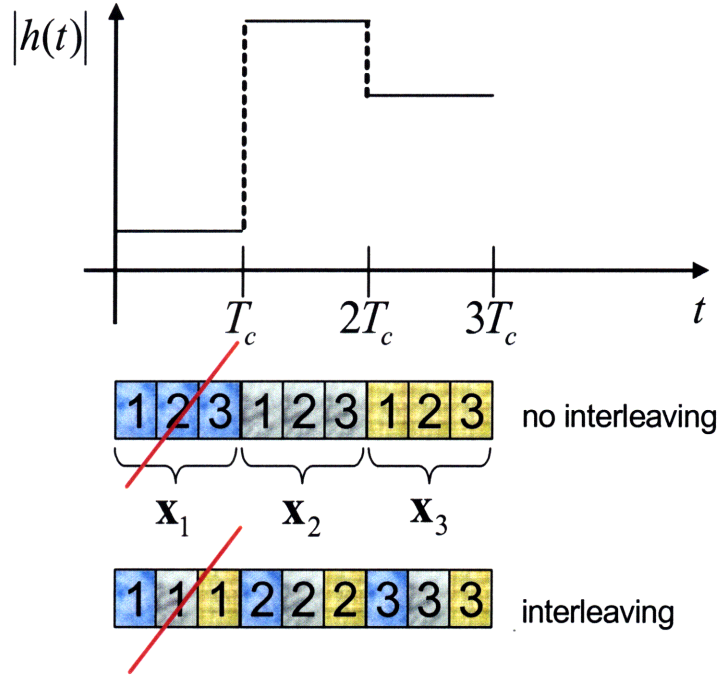
Figure 3-5: Three codewords are transmitted. Each codeword consists of three channel symbols. The codewords are transmitted over successive symbol periods (top) and interleaved (bottom).

assume a flat fading channel model (see Eq. (2.35)); however, the same results apply to the frequency selective model. After demodulation, the received symbols are expressed as

$$y_i = h_i x_i + w_i, \quad i = 1, \ldots, D \tag{3.45}$$

where $h_1, \ldots, h_D$ are independent random variables. Note that we dropped the time index for convenience. It is instructive to put the above equation in vector form as follows

$$\mathbf{y} = \mathbf{Hx} + \mathbf{w} \tag{3.46}$$

where $\mathbf{H} = \mathrm{diag}(h_1, \ldots, h_D)$, $\mathbf{w} = [w_1, \ldots, w_D]^{\mathsf{T}}$ and $\mathbf{y} = [y_1, \ldots, y_D]^{\mathsf{T}}$.

Given $\mathbf{H}$ and $\mathbf{x}$, the received vector $\mathbf{y}$ is conditionally Gaussian with mean $\mathbf{Hx}$ and covariance matrix $N_o \mathbf{I}_D$, where $\mathbf{I}_D$ is the $D \times D$ identity matrix. The conditional pairwise error probability (PEP) of confusing the codeword $\mathbf{x}$ with $\hat{\mathbf{x}}$ when $\mathbf{x}$ is transmitted can be cast as a binary

detection problem for the vector AWGN channel and hence, it can be written as [79]

$$\Pr\left\{\mathbf{x} \to \hat{\mathbf{x}} \mid \mathbf{H}\right\} = Q\left(\frac{\|\mathbf{Hx} - \mathbf{H\hat{x}}\|}{2\sqrt{N_0/2}}\right) = Q\left(\sqrt{\frac{SNR_a}{2}\sum_{i=1}^{D}|h_i|^2\,|x_i - \hat{x}_i|^2}\right) \qquad (3.47)$$

where $Q(\cdot)$ is the complementary cumulative distribution function[3] of an $N(0,1)$ random variable. The receiver structure which achieves the above error probability is the *matched filter receiver*. After reception of $\mathbf{y}$, the receiver decides between $\mathbf{x}$ and $\hat{\mathbf{x}}$ based on the following operation:

$$\frac{(\mathbf{H}(\mathbf{x} - \hat{\mathbf{x}}))^\dagger \mathbf{y}}{\|\mathbf{H}(\mathbf{x} - \hat{\mathbf{x}})\|} \overset{\mathbf{x}}{\underset{\hat{\mathbf{x}}}{\gtrless}} 0. \qquad (3.48)$$

Using the well known inequality [55]

$$Q(x) \le e^{-x^2/2}, \quad x > 0, \qquad (3.49)$$

Eq. (3.47) can be upper bounded as follows:

$$\Pr\left\{\mathbf{x} \longrightarrow \hat{\mathbf{x}}/h_1, \ldots, h_D\right\} \le \exp\left(-\frac{SNR_a}{4}\sum_{i=1}^{D}|h_i|^2\,|x_i - \hat{x}_i|^2\right). \qquad (3.50)$$

Taking the expectation of $\Pr\left\{\mathbf{x} \longrightarrow \hat{\mathbf{x}}/h_1, \ldots, h_D\right\}$ with respect to $h_1, \ldots, h_D$, we have

$$\Pr\left\{\mathbf{x} \longrightarrow \hat{\mathbf{x}}\right\} \le E\left[\exp\left(-\frac{SNR_a}{4}\sum_{i=1}^{D}|h_i|^2\,|x_i - \hat{x}_i|^2\right)\right] \qquad (3.51)$$

Since

$$\min_i |x_i - \hat{x}_i|^2 \le d_E^2, \qquad (3.52)$$

then Eq. (3.51) is upper bounded as

$$\Pr\left\{\mathbf{x} \longrightarrow \hat{\mathbf{x}}\right\} \le E\left[\exp\left(\frac{-d_E^2 SNR_a}{4}\sum_{i=1}^{D}|h_i|^2\right)\right] \qquad (3.53)$$

The above equation manifests that coded modulation and interleaving can average out the channel fade over time, i.e., time diversity is accomplished. For instance, if we assume that h_i

---

[3]$Q(x) = \frac{1}{\sqrt{2\pi}}\int_x^\infty e^{-t^2/2}dt,\ x > 0$

is a second moment ergodic process then by invoking the law of large numbers and using Eq. (3.41) we claim that $\sum_{i=1}^{D} |h_i|^2$ approaches D as $D \to \infty$. Hence, $\Pr\{\mathbf{x} \longrightarrow \hat{\mathbf{x}}\}$ asymptotically behaves as $\exp\left(-d_E^2 \cdot D \cdot SNR_a/4\right)$ which manifests that the fading channel degrades to an AWGN channel.

Under the independent Rician fading assumption, Eq. (3.51) can be expressed as [26]

$$\Pr\{\mathbf{x} \to \hat{\mathbf{x}}\} \le \prod_{i=1}^{D} \frac{1+K}{1+K+\frac{SNR_a}{4}|x_i - \hat{x}_i|^2} \exp\left(-\frac{K\frac{SNR_a}{4}|x_i - \hat{x}_i|^2}{1+K+\frac{SNR_a}{4}|x_i - \hat{x}_i|^2}\right). \qquad (3.54)$$

It is instructive to simplify the above formula by identifying various regimes. When $K \gg \frac{SNR_a}{4}|x_i - \hat{x}_i|^2$, Eq. (3.54) becomes

$$\Pr\{\mathbf{x} \to \hat{\mathbf{x}}\} \le \prod_{i=1}^{D} \exp\left(-\frac{SNR_a}{4}|x_i - \hat{x}_i|^2\right) = \exp\left(-\frac{SNR_a}{4}\|\mathbf{x} - \hat{\mathbf{x}}\|\right). \qquad (3.55)$$

The above result is not surprising since as $K \to \infty$ the fading channel degrades to an AWGN channel and the effect of the Euclidean distance between any pair of codewords is significant for reliable detection. At low SNR_a where $1 + K \gg \frac{SNR_a}{4}|x_i - \hat{x}_i|^2$, Eq. (3.54) becomes

$$\Pr\{\mathbf{x} \to \hat{\mathbf{x}}\} \le \prod_{i=1}^{D} \exp\left(-\frac{K}{K+1}\frac{SNR_a}{4}|x_i - \hat{x}_i|^2\right) = \exp\left(-\frac{K}{K+1}\frac{SNR_a}{4}\|\mathbf{x} - \hat{\mathbf{x}}\|\right). \qquad (3.56)$$

The above result is similar to that of Eq. (3.55) because the dominant source of errors is the noise process rather than the fading process. At high SNR_a and low K where $1 + K \ll \frac{SNR_a}{4}|x_i - \hat{x}_i|^2$, Eq. (3.54) becomes

$$\Pr\{\mathbf{x} \to \hat{\mathbf{x}}\} \le \prod_{i=1}^{d_H(\mathbf{x},\hat{\mathbf{x}})} \frac{(1+K)e^{-K}}{\frac{SNR_a}{4}|x_i - \hat{x}_i|^2} \qquad (3.57)$$

where $d_H(\mathbf{x}, \hat{\mathbf{x}})$ stands for the Hamming distance between the codewords $\mathbf{x}$ and $\hat{\mathbf{x}}$ and equals to the number for which $x_i \ne \hat{x}_i$, $i = 1, \ldots, D$. Clearly, $d_H(\mathbf{x}, \hat{\mathbf{x}}) \le D$. We can rewrite the above equation as

$$\Pr\{\mathbf{x} \to \hat{\mathbf{x}}\} \le \frac{\left((1+K)e^{-K}\right)^{-d_H(\mathbf{x},\hat{\mathbf{x}})}}{d_P(\mathbf{x}, \hat{\mathbf{x}})} \left(\frac{SNR_a}{4}\right)^{-d_H(\mathbf{x},\hat{\mathbf{x}})}. \qquad (3.58)$$

where

$$d_P(\mathbf{x}, \hat{\mathbf{x}}) \triangleq \prod_{i=1}^{d_H(\mathbf{x}, \hat{\mathbf{x}})} |x_i - \hat{x}_i|^2 \tag{3.59}$$

is called the *squared product distance* of the pair $(\mathbf{x}, \hat{\mathbf{x}})$ [79].

Using the union bound [26], an upper bound to the average error probability can be achieved as follows:

$$P_e \leq \sum_{\mathbf{x} \neq \hat{\mathbf{x}}} \Pr\{\mathbf{x} \to \hat{\mathbf{x}}\} = \sum_{\mathbf{x} \neq \hat{\mathbf{x}}} \frac{\left((1+K)e^{-K}\right)^{-d_H(\mathbf{x}, \hat{\mathbf{x}})}}{d_P(\mathbf{x}, \hat{\mathbf{x}})} \left(\frac{SNR_a}{4}\right)^{-d_H(\mathbf{x}, \hat{\mathbf{x}})} \tag{3.60}$$

Among all terms in the above equation, the ones with minimum Hamming distance $d_H(\mathbf{x}, \hat{\mathbf{x}})$ will dominate the sum. Denoting

$$\min_{(\mathbf{x}, \hat{\mathbf{x}})} d_H(\mathbf{x}, \hat{\mathbf{x}}) = d_H \tag{3.61}$$

and

$$\min_{(\mathbf{x}, \hat{\mathbf{x}}): d_H(\mathbf{x}, \hat{\mathbf{x}}) = d_H} d_P(\mathbf{x}, \hat{\mathbf{x}}) = d_P \tag{3.62}$$

the error probability can be asymptotically approximated as

$$P_e \simeq \varepsilon(d_H, d_P) \frac{\left((1+K)e^{-K}\right)^{-d_H}}{d_P} \left(\frac{SNR_a}{4}\right)^{-d_H} \tag{3.63}$$

where $\varepsilon(d_H, d_P)$ is the number of codewords having Hamming distance d_H and squared product distance d_P. Note that P_e decays as $SNR_a^{-d_H}$ and is inversely proportional to d_P. In the communications literature, d_H refers to the time *diversity gain* (also called the *code diversity*) of the code and d_P refers to the *coding gain* of the code. Eq. (3.63) stresses the following rule when short codes are to be used for high SNR fading channels: *codes which maximize both the Hamming and the product squared distance over any pair of codewords must be preferred.* This is not surprising since the major source of errors at high SNR is the multiplicative fading process rather than the noise process so an efficient code should focus on averaging out the channel fade. This is in contrast with the AWGN channel where efficient codes maximize the Euclidean distance over any pair of codewords.

It is significant to point out the difference between the coding and the diversity gain. The

75
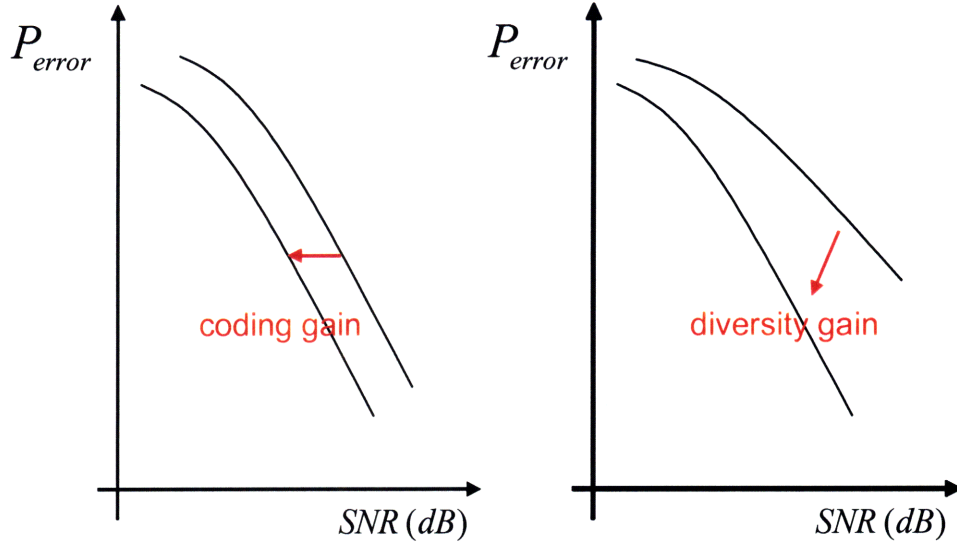
Figure 3-6: Difference between coding gain and diversity gain.

coding gain manifests itself by shifting the BER curve to the left with respect to SNR. On the other hand, diversity gain manifests itself by increasing the slope in the BER curve. Fig. 3-6 highlights the difference between coding and diversity gain. Note that the SNR advantage due to diversity gain increases with SNR but remains constant with coding gain.

Another argument which emphasizes the importance of the diversity gain is the following: it is more effective to maximize the minimum squared product distance for codes with small Hamming distances rather than for codes with large Hamming distances [26]. Suppose we have a code with Hamming distance d_H and minimum squared product distance d_{P1}. Suppose we also find another code with the same d_H but larger minimum squared product distance d_{P2}. From Eq. (3.63), the increase in coding gain due to increasing the minimum squared product distance for the same error probability is

$$SNR_1\,(dB) - SNR_2\,(dB) \simeq \frac{10}{d_H} \log \left(\frac{d_{P_2}}{d_{P_1}} \frac{\varepsilon(d_H, d_{P_1})}{\varepsilon(d_H, d_{P_2})} \right) \ \text{dB}. \tag{3.64}$$

We note that the increase in coding gain in inversely proportional to the Hamming distance. For instance, if $d_{P2}/d_{P1} = 2$, $\varepsilon(d_H, d_{P_1}) = \varepsilon(d_H, d_{P_2})$ and $d_H = 2$, then the increase in coding gain is 1.5 dB where when $d_H = 4$ then the increase in coding gain is only 0.75 dB.

76

3.3.2 Frequency diversity using OFDM

Frequency diversity is achieved by averaging the channel fade over the frequency domain. This presumes that the signal bandwidth is much larger than the coherence bandwidth of the channel or equivalently, the receiver has the ability to resolve multipath. However, multipath channels induce ISI. Consequently, a receiver must accomplish two tasks: (1) eliminate ISI and (2) exploit full frequency diversity. Towards this end, we employ channel coding, interleaving and OFDM modulation. Appendix A shows that the proposed system is analogous to a single-carrier system which combines channel coding, interleaving and linear equalization in the time domain. In addition, Appendix A demonstrates that a system which employs a DFE exploits full frequency diversity without channel coding, thus justifying the huge success of the DFE in UWA communications.

Before we show how frequency diversity is exploited using OFDM, it is informative to present the OFDM system model.

OFDM system model

OFDM is a digital multi-carrier modulation scheme which distributes the channel symbols (e.g., PSK) over a number of sub-carriers[4] that are spaced apart at precise frequencies. In addition, the sub-carriers are overlapped in an orthogonal manner to result in a bandwidth efficient frequency division multiplexing transmission. In practice, OFDM signals are generated using the Fast Fourier Transform (FFT) algorithm, which is easily implementable in hardware.

Another advantage of OFDM over single-carrier schemes is its ability to combat ISI. Channel equalization is simplified, and thus receiver complexity is reduced. That is because OFDM may be viewed as transmitting many parallel low-rates narrowband signals rather than one fast-rate wideband signal. For this reason, OFDM has developed into a popular scheme for wideband digital communication systems (IEEE 802.16, IEEE 802.11a, digital tv, cellular systems, DSL, etc.).

Figure 3-7 shows the components of the OFDM system. A vector of N_c channel symbols $\mathbf{x} = [x_0, ..., x_{N_c-1}]^\mathsf{T}$ is transmitted over different sub-bands (N_c symbols modulate N_c different

---

[4]Sometimes are also called sub-bands or tones
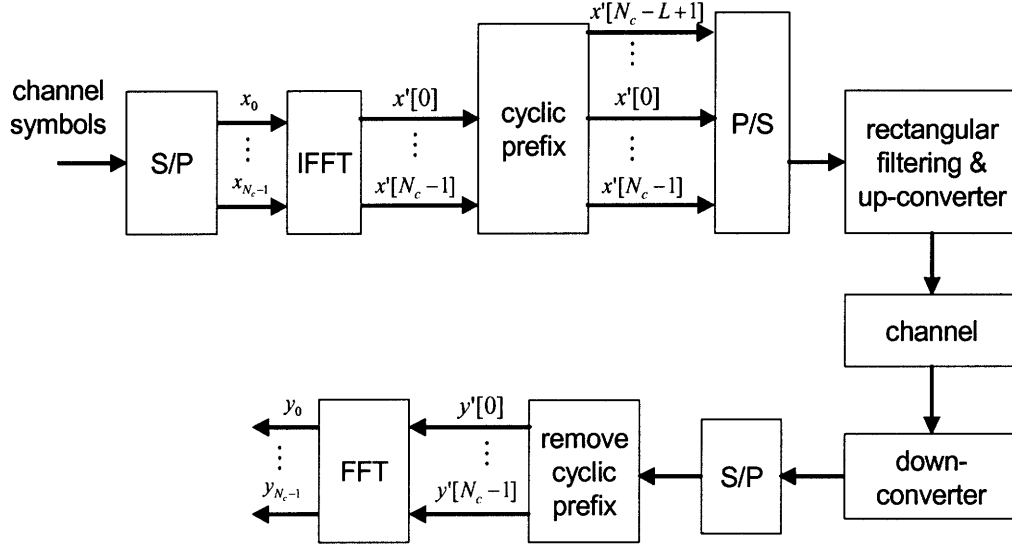
Figure 3-7: Block diagram of OFDM system.

tones) in the frequency domain. If W is the available bandwidth, the spacing between different sub-bands is W/N_c. In practice, it is desired that $W/N_c \ll B_c$ to ensure flat fading for each sub-band and $W/N_c \gg B_d$ to make Doppler spread tolerable. The vector $\mathbf{x}$ is transformed from frequency domain to time domain by using IFFT operations. The resulting vector is denoted as $\mathbf{x}'$ and its entries are computed as follows:

$$x'[n] = \frac{1}{\sqrt{N_c}} \sum_{k=0}^{N_c-1} x_k e^{j2\pi kn/N_c}, n = 0, ..., N_c - 1. \tag{3.65}$$

A guard interval T_g equal to the delay spread $T_d = L/W$ (L equals the number of taps) is introduced between successive vector transmissions in order to eliminate interference from previous vector transmissions caused by multipath propagation. A cyclic prefix $[x'[N_c + L - 1], ..., x'[N_c - 1]]$ is transmitted during the guard interval. Consequently, for every vector $\mathbf{x}'$, an $N_c + L - 1$ vector

$$\mathbf{x}_{cp} = [x'[N_c - L + 1], ..., x'[N_c - 1], x'[0], ..., x'[N_c - 1]]^\mathsf{T} \tag{3.66}$$

is transmitted and $x_{cp}[n] = x'[n - L \bmod N_c]$. Note that the time it takes to transmit the vector

$\mathbf{x}'$ is $(N_c + L)/W$ sec. Then, each vector is serialized, low-pass filtered using a rectangular window, upconverted and passed through the channel.

As we already explained, the UWA channel can be modeled as a tapped delay line filter with time-varying taps (see Eq. (2.34)). The received sequence is given by

$$y'[n] = \sum_{\ell=0}^{L-1} h_\ell[n] x_{cp}[n - \ell] + w'[n], n = 0, ..., N_c + L - 2 \qquad (3.67)$$

where $\mathbf{h}[n] = [h_0[n], \ldots, h_{L-1}[n]]$ denotes the descrete-time channel impulse response at time n and $w'[n]$ models the additive, white, complex Gaussian noise process. Equivalently, the above equation can be expressed as

$$y'[n] = \sum_{\ell=0}^{L-1} h_\ell[n] x'[n - \ell - L \mod N_c] + w'[n], n = 0, ..., N_c + L - 2. \qquad (3.68)$$

The receiver discards the received sequence for $n = 0, ..., L - 2$, hence we can write

$$y'[n] = \sum_{\ell=0}^{L-1} h_\ell[n] x'[n - \ell - L \mod N_c] + w'[n], n = L - 1, ..., N_c + L - 2 \qquad (3.69)$$

or changing the variable n to $m = n - L$ we have

$$y'[m] = \sum_{\ell=0}^{L-1} h_\ell[m + L] x'[m - \ell \mod N_c] + w'[n], m = 0, ..., N_c - 1. \qquad (3.70)$$

Note that $x'[m - \ell \mod N_c]$ for $m < \ell$ corresponds to a value in the cyclic prefix allowing for independent processing of OFDM symbols. Using FFT demodulation, the received signal at the rth sub-carrier is

$$y_r = \frac{1}{\sqrt{N_c}} \sum_{m=0}^{N_c-1} y'[m] e^{-j2\pi rm/N_c}, r = 0, ..., N_c - 1. \qquad (3.71)$$

79

Substituting Eq. (3.70) and (3.65) into Eq. (3.71), the signal component can be written as

$$
\begin{aligned}
y_r &= \sum_{k=0}^{N_c-1} \sum_{\ell=0}^{L-1} x_k \underbrace{\sum_{m=0}^{N_c-1} \frac{1}{N_c} h_\ell[m+L] e^{j2\pi m(k-r)/N_c} e^{-j2\pi k\ell/N_c}}_{G_\ell(k-r)} \\
&= \sum_{k=0}^{N_c-1} \sum_{\ell=0}^{L-1} x_k G_\ell(k-r) e^{-j2\pi k\ell/N_c} \\
&= x_r \underbrace{\sum_{\ell=0}^{L-1} G_\ell(0) e^{-j2\pi r\ell/N_c}}_{\bar{H}_r} + \underbrace{\sum_{k\neq r,k=0}^{N_c-1} \sum_{\ell=0}^{L-1} x_k G_\ell(k-r) e^{-j2\pi k\ell/N_c}}_{B_r}
\end{aligned}
\tag{3.72}
$$

and the noise component can be expressed as

$$
w_r = \frac{1}{\sqrt{N_c}} \sum_{m=0}^{N_c-1} w'[m] e^{-j2\pi rm/N_c}, r = 0, ..., N_c - 1.
\tag{3.73}
$$

Note that $w_0, ..., w_{N_c-1}$ are i.i.d. complex Gaussian random variables since the FFT is a unitary transform. The received signal at the rth sub-carrier can be written as

$$
y_r = x_r \bar{H}_r + B_r + w_r, \quad r = 0, ..., N_c - 1
\tag{3.74}
$$

where $\bar{H}_r$ is a multiplicative fading term and B_r is the intercarrier interference (ICI) term. Note that the time variability (Doppler spread) of the channel during FFT demodulation destroys the orthogonality among the sub-bands resulting in ICI. Due to rectangular filtering at the transmitter, high sidelobes (-13 dB relative to the mainlobe) enter in every sub-band from neighboring sub-bands, hence high levels of ICI can degrade the BER system performance. One approach to suppress ICI is by reducing the height of the sidelobes. This can be accomplished by employing time domain windowing at the transmitter [88].

For N_c sufficiently large, the central limit theorem can be invoked and the ICI can be modeled as a Gaussian random process with some covariance function which depends on the Doppler power spectrum of the channel. It is instructive to put Eq. (3.74) in matrix form. Denoting as $\mathbf{y} = [y_0, ..., y_{N_c-1}]^\mathsf{T}$ and $\mathbf{w} = [w_0, ..., w_{N_c-1}]^\mathsf{T}$, then Eq. (3.74) can be expressed as

follows:

$$\mathbf{y} = \mathbf{U}\mathbf{H}\mathbf{U}^\dagger\mathbf{x} + \mathbf{w} \tag{3.75}$$

where $\mathbf{U}$ stands for the $N_c \times N_c$ DFT matrix given by $[\mathbf{U}]_{k,m} = \exp\left(-j2\pi km/N_c\right)/\sqrt{N_c}$ and

$$\mathbf{H} = \begin{bmatrix} h_0[0] & 0 & \cdots & h_{L-1}[0] & \cdots & h_2[0] & h_1[0] \\ h_1[1] & h_0[1] & \cdots & 0 & \cdots & h_3[1] & h_2[1] \\ \vdots & \vdots & \vdots & \vdots & \vdots & \vdots & \vdots \\ h_{L-1}[L-1] & h_{L-2}[L-1] & \cdots & \cdots & \cdots & 0 & 0 \\ \vdots & \vdots & \vdots & \vdots & \vdots & \vdots & \vdots \\ 0 & \cdots & \cdots & \cdots & \cdots & h_0[N_c-2] & 0 \\ 0 & 0 & \cdots & \cdots & \cdots & h_1[N_c-1] & h_0[N_c-1] \end{bmatrix} \tag{3.76}$$

If the channel is invariant for N_c symbol durations, i.e., $h_\ell[n] = h_\ell$, then $\mathbf{H}$ becomes a circulant matrix (the rows are cyclic shifts of each other). Since every circulant matrix is diagonalized by the DFT matrix of the same size [61], $\mathbf{U}\mathbf{H}\mathbf{U}^\dagger$ becomes a diagonal matrix with diagonal elements equal to the corresponding eigenvalues of $\mathbf{H}$, which are given by

$$H_r = \sum_{\ell=0}^{L-1} h_\ell e^{-j2\pi r\ell/N_c}, \quad r = 0, ..., N_c - 1. \tag{3.77}$$

Note that H_r models the channel frequency response at frequency $f_r = rW/N_c$ and the received signal at the rth sub-carrier is given by

$$y_r = x_r H_r + w_r, \quad r = 0, ..., N_c - 1. \tag{3.78}$$

The above equation demonstrates that OFDM, via the cyclic prefix, transforms any slowly-varying (with respect to the OFDM symbol duration), frequency-selective (ISI) channel to N_c parallel, flat (no ISI) fading channels.

Due to the cyclic prefix, OFDM modulation yields the following bandwidth efficiency:

$$\eta = \frac{\frac{N_c}{T_{OFDM}+T_d}}{W} \frac{\text{symbols/sec}}{\text{total bandwidth}} = \frac{N_c}{N_c + L} \text{ symbols/sec/Hz.} \tag{3.79}$$

Observe that when $N_c \gg L$, OFDM achieves the same bandwidth efficiency as its single carrier counterpart. Furthermore, $L/(N_c + L)$ fraction of the average power is allocated to the cyclic prefix, hence to minimize the power overhead we must choose N_c as large possible. However, mobility and inherent time variability of the channel constraint the largest value N_c can possibly take. The sub-carrier spacing W/N_c must be much greater than the Doppler spread B_d in order for the receiver to unambiguously detect the different modulating sub-carriers.

Achieving full frequency diversity with coded OFDM

Having introduced OFDM, we return back to the main focus of this section, which is the achievable frequency diversity of any coding scheme combined with interleaving and OFDM modulation. Explicit frequency diversity is achieved by coding across different sub-bands. Since the number of sub-bands is designed to be much larger than the coherence bandwidth of the channel, correlated fading exists between consecutive sub-bands. Thus, distributing a code between successive sub-bands will not enhance system's performance against fading. Approximately the number of uncorrelated sub-bands is W/B_c so enhanced fading mitigation is possible if a code is distributed across sub-bands separated by at least B_c.

For our purposes, we assume that the impulse response of the channel $\mathbf{h} = [h_0, \ldots, h_{L-1}]$ is invariant within one OFDM symbol duration and each channel tap corresponds to an independent complex Gaussian random variable with unit second moment. Hence, the channel exhibits L diversity branches. In frequency domain, we know that

$$B_c \approx \frac{1}{4T_d} = \frac{W}{4L} \tag{3.80}$$

so approximately

$$\frac{B_c}{W/N_c} \approx \frac{N_c}{4L} \tag{3.81}$$

are the number of successive sub-bands whose channel gains are heavily correlated.

An interleaved codeword $\mathbf{x}$ of M channel symbols is transmitted during one OFDM symbol duration. Interleaving is performed such that successive symbols of the codeword are transmitted across sub-bands separated by $W/4L$. The authors in [86] showed that the diversity order of $\min(d_H, L)$ is achieved, where d_H is the Hamming distance of the code.

Following (3.78), the received symbol at the rth sub-carrier is given by

$$y_r = x_r H_r + w_r \qquad (3.82)$$

where x_r is the transmitted symbol and H_r is given by Eq. (3.77) or alternatively by the formula

$$H_r = \mathbf{u}_{N_c}^\dagger(r)\mathbf{h} \qquad (3.83)$$

where

$$\mathbf{u}_{N_c}(r) = [1 \ \exp\left(-j2\pi r/N_c\right) \ \ldots \exp\left(-j2\pi r(L-1)/N_c\right)]^\mathsf{T} \qquad (3.84)$$

is an $L \times 1$ vector. Since any two codewords $\mathbf{x}, \hat{\mathbf{x}}$ differ by $d_H(\mathbf{x}, \hat{\mathbf{x}})$ symbols, the conditional PEP is upper bounded as follows:

$$\Pr\{\mathbf{x} \longrightarrow \hat{\mathbf{x}}/H_1, \ldots, H_M\} \leq \exp\left(-\frac{SNR_a}{4} \sum_{r, d_H(\mathbf{x}, \hat{\mathbf{x}})} |H_r|^2 |x_r - \hat{x}_r|^2\right) \qquad (3.85)$$

where $\sum_{r, d_H(\mathbf{x}, \hat{\mathbf{x}})}$ means that the summation is taken over $d_H(\mathbf{x}, \hat{\mathbf{x}})$ different values of r. Substituting (3.83) into (3.85) we have

$$\Pr\{\mathbf{x} \longrightarrow \hat{\mathbf{x}}/h_0, \ldots, h_{L-1}\} \leq \exp\left(-\frac{SNR_a}{4} \sum_{r, d_H(\mathbf{x}, \hat{\mathbf{x}})} \left\|\mathbf{u}_{N_c}^\dagger(r)\mathbf{h}\right\|^2 |x_r - \hat{x}_r|^2\right) \qquad (3.86)$$

$$\leq \exp\left(-d_E^2 \frac{SNR_a}{4} \mathbf{h}^\dagger \underbrace{\left(\sum_{r, d_H(\mathbf{x}, \hat{\mathbf{x}})} \mathbf{u}_{N_c}(r)\mathbf{u}_{N_c}^\dagger(r)\right)}_{\mathbf{A}} \mathbf{h}\right). \qquad (3.87)$$

In [86], it is shown that the rank of $\mathbf{A}$ is $D = \min(d_H(\mathbf{x}, \hat{\mathbf{x}}), L)$. In addition, $\mathbf{A}$ has real, non-negative eigenvalues since it is a positive semidefinite matrix. Invoking the singular value decomposition, $\mathbf{A} = \mathbf{V}\mathbf{\Lambda}\mathbf{V}^\dagger$ where $\mathbf{V}$ is a $L \times L$ unitary matrix, $\mathbf{\Lambda} = \text{diag}(\lambda_1^2, \ldots, \lambda_L^2)$, and λ_i, $i = 1, \ldots, L$ denote the singular values of $\mathbf{A}$ in decreasing order. Hence, the PEP can be written as

$$\Pr\{\mathbf{x} \longrightarrow \hat{\mathbf{x}}\} \leq E\left[\exp\left(-d_E^2 \frac{SNR_a}{4} \sum_{i=1}^D \lambda_i^2 \left|\tilde{h}_i\right|^2\right)\right] \qquad (3.88)$$

where $\tilde{\mathbf{h}} = \mathbf{Vh}$. Since $\mathbf{V}$ is unitary, $\tilde{\mathbf{h}}$ is a complex Gaussian random vector with covariance matrix $\mathbf{I}_{N_t}$. The above formula is analogous to Eq. (3.51), hence if the Rician factor K is such that $1 + K \ll \frac{SNR_a}{4}\lambda_i^2$ the PEP can be expressed as

$$\Pr\{\mathbf{x} \to \hat{\mathbf{x}}\} \leq \left(d_E^2(1+K)e^{-K}\right)^{-D} \left(\prod_{i=1}^{D}\lambda_i^2\right)^{-1} \left(\frac{SNR_a}{4}\right)^{-D}. \qquad (3.89)$$

From the above equation, it is clear that the achievable frequency diversity of a code with Hamming distance d_H for an L-tap Rician fading channel is

$$\min(d_H, L) \qquad (3.90)$$

and the coding gain is approximately equal to $\left(d_E^2\right)^{\min(d_H,L)}$. The authors in [86] didn't observe that efficient averaging of the channel fade highly depends on the relative magnitude of the eigenvalues of $\mathbf{A}$, which in turn depends on the frequency separation of the sub-carriers employed to transmit the codeword, i.e, the interleaving depth. To ensure relatively large eigenvalues, large interleaving depth is required.

3.3.3 Receive diversity

Spatial diversity at the receiver, namely *receive diversity*, occurs when sufficiently far apart hydrophones are employed providing the receiver with almost independently faded replicas of the transmitted signal. The required hydrophone separation depends on the environment as well as on the carrier frequency. Receive diversity occurs at no penalty in bandwidth efficiency or delay while providing an increase in the SNR. On the contrary, time or frequency diversity incurs a penalty in bandwidth efficiency due to coding and an expense in decoding delay due to interleaving.

A pedagogical approach to provide insight on receive diversity is to consider a flat fading channel and N_r receive hydrophones. If $x[m]$ is the transmitted channel symbol and $\mathbf{h} = [h_1[m], \ldots, h_{N_r}[m]]^{\mathsf{T}}$ denotes the vector of channel fades as seen by the different hydrophones, then the received signal can be expressed as

$$\mathbf{y} = \mathbf{h}x[m] + \mathbf{w} = \mathbf{H}\left(1x[m]\right) + \mathbf{w} \qquad (3.91)$$

where $\mathbf{H} = \text{diag}(h_1[m], \ldots, h_{N_r}[m])$, $\mathbf{w} = [w_1[m], \ldots, w_{N_r}[m]]^\mathsf{T}$, $\mathbf{y} = [y_1[m], \ldots, y_{N_r}[m]]^\mathsf{T}$ and $\mathbf{1}$ is a $N_r \times 1$ vector of unities. This above formula is analogous to Eq. (3.46). Hence, after matched filtering (or maximum-ratio combining), the achievable diversity is of order N_r.

In addition to diversity gain, the average SNR is enhanced by a factor of N_r due to array gain, which is expressed as $10\log_{10}(N_r)$ in dB. This is straightforward to see by computing the average received SNR per symbol duration:

$$\frac{E\left[\sum_{i=1}^{N_r} |h_i|^2\right] E\left[|x[m]|^2\right]}{N_0} = N_r \cdot SNR_a. \tag{3.92}$$

Note that even if $h_i[m]$ are fully correlated, namely $h_i[m] = h$, $i = 1, \ldots, N_r$, then although the power gain remains $10\log_{10}(N_r)$ dB, the diversity gain becomes 1 since no fade averaging over space is performed.

3.3.4 Transmit diversity using space-time codes

Spatial diversity at the transmitter, namely *transmit diversity*, occurs when sufficiently far apart projectors are employed. To exploit transmit diversity, space-time signaling techniques must be employed before transmission. To acknowledge this, suppose the same channel symbol is transmitted using two projectors and is received at a single hydrophone. Again for simplicity, let us assume flat fading conditions between each projector and the receive hydrophone. Then, the received signal is written as

$$y[m] = \frac{1}{\sqrt{2}}(h_1[m] + h_2[m])x[m] + w[m]. \tag{3.93}$$

Note that $(h_1[m] + h_2[m])/\sqrt{2}$ is also a complex Gaussian random variable with unit second moment. As a result, the above equation can be equivalently written as $y[m] = h[m]x[m] + w[m]$ where $h[m]$ is a complex Gaussian random variable with unit second moment. Obviously, this simple approach does not provide any transmit diversity.

A simple scheme to achieve transmit diversity of order N_t is to take any time diversity codeword of blocklength N_t and transmit it over N_t projectors using the following technique: transmit each coded symbol over a different projector while keeping the rest $N_t - 1$ projectors

silent. This heuristic coding scheme is a special case of a *space-time code*. As of today, the space-time codes in [40] are the most promising codes to exploit full transmit diversity. In Sec. 3.3.4 we showed that a good time diversity code tries to maximize both the minimum Hamming distance and the minimum squared product distance between any two codewords. There is an analogous notion for space-time codes.

Let us consider a system with N_t transmit projectors and one receive hydrophone. Let the $N_t \times N$ matrix $\mathbf{X}$ be the transmitted space-time code. Each element of the matrix is a channel symbol x and at every symbol duration, a column of $\mathbf{X}$ is simultaneously transmitted over the channel via the N_t projectors. Thus the space-time codeword needs N symbol durations to be transmitted. For convenience, we assume that the channel remains constant during the transmission of $\mathbf{X}$. In this case, the channel vector is denoted as $\mathbf{h} = [h_1^*, \ldots, h_{N_t}^*]^\mathsf{T}$. The received signal can be written as

$$\mathbf{y}^\mathsf{T} = \frac{1}{\sqrt{N_t}}\mathbf{h}^\dagger\mathbf{X} + \mathbf{w}^\mathsf{T} \tag{3.94}$$

where $\mathbf{y} = [y[1], \ldots, y[N]]^\mathsf{T}$ and $\mathbf{w} = [w[1], \ldots, w[N]]^\mathsf{T}$. Given the receiver has perfect knowledge of $\mathbf{h}$, the conditional PEP of confusing the codeword $\mathbf{X}$ with $\hat{\mathbf{X}}$ when $\mathbf{X}$ is transmitted is

$$\Pr\left\{\mathbf{X} \longrightarrow \hat{\mathbf{X}}/h_1^*, \ldots, h_{N_t}^*\right\} = Q\left(\frac{\frac{1}{\sqrt{N_t}}\left\|\mathbf{h}^\dagger\left(\mathbf{X} - \hat{\mathbf{X}}\right)\right\|}{2\sqrt{N_0/2}}\right) \tag{3.95}$$

$$\leq \exp\left(-\frac{SNR_a}{4N_t}\mathbf{h}^\dagger\left(\mathbf{X} - \hat{\mathbf{X}}\right)\left(\mathbf{X} - \hat{\mathbf{X}}\right)^\dagger\mathbf{h}\right) \tag{3.96}$$

Using the singular value decomposition (SVD), the $N_t \times N_t$ matrix $\left(\mathbf{X} - \hat{\mathbf{X}}\right)\left(\mathbf{X} - \hat{\mathbf{X}}\right)^\dagger$ can be expressed as

$$\left(\mathbf{X} - \hat{\mathbf{X}}\right)\left(\mathbf{X} - \hat{\mathbf{X}}\right)^\dagger = \mathbf{V}\Lambda\mathbf{V}^\dagger \tag{3.97}$$

where $\mathbf{V}$ is a $N_t \times N_t$ unitary matrix and Λ is a $N_t \times N_t$ diagonal matrix with the squared singular values of $\mathbf{X} - \hat{\mathbf{X}}$ on the diagonal. Let λ_i, $i = 1, \ldots, D$ denote the singular values of $\mathbf{X} - \hat{\mathbf{X}}$ and $D = \text{rank}(\mathbf{X} - \hat{\mathbf{X}})$. A necessary condition for $D = N_t$ is when $N_t \leq N$, namely the blocklength of the code must be larger that the total number of the projectors. The PEP can

be written as [40]

$$\Pr\left\{\mathbf{X} \longrightarrow \hat{\mathbf{X}}\right\} \leq E\left[\exp\left(-\frac{SNR_a}{4N_t}\sum_{i=1}^{D}\lambda_i^2\left|\tilde{h}_i\right|^2\right)\right]$$

where $\tilde{\mathbf{h}} = \mathbf{V}\mathbf{h}$. Since $\mathbf{V}$ is a unitary transform, $\tilde{\mathbf{h}}$ is a complex Gaussian random vector with covariance matrix $\mathbf{I}_{N_t}$. If the Rician factor K is such that $1 + K \ll \frac{SNR_a}{4}\lambda_i^2$, the PEP becomes

$$\Pr\left\{\mathbf{X} \longrightarrow \hat{\mathbf{X}}\right\} \leq \left(\frac{SNR_a}{4N_t}\right)^{-D}\prod_{i=1}^{D}\frac{(1+K)e^{-K}}{\lambda_i^2} \tag{3.98}$$

$$= \left(\frac{SNR_a}{4N_t}\right)^{-D}\frac{\left((1+K)e^{-K}\right)^D}{\det\left(\left(\mathbf{X}-\hat{\mathbf{X}}\right)\left(\mathbf{X}-\hat{\mathbf{X}}\right)^\dagger\right)}. \tag{3.99}$$

Consequently, the achievable transmit diversity of the space-time code is the minimum rank of $\mathbf{X} - \hat{\mathbf{X}}$ over all pairs $\left(\mathbf{X}, \hat{\mathbf{X}}\right)$. In addition, the coding gain is determined by the minimum of the determinant of $\left(\mathbf{X} - \hat{\mathbf{X}}\right)\left(\mathbf{X} - \hat{\mathbf{X}}\right)^\dagger$ over all pairs $\left(\mathbf{X}, \hat{\mathbf{X}}\right)$. Note in the special case where the space-time code comes from a time diversity code, $\mathbf{X}$ becomes an $N_t \times N_t$ diagonal matrix and so the determinant criterion coincides with the squared product distance criterion, i.e.,

$$\det\left(\left(\mathbf{X}-\hat{\mathbf{X}}\right)\left(\mathbf{X}-\hat{\mathbf{X}}\right)^\dagger\right) = \prod_{i=1}^{N_t}|x_i - \hat{x}_i|^2. \tag{3.100}$$

Chapter 4

Proposed OFDM Systems

Coded modulation refers to the idea of jointly optimizing coding and modulation in order to improve the performance of digital communications. The choice of the coded modulation scheme heavily depends on the specific application. If the powerful turbo codes [20] or LDPC codes are employed, reliable transmission is achieved [89], [90] because these codes having relatively large block lengths ($\approx 10^4$ bits/codeword) manage to average out both channel fading and noise. Although these codes may be well suited for data transmission, for delay sensitive applications, e.g., real-time underwater video transmission, are ill-suited because they suffer from considerable decoding complexity (need iterative decoding) and delay due to the large interleaving depth.

If the codewords are relatively short ($\approx 10^2$ bits/codeword), then the statistical channel model has a considerable impact on the choice of the coded modulation scheme. As we explained in Sec. 3.3.4, codes optimized for the Rician channel with low K parameter maximize their minimum Hamming distance between error events while codes optimized for the Rician channel with high K parameter maximize their free Euclidean distance (the minimum Euclidean distance between any two codewords). In practice, the UWA channel is not long-term stationary, especially when the transmitter and/or the receiver are mobile. A coded modulation scheme with robust (probably not optimal) performance over a variety of channel conditions is the main interest of this thesis.

An instructive way to address the problem of designing coded modulation for fading channels with time-varying statistics is to assume a channel model, which fluctuates in time between

the extremes of Rayleigh fading and AWGN. In this case, codes must exhibit both large Hamming and free Euclidean distance. This problem becomes easy when binary modulation is employed, such as 2-PAM or 2-FSK, because for any linear binary code, the Hamming distance is proportional to the free Euclidean distance so a code optimized for the AWGN channel is also optimized for the Rayleigh fading channel, and consequently for the Rice fading channel which can be seen as an "intermediate" case between the latter two [16]. If multilevel/phase modulation is considered, e.g., PSK or QAM, two main approaches are found in the literature: (1) coupling of channel coding and modulation in one entity and (2) treating channel coding and modulation as two separate entities [50].

If coding and modulation are combined in a single entity, the most applicable approach is trellis coded modulation (TCM). TCM was originally developed by Ungerboeck [8] for the AWGN channel and is a joint convolutional code and symbol mapper design. TCM achieves a large coding gain without sacrificing bandwidth via a signal set expansion. In a characteristic example, a four state, 2/3 rate, 8-PSK TCM code accomplishes 3 dB gain relative to uncoded 4-PSK. Since the original Ungerboeck codes yield low code diversity, new TCM codes were designed for fading channels, emphasizing on maximizing the minimum Hamming distance [14],[15]. However, this improvement is achieved at the expense of reducing the free Euclidean distance, leading to a performance penalty over non-fading channels.

If coding and modulation are treated independently, then an increase in both the Hamming and the free Euclidean distance is possible by using a bit-wise interleaver at the encoder output prior to modulation. This idea was first conceived by Zehavi [19], who combined a convolutional encoder, a bit-interleaver and an 8-PSK modulator via Gray mapping. By using an appropriate bit metric at the Viterbi decoder, he managed to render the code diversity of this system equal to the Hamming distance of the convolutional code. Zehavi's coded modulation scheme showed superior performance in flat Rayleigh fading as opposed to a TCM system with the same data rate and decoding complexity. In [42], the idea of separating coding from modulation using bit-wise interleaving was extended to general constellations and was termed bit-interleaved coded modulation (BICM).

To increase the reliability of UWA communications, the classic approach is to use multiple hydrophones at the receiver and employ maximum-ratio combining (MRC) of the received

signals [21]. Recent results in space diversity systems has shown that multiple transmit antennas can be used to provide extra diversity, thus further system performance improvement can be achieved. Transmit diversity is more difficult to achieve than receive diversity for two reasons: (1) the receiver always knows the channel better than the transmitter; (2) it is a challenging design problem: the transmitter is allowed to concurrently transmit different signals from different antennas. As of today, the most efficient transmit diversity method is offered by the recently proposed family of space-time trellis codes (STTC) [40]. These codes are a joint design of channel coding, modulation and transmit diversity and their encoding/decoding complexity is comparable to the TCM codes. Addressing the issue of decoding complexity, Alamouti [45] discovered a remarkable scheme for using two transmit antennas. Although Alamouti's scheme is less complex than STTC for two antennas, it yields inferior performance. Despite the performance loss, Alamouti's scheme is appealing in terms of its complexity and performance, thus motivated the authors in [48] to generalize Alamouti's scheme to an arbitrary number of transmit antennas, yielding the family of space-time block codes (STBCs).

Chapter summary: In this chapter we begin our discussion by proposing two single projector systems for investigation. The first system combines a 2/3 rate, 8-PSK TCM encoder, a symbol interleaver and OFDM modulation while the second systems combines a 16-QAM BICM scheme based on a 1/2-rate convolutional encoder with OFDM modulation. Then, we extend these two systems to accommodate multiple projectors so that transmit diversity is exploited. Towards this end, we employ STBCs for two and three transmit antennas. Pilot-symbol-aided channel estimation for multi-projector OFDM systems is discussed. Finaly, we compute and compare the BER performance of the proposed systems over a variety of simulated multipath fading channels.

4.1 TCM-OFDM system

In this section we consider TCM for improving the performance of UWA communications. TCM is a joint design of a convolutional encoder and a bit labeling over a signal set (constellation). The goal of TCM is to introduce no data-rate penalty with respect to uncoded transmission and to achieve superior performance for the same SNR. For instance, assume the desired throughput

is 2 bits/sec/Hz. One possible solution is to choose uncoded 4-PSK. Another solution is to employ a 2/3-rate convolutional code combined with an 8-PSK signal set. The latter option yields throughput of $\frac{2}{3}3$ bits/sec/Hz; the same as uncoded 4-PSK. If it also provides sufficient coding gain, which compensates for the shrinking in the distance between the symbols in the expanded signal set, then the TCM scheme is to provide a benefit. Depending on the channel model (e.g., AWGN or Rayleigh fading), different bit labeling strategies exist and exhaustive computer algorithms search for the convolutional code parameters with the desired rate and trellis complexity. The interesting reader is directed to [26] for further discussion on TCM design guidelines.

As we explained in Sec. 3.3.1, for large values of the K Rician factor ($K = \infty$ corresponds to the AWGN channel), the primary design parameter is the maximization of the minimum Euclidean distance between any two codewords while their Hamming distance (code diversity) becomes a secondary consideration. For low values of the K Rician factor ($K = 0$ corresponds to the Rayleigh fading channel), the primary design parameter is both the maximization of the Hamming distance and the squared product distance between any two codewords while their minimum Euclidean distance becomes a secondary consideration. Thus, as the fading channel model fluctuates between Rayleigh fading and AWGN, the significance of these primary and secondary considerations shift relative to each other. In conventional TCM codes, i.e., codes which assign one symbol per branch in their trellis, if parallel transitions in the trellis structure are allowed, then the code diversity is always one, hence the error performance of the code is inversely proportional to SNR in fading channels with high SNR. Consequently, we argue that parallel transitions should be avoided if TCM codes are to be used over a variety of channel conditions and robust performance is desired. An alternative approach which manages to increase the code diversity by allowing parallel transitions was proposed in [14]. These codes are referred to as multiple trellis coded modulation (MTCM) and are not addressed in this work.

Now we describe a system which combines TCM encoding and OFDM modulation through a symbol interleaver, as seen in Fig. 4-1(a). The proposed system allows us to transmit different symbols of a codeword across different coherent bands of the channel, thus frequency diversity is exploited. In addition, ISI is eliminated by design without the need of complex equalizers. If W
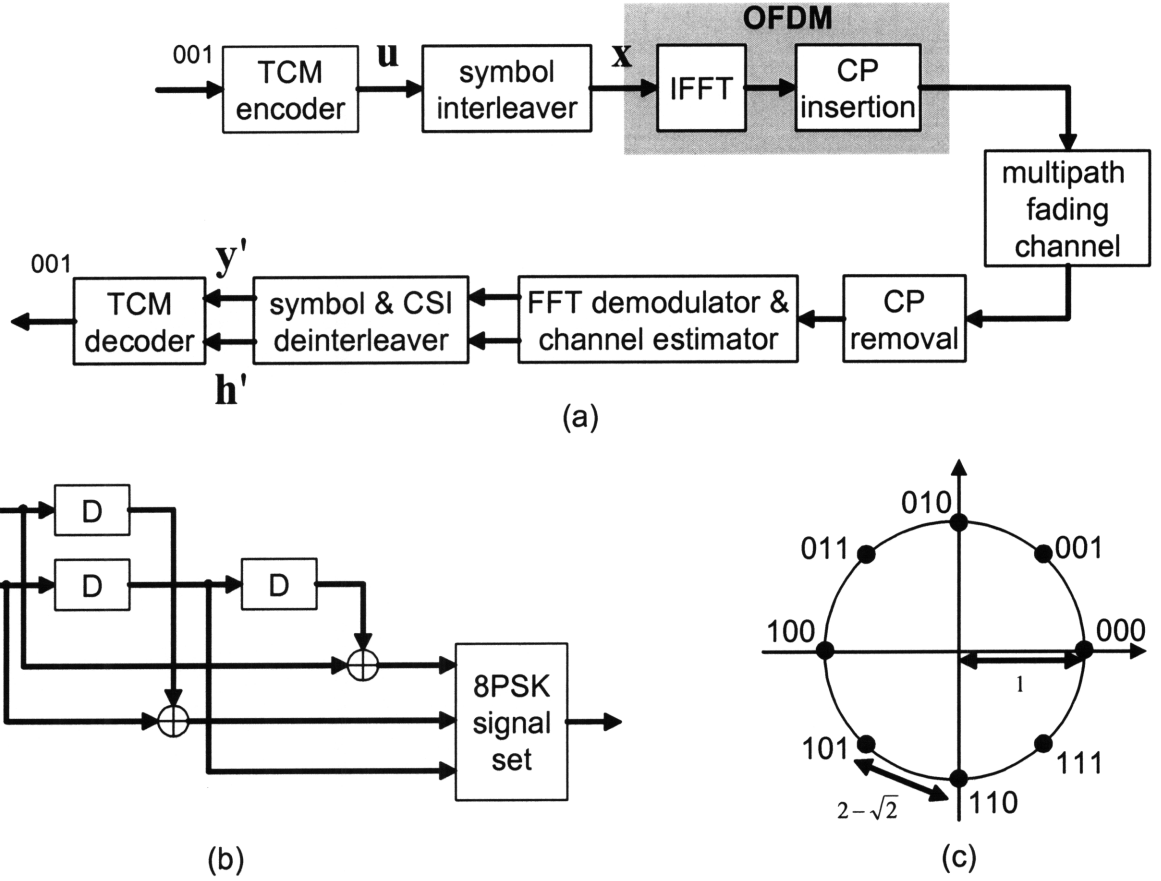
Figure 4-1: The proposed TCM-OFDM system: (a) block diagram; (b) structure of the 2/3-rate 8PSK TCM encoder [26]. D denotes a shift register. At any time, two input bits combined with the stored bits in the shift registers produce three output bits. (c) Bit labeling of the 8-PSK constellation.

is the available bandwidth and N_c is the number of the sub-carriers of the OFDM modulator, the OFDM symbol duration is N_c/W. We assume that a codeword is transmitted over M consecutive OFDM symbols, hence the incoming bit stream is grouped into blocks of $2MN_c$ bits each and each block is encoded by using a 2/3-rate, 8 state, TCM encoder to produce a block of $3MN_c$ coded bits. The structure of the TCM encoder is illustrated in Fig. 4-1(b). The block of coded bits is broken into sub-blocks of 3 bits each, which are one-to-one mapped onto complex symbols drawn from an 8-PSK signal set $\Omega = \{u : u_i = e^{j2\pi i/4}, \ i = 0, \ldots, 7\}$ with average unit energy. The bit labeling of the 8-PSK constellation is highlighted in Fig. 4-1(c). The coded 8-PSK symbol sequence of length MN_c is denoted by $\mathbf{u} = (u_0, \ldots, u_{M(N_c-1)})$. The

sequence $\mathbf{u}$ is interleaved to generate a vector $\mathbf{x} = [\mathbf{x}_1^\mathsf{T}, ..., \mathbf{x}_M^\mathsf{T}]^\mathsf{T}$ of M OFDM symbols, where $\mathbf{x}_i^\mathsf{T} = \left[x_0^i, ..., x_{N_c-1}^i\right]$ is the OFDM symbol transmitted over the ith OFDM symbol interval.

The received coded symbol modulating the rth sub-carrier during the ith OFDM symbol period is given by Eq. (3.74):

$$y_r^i = x_r^i \bar{H}_r^i + C_r^i + w_r^i, \ \ r = 0, ..., N_c - 1, \ \ i = 1, ..., M, \tag{4.1}$$

where $\bar{H}_r^i$ is a multiplicative fading term, C_r^i is the ICI term and w_r^i is the additive white Gaussian noise term with zero mean and variance N_0. The output vector $\mathbf{y}$ and the channel-state information (CSI) vector $\left[\bar{H}_0^1, \bar{H}_1^1, ..., \bar{H}_{N_c-1}^M\right]$ are deinterleaved to produce the vectors $\mathbf{y}' = \left[y_0', ..., y_{M(N_c-1)}'\right]$ and $\mathbf{h}' = \left[H_0', ..., H_{M(N_c-1)}'\right]$, respectively. Given the transmitter knows the channel coherence bandwidth B_c, approximately $N_c B_c / W$ sub-carriers are heavily correlated, so the depth of the interleaver must be greater than $N_c B_c / W$. In addition, long interleaving depth ensures less uncorrelated ICI terms C_r^i between successive coded symbols. For our purposes, we assume ideal interleaving/deinterleaving, thus after deinterleaving the channel can be modeled as memoryless, i.e.,

$$\Pr\left\{\mathbf{y}'/\mathbf{u}, \mathbf{h}'\right\} = \prod_{k=0}^{M(N_c-1)} \Pr\left\{y_k'/u_k, h_k'\right\}. \tag{4.2}$$

The vectors $\mathbf{y}'$ and are fed to the TCM decoder, which performs ML decoding. The ML decoder chooses the coded sequence which most likely corresponds to $\mathbf{u}$ by computing the maximum of the likelihood function $\Pr\left\{\mathbf{y}'/\mathbf{u}, \mathbf{h}'\right\}$ or the log-likelihood function $\ln \Pr\left\{\mathbf{y}'/\mathbf{u}, \mathbf{h}'\right\}$. Assuming perfect CSI at the receiver and considering the noise plus the ICI as a white complex Gaussian process, ML decoding is reduced to maximizing the quantity

$$\sum_{k=0}^{M(N_c-1)} -\left|y_k' - \left|H_k'\right| u_k\right|^2 \tag{4.3}$$

over all possible code sequences $\mathbf{u}$. TCM schemes are described by a trellis diagram so each TCM codeword is represented by a trellis path. Finding the maximum of the above quantity is equivalent to finding the path through the TCM trellis which is closest to the received sequence $\mathbf{y}'$ in the Euclidean distance sense. An efficient search algorithm which finds the most likely

path corresponding to the transmitted codeword is the well known Viterbi algorithm [55].

Note that the ML decoder minimizes the sequence error probability and not the symbol (or equivalently the bit) error probability. Hence, the performance of the ML decoder serves as an upper bound on the performance of the optimal symbol-by-symbol decoder. The latter decoder, also known as the maximum a posteriori (MAP) decoder, maximizes the a posterior probability of detecting a transmitted symbol u_i given the entire received sequence $\mathbf{y}'$ from the demodulator, namely $\Pr\left\{u_i/\mathbf{y}'\right\}$. The MAP decoder is implemented by a number of iterative algorithms, such as the BCJR algorithm [6] or the Abend-Fritchman algorithm [4]. The major drawback of these iterative decoders is their computational complexity, which can be 3 to 4 times larger than the computational complexity of the Viterbi algorithm [55].

Computing the BER probability of the above system is quite tedious, if ICI is included in the channel model. Nevertheless, useful performance insight can be obtained if we neglect ICI, i.e., we assume that the channel is invariant within M OFDM symbol periods. The shortest error event of length d_H between any two codewords happens when two paths diverge from some state in the trellis and they merge back after traveling d_H different branches, thus their corresponding codewords differ in d_H consecutive symbols. This is equivalent to saying that the Hamming distance of the code equals d_H. Assume that the codewords $\mathbf{u}$ and $\hat{\mathbf{u}}$ constitute the shortest error event of length d_H, then the PEP of confusing the codeword $\mathbf{u}$ with $\hat{\mathbf{u}}$ when $\mathbf{u}$ is transmitted is

$$
\begin{aligned}
\Pr\left\{\mathbf{u} \to \hat{\mathbf{u}}/\mathbf{h}'\right\} &= \Pr\left\{\sum_{k=0}^{M(N_c-1)} -\left|y'_k - \left|H'_k\right|\hat{u}_k\right|^2 > \sum_{k=0}^{M(N_c-1)} -\left|y'_k - \left|H'_k\right|u_k\right|^2\right\} \\
&= \Pr\left\{\sum_{k=\ell}^{\ell+d_H-1} \left|y'_k - \left|H'_k\right|\hat{u}_k\right|^2 - \left|y'_k - \left|H'_k\right|u_k\right|^2 < 0\right\} \\
&= Q\left(\sqrt{\dfrac{\sum_{k=\ell}^{\ell+d_H-1}\left|H'_k\right|^2\left|\hat{u}_k - u_k\right|^2}{2N_0}}\right) \leq \exp\left(-\dfrac{1}{4N_0}\sum_{k=\ell}^{\ell+d_H-1}\left|H'_k\right|^2\left|\hat{u}_k - u_k\right|^2\right).
\end{aligned}
$$

The above expression is analogous to Eq. (3.85), thus an upper bound of $\Pr\left\{\mathbf{u} \to \hat{\mathbf{u}}\right\}$ is given by Eq. (3.89) leading to the following conclusions:

1. The maximum diversity order of the proposed TCM-OFDM system over a Rician fading channel with L taps is $D = \min(d_H, L)$. Since the Hamming distance of the TCM encoder is 2 [26], the maximum frequency diversity order of the TCM-OFDM system remains 2 when the channel exhibits more than two physical paths.

2. The coding gain of the proposed TCM-OFDM is proportional to $\left(d_E^2\right)^D$, where $d_E = 2 - \sqrt{2}$ for 8-PSK constellations with unit average energy.

4.2 BICM-OFDM system

In this section, we consider BICM as the coded modulation scheme. In general, BICM combines a channel encoder, a bit interleaver and a memoryless mapper over a signal set. As opposed to TCM, BICM treats channel coding and bit labeling as two independent entities, hence it is more flexible in adjusting the data rate and/or complexity of the communication system. Another advantage of BICM is its high diversity since appropriate bit interleaving manages to render the code diversity equal to the minimum number of distinct bits (rather than symbols) between any two codewords (i.e., the binary Hamming distance of the code). Indeed in [42], a BICM system employing a convolutional encoder and Gray mapping (Gray mapping ensures that symbols separated by the minimum Euclidean distance d_E differ by one binary digit in their corresponding binary address) at the transmitter and the Viterbi decoder with an appropriate bit metric at the receiver achieved code diversity equal to the binary Hamming distance of the convolutional code over an ideally interleaved flat Rayleigh fading channel. Thus, convolutional codes with maximum Hamming distance are optimal when BICM schemes are considered. Fortunately, the best convolutional codes for many rates and complexities are already known [55] so there is no need to search for new binary codes.

The proposed TCM scheme of Sec. 4.1 achieves code diversity of 2, data rate of 2 bits/sec/Hz and yields a trellis complexity of $2^2 2^3 = 32$, where 2^2 are the number of branches merging in each state (2 is the number of the input bits) and 2^3 is the number of states at each trellis step (3 is the number of memory elements). To design a BICM scheme with the same throughput and complexity but with higher code diversity, we consider the following two choices: (1) concatenation of a 2/3-rate, 3 state convolutional encoder with an 8-PSK signal set; (2) concatenation

of a 1/2-rate, 4 state convolutional encoder with a 16-QAM signal set. In the former case, the best convolutional code yields Hamming distance of 5 while in the latter case the best convolutional code yields Hamming distance of 8 [55]. Thus, a straightforward way to increase the code diversity of the BICM system while maintaining the same data rate and trellis complexity is the concatenation of a low-rate convolutional code with an expanded signal set. However, this approach might not be always practical for the BERs of interest since the expanded signal set reduces the minimum Euclidean distance of the constellation. To verify that the combination of a 1/2-rate convolutional code with 16-QAM is worth pursuing, we use the expression of the asymptotic bit error performance of BICM over flat Rayleigh fading [42]

$$\log_{10} P_b = \frac{-d_H}{10} \left((R \cdot d)_{dB} + \left(\frac{E_b}{N_0} \right)_{dB} \right) + \text{constant} \qquad (4.4)$$

where P_b stands for the bit error probability, d_H is the Hamming distance of the convolutional code, R is the information rate and d is a constant which depends on the bit labeling of the signal constellation. Clearly, d_H dictates the slope (diversity gain) of the bit error curve while $R \cdot d$ dictates the horizontal offset (coding gain). The goal is to evaluate the point $(\log_{10} P_b, (E_b/N_0)_{dB})$ at which the two considered bit error curves intersect. For a 8-PSK signal constellation with Gray mapping, d equals 0.96 while for a 16-QAM signal constellation with Gray mapping d equals 0.4923 [42]. Using Eq. (4.4), we obtain a crossover at $E_b/N_0 = 2.97$ dB, thus the signal set expansion provides a coding gain at almost any BER of interest.

We now describe a system which combines BICM with OFDM, as seen in Fig. 4-2(a). The reason behind this combination is obvious based on the discussion so far; OFDM facilitates frequency diversity by transmitting coded bits across different coherent bands and eliminates ISI. Once again, we assume that a codeword is transmitted over M consecutive OFDM symbols. The incoming bit stream is grouped into blocks of $2MN_c$ bits each and each block is encoded by using a 1/2-rate, 16 state, convolutional encoder to produce a block of $4MN_c$ coded bits. The structure of the convolutional encoder is illustrated in Fig. 4-2(b). A bit interleaver permutes the order of the coded bits before they are broken into sub-blocks of 4 bits each. Then, each sub-block is one-to-one mapped onto a complex symbol drawn from a 16-QAM signal set $\Delta = \left\{ u : u = (d_1 + jd_2)/\sqrt{10}, \ d_{1,2} = \pm 1, \pm 3 \right\}$ with average unit energy. Gray mapping is used
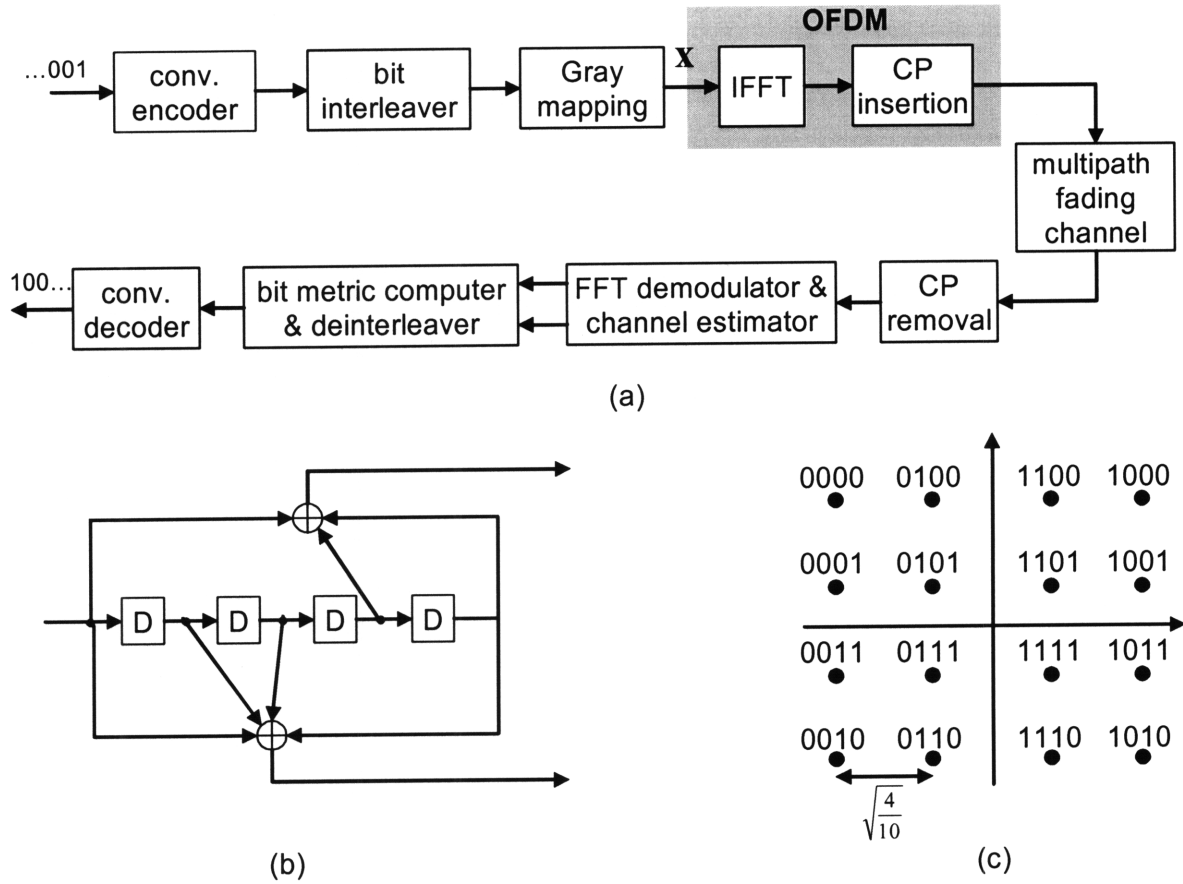
Figure 4-2: The proposed BICM-OFDM system: (a) block diagram; (b) structure of the 1/2-rate, 16-state convolutional encoder [55]. D denotes a shift register. At any time, one input bit combined with the stored bits in the shift registers produce two output bits. (c) Bit labeling of the 16-QAM constellation.

to map the coded bits into channel symbols. The Gray mapping for the 16-QAM constellation is highlighted in Fig. 4-2(c). The resulting coded 16-QAM symbol vector of length MN_c, denoted by $\mathbf{x} = [\mathbf{x}_1^{\mathsf{T}}, ..., \mathbf{x}_M^{\mathsf{T}}]^{\mathsf{T}}$, becomes the input of the OFDM modulator. $\mathbf{x}_i^{\mathsf{T}} = \left[x_0^i, ..., x_{N_c-1}^i \right]$ is the OFDM symbol transmitted over the ith OFDM symbol interval.

After FFT demodulation, the received coded symbol modulating the rth sub-carrier during the ith OFDM symbol period is given by Eq. (3.74):

$$y_r^i = x_r^i \bar{H}_r^i + C_r^i + w_r^i, \ \ r = 0, ..., N_c - 1, \ i = 1, ..., M, \tag{4.5}$$

where $\bar{H}_r^i$ is a multiplicative fading term, C_r^i is the ICI term and w_r^i is the additive white Gaussian noise term with zero mean and variance N_0. Then, log-likelihood bit metrics are computed for the two possible values of each coded bit. Let $l^k(x)$ denote the kth bit of the label of a channel symbol $x \in \Delta$ and $\Delta_b^k = \{x | x \in \Delta, l^k(x) = b\}$ denote the subset of all the channel symbols whose label has the value $b \in \{0, 1\}$ in position k. Fig. 4-3 highlights the eight different partitions the 16-QAM signal set can afford. The four shaded regions correspond to the following subsets:

$$\Delta_1^1 = \left\{ u : u = (d_1 + jd_2)/\sqrt{10}, \ d_1 = 1, 3, \ d_2 = \pm 1, \pm 3 \right\} \tag{4.6}$$

$$\Delta_1^2 = \left\{ u : u = (d_1 + jd_2)/\sqrt{10}, \ d_1 = \pm 1, \ d_2 = \pm 1, \pm 3 \right\} \tag{4.7}$$

$$\Delta_1^3 = \left\{ u : u = (d_1 + jd_2)/\sqrt{10}, \ d_1 = \pm 1, \pm 3, \ d_2 = -1, -3 \right\} \tag{4.8}$$

$$\Delta_1^4 = \left\{ u : u = (d_1 + jd_2)/\sqrt{10}, \ d_1 = \pm 1, \pm 3, \ d_2 = \pm 1 \right\}. \tag{4.9}$$

The four unshaded regions correspond to the subsets:

$$\Delta_0^i = \Delta - \Delta_1^i, \ i = 1, 2, 3, 4. \tag{4.10}$$

The optimum bit-by-bit decoder maximizes the a posteriori probability

$$\Pr \left\{ l^k(x_r^i) = b/\mathbf{y} \right\} = \sum_{x_r^i \in \Delta_b^k} \Pr \left\{ x_r^i/\mathbf{y} \right\} \tag{4.11}$$

$$\sim \sum_{x_r^i \in \Delta_b^k} \Pr \left\{ \mathbf{y}/x_r^i \right\} \Pr \left\{ x_r^i \right\}, \ k = 1, 2, 3, 4; \ b = 0, 1. \tag{4.12}$$

where the common terms to all k and b are discarded. The optimum decoder is too complex to compute in practice, therefore a suboptimal decoder computes eight bit metrics based on the received signal y_r^i as follows [42]:

$$\mu \left(l^k(x_r^i) = b, y_r^i \right) = \Pr \left\{ l^k(x_r^i) = b/y_r^i, \bar{H}_r^i \right\}$$

$$= \sum_{x_r^i \in \Delta_b^k} \Pr \left\{ x_r^i/y_r^i, \bar{H}_r^i \right\}$$

$$\sim \sum_{x_r^i \in \Delta_b^k} \Pr \left\{ y_r^i/x_r^i, \bar{H}_r^i \right\} \Pr \left\{ x_r^i \right\}, \ k = 1, 2, 3, 4; \ b = 0, 1. \tag{4.13}$$

To further simplify the decoder, we assume that the prior probabilities $\Pr\left\{x_r^i\right\}$ are equal, hence the receiver generates the following eight bit metrics:

$$
\begin{aligned}
\mu\left(l^k(x_r^i) = b, y_r^i\right) &= \ln \sum_{x_r^i \in \Delta_b^k} \Pr\left\{y_r^i / x_r^i, \bar{H}_r^i\right\} \\
&\approx \max_{x_r^i \in \Delta_b^k} \ln \Pr\left\{y_r^i / x_r^i, \bar{H}_r^i\right\} \qquad (4.14) \\
&= \min_{x_r^i \in \Delta_b^k} \left\| y_r^i - \left|\bar{H}_r^i\right| x_r^i \right\|, \quad k = 1, 2, 3, 4; \ b = 0, 1. \qquad (4.15)
\end{aligned}
$$

Note that in (4.14) we used the log-sum approximation, which is valid in high SNR. The bit metrics are deinterleaved and become the input to the convolutional decoder, which performs ML decoding using the Viterbi algorithm. At each trellis step, the branch metric corresponding to each of the 16 possible 2 binary tuples (b_1, b_2) is the sum of the corresponding bit metrics. Since the bit interleaver is designed such that consecutive coded bits are transmitted over different coherent bands of the channel, the fade correlation within the branch as well as between successive branches is broken leading to efficient performance of the decoder.

One known pitfall of BICM is that its increased diversity order comes at the expense of reduced Eulcidean distance between the codewords. Due to random modulation caused by the bit interleaver, the free Euclidean distance can be easily shown to be $d_H d_E^2$, where d_E is the minimum Euclidean distance of the symbol constellation. For 16-QAM, $d_E = \sqrt{0.4}$ thus for the proposed BICM system the free Euclidean distance is 3.2 while the proposed TCM system yields free Euclidean distance of 4.59 [26]. Thus, the TCM system has an SNR advantage of 1.57 dB for the AWGN channel or for Rician channels with high K factor. In general, the free Euclidean distance of BICM is always smaller than its TCM counterpart, therefore BICM is less efficient in non-fading channels.

Now we comment on the effectiveness of Gray mapping. Referring to Fig. 4-3, Gray mapping ensures that the number of nearest neighbors between the subsets Δ_0^i and Δ_1^i is four, which is the smallest possible. This is considered optimal when ML decoding is used. In [66], it is shown that no performance improvement is accomplished when a combination of Gray mapping and iterative decoding is used. This can be explained as follows: consider the case where three out four bits are perfectly known via decoding feedback. Then, the effective modulation for that bit position becomes binary modulation (2-PAM), thus the minimum intersubset distance

Bit 1

0000 0100 1100 1000

0001 0101 1101 1001

0011 0111 1111 1011

0010 0110 1110 1010

Bit 2

0000 0100 1100 1000

0001 0101 1101 1001

0011 0111 1111 1011

0010 0110 1110 1010

Bit 3

0000 0100 1100 1000

0001 0101 1101 1001

0011 0111 1111 1011

0010 0110 1110 1010

Bit 4

0000 0100 1100 1000

0001 0101 1101 1001

0011 0111 1111 1011

0010 0110 1110 1010
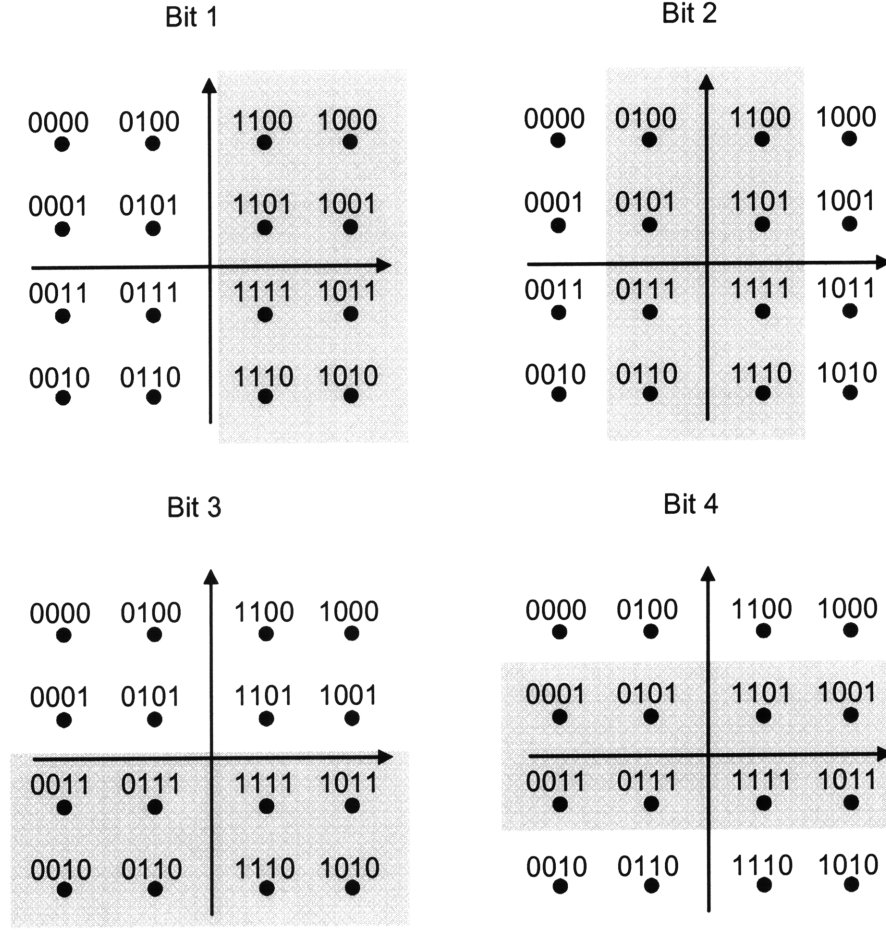
Figure 4-3: Partition of the 16-QAM signal. Each shaded region correspond to all the transmitted symbols whose binary digit at the ith position is 1.

(minimum distance between subsets Δ_0^i and Δ_1^i) is significant. Obviously, Gray labeling is not effective since the minimum intersubset distance remains fixed. This observation motivated the authors in [66] to device a "mixed labeling" strategy for 8-PSK constellations with increasing minimum intersubset distance so when combined with iterative decoding the new system achieves better performance than the conventional BICM over both Gaussian and Rayleigh fading channels at the expense of higher computational complexity.

Since BICM is a trellis based scheme and Viterbi decoding is considered, the BER performance expression of the BICM-OFDM is analogous to TCM-OFDM when ICI is not included. Hence, we can directly state:
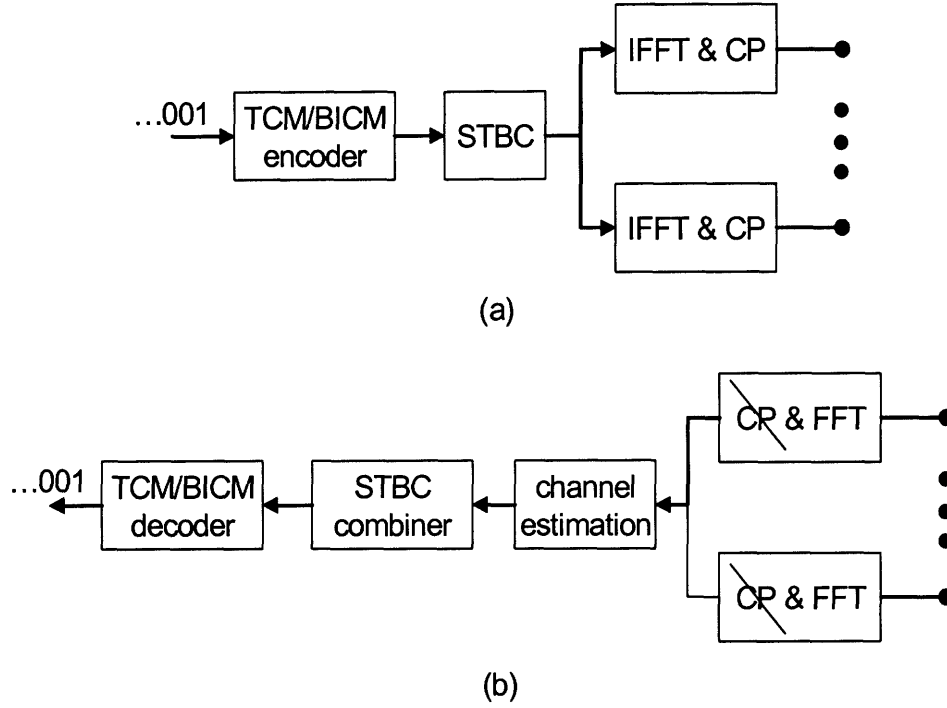
Figure 4-4: STBC-OFDM block diagram: (a) transmitter (b) receiver

1. The maximum diversity order of the proposed BICM-OFDM system over slow fading Rician channels with L taps equals $D = \min(8, L)$.

2. The coding gain of the proposed TCM-OFDM is proportional to $\left(d_E^2\right)^D$, where $d_E = \sqrt{0.4}$ for 16-QAM constellations with unit average energy.

4.3 Combining TCM/BICM with STBC and OFDM

MIMO systems employing STBCs can be easily used in conjuction with OFDM modulation yielding a low-complexity, high-data-rate system with increased reliability relative to its SISO counterpart. A MIMO-OFDM system treats each sub-carrier as an independent MIMO flat fading channel provided that the Doppler effects among all the transmit and receive transducers have been compensated [90]. In this section, we extend the TCM-OFDM and BICM-OFDM systems so that N_t projectors and N_r hydrophones are incorporated in order to exploit spatial diversity. In particular, we consider TCM/BICM as an outer code concatenated with an inner

STBC [69]. This approach provides increased reliability relative to systems employing only STBCs in conjuction with OFDM since an STBC-OFDM system does not guarantee that different parts of a codeword are jointly mapped across all different projectors and different coherent bands [57]. In other words, STBC-OFDM systems do not always exploit full space-frequency diversity. By using channel coding as an outer code and an STBC as an inner code, the effective code blocklength becomes larger, hence the proposed system is able to harvest higher diversity gains.

Fig. 4-4(a) shows the block diagram of the transmitter. After TCM/BICM encoding, a rate-M/N STBC is applied to a vector of M OFDM symbols, which is denoted by the $MN_c \times 1$ vector

$$\mathbf{x} = \begin{bmatrix} \mathbf{x}_1 \\ \vdots \\ \mathbf{x}_M \end{bmatrix},$$ (4.16)

where each $\mathbf{x}_i$ is an $N_c \times 1$ vector of channel symbols. The encoder output is a $N_c N_t \times N$ column orthogonal matrix

$$\mathbf{G} = \begin{bmatrix} \mathbf{c}_1^1 & \mathbf{c}_2^1 & \dots & \mathbf{c}_N^1 \\ \mathbf{c}_1^2 & \mathbf{c}_2^2 & \dots & \mathbf{c}_N^{N_t} \\ \vdots & \vdots & \ddots & \vdots \\ \mathbf{c}_1^{N_t} & \mathbf{c}_2^{N_t} & \dots & \mathbf{c}_N^{N_t} \end{bmatrix}$$ (4.17)

where each OFDM symbol $\mathbf{c}_t^i$ is transmitted from the ith antenna at time slot t and is composed by a linear combinations of $(\mathbf{x}_1, \dots, \mathbf{x}_M)$ and their conjugates. All OFDM symbols in the same column of $\mathbf{G}$ are simultaneously transmitted by all transmit antennas and all OFDM symbols in the same row of $\mathbf{G}$ are transmitted in consecutive time slots. In this work, systems with two and three projectors are considered. When two projectors are used ($N_t = 2$), a rate-2/2 STBC [48] is employed (also known as the *Alamouti* STBC) where the output of the STBC encoder is expressed as

$$\mathbf{G}_{2/2} = \begin{bmatrix} \mathbf{x}_1 & -\mathbf{x}_2^* \\ \mathbf{x}_2 & \mathbf{x}_1^* \end{bmatrix}.$$ (4.18)

When three projectors are used ($N_t = 3$), a rate-3/4 STBC [48] is employed where the output

of the STBC encoder is expressed as

$$\mathbf{G}_{3/4} = \begin{bmatrix} \mathbf{x}_1 & -\mathbf{x}_2^* & \mathbf{x}_3^*/\sqrt{2} & \mathbf{x}_3^*/\sqrt{2} \\ \mathbf{x}_2 & \mathbf{x}_1^* & \mathbf{x}_3^*/\sqrt{2} & -\mathbf{x}_3^*/\sqrt{2} \\ \mathbf{x}_3/\sqrt{2} & \mathbf{x}_3/\sqrt{2} & \left(-\mathbf{x}_1 - \mathbf{x}_1^* + \mathbf{x}_2 - \mathbf{x}_2^*\right)/2 & \left(\mathbf{x}_1 - \mathbf{x}_1^* + \mathbf{x}_2 + \mathbf{x}_2^*\right)/2 \end{bmatrix} \qquad (4.19)$$

For our purposes, let us assume that the channel remains constant over N consecutive OFDM symbol durations, let us denote the ℓth tap of the impulse response between the ith $(i = 1, \ldots, N_r)$ hydrophone and the jth $(j = 1, \ldots, N_t)$ projector by $h_{i,j,\ell}$, $\ell = 1, \ldots, L$, where L is the maximum delay spread of all the individual $N_t N_r$ SISO channels. In matrix form, the impulse response of the MIMO channel can be written as a sequence of matrices $\mathbf{h}_\ell$, $\ell = 1, \ldots, L$, where $[\mathbf{h}_\ell]_{i,j} = h_{i,j,\ell}$. In addition, let us denote $H_{i,j,k}$ the frequency gain between the ith hydrophone and the jth projector for the kth sub-carrier. $H_{i,j,k}$ is given by

$$H_{i,j,k} = \sum_{\ell=0}^{L-1} h_{i,j,\ell} e^{-j2\pi \frac{\ell k}{N_c}}, \quad k = 0, \ldots N_c - 1. \qquad (4.20)$$

Hence, the $N_r \times N_t$ matrix corresponding to the MIMO channel for the kth sub-carrier is related to $\mathbf{H}_\ell$ via

$$\mathbf{H}_k = \sum_{\ell=0}^{L-1} \mathbf{h}_\ell e^{-j2\pi \frac{\ell k}{N_c}}, \quad k = 0, \ldots N_c - 1. \qquad (4.21)$$

Fig. 4-4(a) shows the block diagram of the receiver. After CP removal, FFT demodulation and channel estimation, the signal received at the kth sub-carrier is given by [74]

$$\mathbf{Y}_k = \mathbf{H}_k \mathbf{G}_k + \mathbf{N}_k, \quad k = 0, \ldots N_c - 1. \qquad (4.22)$$

where $\mathbf{Y}_k$ is an $N_r \times N$ matrix reflecting the signals received across the N_r hydrophones during the N OFDM symbol signaling, $\mathbf{G}_k$ is a $N_t \times N$ matrix generated by replacing each vector $\mathbf{c}_t^i$ in Eq. (4.17) with its kth element and $\mathbf{N}(k)$ is the noise matrix. Eq. (4.22) manifests that OFDM modulation transforms the frequency selective MIMO channel into N_c orthogonal flat fading $N_r \times N_t$ MIMO channels. ML decoding for any STBC is based only on linear processing at the receiver due to the orthogonal structure of $\mathbf{G}$.

For the $\mathbf{G}_{2/2}$ STBC, at the first OFDM slot, channel symbols $x_{1,k}$ and $x_{2,k}$ are simulta-

neously transmitted from antennas one and two over the kth sub-carrier, respectively. At the second OFDM slot, symbols $-x_{2,k}^*$ and $x_{1,k}^*$ are transmitted simultaneously from antennas one and two, respectively. The received signals at hydrophone i during the first and second OFDM periods are given by

$$y_{i,k}[1] \quad = \quad H_{i,1,k}x_{1,k} + H_{i,2,k}x_{2,k} + w_{i,k}[1] \tag{4.23}$$

$$y_{i,k}[2] \quad = \quad -H_{i,1,k}x_{2,k}^* + H_{i,2,k}x_{1,k}^* + w_{i,k}[2]. \tag{4.24}$$

Note that $y_{i,k}[1]$ contains symbols $x_{1,k}$ and $x_{2,k}$, while $y_{i,k}[2]$ contains their conjugates. In order to decode the transmitted symbols, we need to decouple $x_{1,k}$ and $x_{2,k}$ from the above $2x2$ system of equations. This is achieved by performing the following operations [49]:

$$\tilde{y}_{1,k} \quad = \quad y_{i,k}[1]H_{i,1,k}^* + (y_{i,k}[2])^* H_{i,2,k} \tag{4.25}$$

$$= \quad \left(\frac{1}{\sqrt{2}} \sum_{j=1}^{2} |H_{i,j,k}|^2 \right) x_{1,k} + \tilde{w}_{1,k} \tag{4.26}$$

$$\tilde{y}_{2,k} \quad = \quad y_{i,k}[1]H_{i,2,k}^* - (y_{i,k}[2])^* H_{i,1,k}$$

$$= \quad \left(\frac{1}{\sqrt{2}} \sum_{j=1}^{2} |H_{i,j,k}|^2 \right) x_{2,k} + \tilde{w}_{2,k} \tag{4.27}$$

where $\tilde{w}_{1,k}$, $\tilde{w}_{2,k}$ are i.i.d. complex Gaussian noise terms with variance $\sum_{j=1}^{2} |H_{i,j,k}|^2 N_0$ each. Eq. (4.26) and (4.27) indicate that the Alamouti STBC transforms the original 2×1 channel into two independent SISO channels, each of which has diversity order two. The second order diversity can be explained by observing the fading term $\sum_{j=1}^{2} |H_{i,j,k}|^2$. It is the sum of squares of two independent complex Gaussian random variables, therefore it has two degrees of freedom. Thus, if either of the SISO channels is in a deep fade, the other channel may still provide a reliable link for each transmitted symbol. On the other hand, in a conventional SISO system, there is only a single link, which may be severely attenuated by a deep fade.

The STBC decoder can be readily extended to employing N_r hydrophones. It is relative straightforward to see that after ML decoding the effective channel for $x_{1,k}$ and $x_{2,k}$ becomes

$$\breve{y}_{i,k} = \left(\frac{1}{\sqrt{2}} \sum_{i=1}^{N_r} \sum_{j=1}^{2} |H_{i,j,k}|^2 \right) x_{i,k} + \breve{w}_{i,k}, \ \ i = 1,2 \tag{4.28}$$

104

where $\breve{w}_{1,k}$, $\breve{w}_{2,k}$ are i.i.d. complex Gaussian noise terms with variance $\sum_{i=1}^{N_r} \sum_{j=1}^{2} \left| H_{i,j,k} \right|^2 N_0$ each. Obviously, the Alamouti STBC transforms the original $2 \times N_r$ channel into two independent scalar channels, each of which has diversity order $2N_r$ (full spatial diversity) provided that all the propagation paths between the two projectors and the N_r hydrophones are independent.

Similarly, the received signals at the ith hydrophone, when the $\mathbf{G}_{3/4}$ STBC is transmitted, are given by

$$
\begin{aligned}
y_{i,k}[1] &= H_{i,1,k} x_{1,k} + H_{i,2,k} x_{2,k} + \frac{H_{i,3,k} x_{3,k}}{\sqrt{2}} + w_{i,k}[1] \\
y_{i,k}[2] &= -H_{i,1,k} x_{2,k}^* + H_{i,2,k} x_{1,k}^* + \frac{H_{i,3,k} x_{3,k}}{\sqrt{2}} + w_{i,k}[2] \\
y_{i,k}[3] &= \left(H_{i,1,k} + H_{i,2,k} \right) \frac{x_{3,k}^*}{\sqrt{2}} - \frac{H_{i,3,k}}{2} \left(x_{1,k} + x_{1,k}^* - x_{2,k} + x_{2,k}^* \right) + w_{i,k}[3] \\
y_{i,k}[4] &= \left(H_{i,1,k} - H_{i,2,k} \right) \frac{x_{3,k}^*}{\sqrt{2}} + \frac{H_{i,3,k}}{2} \left(x_{1,k} - x_{1,k}^* + x_{2,k} + x_{2,k}^* \right) + w_{i,k}[4].
\end{aligned}
$$

Note that the channel remains fixed for $N = 4$ OFDM symbol durations. To decouple $x_{1,k}$, $x_{2,k}$ and $x_{3,k}$ from the above 4x3 system of equations, the receiver performs the following operations [49]:

$$
\begin{aligned}
&y_{i,k}[1] H_{i,1,k}^* + (y_{i,k}[2])^* H_{i,2,k} + \frac{(y_{i,k}[4] - y_{i,k}[3]) H_{i,3,k}^*}{2} - \frac{(y_{i,k}[3] + y_{i,k}[4])^* H_{i,3,k}}{2} \\
&y_{i,k}[1] H_{i,2,k}^* - (y_{i,k}[2])^* H_{i,1,k} + \frac{(y_{i,k}[4] + y_{i,k}[3]) H_{i,3,k}^*}{2} + \frac{(-y_{i,k}[3] + y_{i,k}[4])^* H_{i,3,k}}{2} \\
&\frac{(y_{i,k}[1] + y_{i,k}[2]) H_{i,3,k}^*}{\sqrt{2}} + \frac{y_{i,k}[3] \left(H_{i,1,k} + H_{i,2,k} \right)}{\sqrt{2}} + \frac{(y_{i,k}[4])^* \left(H_{i,1,k} - H_{i,2,k} \right)}{\sqrt{2}}
\end{aligned}
$$

hence, the effective channel for each of the transmitted symbols $x_{i,k}$ becomes:

$$
\tilde{y}_{i,k} = \left(\frac{1}{\sqrt{3}} \sum_{j=1}^{3} \left| H_{i,j,k} \right|^2 \right) x_{i,k} + \tilde{w}_{i,k}, \quad i = 1, 2, 3. \tag{4.29}
$$

where $\tilde{w}_{i,k}$, $i = 1, 2, 3$ are i.i.d. complex Gaussian noise terms with variance $\sum_{j=1}^{3} \left| H_{i,j,k} \right|^2 N_0$. Eq. (4.29) shows that the $\mathbf{G}_{3/4}$ STBC transforms the original 3x1 channel into three independent scalar channels, each of which has diversity order three. If N_r hydrophones are used at
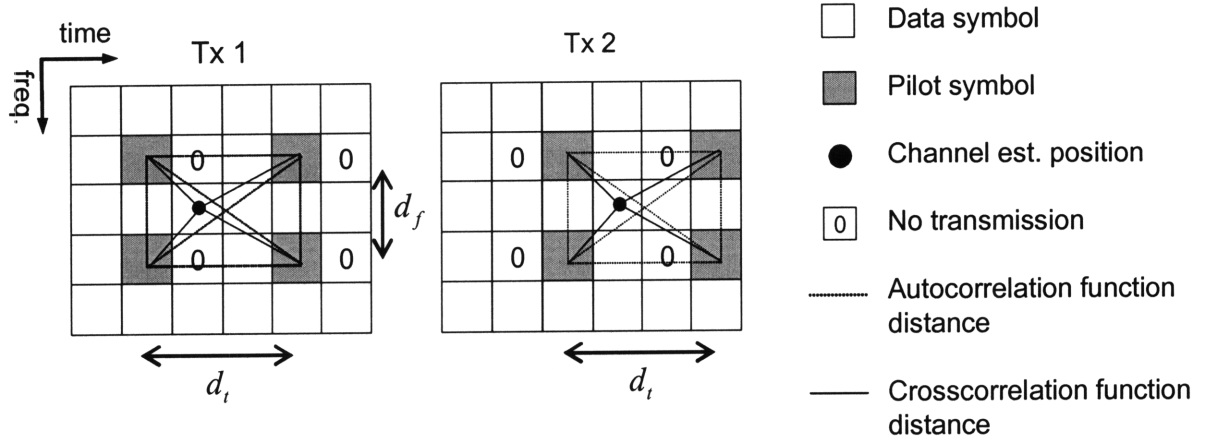
Figure 4-5: Pilot-symbol arrangement for OFDM systems with two transmit antennas.

the receiver, it is easy to show that the effective channel for each of the transmitted symbols is

$$\breve{y}_{i,k} = \left(\frac{1}{\sqrt{3}} \sum_{i=1}^{N_r} \sum_{j=1}^{3} \left|H_{i,j,k}\right|^2\right) x_{i,k} + \breve{w}_{i,k}, \;\; i = 1,2,3. \tag{4.30}$$

Hence, the $\mathbf{G}_{3/4}$ STBC turns the $3 \times N_r$ channel into three independent SISO channels, each of which has diversity order $3N_r$ (full spatial diversity) provided that all the propagation paths between the three projectors and the N_r hydrophones are independent.

After decoupling the signals from each projector (STBC combining), the decision metrics sequence (each element of the sequence is described by either Eq. (4.28) or Eq. (4.30)) associated with each transmitted TCM/BICM codeword is fed into the Viterbi decoder. By computing the average error probability, the overall diversity gain of the proposed MIMO-OFDM systems is $N_t N_r \min(d_H, L)$ [86], where d_H is the Hamming distance of the TCM/BICM code.

4.4 Robust channel estimation for OFDM systems

Estimating the time-varying frequency response $H(f,t)$ of the channel is particularly attractive in OFDM systems. In this thesis, we use pilot-symbol-aided channel estimation with 2-D Wiener originally proposed in [36] for SISO systems. Pilot-symbol-aided channel estimation is accomplished by multiplexing training symbols known to the receiver into the data stream. If

the distances of the pilot symbols in time and frequency direction are chosen sufficiently far apart with respect to Doppler spread and coherence bandwidth respectively, the overhead is significantly reduced because time and frequency correlation of the transfer function is exploited. A rectangular arrangement of the pilot symbols is chosen, as shown in Fig. 4-5, however, other arrangements are also possible (e.g., a diagonal grid [59]). Let d_f stand for the distance in sub-carriers (recall the sub-carrier distance is W/N_c) between two pilot symbols in frequency and d_t denotes the distance in OFDM symbol slots (recall that one OFDM symbol slots consists of the OFDM symbol duration $T_{OFDM} = N_c/W$ plus the cyclic prefix duration, which equals to the delay spread of the channel) between two pilot symbols in time. Assuming the maximum channel delay spread T_d and the maximum channel one-sided Doppler spread f_d are known to the system designer, then the 2-D sampling theorem requires that

$$d_t \leq \frac{1}{2f_d(T_{OFDM} + T_d)} \text{ and } d_f \leq \frac{1}{T_d W/N_c} \qquad (4.31)$$

When multiple projectors are used, the pilot symbols are transmitted in an orthogonal manner, namely, when a projector transmits a pilot symbol during a specific time-frequency slot all the other projectors are kept silent during that slot. This simple scheme avoids pilot symbols transmitted from different projectors to interfere with each other when channel estimation is performed. Fig. 4-5 illustrates how the pilot symbols are distributed in the time-frequency plane when two projectors are employed. This pilot symbol arrangement can be readily extended to an arbitrary number of projectors.

Channel estimation using 2-D Wiener filtering is now described. Suppose we want to estimate the channel gain $H_{i,j,k}[n]$ of the kth sub-carrier during the nth OFDM symbol time between the jth projector and the ith hydrophone. The procedure is the same for all (i, j) pairs, so for the rest of the discussion we neglect the indexes i and j for notation simplicity. Based on our OFDM system model (Sec. 3.3.2), the received signal is given by Eq. (3.78)

$$y_k[n] = H_k[n]x_k[n] + w_k[n] \qquad (4.32)$$

where $x_k[n]$ is the transmitted symbol and $w_k[n]$ is the noise term with average power $E\left[|w_k[n]|^2\right] = N_0$. If we mark the frequency and time locations of the pilot symbols as k' and n', respectively

and denote Ω as the set of the pilot symbol locations with $|\Omega| = N_{tap}$, then the channel estimates $\hat{H}_{k'}[n']$ at these locations are obtained as follows:

$$\hat{H}_{k'}[n'] = \frac{y_{k'}[n']}{x_{k'}[n']} = H_{k'}[n'] + \frac{w_{k'}[n']}{x_{k'}[n']}, \ k', n' \in \Omega \tag{4.33}$$

The complete channel response is given by

$$\hat{H}_k[n] = \sum_{\{k',n'\}\in\Omega} \omega_{k,k'}[n, n']\hat{H}_{k'}[n'] \tag{4.34}$$

where $\omega_{k,k'}[n, n']$ is the shift-variant 2-D impulse response of the filter with N_{tap} taps. The filter taps minimize the error

$$e_k[n] = H_k[n] - \hat{H}_k[n] \tag{4.35}$$

in the mean square sense, namely, $\omega_{k,k'}[n, n']$ are selected such that $E\left[|e_k[n]|^2\right]$ is minimized. This is accomplished by invoking the orthogonality principle in linear mean square estimation, which states that the mean square error $e_k[n]$ is orthogonal to all initial estimates $\hat{H}_{k''}[n'']$ for every $k'', n'' \in \Omega$. Mathematically, this is expressed as

$$E\left[e_k[n]\hat{H}^*_{k''}[n'']\right] = 0, \ \forall \ k'', n'' \in \Omega. \tag{4.36}$$

Substituting Eq. (4.34) and (4.35) into Eq. (4.36) leads to the well known Wiener-Hopf equations:

$$E\left[H_k[n]\hat{H}^*_{k''}[n'']\right] = \sum_{\{k',n'\}\in\Omega} \omega_{k,k'}[n, n']E\left[\hat{H}_{k'}[n']\hat{H}^*_{k''}[n'']\right], \ \forall k', k'', n', n'' \in \Omega. \tag{4.37}$$

The continuous correlation function of the channel frequency response is given by

$$R_H(\Delta f, \Delta t) \triangleq E\left[H(f + \Delta f, t + \Delta t)H^*(f, t)\right] \tag{4.38}$$

so it is easy to see that the discrete cross-correlation function becomes

$$
\begin{aligned}
\gamma\left(k - k'', n - n''\right) &= E\left[H_k[n]\hat{H}_{k''}^*[n'']\right] \\
&= R_H\left((k - k'')\frac{W}{N_c}, (n - n'')(T_d + T_{OFDM})\right)
\end{aligned}
$$

(4.39)

and the discrete auto-correlation function is

$$
\begin{aligned}
R\left(k' - k'', n' - n''\right) &\triangleq E\left[\hat{H}_{k'}[n']\hat{H}_{k''}^*[n'']\right] \\
&= \gamma\left(k' - k'', n' - n''\right) + N_0\delta(k' - k'', n' - n'')
\end{aligned}
$$

(4.40)

Consequently, Eq. (4.37) can be written in matrix form as

$$
\gamma_{k,n} = \mathbf{R}\omega_{k,n}
$$

(4.41)

where $\gamma_{k,n}$ is the cross correlation vector of length N_{tap} and $\mathbf{R}$ is the $N_{tap} \times N_{tap}$ autocorrelation matrix. Thus, the optimum 2-D Wiener filter is given by

$$
\omega_{k,n} = \mathbf{R}^{-1}\mathbf{v}_{k,n}.
$$

(4.42)

In practice, the channel statistics are unknown and difficult to obtain since they depend on the fluctuations of the environment. Hence, a robust, non-adaptive selection of the filter taps is considered, namely, a fixed set of filter coefficients is designed which can cope with a wide variety of power density spectra with different shapes and maximum values. We base our design on the assumption that the correlation of the channel frequency response $R_H(\Delta f, \Delta t)$ can be separated into the multiplication of time and frequency domain correlation functions. This assumption is widely used in narrowband radio channels [36],[44],[59] and can be justified for UWA channels with relative narrow bandwidth and small range (this is the type of channel we dealt with during our experiment), so that the absorption loss is (almost) constant across the entire bandwidth.

To illustrate the separation property, we use the following (simplified) baseband channel

response

$$H(f, t) = \sum_p a_p(t) e^{-j2\pi f \tau_p}, \tag{4.43}$$

where τ_p is the delay of the pth path and $a_p(t)$ is a WSS narrowband complex Gaussian process. In addition, we assume that $a_p(t)$ is independent for different paths and has the same normalized correlation function $\gamma_f(\Delta t)$ for all p, i.e.,

$$R_{a_p}(\Delta t) = E\left[a_p(t + \Delta t) a_p^*(t)\right] = \sigma_p^2 \gamma_t(\Delta t). \tag{4.44}$$

σ_p^2 stands for the average power of path p. The above equation implies a rich scattering environment, where the angle of arrival of the received signal is a uniformly distributed random variable. Under the above assumptions, the correlation function of the channel frequency response can be expressed as

$$\begin{aligned} R_H(\Delta f, \Delta t) &= \sum_p E\left[a_p(t + \Delta t) a_p^*(t)\right] e^{-j2\pi \Delta f \tau_p} \\ &= \gamma_t(\Delta t) \left(\sum_p \sigma_p^2 e^{-j2\pi \Delta f \tau_p}\right) \\ &= \gamma_t(\Delta t) \gamma_f(\Delta f). \end{aligned} \tag{4.45}$$

Note that $\gamma_t(\Delta t)$ is a Fourier transform pair with the Doppler power spectrum $S_t(f)$ of the channel and $\gamma_f(\Delta f)$ is a Fourier transform pair with the delay power density $S_f(\tau)$ of the channel.

Based on the separation property of $R_H(\Delta f, \Delta t)$, the authors in [44] proved that if the filter taps are adapted to a uniform delay power density spectrum and a uniform Doppler power density spectrum then any mismatch in $\gamma_t(\Delta t)$ and/or $\gamma_f(\Delta f)$ will not degrade the performance of the channel estimator. Hence, by choosing

$$S_f(\tau) = \left\{ \begin{array}{l} \frac{1}{T_d}, |\tau| \leq \frac{T_d}{2} \\ 0, \text{ otherwise} \end{array} \right\} \tag{4.46}$$

and

$$S_t(f) = \left\{ \begin{array}{l} \frac{1}{2f_d}, |f| \leq f_d \\ 0, \text{ otherwise} \end{array} \right\} \tag{4.47}$$

the optimum filter taps are computed using the discrete cross-correlation function

$$\gamma\left(k - k'', n - n''\right) = \operatorname{sinc}\left(\pi T_d\left(k - k''\right)\frac{W}{N_c}\right)\operatorname{sinc}\left(2\pi f_d\left(n - n''\right)\left(T_d + T_{OFDM}\right)\right) \quad (4.48)$$

and also the discrete auto-correlation function

$$
\begin{aligned}
R\left(k' - k'', n' - n''\right) &= \operatorname{sinc}\left(\pi T_d\left(k' - k''\right)\frac{W}{N_c}\right)\operatorname{sinc}\left(2\pi f_d\left(n' - n''\right)\left(T_d + T_{OFDM}\right)\right) \\
&\quad + N_0\delta(k' - k'', n' - n'').
\end{aligned}
\quad (4.49)
$$

4.5 Simulation results

Here, the BER performances of the proposed TCM-OFDM and BICM-OFDM system using simulated data are computed. We consider various combinations of interleavers, channels and number of receive hydrophones. The results of this section are informative towards assessing the performance of the proposed systems uisng experimental data (see Sec. 5.3).

In all simulations, the bandwidth is $W = 4$ kHz, the number of sub-carriers are $N_c = 128$ and 25 msec is the cyclic prefix duration ($N_{cp} = 99$). For every system, information bits are formed into packets of 30 OFDM symbols each before transmission. The channel symbols are drawn from unit energy constellations and when N_r receive hydrophones are employed, the transmit energy is divided by N_r to compensate for the array gain. The physical path delays are spaced at integer multiples of W^{-1}, thus the number of physical paths is equal to the number of non-zero taps of the channel impulse response. Although this doesn't reflect reality, it helps us to have full control over the channel's frequency diversity. Finally, we assume that the receiver has perfect knowledge of the values of each channel tap.

Simulation tests for Rayleigh and Rician fading channels are reported below. The results are obtained using the following steps:

1. For each receive hydrophone, we generate a random channel realization. Each physical path is characterized by a uniform Doppler power spectrum with maximum one sided frequency f_d and is modeled as an independent, complex Gaussian random variable. If Rayleigh fading is considered, then each random variable has zero mean and variance $1/L$, where L is the total number of physical paths. If Rician fading is assumed, we

consider equal powers for the line-of-sight and the diffused signal components, therefore each random variable has mean $\sqrt{1/2L}$ and variance $1/2L$. Hence, we impose the average received symbol energy to be one regardless of the multipath structure. Consequently, the average received SNR for any system-channel combination is $1/N_0$, where N_0 is the power spectral density of the white additive complex Gaussian noise process.

2. Process 30 OFDM symbols.

3. Compute the information bit errors.

4. Repeat the steps above hundreds/thousands of times to produce a distribution of the BER.

All BER results are plotted with respect to E_b/N_0, which denotes the ratio between the average received energy per information bit and the noise power spectral density. The ratio E_b/N_0 in dB is given by

$$
\begin{aligned}
\left(\frac{E_b}{N_0}\right)_{dB} =\ & \left(\frac{1}{N_0}\right)_{dB} - 10\log_{10} N_r \\
& -10\log_{10}\left(\text{(code rate)} \times \log_2\text{(constellation size)} \times \frac{N_c}{N_c + N_{cp}}\right)
\end{aligned}
\tag{4.50}
$$

where $10\log_{10} N_r$ is the array gain due to multiple receive hydrophones and (code rate) $\times$ $\log_2$(constellation size)$\times N_c/(N_c + N_{cp})$ denotes the bandwidth efficiency (bits/sec/Hz) of the coded modulation scheme. When N_r receive hydrophones are used, the TCM-OFDM and BICM-OFDM systems are denoted as TCM1xN_r and BICM1xN_r, respectively.

BER performance exploiting frequency diversity

SISO fading channels with various number of physical paths are considered. During each packet transmission, the channel gains are fixed, i.e., $f_d = 0$. Since the channel is invariant, time diversity is not available so the individual impact of frequency diversity towards improving the link performance is investigated here. The coded bits/symbols are interleaved within the packet and the interleaving depth is 4 sub-carriers.

Fig. 4-6(a) shows the BER performance of the TCM1x1 system over Rayleigh fading channels with different delay spreads. We note that as the number of channel paths increases, the

slope of the BER reaches its maximum value when the channel delay spread is 5 msec (4 non-zero taps). This means that the TCM1x1 cannot exploit the extra frequency diversity when the non-zero taps increase beyond four. An interesting observation is that for higher delay spreads, the system exhibits a slightly larger coding gain. The significant role of frequency diversity in improving the performance of the coded system is proved by the following observation: TCM1x1 requires 6 dB less power for a BER of 10^{-3} as the delay spread increases from 1 msec to 15 msec. In addition, the BER performance of the TCM1x1 over the AWGN channel is plotted to show the ultimate system performance when the channel fade is completely averaged out. Clearly, the performance gap between the two channels indicates that further improvement can be accomplished if other types of diversity are exploited (e.g. spatial diversity).

Fig. 4-6(b) shows the BER performance of the BICM1x1 system over the same channels. Note that as the number of channel taps increases, the slope of the BER reaches its maximum value when the channel has eight non-zero channel taps (15 msec delay spread). This means that the BICM1x1 cannot exploit the extra frequency diversity when the channel non-zero taps increase beyond eight. Again, we note that as the delay spread increases from 15 msec to 25 msec, that system presents a slightly higher coding gain. The impact of frequency diversity in improving the performance of the system is also pronounced here; BICM1x1 requires 7 dB less power for a BER of approximately 10^{-3} as the delay spread increases from 1 msec to 25 msec. In addition, the BER performance of the BICM1x1 over the AWGN channel is illustrated to show the ultimate system performance when the channel fade is completely averaged out.

Fig. 4-6(c) combines the results of Fig. 4-6(a) and (b) to compare the BER performances of TCM1x1 and BICM1x1. For the AWGN channel, TCM1x1 has an 1.57 dB power advantage at high E_b/N_0 due to its higher coding gain (4.59 as opposed to 3.2 for the BICM1x1). For Rayleigh fading channel with two diversity branches, both TCM1x1 and BICM1x1 attain the same BER slope, however TCM1x1 performs slightly better because it achieves a higher coding gain. For all other channels, BICM1x1 performs better at high E_b/N_0 due to its higher code diversity (8 as opposed to 2 for the TCM1x1). The impact of the code diversity in boosting the code performance is best seen when the fading channel provides eight physical paths. Then, BICM1x1 attains a much steeper BER slope than its TCM counterpart since it can exploit all eight diversity paths while TCM1x1 cannot. For instance, BICM1x1 needs 3 dB less power to

achieve a BER of $2 \cdot 10^{-4}$.

Fig. 4-7(a) and (b) illustrate the BER performances of TCM1x1 and BICM1x1 over Rician fading channels with different delay spreads. In addition, the corresponding performances over Rayleigh fading are shown for comparison. Clearly, both systems perform better in Rician fading. The line-of-sight component of the channel, makes both systems to attain approximately 1 dB higher coding gain. Note that the slope of the BER curves remains the same for all delay spreads and for both types of fading implying that the systems are able to harvest the same amount of frequency diversity. These simulation results manifest that both systems obtain a robust performance in both Rayleigh and Rician fading channels.

To conclude, the above simulation results manifest that in delay-limited fading channels, the code performance strongly depends on its code diversity, thus codes with higher code diversity (Hamming distance) must be preferred.

BER performance exploiting time and frequency diversity

To investigate the impact of time diversity on the BER performance, we let the channel to become time-varying within each packet period. On the other hand, the Doppler spread of the channel generate ICI in OFDM systems, which in turn may induce an error floor in the BER performance. To keep the system complexity low, the receiver doesn't compensate for ICI, therefore time-diversity will be beneficial if it manages to offset the SNR loss due to ICI. In addition, the interleaving depth is increased to ensure that codewords span *both* different coherent bands and different coherent time periods, i.e., *both* time and frequency diversity is exploited. Here, we model two Rayleigh fading channels. The first channel generates $f_d = 2$ Hz maximum one-sided Doppler spread and the interleaving depth (in sub-carriers) is 32. The second channel generates $f_d = 5$ Hz maximum one-sided Doppler spread and the interleaving depth is 64. Observe that the second channel has a smaller T_c (coherence time) than the first, thus it may provide higher time diversity order, but at the expense of stronger ICI.

In Fig. 4-8(a) we compare the BER performance of TCM1x1 for various delay and Doppler spreads. For channels with two non-zero taps (1 msec delay spread), the BER performance is improved as the Doppler spread increases from 0 to 5 Hz. This is due to the code diversity being large enough to exploit full multipath diversity as well as time diversity. On the other
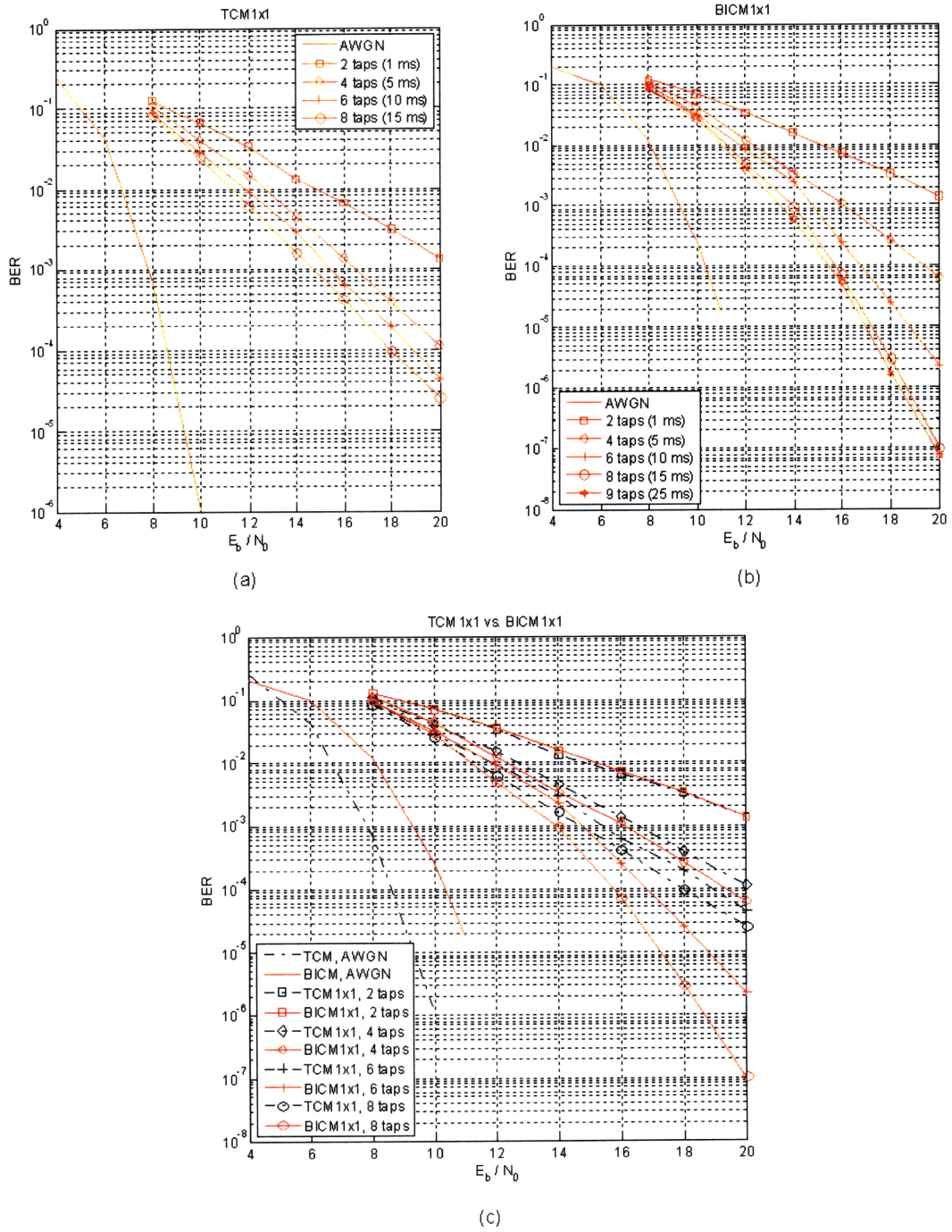
Figure 4-6: BER performances for TCM1x1 and BICM1x1 over various frequency selective Rayleigh fading channels and the AWGN channel (a) TCM1x1, (b) BICM1x1 (c) comparison between TCM1x1 and BICM1x1.
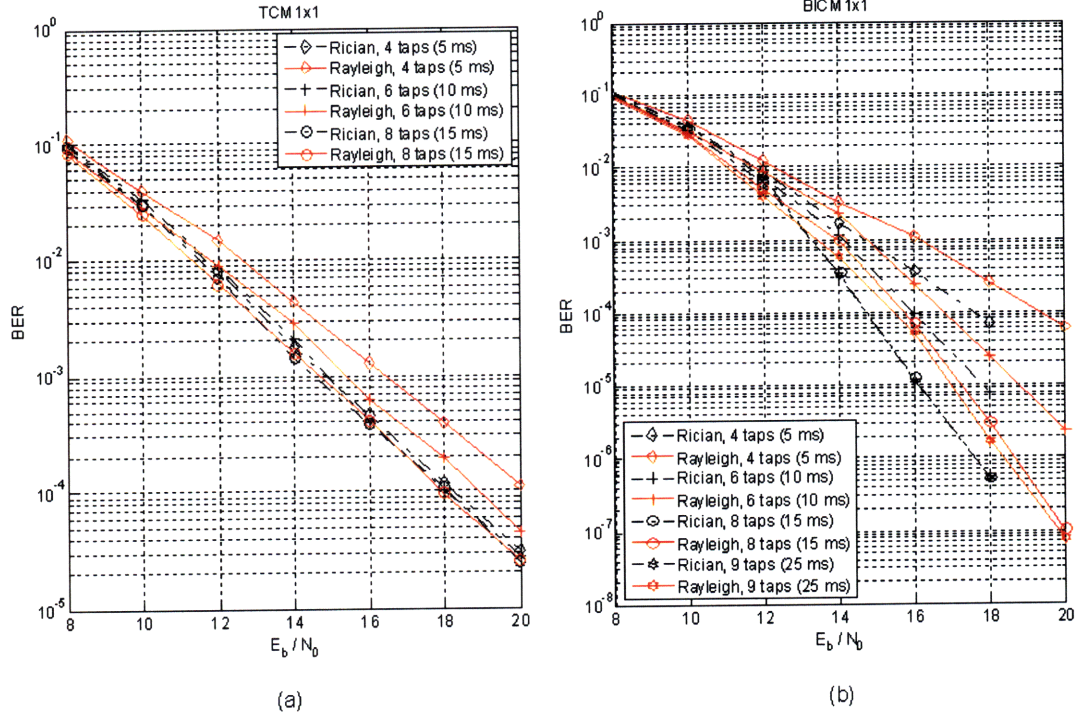
Figure 4-7: BER performances for TCM1x1 and BICM1x1 over various frequency selective Rician and Rayleigh fading channels: (a) TCM1x1, (b) BICM1x1.

hand, as the number of non-zero taps increases from two to eight, the frequency (multipath) diversity order becomes higher so the TCM code fails to exploit time diversity resulting in performance degradation relative to zero Doppler channels due to ICI. For instance, the channel characterized by 10 msec delay spread and 10 Hz Doppler spread yields the worst performance since it generates stronger ICI while the channel characterized by 10 msec delay spread and 0 Doppler spread yields the best performance since it doesn't produce any ICI.

The beneficial impact of time diversity is more pronounced in BICM1x1 for lower delay spread values, as seen in Fig. 4-8(b). For 1 msec delay spread, since the code diversity of the BICM1x1 is large enough to exploit both time and frequency diversity, the BER performance is improved relative to the 0 Doppler channel regardless the ICI increase. For instance, 5 dB less power is needed for a BER of approximately 10^{-3} when f_d increases from 0 to 5 Hz. Note that when the delay spread is 5 msec, the channel with 2 Hz Doppler bears a better performance

than the channel with 5 Hz Doppler. Observe that for a 10^{-4} BER, the 2 Hz channel has a 3 dB power advantage over the 5 Hz channel. This 3 dB loss due to ICI could motivate receiver structures, such as frequency domain equalizers, that compensate for the ICI. Finally, when the delay spread becomes 15 msec, the BER performance degrades as f_d increases from 0 to 5 Hz, since not only the code fails to exploit the available time diversity but also the ICI introduces an error floor.

BER performance exploiting space and frequency diversity

Here, we examine the impact of receive diversity on improving the BER performance of the link. Once again, we assume fixed channel gains during each packet transmission ($f_d = 0$). In every sub-band, the received signals from each hydrophone are weighted with respect to their corresponding channel gains and then summed, i.e., MRC is performed at the receiver. In Fig. 4-9(a) we compare the BER performances between TCM1x1 and TCM1x2. As expected, TCM1x2 outperforms TCM1x1 since TCM1x2 achieves twice the diversity gain of TCM1x1 (the total diversity gain is multiplicative in the number of receive hydrophones). Note for example, at $P_b = 10^{-4}$, the power advantage for TCM1x2 is about 5 dB when the channel has six non-zero channel paths. Similarly, BICM1x2 outperforms BICM1x1, as shown in Fig. 4-9(b). At $P_b = 10^{-4}$, the power advantage for BICM1x2 is about 4 dB when the channel has six non-zero channel paths. These results indicate that spatial diversity is very effective in improving the performance of weak codes and also justify the huge success in employing receive arrays in UWA communications.

In Fig. 4-9(c) we compare the BER performances between BICM1x2 and TCM1x2. Since both systems achieve full spatial diversity, their performance difference will be based on the amount of frequency diversity order each system can achieve. For 1 msec delay spread, both systems achieve full frequency and space diversity, however TCM1x2 performs better due to its higher coding gain. As the delay spread increases from 1 msec to 10 msec, the available frequency diversity also increases, thus BICM1x2 performs better at high E_b/N_0 since it manages to harvest more frequency diversity than its TCM1x2 counterpart. We stress that exactly the same results (with a slight increase in receiver/transmitter complexity) would be achieved if instead of two hydrophones and one projector we used two projectors and one hydrophone and
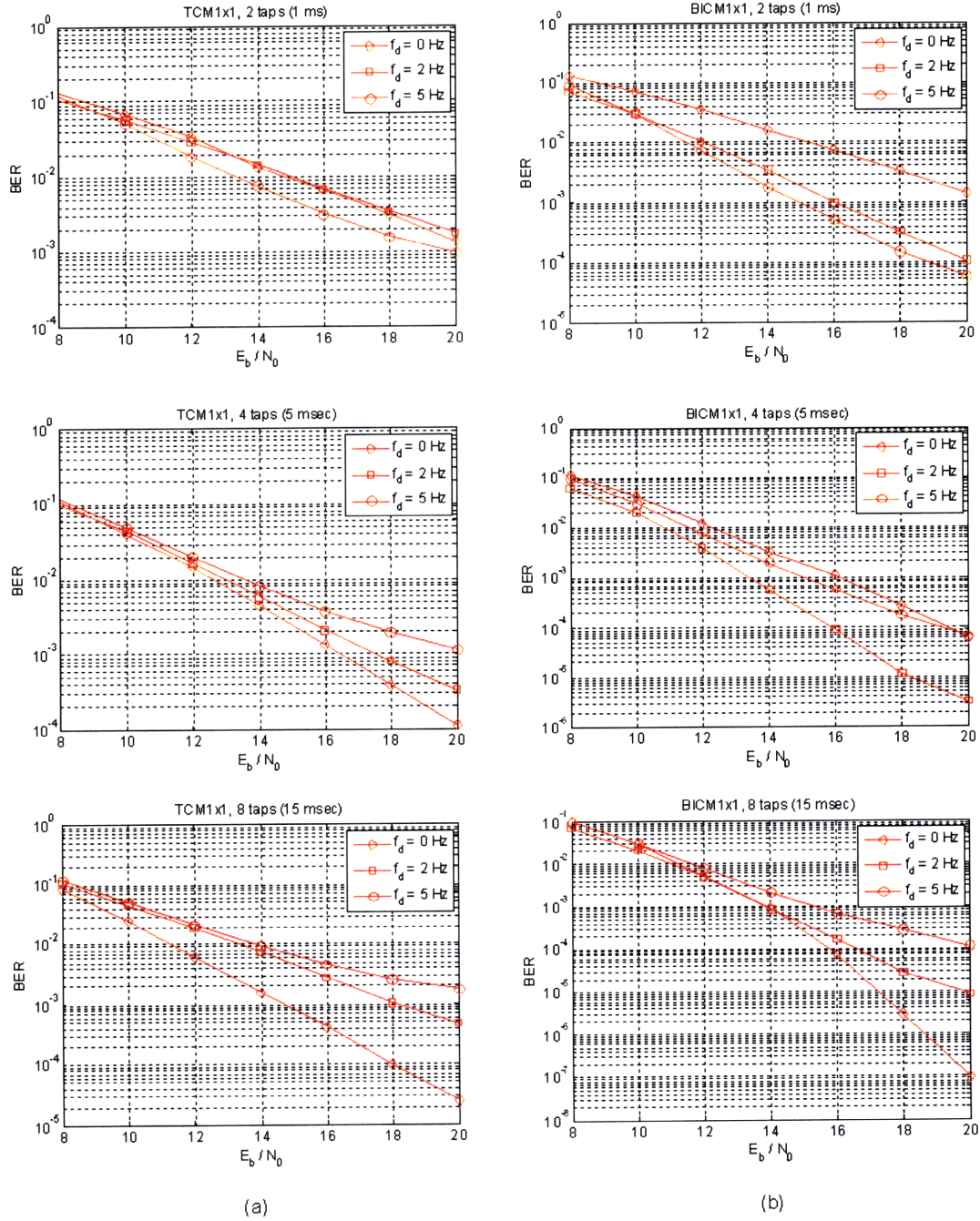
Figure 4-8: BER performances of TCM1x1 and BICM1x1 over Rayleigh fading channels with various delay and Doppler spreads: (a) TCM1x1, (b) BICM1x1.

118

the channel encoder/decoder was coupled with the Alamouti space-time encoder/decoder. This is because the Alamouti space-time code does not generate any throughput loss with respect to the 1x2 system and also it obtains second order spatial (transmit) diversity provided that the channel remains fixed for two OFDM symbol durations.

In Fig. 4-9(d), a remarkable result is presented[1]. When six receive hydrophones are used, the frequency-selective fading channel turns into an AWGN-like channel due to the ability of both systems to average out the channel fade by exploiting full space and frequency diversity. This is proved by the fact that the BER performances of both systems approach their corresponding performances for the AWGN channel as the frequency diversity increases. Since the free Euclidean distance is the key parameter to achieve better performance in AWGN channels, TCM1x6 outperforms BICM1x6. Hence, we claim that coded modulation schemes optimal for the AWGN channel perform better than schemes optimal for fading channels, as the number of space diversity branches increases.

---

[1]Tha authors in [35] derived a similar result for Rayleigh flat fading channels with receive diversity.
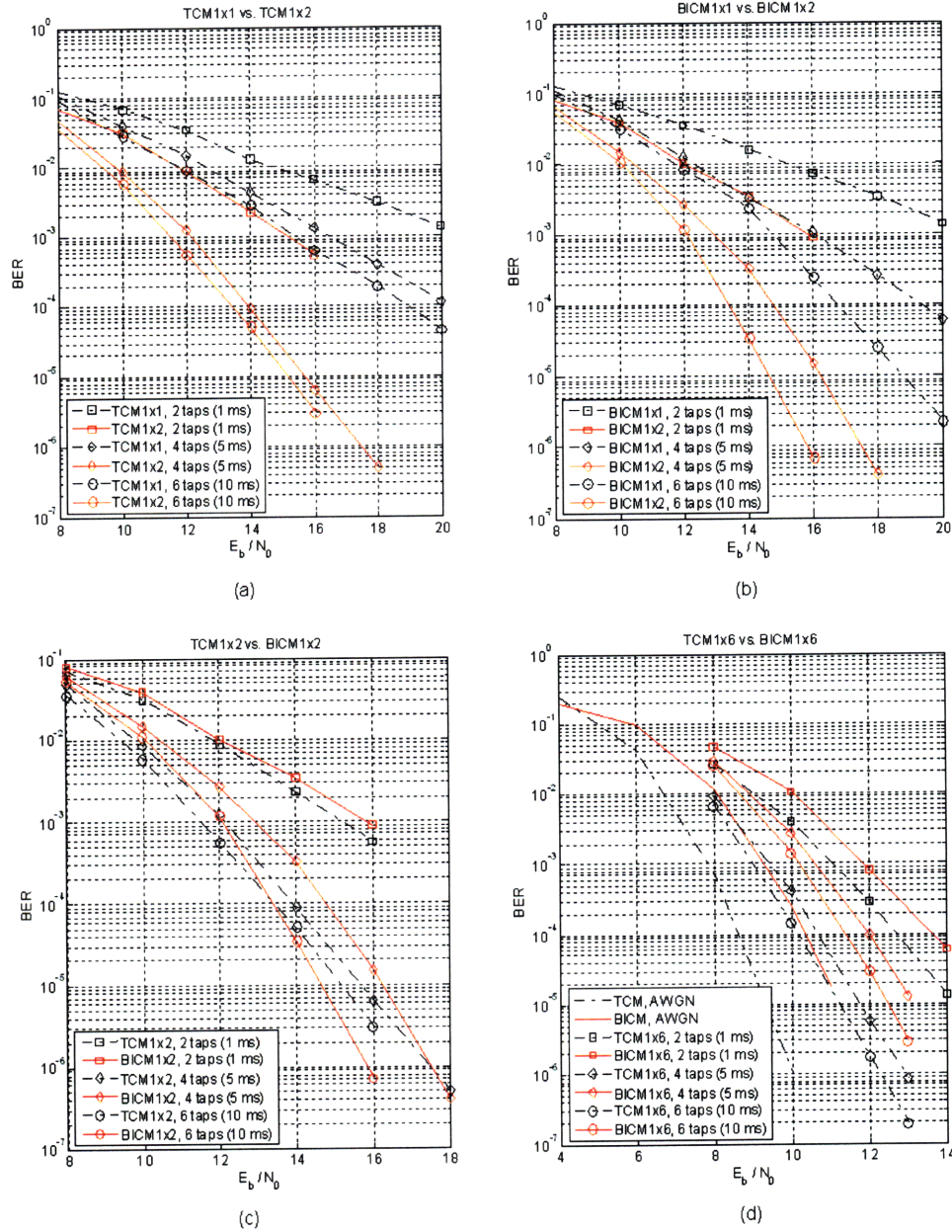
Figure 4-9: BER performances of TCM-OFDM and BER performance for TCM-OFDM and BICM-OFDM for various delays spreads and receive hydrophones: (a) comparison between TCM1x1 and TCM1x2, (b) comparison between BICM1x1 with BICM1x2, (c) comparison between BICM1x2 and TCM1x2, (d) comparison between BICM1x6 and TCM1x6.

Chapter 5

Experimental Results

In this chapter, we begin our discussion by describing the Rescheduled Acoustic Communications Experiment (RACE' 08). Then, the channel characterization is presented based on a set of estimated impulse responses and scattering functions. Finally, the systems introduced in the previous chapter, namely, TCM-OFDM, BICM-OFDM, TCM-STBC-OFDM, and BICM-STBC-OFDM, are investigated in terms of their BER performance based on decoding field data.

5.1   Description of RACE'08

The results of this chapter are derived by processing experimental data recorded during the Rescheduled Acoustic Communications Experiment (RACE) in Narragansett Bay, RI, in March 2008. The experiment location is illustrated in Fig. 5-1(a) and the experimental setup is shown in Fig. 5-1(b). The transmitter consisted of a three-sensor line array with 60 cm inter-sensor spacing and a separate primary transducer, which was 1 m above the uppermost element of the line array and 4 m above the sea-bottom. The transmitter was mounted on a rigid tripod and the depth at the transmitter site was 9 m. At 400 m and 1 km horizontal range north from the transmitter, two receivers were mounted on a 2 m tall rigid tripod. The receiver at 400 m range was a 24 sensor vertical array with 5 cm inter-sensor spacing. The receiver at 1000 m range was a 12 sensor line array with 12 cm inter-sensor spacing. The depth at the receiver locations was approximately 10 m. The sampling frequency of both transmitting and receiving
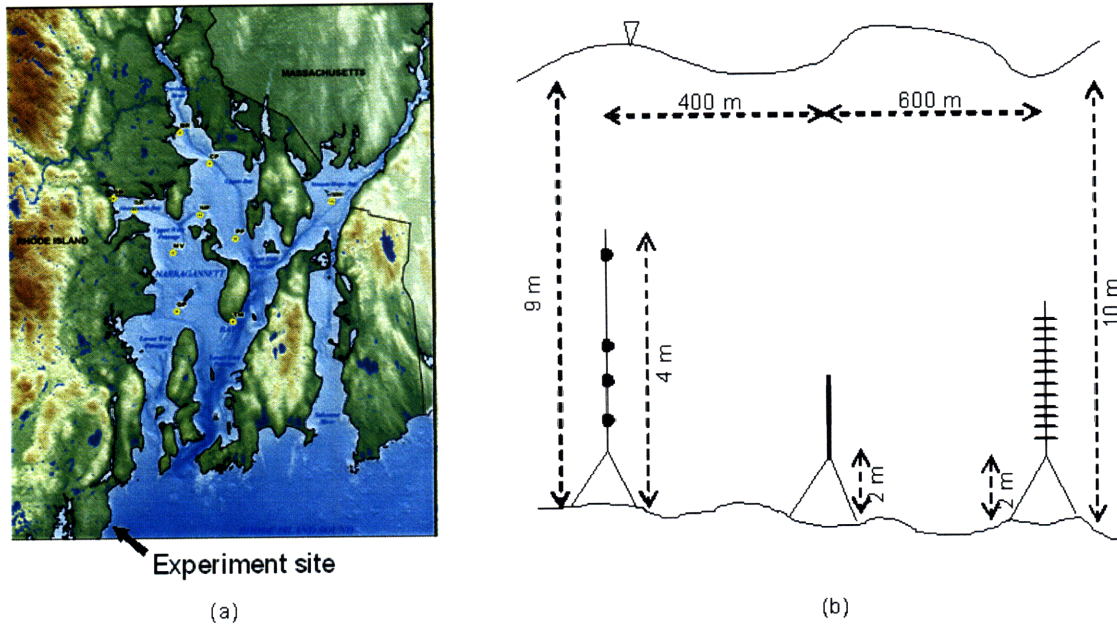
Figure 5-1: RACE'08: (a) Experiment site in Naragansett Bay, RI. (b) Schematic representation of the experimental setup.

systems was 39062.5 samples/sec and they also incorporated anti-aliasing filters with 18.5 kHz cut-off frequency.

The primary source transducer was an ITC-1007 transducer while the source array transducers were AT-12ET transducers. Both transducer types had omnidirectional beam patterns in the horizontal and their output level is shown in Fig. 5-2. In addition, every receive hydrophone in both arrays had a flat frequency response across the 8000-18000 Hz band. The total emitted signal level was 185 dB re 1μPa at 1 m away from the source(s).

The signals intended for estimating the channel delay spread function were transmitted from the ITC-1007 and used the 8000-18000 Hz band, hence maximum delay resolution afforded by the hardware was achieved. These signals were pre-compensated before transmission to yield a "flat" response system between the transmit and receive transducers. The communication signals, on the other hand, occupied a small band of 3906.25 Hz centered at 12 kHz and no pre-compensation was applied.
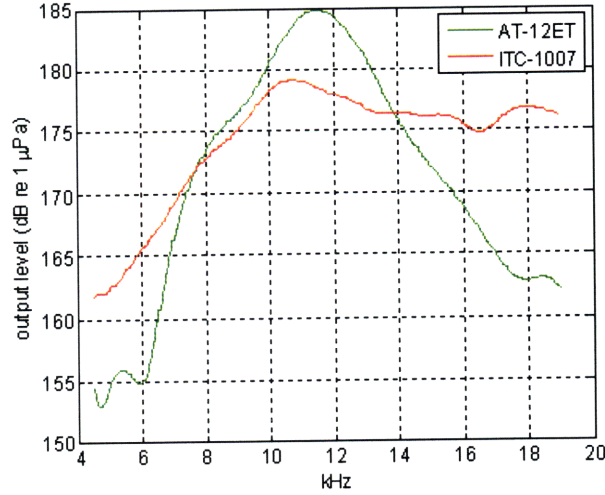
Figure 5-2: Transmit output levels of the transducers used in RACE'08.
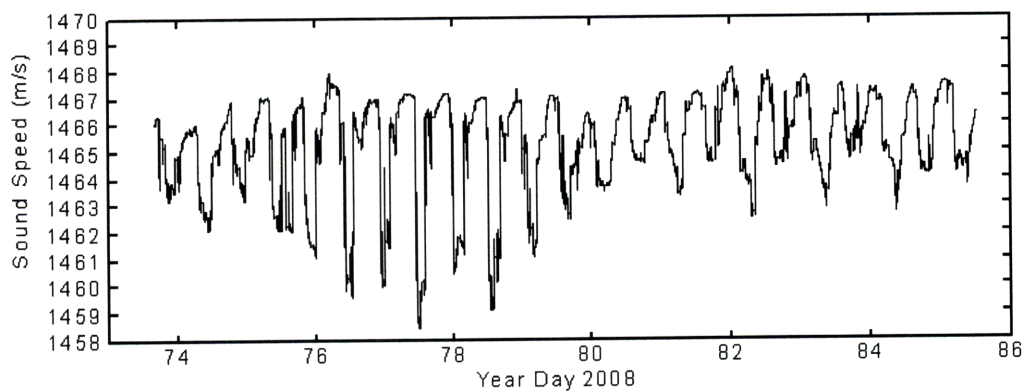
5.2   Channel characterization

Fig. 5-3 shows measurements of the wind speed, the surface waveheight and the sound speed, recorded during a period of the experiment. In all the plots, the x-axis indicates the Julian Date of the experiment. For example, the Julian date 74 corresponds to March 14th, 2008, the Julian date 75 corresponds to March 15th and so on. The wind speed was measured by an anemometer mounted at the shore. The surface height was computed by using 200 μsec chirp pulses transmitted every 0.25 sec from the WHOI upward looking broadband backscattering system, which was mounted 1 m above the sea bottom. The same system recorded temperature and salinity of the sea water enabling us to compute how the sound speed was changing at the system's location. Clearly, significant environmental variations took place during the experiment, and since both the transmitter and the receiver were idle, any rapid amplitude fluctuations of the received signal (signal fading) are attributed to environmental changes. To validate this, below we compute a set of channel impulse responses and scattering functions corresponding to dates 74 and 75. During these dates, a sudden increase in the wind speed caused an increase in the sea-surface roughness, as the shaded areas of Fig. 5-3 illustrate.
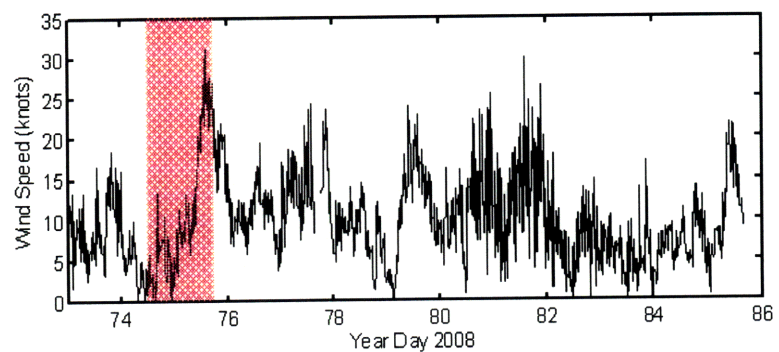
(a)
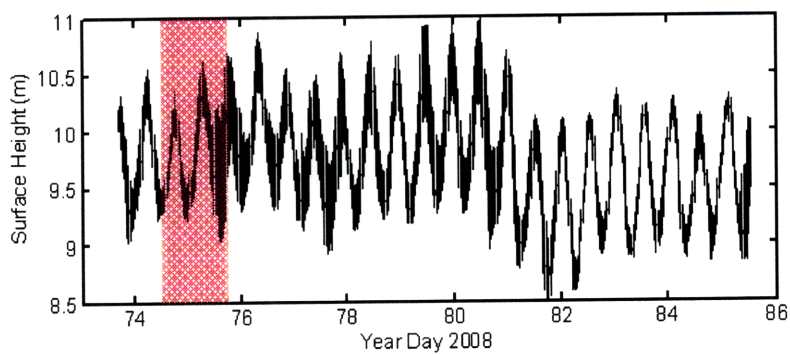
(b)

(c)

Figure 5-3: Enviromental data recorded during dates 73-85 of RACE'08: (a) wind speed, (b) surface height, (c) sound speed at a specific location 1 m above the sea bottom.

Temporal characterization

Now we characterize the channels our probing signals experienced by a set of impulse responses and scattering functions. The probing signal was a 55 second long, continuous repetition of a binary amplitude modulated, 4095 symbol length, m-sequence. The bandwidth of the m-sequence was 10 kHz, so its total duration was 0.41 sec. The probing signal was translated to baseband, low-pass filtered and downsampled by a factor of 2, before cross-correlating it with the transmitted m-sequence to produce an estimate of the time-varying impulse response. Although this estimate becomes rough when the channel changes faster than 0.41 sec, yet useful conclusions can be extracted. Figures 5-4 - 5-7 illustrate the temporal evolution of the amplitude of the estimated channel delay-spread function over a three minute interval. The horizontal axis represents delay, the vertical axis represents absolute time and the colorbar represents the amplitude. The channel estimates were computed by processing data sets, received during dates 74 and 75. The time written in the title of every plot represents the actual transmission time of the first probing signal followed by other two sequential probe transmissions. Between two successive probe transmissions there was a 5 sec pause. In all the plots, the intensity ranges from 0 to 1. Moreover, all plots are overlaid with white dashed lines, which indicate the predicted times of several important signal arrival times. These arrivals are computed relative to the true direct path arrival time. These lines are numbered from 1 to 6 and should be interpreted as follows:

1. line 1 denotes the delay of both the true direct and the predicted first bottom bounce arrival. This is due to the fact that their path delay difference is much less than 0.1 msec, which is the maximum delay resolution of the probe signal.

2. line 2 denotes the delay of the nominal first surface bounce arrival relative to line 1.

3. line 3 denotes the delay of the nominal surface-bottom bounce arrival relative to line 1.

4. line 4 denotes the delay of the nominal bottom-surface bounce arrival relative to line 1.

5. line 5 denotes the delay of the nominal bottom-surface-bottom bounce arrival relative to line 1.

6. line 6 denotes the delay of the nominal surface-bottom-surface bounce arrival relative to line 1.

These nominal signal arrivals were predicted by running a 2-D ray propagation algorithm assuming constant sound speed profile, flat bottom and flat sea surface. We stress that the 1000 m channel has a shorter nominal multipath spread than that of the 400 m channel.

During date 74, the 400 m waveguide exhibited maximum delay spread of about 0.5 msec (an exception occurs at 2:00 am where a head wave appeared 0.5 msec prior to the direct arrival), as seen by Fig. 5-4. Note that the multipath arrival times appear relatively stable and the true arrival times agree with the predicted ones. Based on the plots we can claim that the true multipath consists of the following four components: direct arrival, first bottom bounce arrival, first surface bounce arrival and first surface-bottom bounce arrival (lines 1-3). A delay spread of 0.5 msec resulted to an ISI span of about 2 symbols for signaling at a rate of 3906.25 symbols/sec. Also note shifted the multipath arrival times are shifted in delay due to the hourly changes of the sound speed. Fig. 5-5 indicates that the 1000 m waveguide exhibited a maximum delay spread of about 1 msec, which yields an ISI span of about 4 symbols. Contrary to the 400 m waveguide, the multipath arrival structure appears unstable and the impulse response demonstrates stronger amplitude fluctuations. This can be explained as follows: since the nominal arrival times are very close relative to each other (fractions of a msec), even small surface fluctuations (i.e., reflections from wave troughs and crests) can cause different multipath components to arrive either earlier or later than their nominal arrival times. As a result, their constructive/destructive interference produces an unpredictable arrival pattern.

The plots in Figures 5-6 and 5-7 are computed by processing data sets, received at different hours during the date 75. Clearly, in both waveguides the impulse response appears highly time-varying with random multipath structure as opposed to the previous day. The reason is rather obvious; rough seas cause the specular reflection point of the sea surface to rapidly move either above or below the average sea surface yielding either later or earlier arrival delays than the predicted ones. Note that the delay spread of the 1000 m channel was increased by approximately 1 msec relative to the previous day.

We complement the previous results by computing channel scattering functions using different data sets. Fig. 5-8 shows the estimated scattering functions of the channel as seen by

the 6th sensor of the 1000 m station array, and the 12th sensor of the 400 m station array. The intensity plots of the scattering function are in dB scale. The scattering function computation method is deferred in the Appendix B. During the 74th day, the scattering functions for both channels demonstrate little Doppler spread since the channel fluctuations are benign. On the contrary, a Doppler spread of 1 Hz and 2 Hz was experienced in the 400 m and 1000 m channels respectively during the 75th day.

Spatial characterization

Now we examine the spatial coherence of the channel based on cross-correlating the output of different sensors of the array. Spatial coherence gives significant insight on the efficiency of receive diversity techniques. Fig. 5-9 shows the magnitude of cross-correlation functions for several sensor outputs from data received in the 400 m range station for two different days. Significant decorrelation happens when sensors are separated by more than 40 cm, which corresponds to approximately 4λ at 12 kHz, λ being the acoustic wavelength. Note, however, that as the sensor separation increases beyond the 16th element (80 cm), the correlation increases again implying that the spatial correlation function demonstrates a periodic structure along the the water column. Fig. 5-10 depicts the magnitude of cross-correlation functions from data taken from the 1000 m range station for the same dates. Significant decorrelation happens when sensors are separated by more than 48 cm, which corresponds to approximately 4λ. Note that in this case, the correlation does not appear to be periodic across the length of the array. In all cases, the averaging window was 0.8 sec.

Based on the previous discussion, both channels are not fully saturated since there is a significant intersensor spatial coherence. However, the 1000 m waveguide appears more saturated than the 400 m one validating the argument that channel coherence decreases as the range increases [43]. In addition, using consecutive sensors is inefficient in terms of exploiting receive diversity but rather is effective for coherent spatial filtering.

Noise characterization

Fig. 5-11 shows the power spectral density of the ambient noise after passing through a bandpass filter to remove the out-of-band noise. A selected set of results is shown. As expected, the
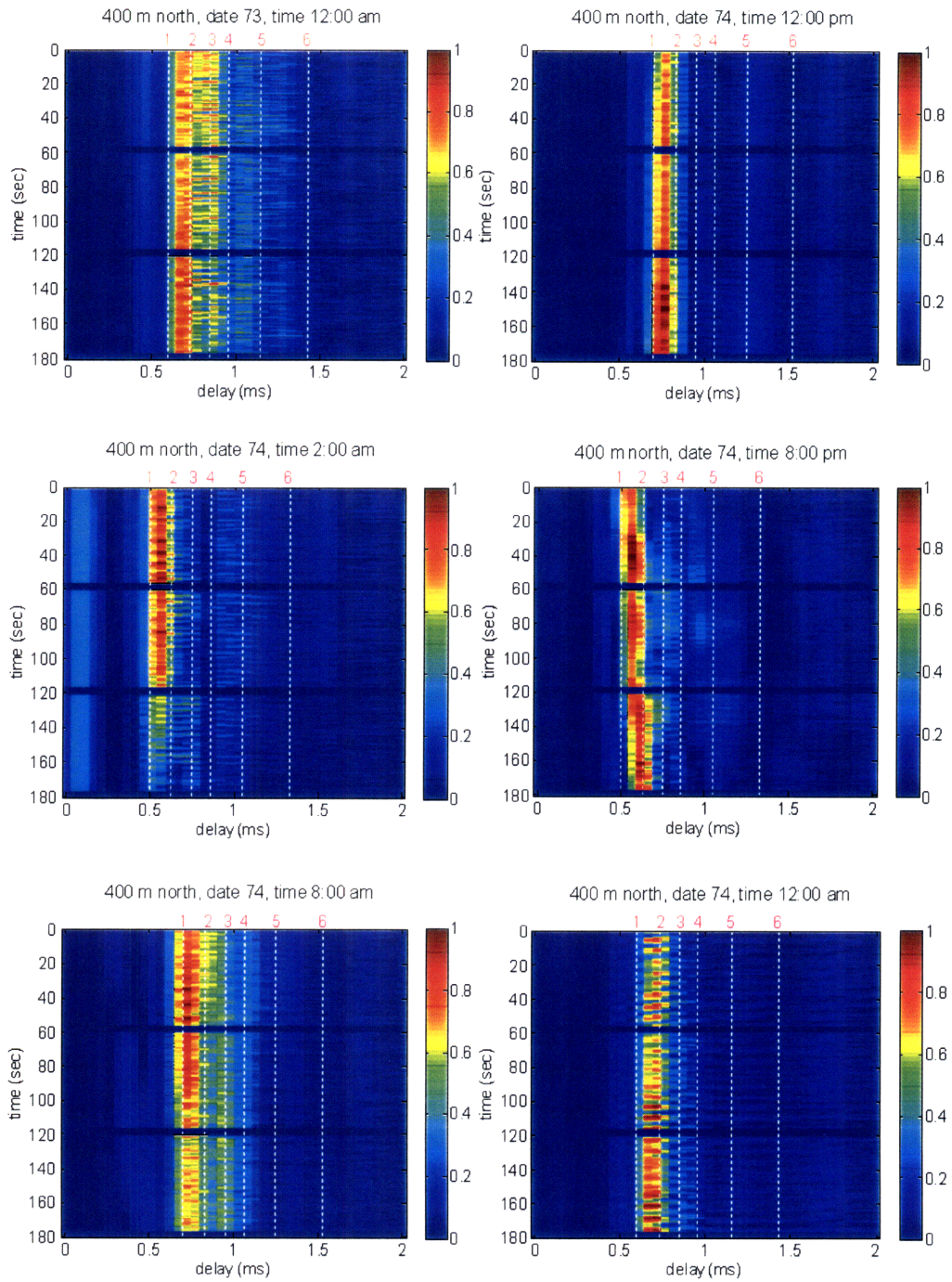
Figure 5-4: Date 74 of RACE'08. Snapshots of the estimated time-varying channel impulse response as seen by the 12th sensor of the 400 m range station array.
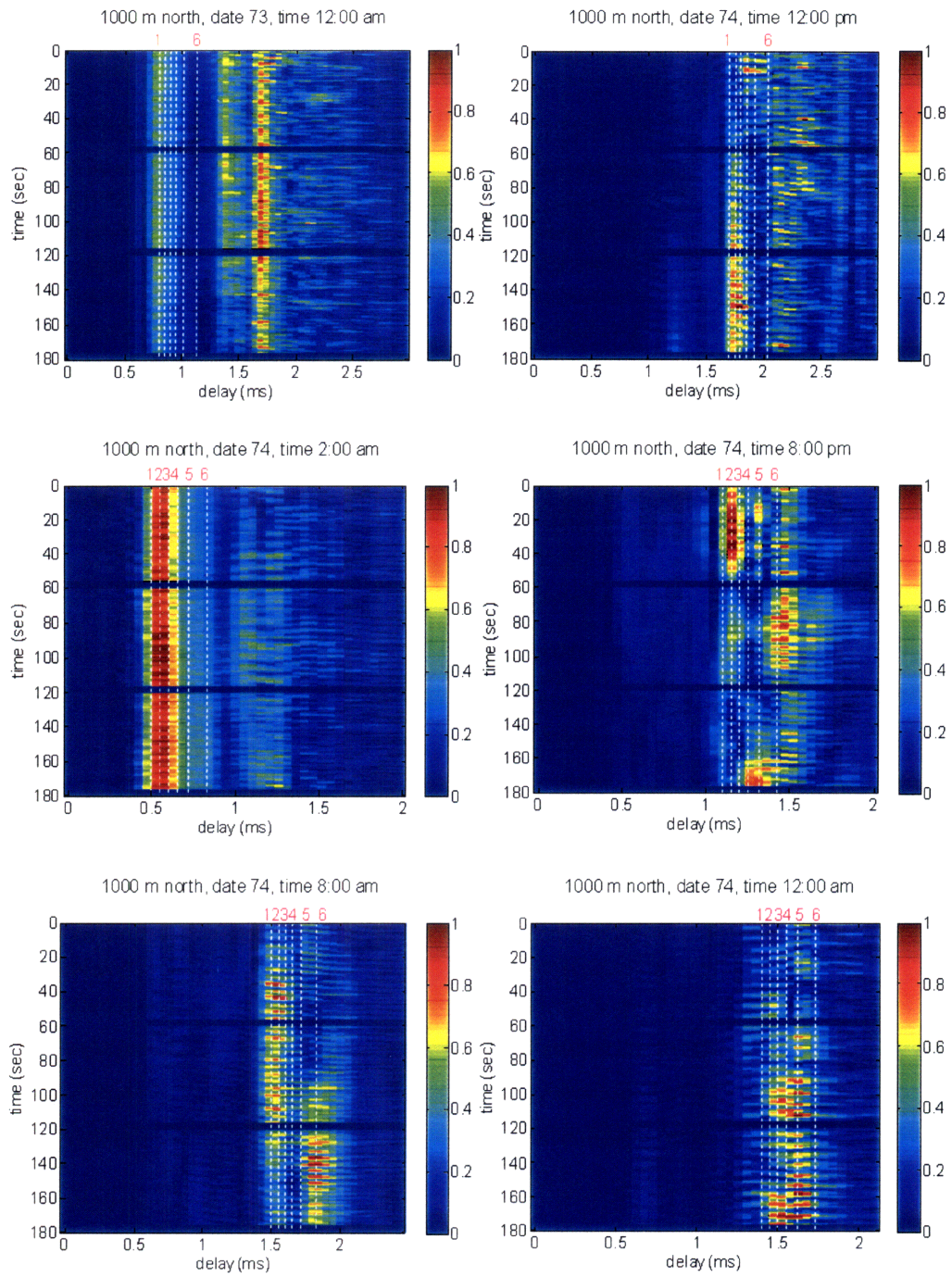
Figure 5-5: Date 74 of RACE'08. Snapshots of the estimated time-varying channel impusle response as seen by the 6th sensor of the 1000 m range station array.
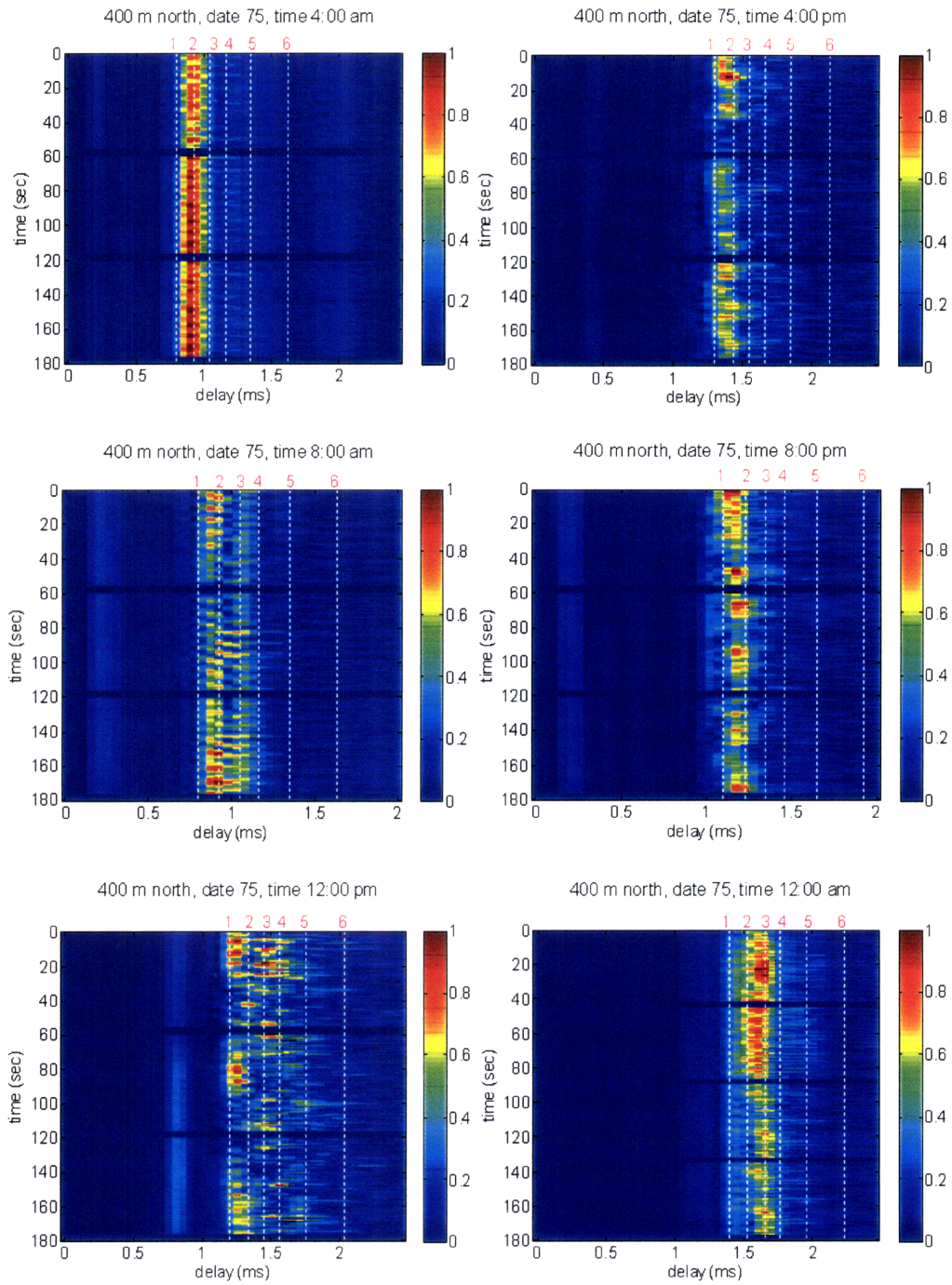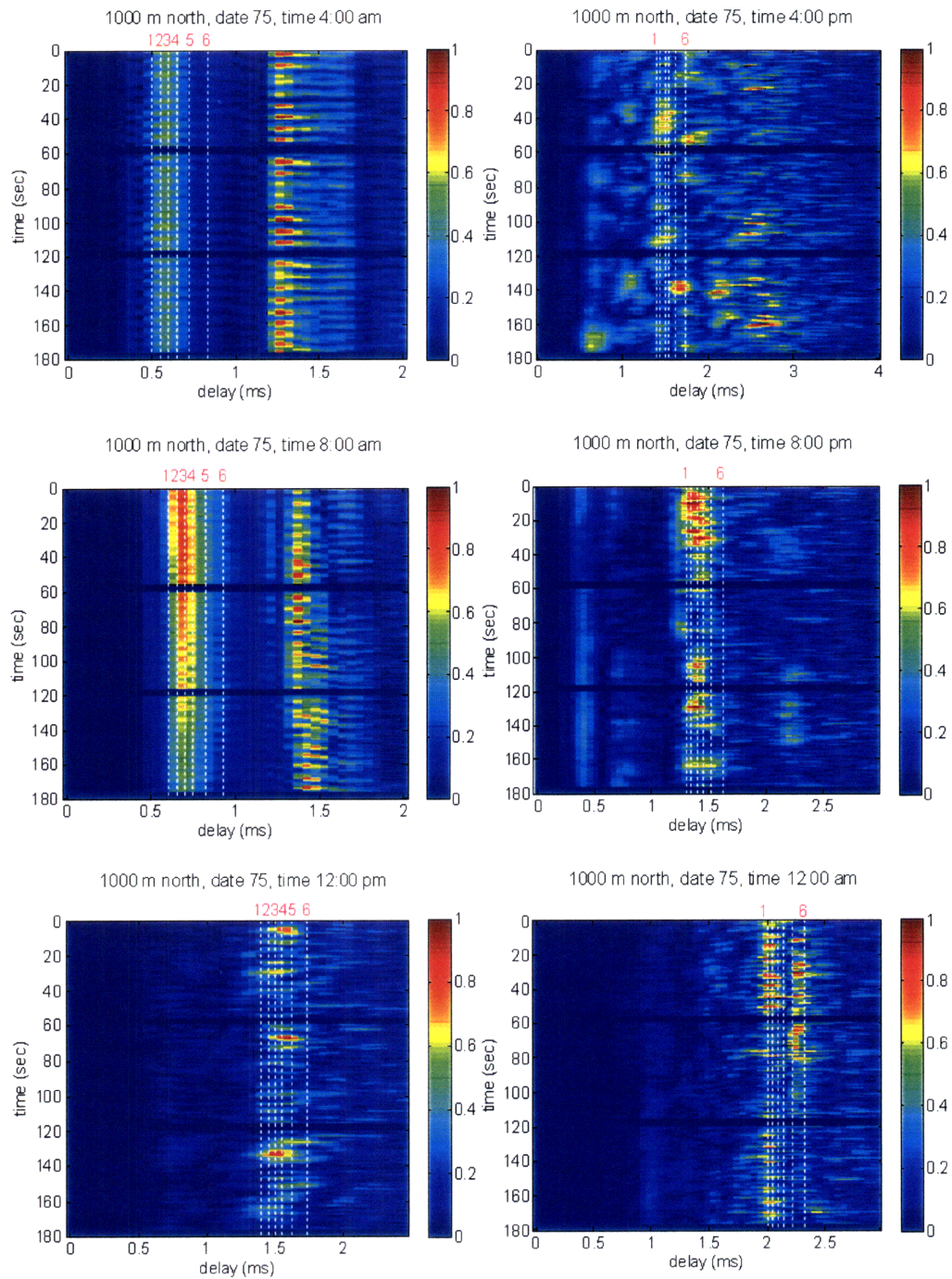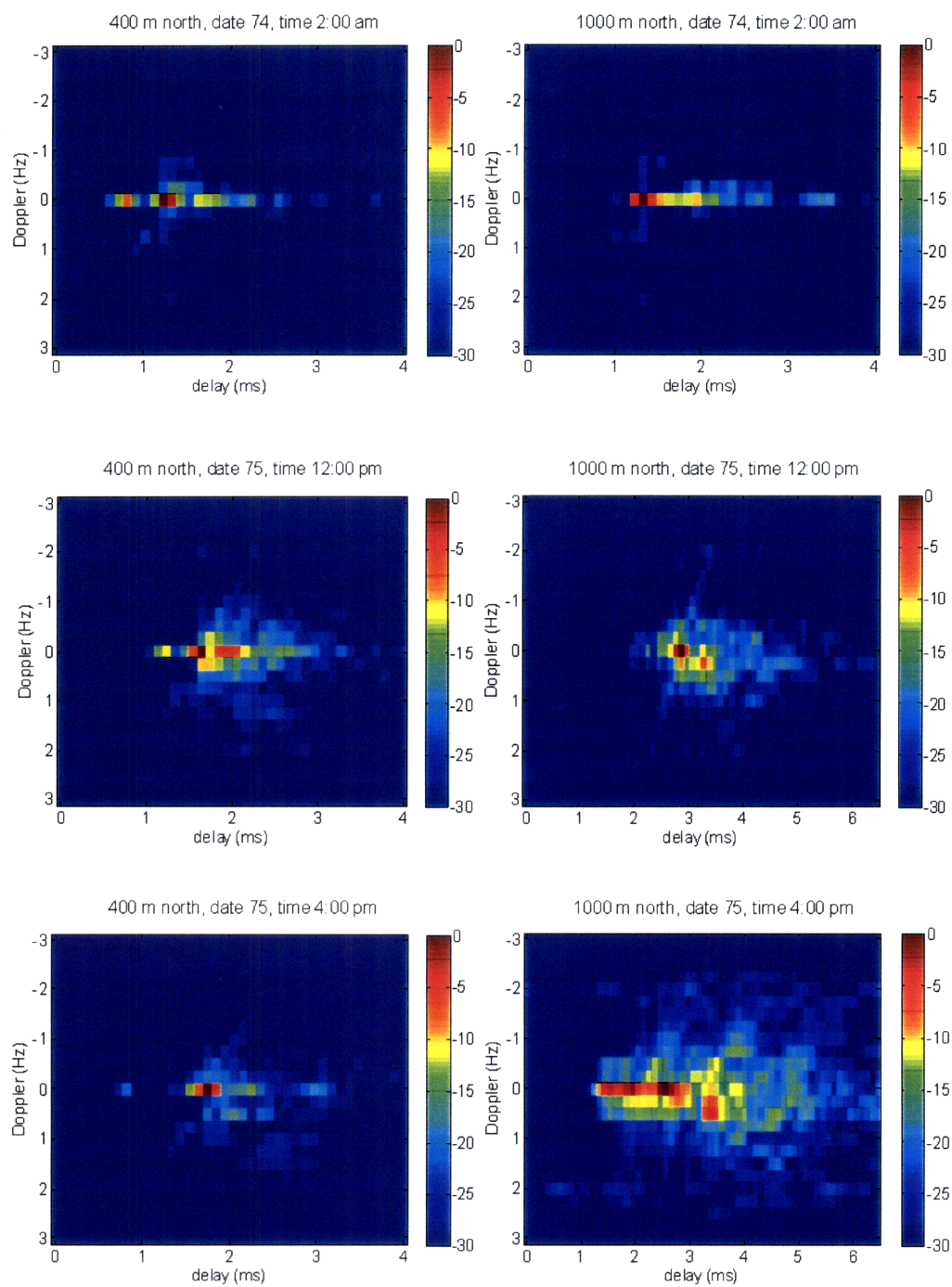
Figure 5-6: Date 75 of RACE'08. Snapshots of the estimated time-varying channel impusle response as seen by the 12th sensor of the 400 m range station array.

130

Figure 5-7: Date 75 of RACE'08. Snapshots of the estimated time-varying channel impusle response as seen by the 6th sensor of the 1000 m range station array.

Figure 5-8: Intensity plots of the estimated scattering function for both 400 m and 1000 m stations by processing data received during dates 74 and 75.
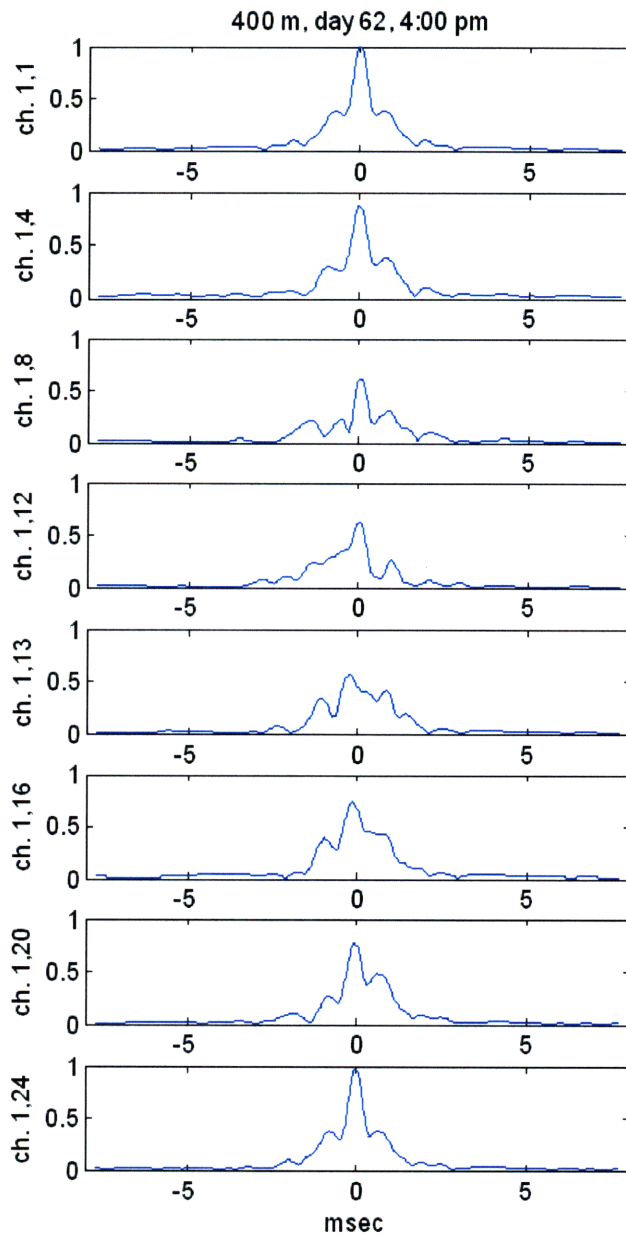
Figure 5-9: Unbiased cross-correlation functions between sensor outputs 4, 8, 12, 13, 16, 20, 24 and output 1. The first plot from the top is the auto-correlation of sensor output 1. Data were taken from the 400 m range station during date 62 at 4:00 pm.
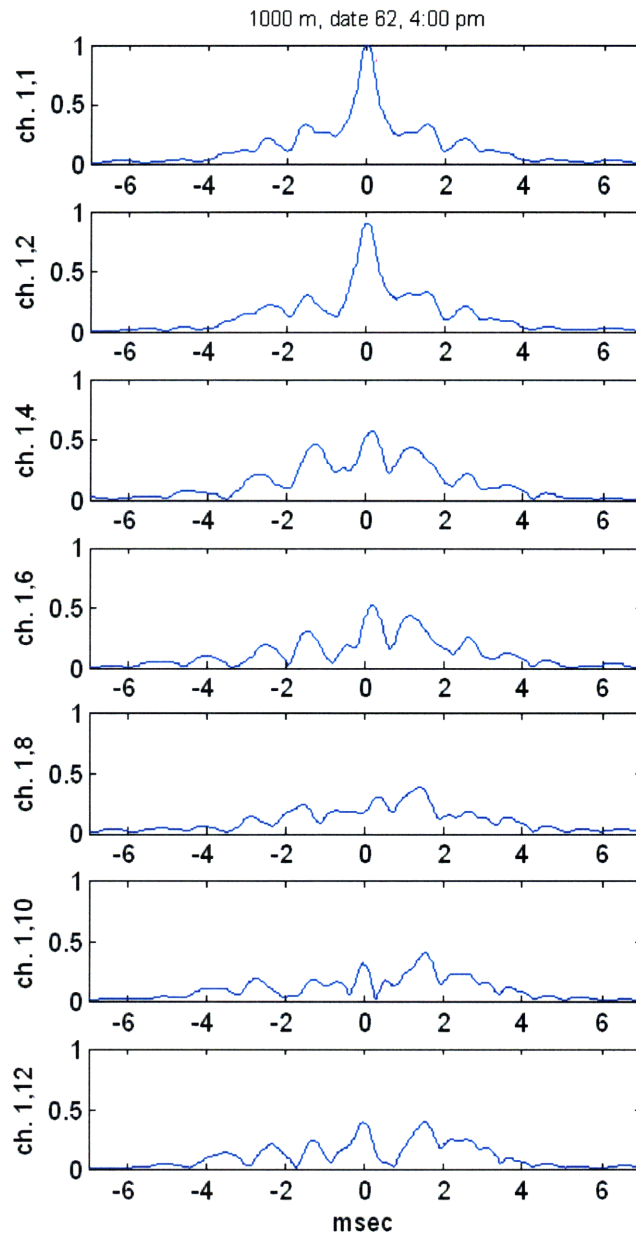
133

Figure 5-10: Unbiased cross-correlation function between sensor outputs 2, 4, 6, 8, 10, 12, and output 1. The first plot from the top is the auto-correlation of sensor output 1. Data were taken from the 1000 m range station during date 62 at 4:00 pm.
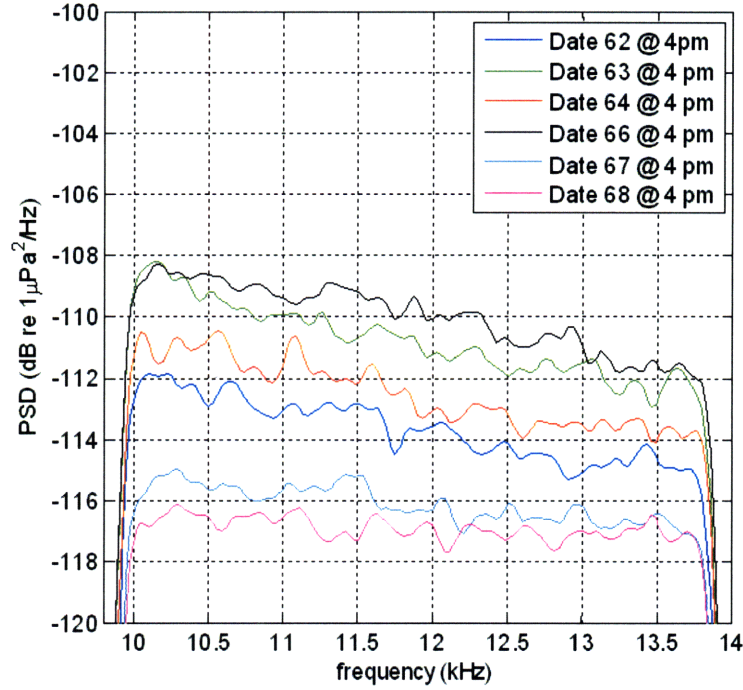
Figure 5-11: Power spectrum density of ambient noise for dates 62-68 at 4pm. All measurements were taken from the 1000m range station.

spectrum level decreases slowly with frequency for the band of interest.

5.3 Decoding results

Here, we provide an extensive set of BER results for the TCM-based and BICM-based systems by decoding field data received during RACE'08. The transmitted bits were organized into packets and each packet generated a TCM-based communication signal followed by its BICM-based counterpart. Each packet was retransmitted every four hours during the same day. We call this 4 hour period as an *epoch*.

# of sub-carriers N_c	Expected channel delay spread T_d (msec)	Expected channel Doppler f_d (Hz)	Pilot symbol distances (N_t, N_f)	# of information bits	Effective bit-rate (bits/sec)
128	7	2	$(4, 2)$	4596	5500
128	7	4	$(2, 2)$	2036	4700
128	12	2	$(3, 1)$	2560	3570
128	12	4	$(2, 1)$	1280	2600
256	7	2	$(2, 3)$	4600	5800
256	7	4	$(1, 3)$	2040	4700
256	12	2	$(2, 2)$	4084	4800
256	12	4	$(1, 2)$	1524	3300
512	7	2	$(1, 5)$	4896	5900
512	7	4	$(1, 5)$	4896	5900
512	12	2	$(1, 3)$	4080	4800
512	12	4	$(1, 3)$	4080	4800

Table 5.1: Signal parameters and corresponding bit-rates for system with one projector.

5.3.1 Single projector systems

In this section, we compare the BER performance between the TCM-OFDM system (Sec. 4-1) and the BICM-OFDM system (Sec. 4.2). The symbol/bit interleaving was chosen to be random across the entire length of each packet in order to ensure time diversity. Packets with various combinations of number of sub-carriers, T_d (expected channel delay spread), f_d (expected channel one-sided Doppler spread) and pilot symbol distances were tested. These combinations, the number of information bits in each packet, and the corresponding packet data rate (after coding and excluding pilot symbols) are organized in Table 5.1. Signals were transmitted from the ITC-1007 only.

We now compare the BER performances of TCM-OFDM and BICM-OFDM based on the packets received at the 1000 m range station. A selected set of decoding results and comparisons are presented in Figures 5-12 - 5-19. Note that at various epochs a different number of TCM and BICM packets were decoded. This is because many of the transmitted packets were corrupted by unknown interference. In all plots, $BER = 0$ is plotted as $BER = 10^{-6}$ for visualization. Label 1x1 indicates that one transmit and one receive hydrophone (the 12th sensor) were used for decoding each packet. Similarly, labels 1x2 and 1x3 indicate that a combination of two

Date	useful # of packets	1x1 BICM	1x1 TCM	1x2 BICM	1x2 TCM	1x3 BICM	1x3 TCM
March 1st (61)	46	**39**	32	**44**	42	**44**	43
March 2nd (62)	33	**22**	11	**33**	30	**33**	33
March 3rd (63)	41	**38**	26	**40**	39	**40**	39
March 4th (64)	44	**33**	11	**43**	42	**43**	42
March 5th (65)	62	**59**	39	**62**	56	**62**	58
March 6th (66)	63	**48**	40	**62**	61	**63**	61
March 7th (67)	45	**37**	36	**43**	41	**44**	42
March 25th (85)	37	**34**	27	**37**	36	**37**	37

Table 5.2: Number of error-free packets received at 1000 m range station during dates 61-68, 85 for TCM1xn and BICM1xn.

(6th and 12th) and three (1st, 6th and 12th) receive sensors were used to decode the packets, respectively. The choice of sensors is justified by the decoding results, seen in Figures 5-20 and 5-21. Various packets were decoded by using either pair (1, 2) or pair (1,12) of receive sensors. Obviously, employing pair (1,2) does not aid spatial diversity since these sensors exhibit highly correlated channel gains. From all BER plots, BICM clearly performs better than TCM, especially when one receive sensor is employed. When two or three sensors were employed, BICM performs marginally better. The success of BICM relative to TCM is also evident in Table 5.2, which shows the number of error-free packets for each method.

These experimental results show that the advantage of having a higher Hamming distance is a key parameter to obtaining robust performance over UWA channels with low spatial diversity. The BICM scheme is more successful due to its higher Hamming distance (eight as opposed to two for TCM), which allows it to harvest more efficiently the channel's inherent time and frequency diversity. This result is in accord with the simulation results shown in Sec. 4.5, which have also proven the superiority of BICM in Rayleigh/Rician multipath fading channels with low spatial diversity.
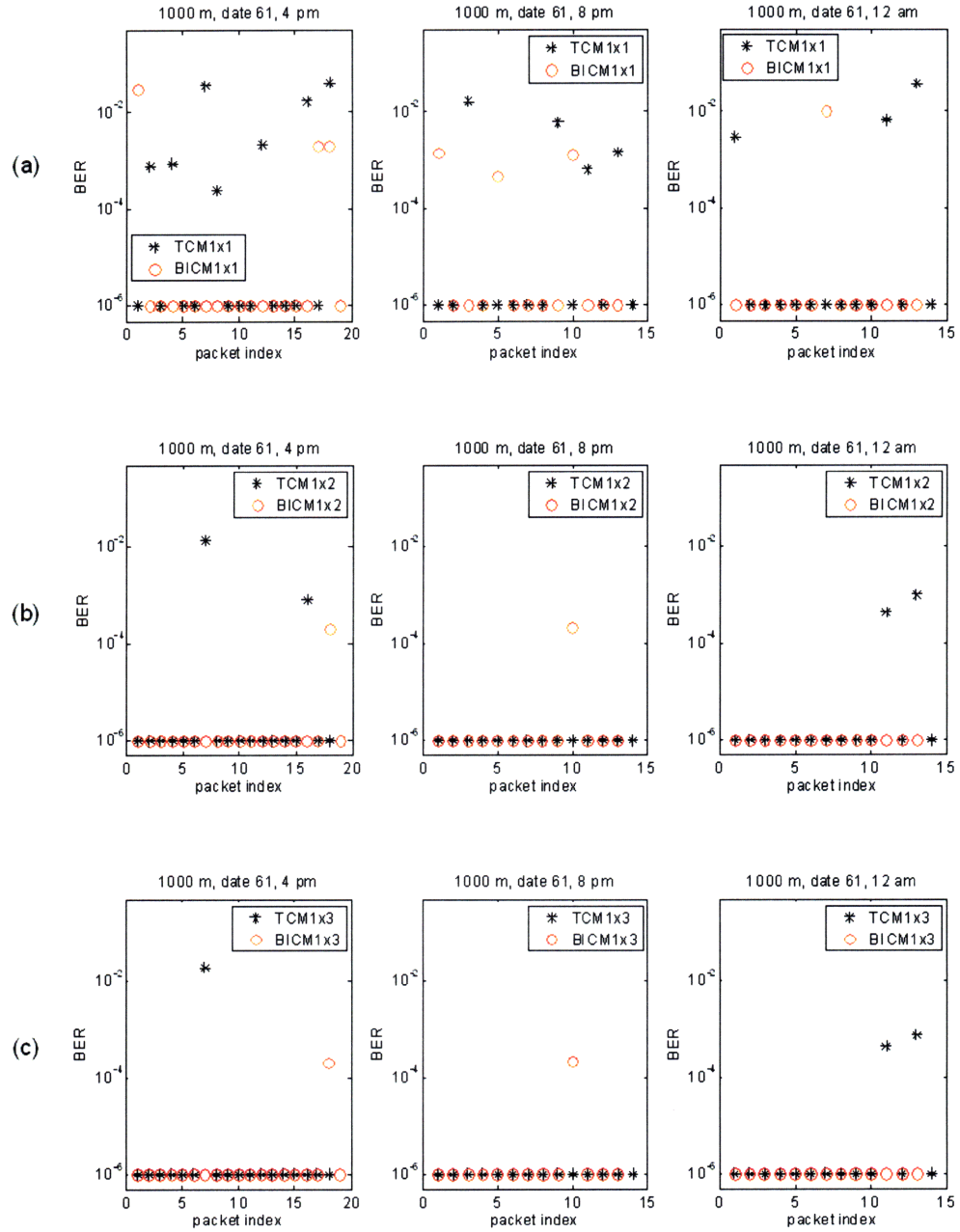
Figure 5-12: BER plots corresponding to date 61, 1000 m range station; (a) TCM/BICM systems with one transmit and one receive hydrophone (1x1); (b) TCM/BICM systems with one transmit and two receive hydrophones (1x2); (c) TCM/BICM systems with one transmit and three receive hydrophones (1x3).
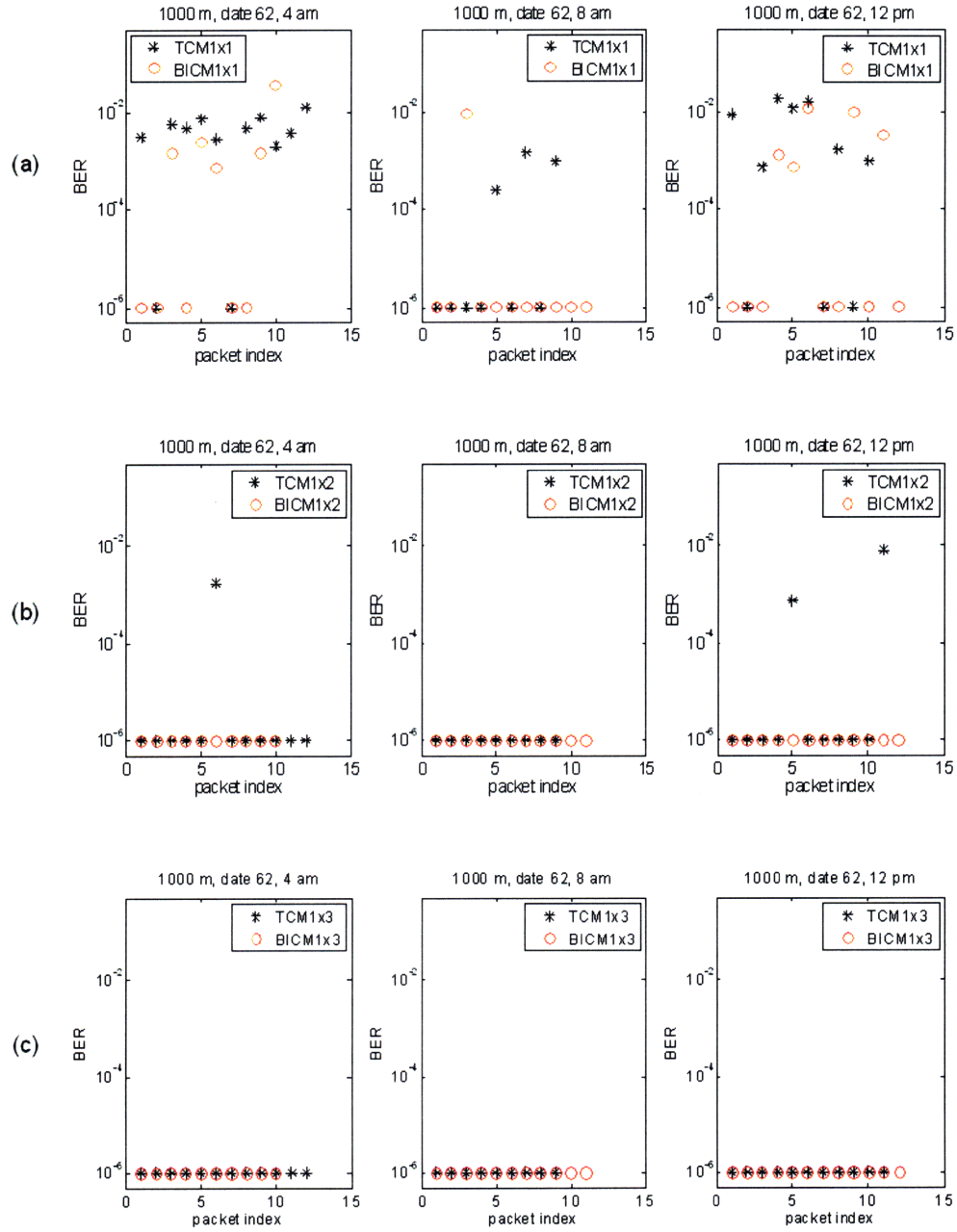
Figure 5-13: BER plots corresponding to date 62, 1000 m range station; (a) TCM/BICM systems with one transmit and one receive hydrophone (1x1); (b) TCM/BICM systems with one transmit and two receive hydrophones (1x2); (c) TCM/BICM systems with one transmit and three receive hydrophones (1x3).
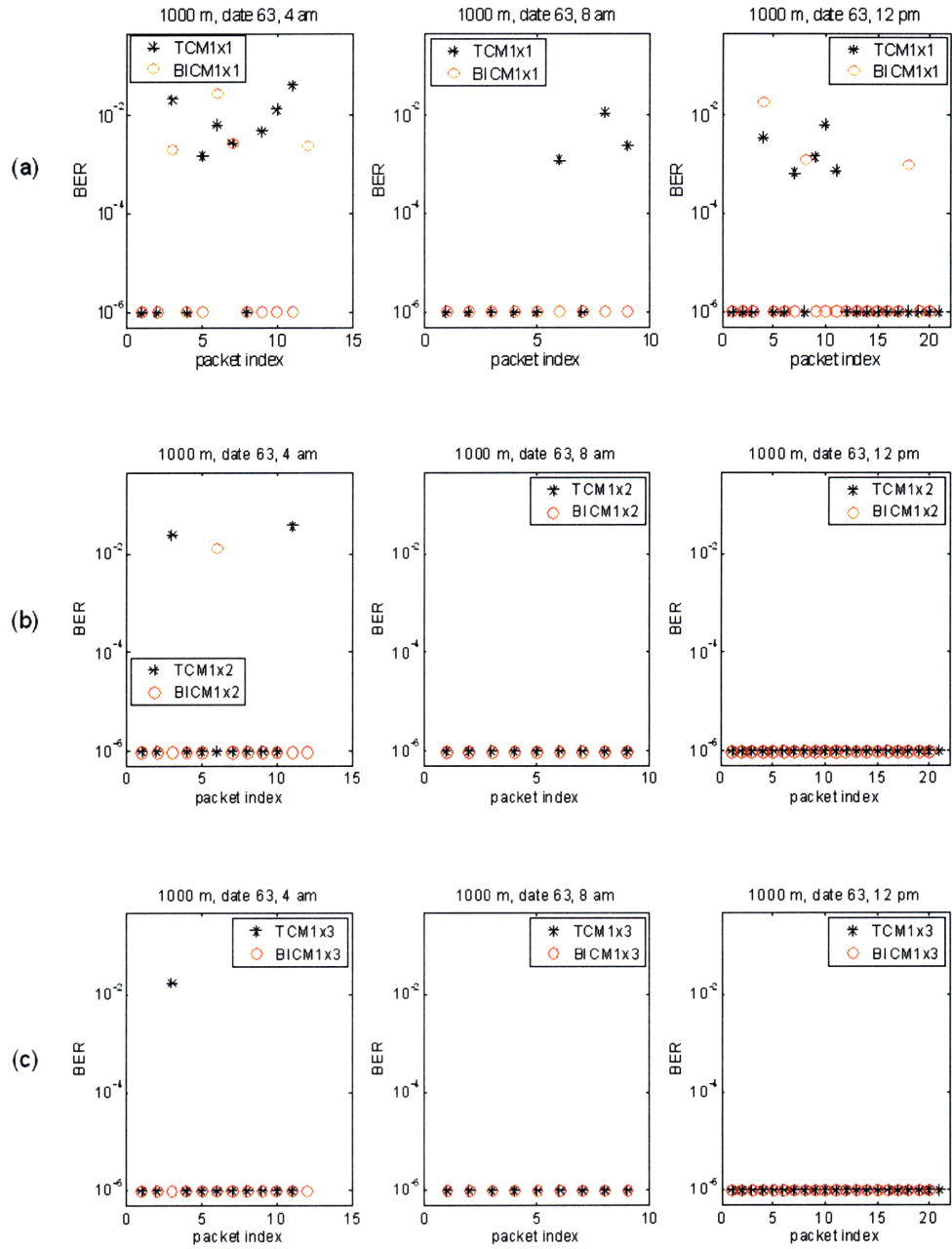
Figure 5-14: BER plots corresponding to date 63, 1000 m range station; (a) TCM/BICM systems with one transmit and one receive hydrophone (1x1); (b) TCM/BICM systems with one transmit and two receive hydrophones (1x2); (c) TCM/BICM systems with one transmit and three receive hydrophones (1x3).
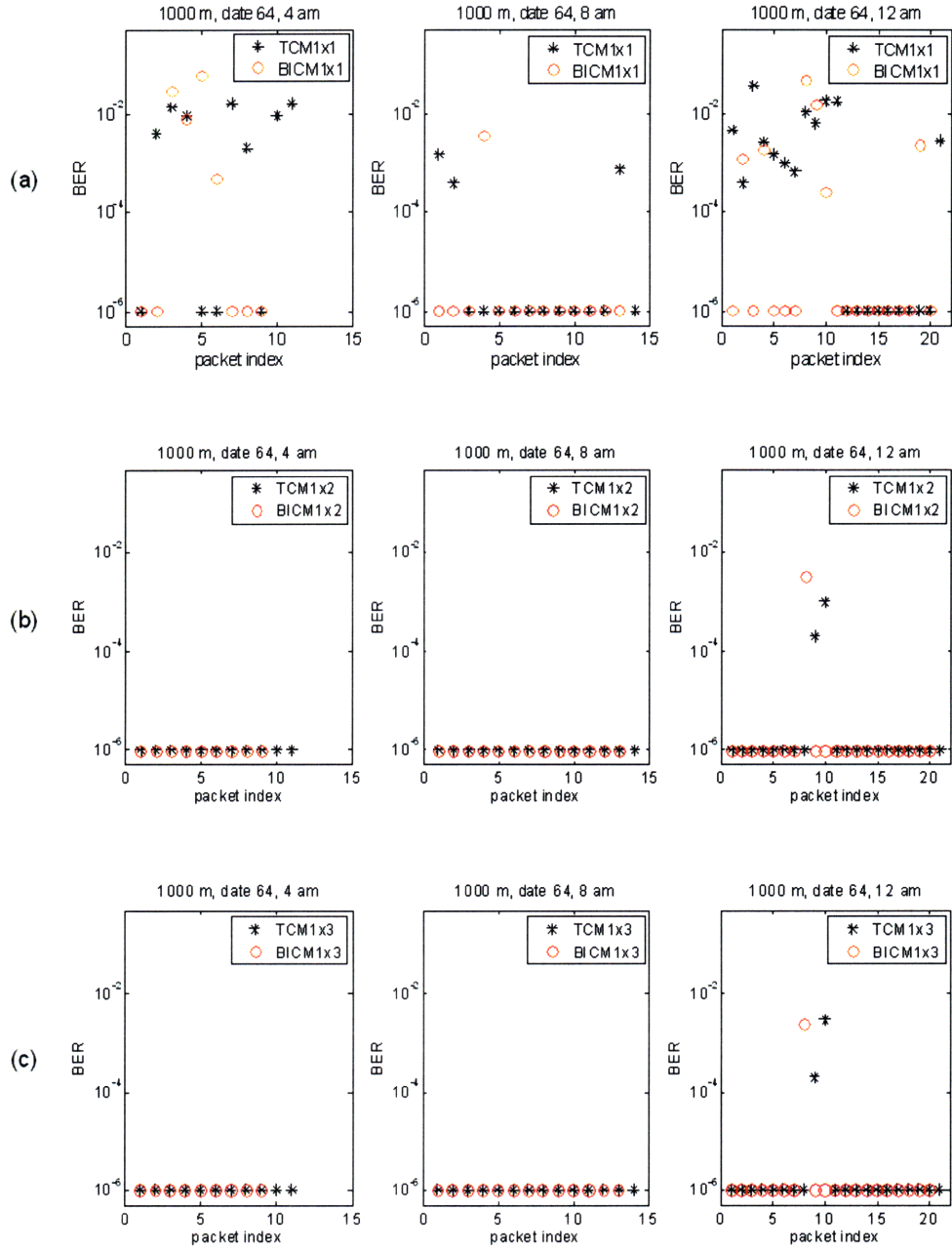
Figure 5-15: BER plots corresponding to date 64, 1000 m range station; (a) TCM/BICM systems with one transmit and one receive hydrophone (1x1); (b) TCM/BICM systems with one transmit and two receive hydrophones (1x2); (c) TCM/BICM systems with one transmit and three receive hydrophones (1x3).

Figure 5-16: BER plots corresponding to date 65, 1000 m range station; (a) TCM/BICM systems with one transmit and one receive hydrophone (1x1); (b) TCM/BICM systems with one transmit and two receive hydrophones (1x2); (c) TCM/BICM systems with one transmit and three receive hydrophones (1x3).
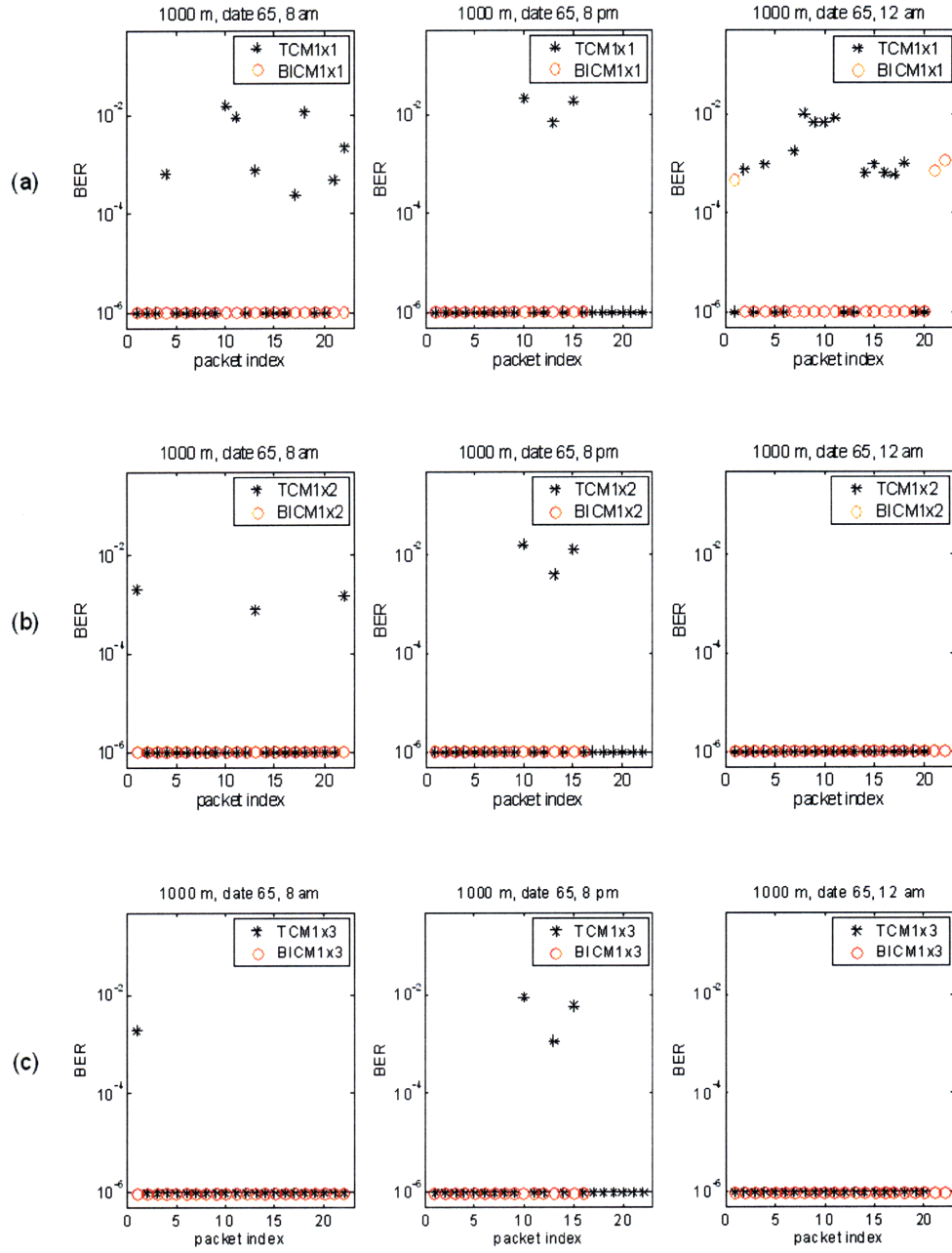
Figure 5-17: BER plots corresponding to date 66, 1000 m range station; (a) TCM/BICM systems with one transmit and one receive hydrophone (1x1); (b) TCM/BICM systems with one transmit and two receive hydrophones (1x2); (c) TCM/BICM systems with one transmit and three receive hydrophones (1x3).

Figure 5-18: BER plots corresponding to date 67, 1000 m range station; (a) TCM/BICM systems with one transmit and one receive hydrophone (1x1); (b) TCM/BICM systems with one transmit and two receive hydrophones (1x2); (c) TCM/BICM systems with one transmit and three receive hydrophones (1x3).
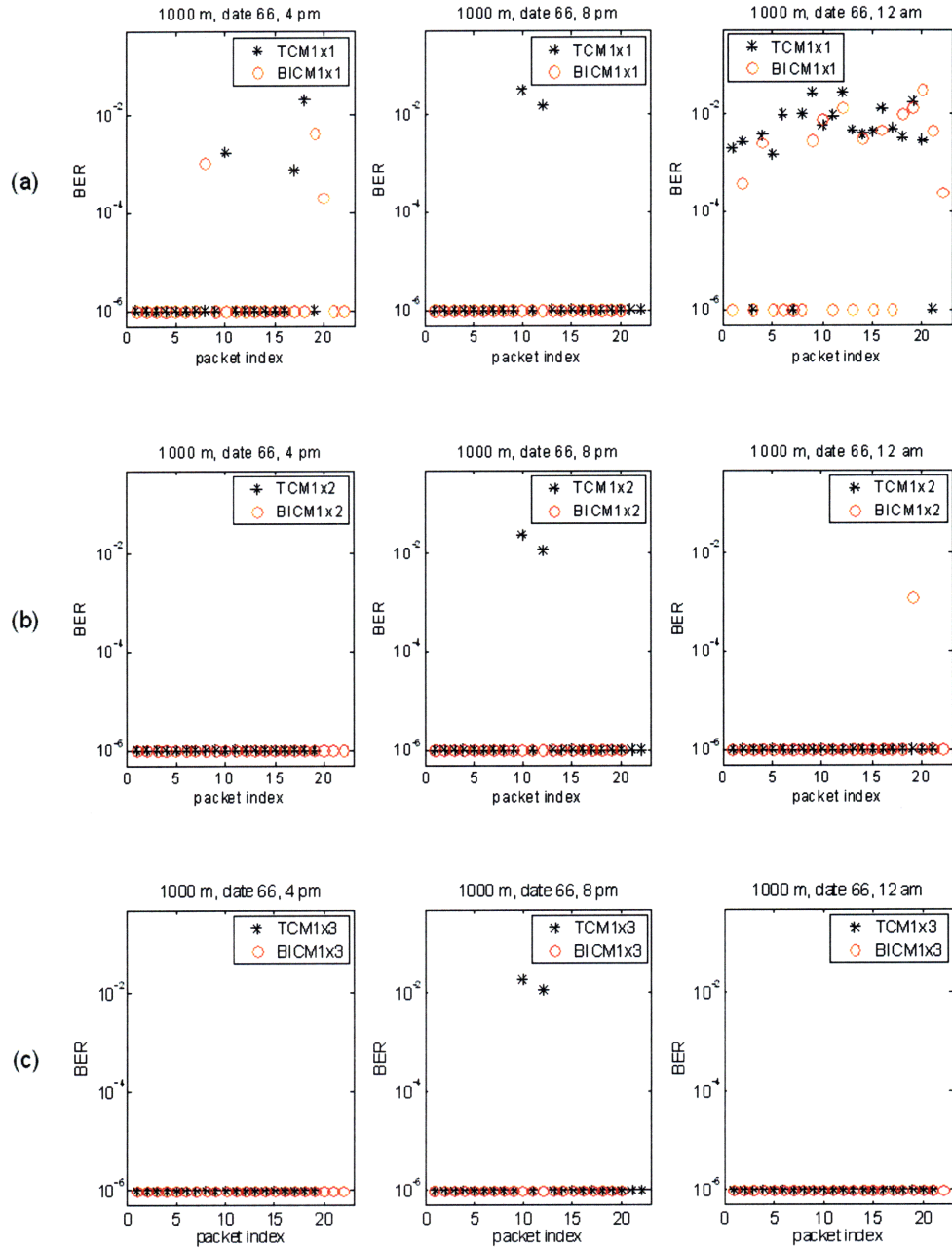
Figure 5-19: BER plots corresponding to date 85, 1000 m range station; (a) TCM/BICM systems with one transmit and one receive hydrophone (1x1); (b) TCM/BICM systems with one transmit and two receive hydrophones (1x2); (c) TCM/BICM systems with one transmit and three receive hydrophones (1x3).
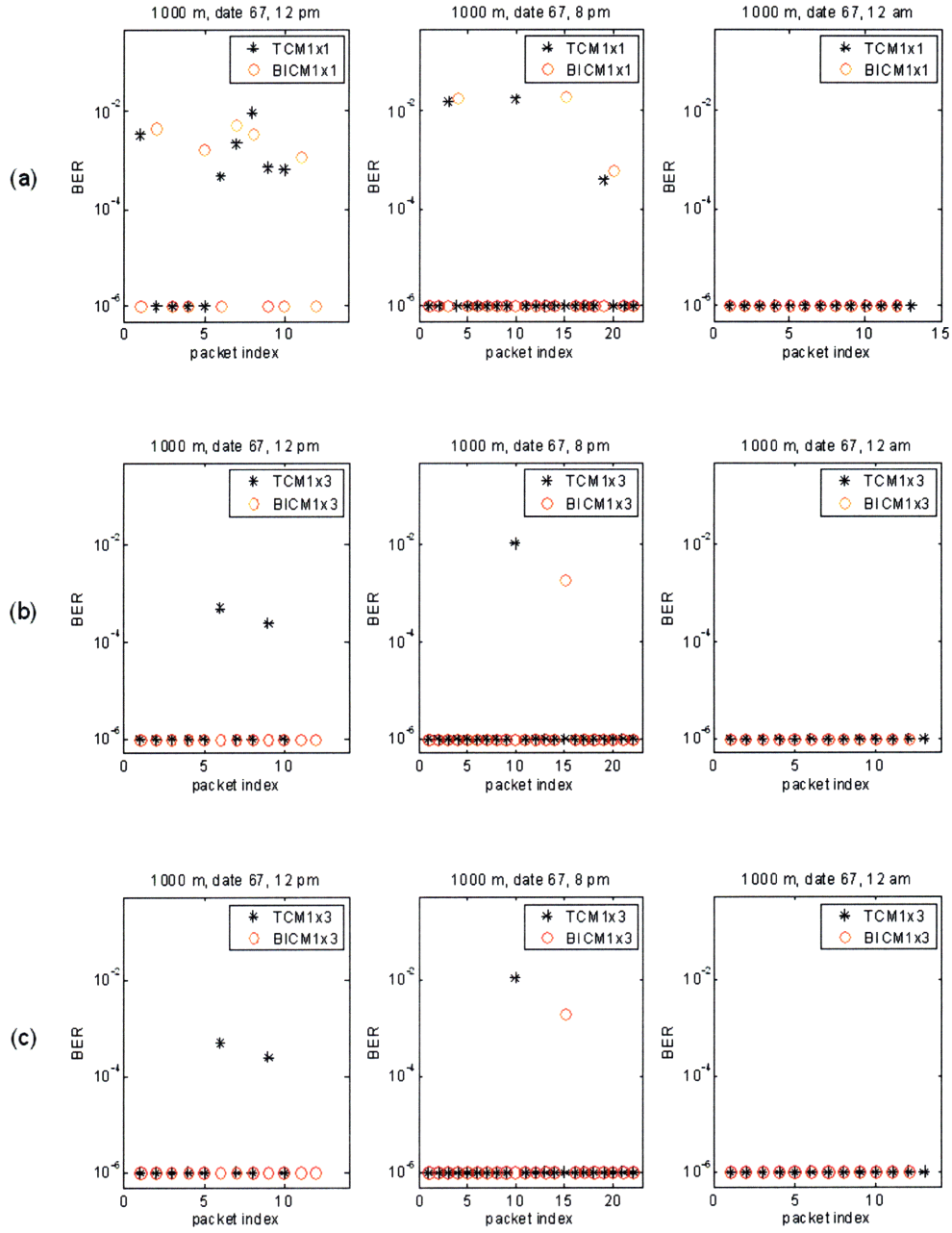
145

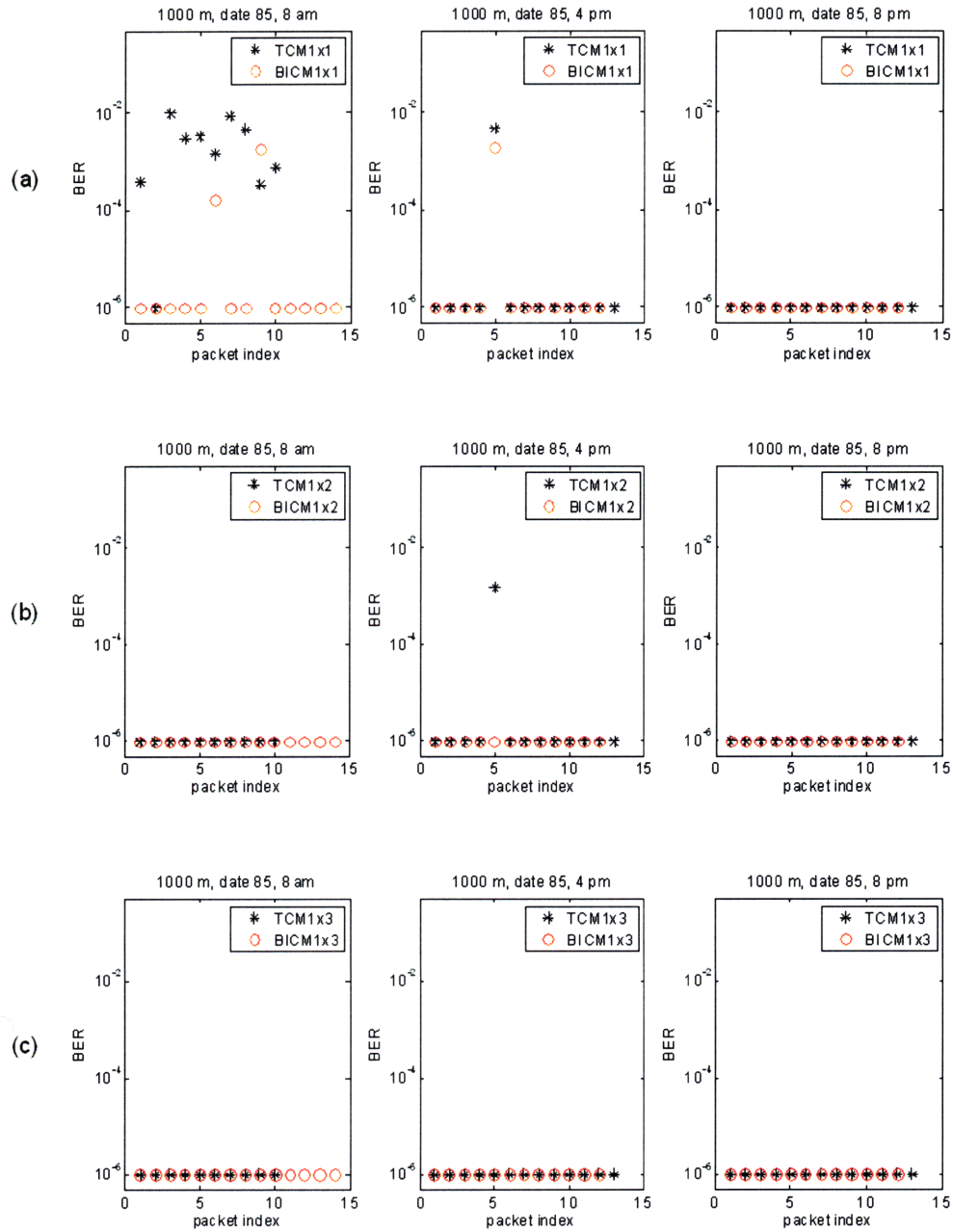Figure 5-20: BER comparison of two decoding options. The first option uses the sensor pair (1,2) while the second option uses the sensor pair (1,12). Data were taken during date 61. The left column involves only TCM data while the right column involves only BICM data.
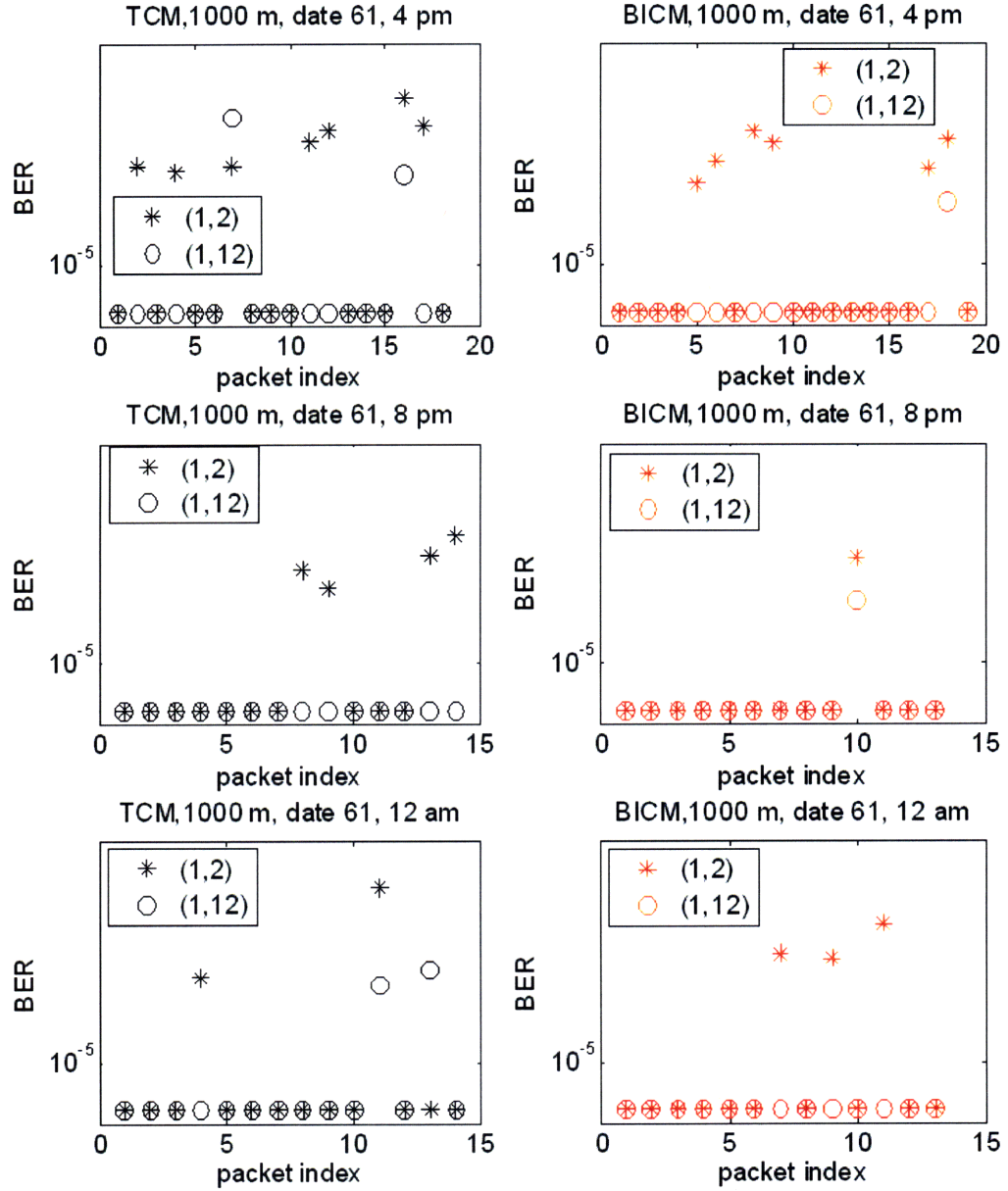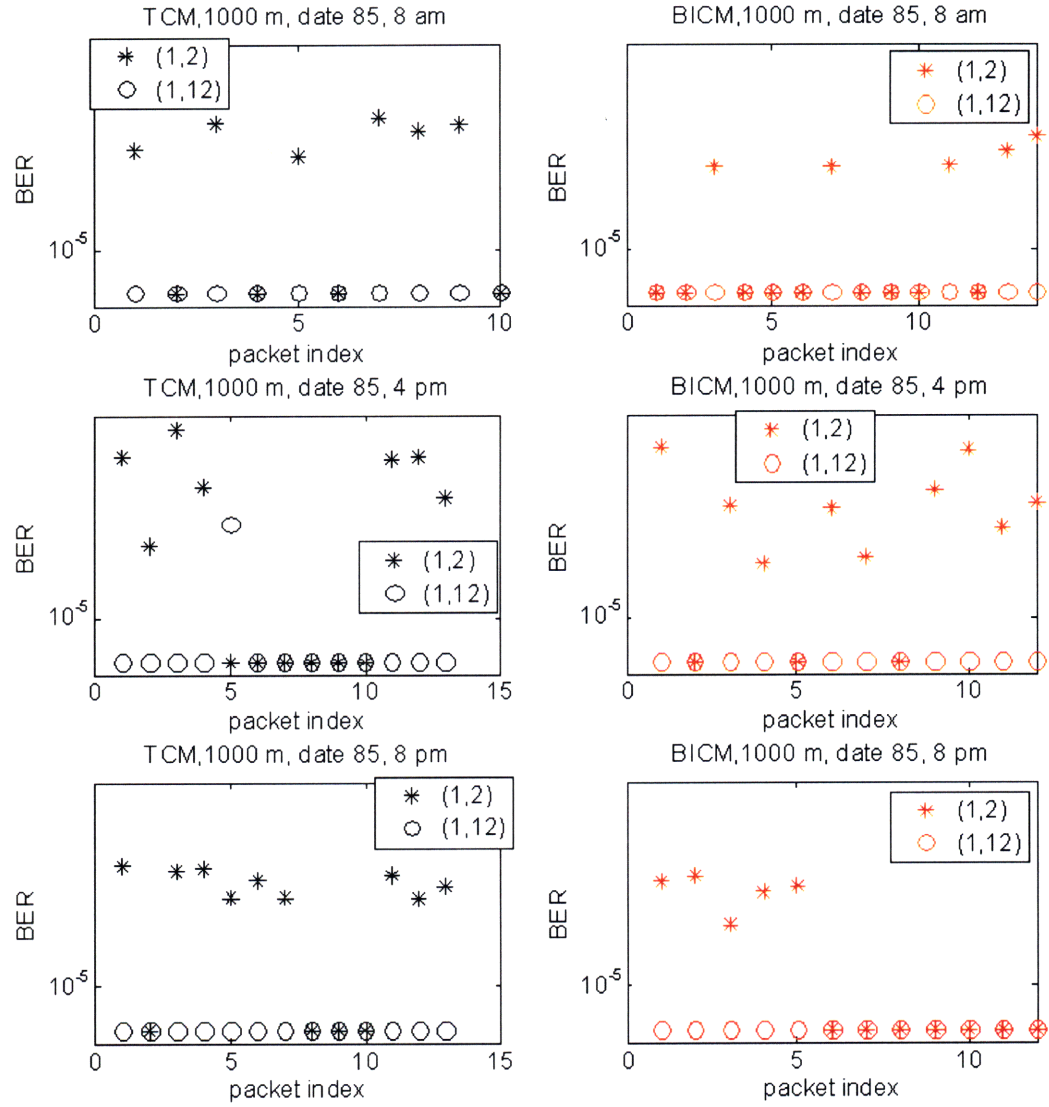
Figure 5-21: BER comparison of two decoding options. The first option uses the sensor pair (1,2) while the second option uses the sensor pair (1,12). Data were taken during date 85. The left column involves only TCM data while the right column involves only BICM data.

# of sub-carriers N_c	Expected channel delay spread T_d (msec)	Expected channel Doppler f_d (Hz)	Pilot symbol distances (N_t, N_f)	# of information bits	Effective bit-rate (bits/sec)
128	5	0.5	(2, 2)	13548	6200
128	5	1	(2, 2)	5356	5400
128	8	0.5	(2, 2)	11500	5700
128	8	1	(2, 2)	5356	5100

Table 5.3: Signal parameters and corresponding bit-rates for system with two projectors

# of sub-carriers N_c	Expected channel delay spread T_d (msec)	Expected channel Doppler f_d (Hz)	Pilot symbol distances (N_t, N_f)	# of information bits	Effective bit-rate (bits/sec)
128	5	0.5	(2, 2)	11862	4100
128	5	1	(2, 2)	7254	3700
128	8	0.5	(2, 2)	11862	3800
128	8	1	(2, 2)	2646	2300

Table 5.4: Signal parameters and corresponding bit-rates for system with three projector

5.3.2 Multiple projector systems

In this section, we report and compare the BER performance between the TCM-STBC-OFDM and BICM-STBC-OFDM systems (see Sec. 4.3). Once again, the symbol/bit interleaving was chosen to be random across the entire length of each packet to ensure time diversity. Tables 5.3 and 5.4 show the packet parameters and their corresponding data rates for both two and three projector systems. The number of sub-carriers was limited to 128 to meet the constraint imposed by the space-time decoder; the channel must remain invariant for two OFDM symbols (for two projector systems) or four OFDM symbols (for three projector systems). For two projector systems, the ITC-1007 and the first projector of the line array were used. For three projector systems, the ITC-1007 and the first two projectors of the line array were used.

A selected set of decoding results are presented in Figures 5-22-5-25 for the 400 m link and Figures 5-26 - 5-32 for the 1000 m link. In all plots, $BER = 0$ is plotted as $BER = 10^{-6}$ for visualization. Label 2x1 indicates that two transmit and one receive hydrophone (the 12th sensor) were used for decoding each packet. Similarly, labels 2x2 and 2x3 indicate that a combination of two (6th and 12th) and three (1st, 6th and 12th) receive sensors were used

148

Date	Total	2x1		2x2		2x3	
		BICM	TCM	BICM	TCM	BICM	TCM
March 20th (80)	32	5	**10**	9	**26**	10	**28**
		3x1		3x2		3x3	
March 20th (80)	32	26	**31**	30	**32**	32	**32**
March 21st (81)	48	33	**48**	40	**47**	43	**48**
March 22nd (82)	48	19	**37**	27	**39**	29	**41**

Table 5.5: Number of error-free packets at 400 m range station received during dates 80-83 for TCM2xn, BICM2xn, TCM3xn, BICM3xn,

to decode the packets respectively. A similar description applies to labels 3x1, 3x2 and 3x3. From all BER plots, it is clear that TCM performs better than BICM, especially when two or more receive sensors are employed. This is also evident from Tables 5.5 and 5.6, which shows the number of error-free packets per day for each method. As opposed to the single projector systems, here TCM performs better than BICM. This result is in accord with the simulation results shown in Sec. 4.5 which have also proven the superiority of TCM in channels with increased spatial diversity. This is because the UWA channel is transformed into an AWGN-like channel since the channel fade is averaged out as the number of diversity branches increases. The parameter that dictates the performance of a coded modulation scheme in the AWGN channel is the free Euclidean distance, consequently TCM performs better because its free distance is 4.59 as opposed to 3.2 for BICM. Hence, we experimentally verified that a coded modulation scheme, designed to be optimal for the AWGN, yields a robust performance over UWA channels with increased spatial diversity.

149

Date	Total	2x1		2x2		2x3	
		BICM	TCM	BICM	TCM	BICM	TCM
March 20th (80)	12	3	**6**	7	**11**	11	**12**
March 21st (81)	8	1	**3**	2	**8**	4	**8**
		3x1		**3x2**		**3x3**	
March 20th (80)	24	2	**12**	19	**22**	22	**24**
March 21st (81)	30	12	**19**	15	**20**	16	**22**
March 22nd (82)	23	15	**17**	16	**20**	18	**23**
March 23rd (83)	24	13	**17**	13	**23**	21	**24**
March 24th (84)	12	4	**8**	8	**12**	9	**12**

Table 5.6: Number of error-free packets received at 1000 m range station during dates 80-83 for TCM2xn, BICM2xn, TCM3xn, BICM3xn,

Figure 5-22: BER plots corresponding to date 80, 400 m range station; (a) TCM/BICM systems with two transmit and one receive hydrophone (2x1); (b) TCM/BICM systems with two transmit and two receive hydrophones (2x2); (c) TCM/BICM systems with two transmit and three receive hydrophones (2x3).

Figure 5-23: BER plots corresponding to date 80, 400 m range station; (a) TCM/BICM systems with three transmit and one receive hydrophone (3x1); (b) TCM/BICM systems with three transmit and two receive hydrophones (3x2); (c) TCM/BICM systems with three transmit and three receive hydrophones (3x3).
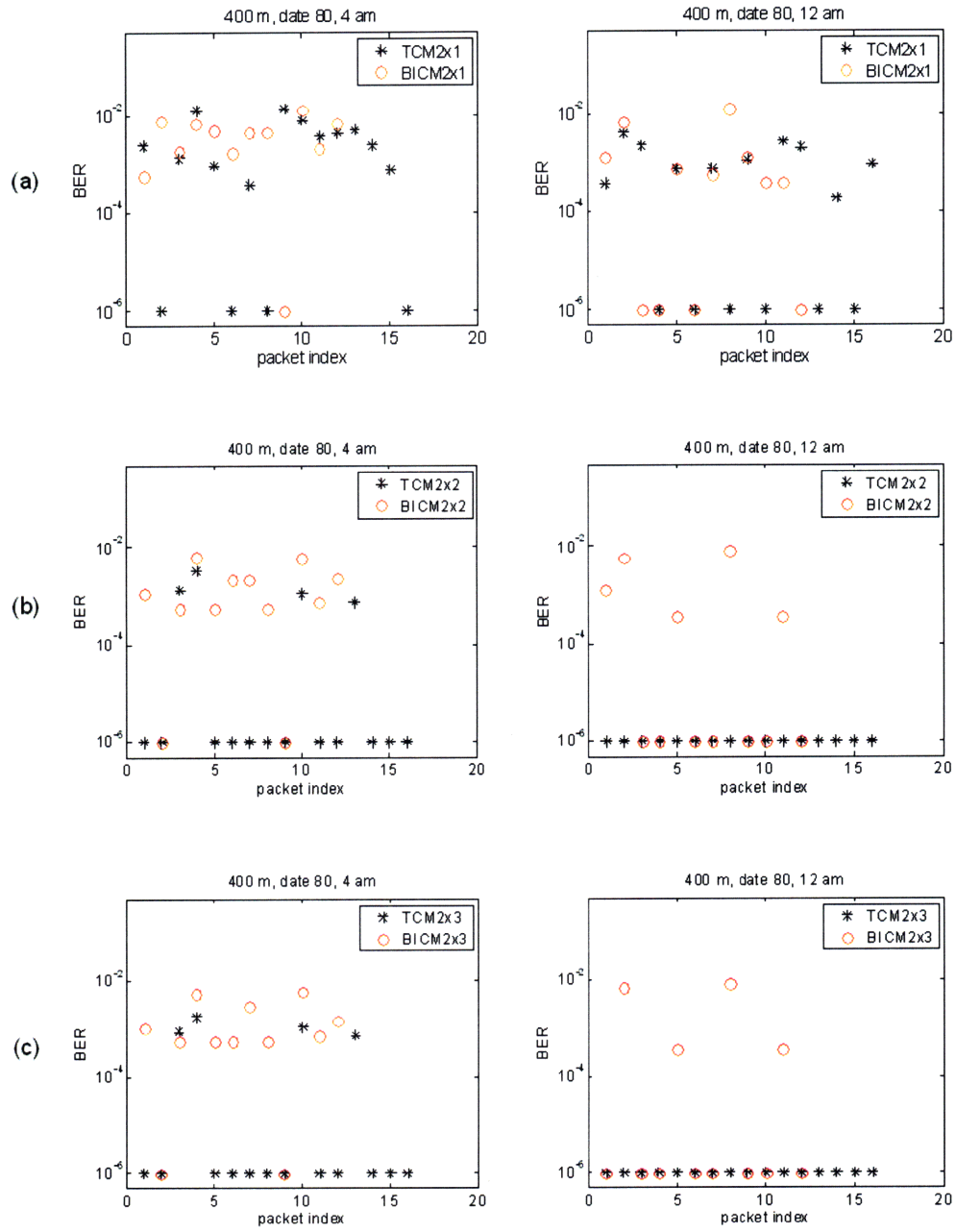
Figure 5-24: BER plots corresponding to date 81, 400 m range station; (a) TCM/BICM systems with three transmit and one receive hydrophone (3x1); (b) TCM/BICM systems with three transmit and two receive hydrophones (3x2); (c) TCM/BICM systems with three transmit and three receive hydrophones (3x3).

153

Figure 5-25: BER plots corresponding to date 82, 400 m range station; (a) TCM/BICM systems with three transmit and one receive hydrophone (3x1); (b) TCM/BICM systems with three transmit and two receive hydrophones (3x2); (c) TCM/BICM systems with three transmit and three receive hydrophones (3x3).

154

Figure 5-26: BER plots corresponding to date 80, 1000 m range station; (a) TCM/BICM systems with two transmit and one receive hydrophone (2x1); (b) TCM/BICM systems with two transmit and two receive hydrophones (2x2); (c) TCM/BICM systems with two transmit and three receive hydrophones (2x3).
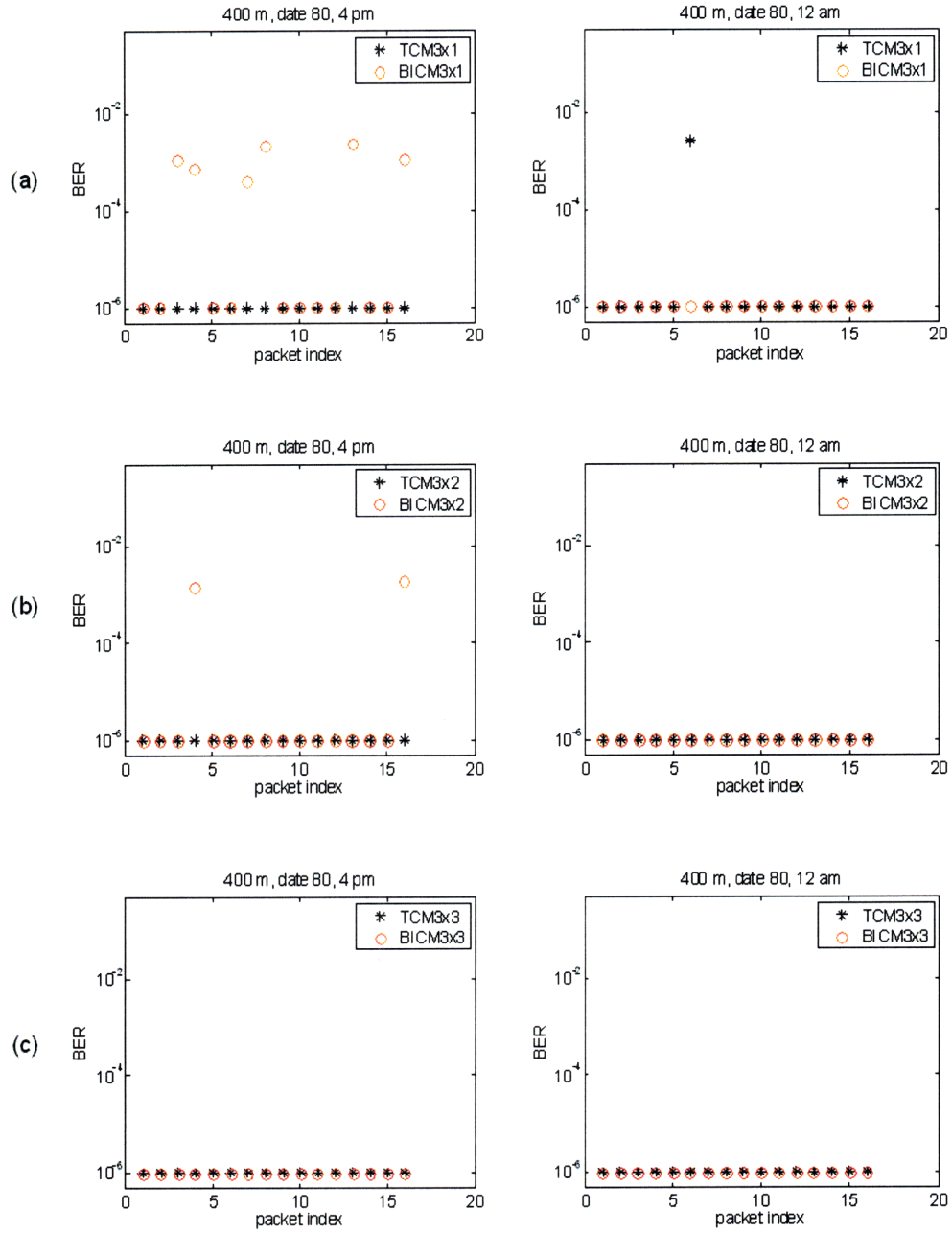
155

Figure 5-27: BER plots corresponding to date 80, 1000 m range station; (a) TCM/BICM systems with three transmit and one receive hydrophone (3x1); (b) TCM/BICM systems with three transmit and two receive hydrophones (3x2); (c) TCM/BICM systems with three transmit and three receive hydrophones (3x3).
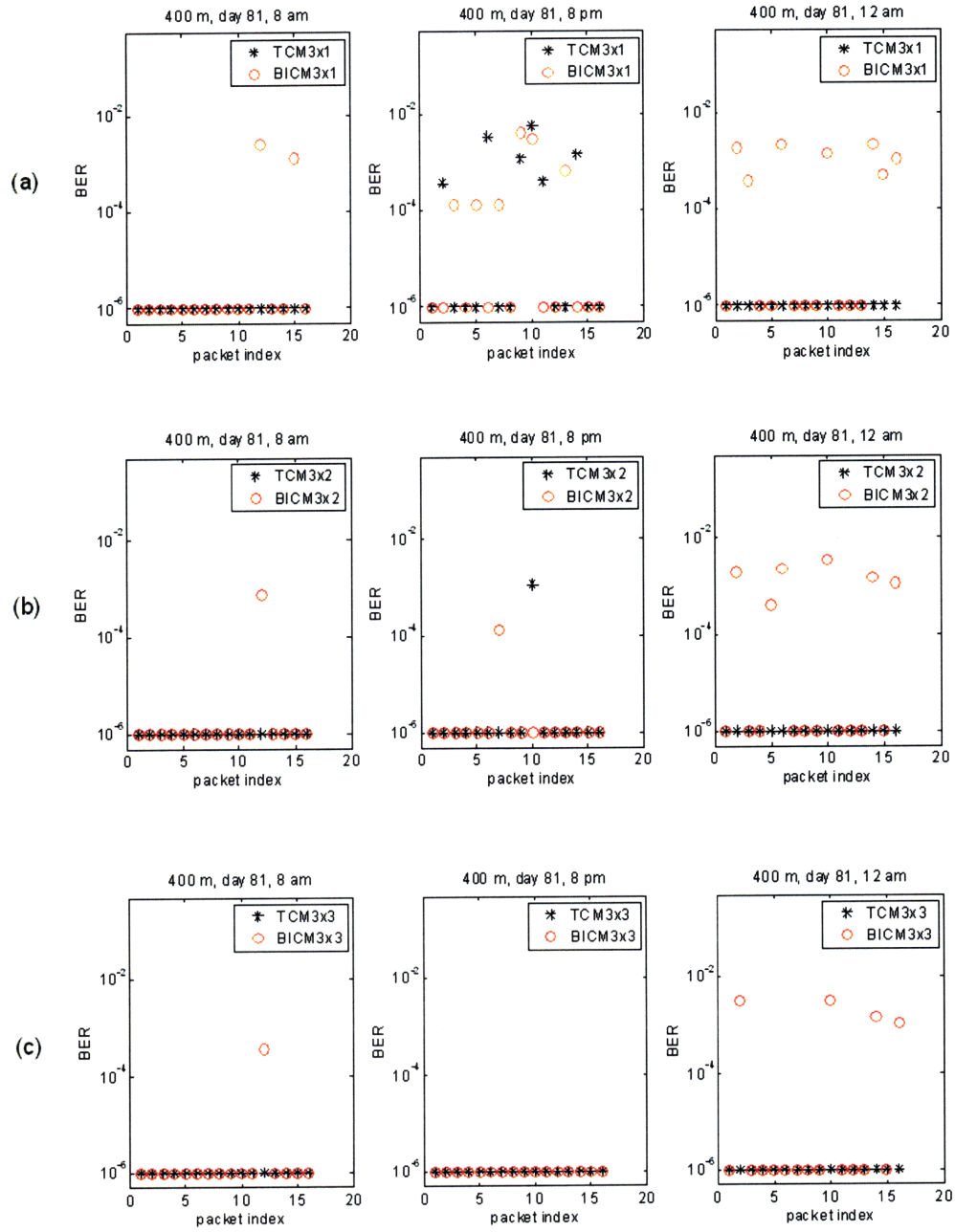
156
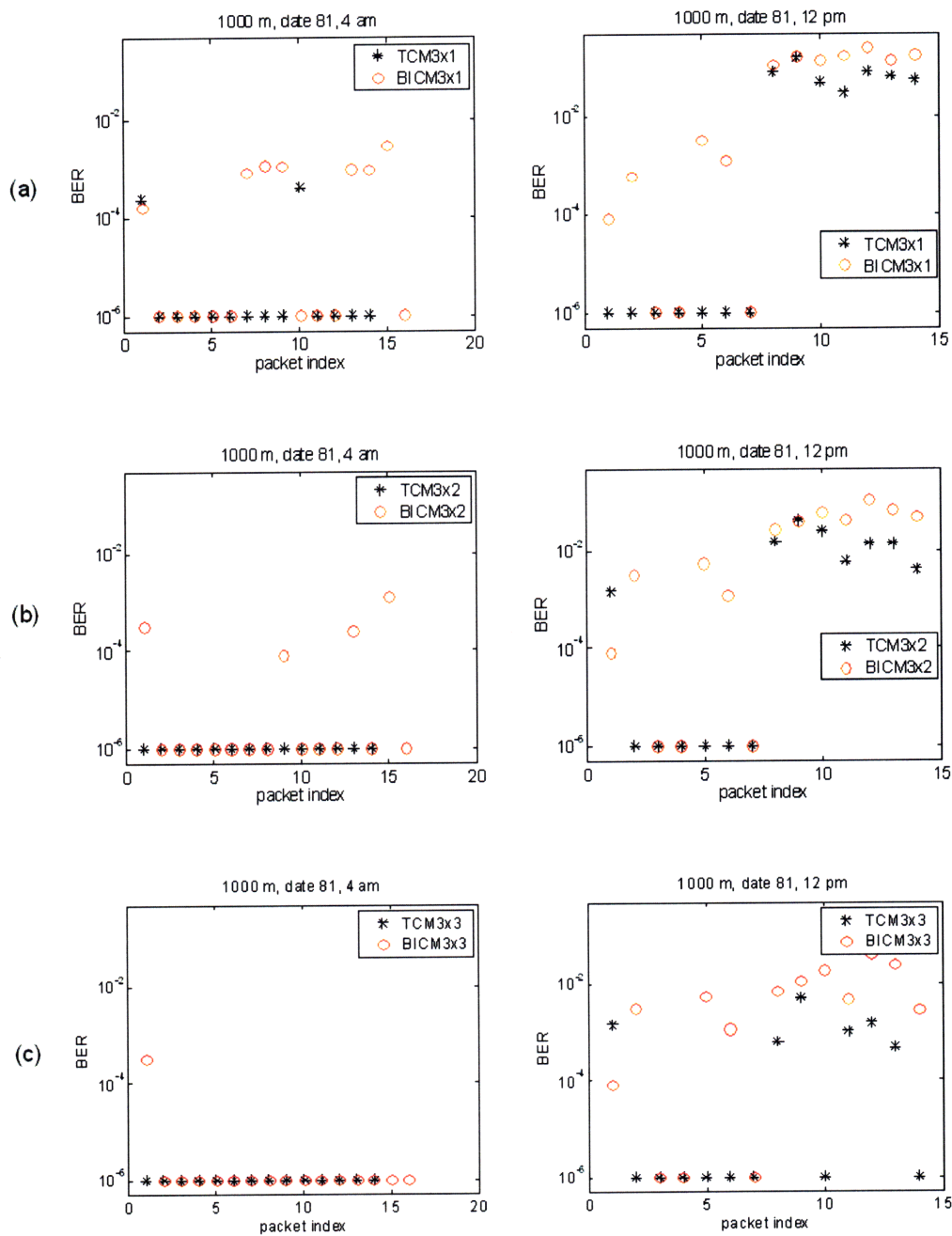
Figure 5-28: BER plots corresponding to date 81, 1000 m range station; (a) TCM/BICM systems with three transmit and one receive hydrophone (3x1); (b) TCM/BICM systems with three transmit and two receive hydrophones (3x2); (c) TCM/BICM systems with three transmit and three receive hydrophones (3x3).
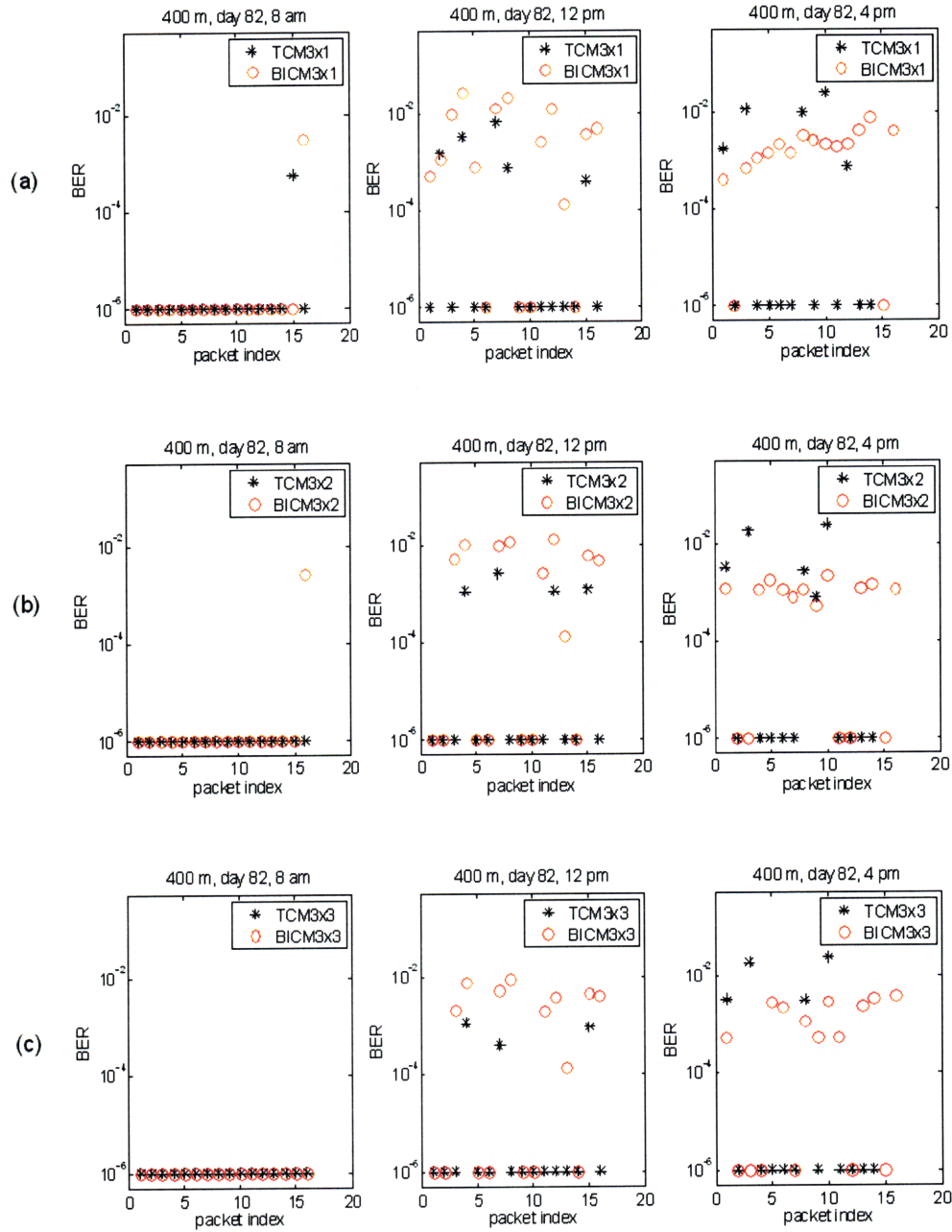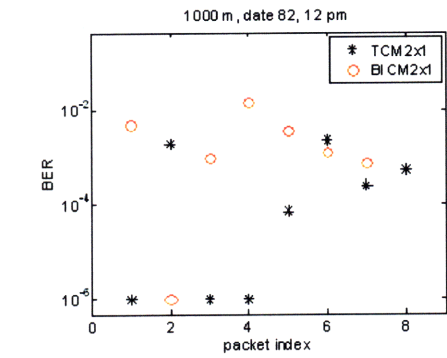
(a)
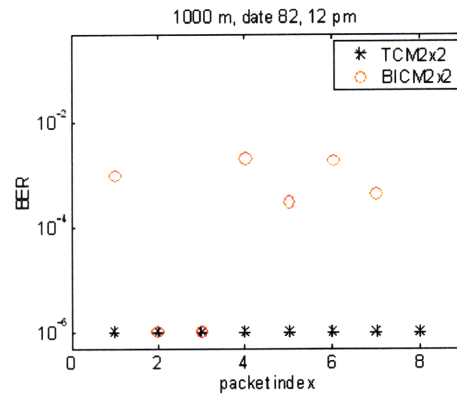
(b)
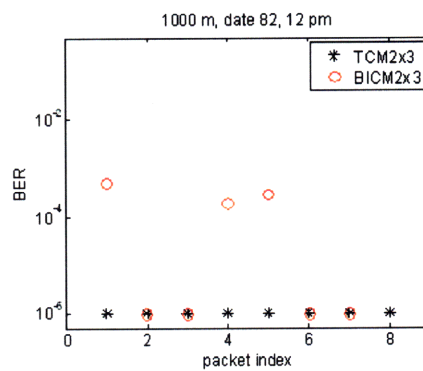
(c)

Figure 5-29: BER plots corresponding to date 82, 1000 m range station; (a) TCM/BICM systems with two transmit and one receive hydrophone (2x1); (b) TCM/BICM systems with two transmit and two receive hydrophones (2x2); (c) TCM/BICM systems with two transmit and three receive hydrophones (2x3).
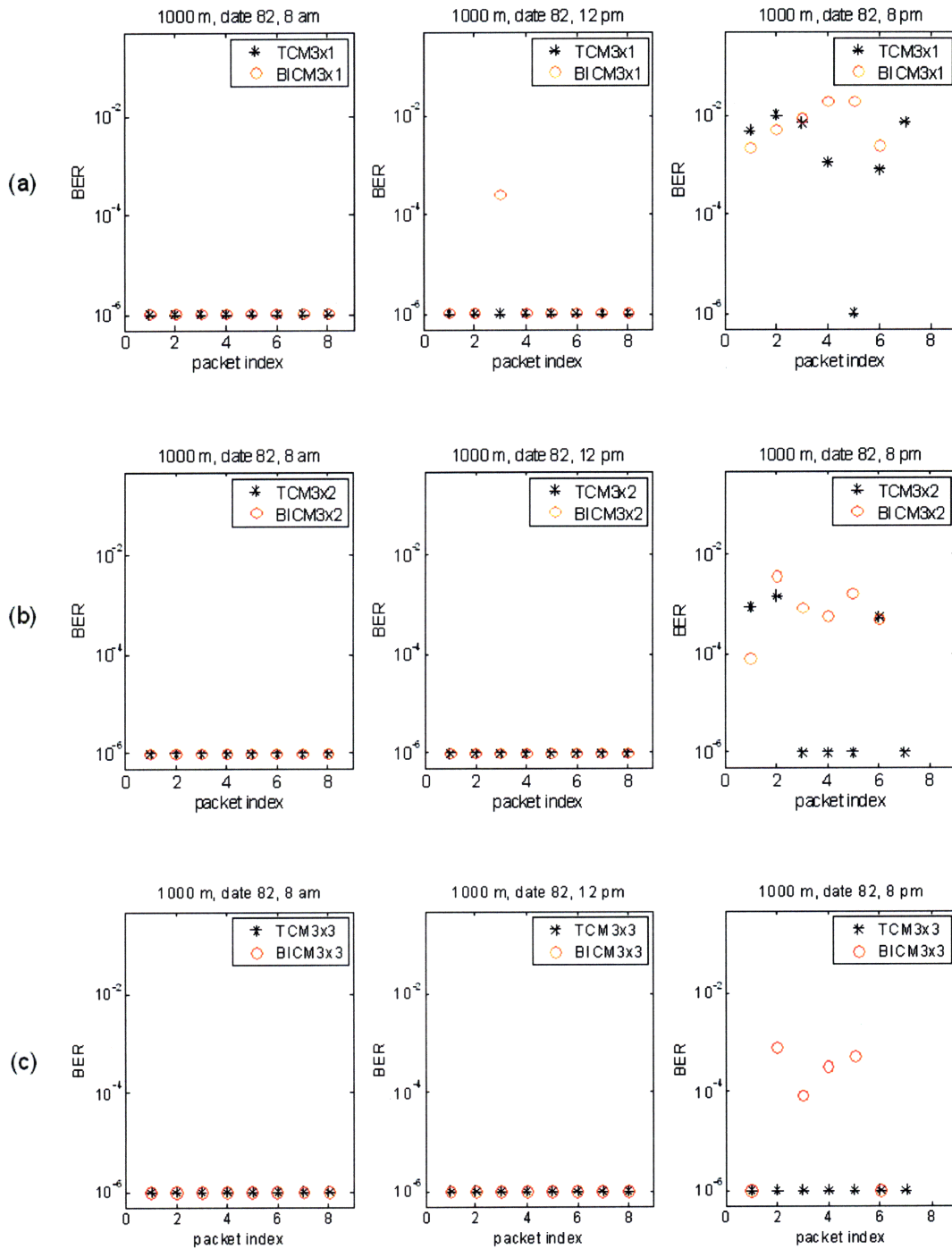
Figure 5-30: BER plots corresponding to date 82, 1000 m range station; (a) TCM/BICM systems with three transmit and one receive hydrophone (3x1); (b) TCM/BICM systems with three transmit and two receive hydrophones (3x2); (c) TCM/BICM systems with three transmit and three receive hydrophones (3x3).
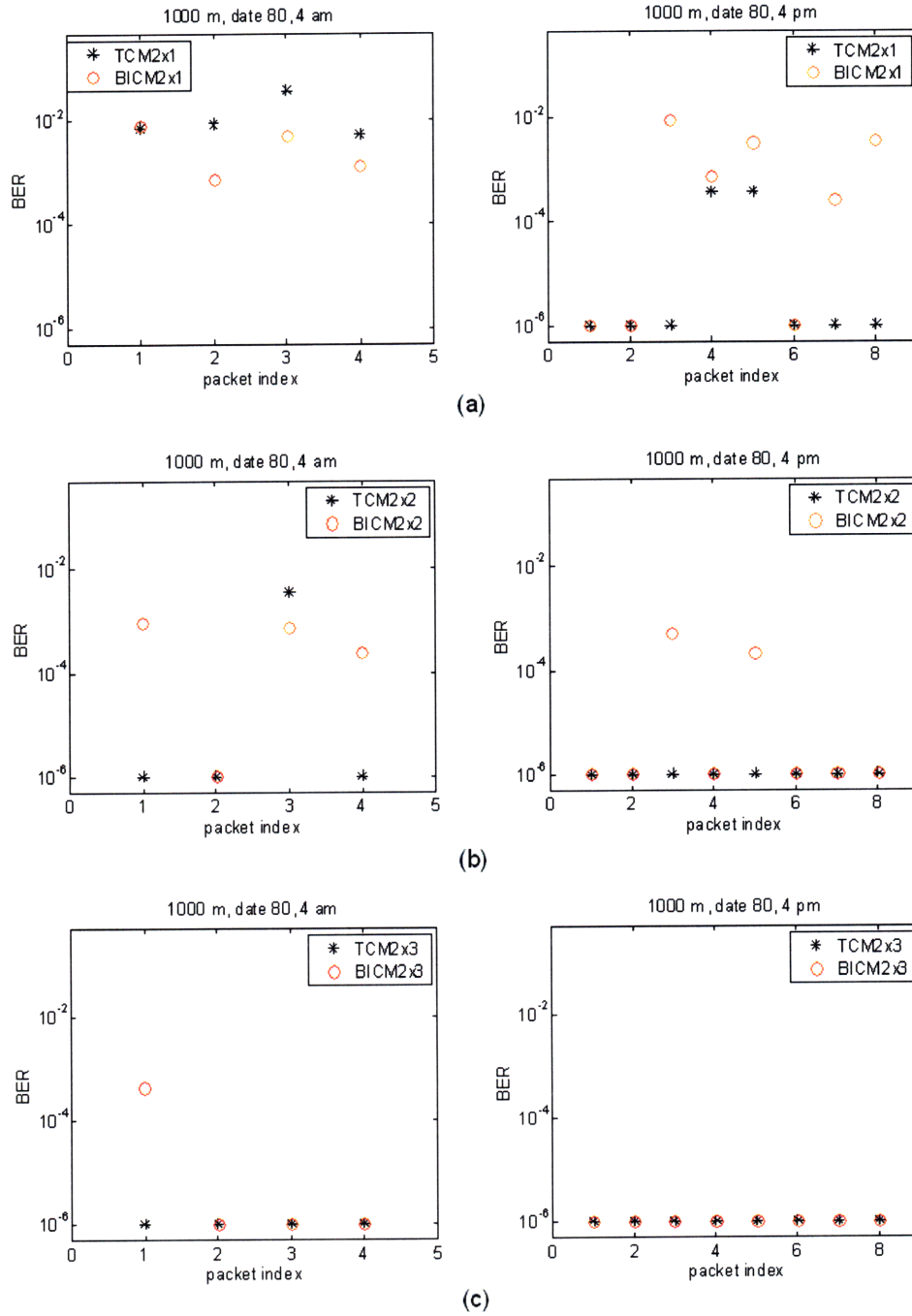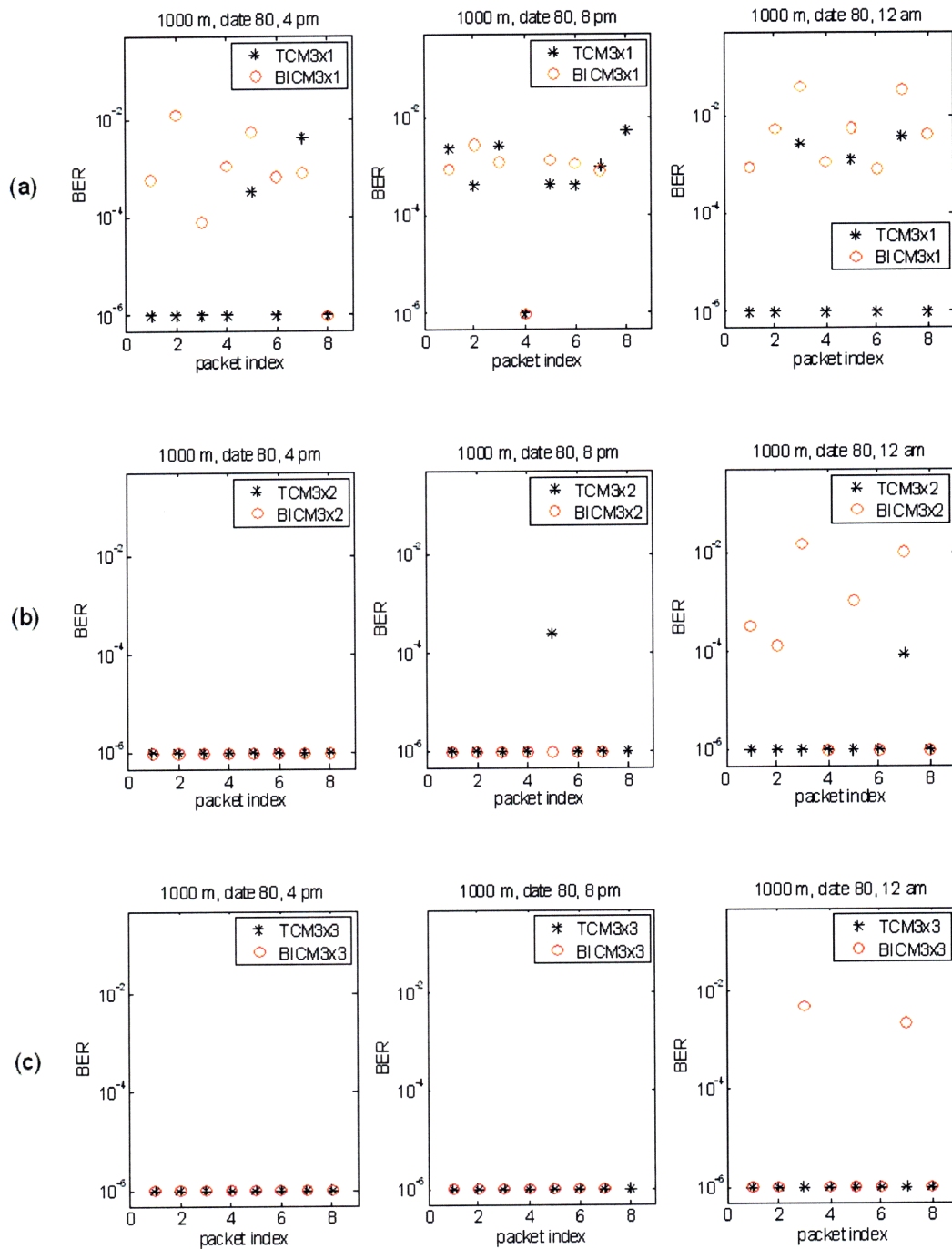
159
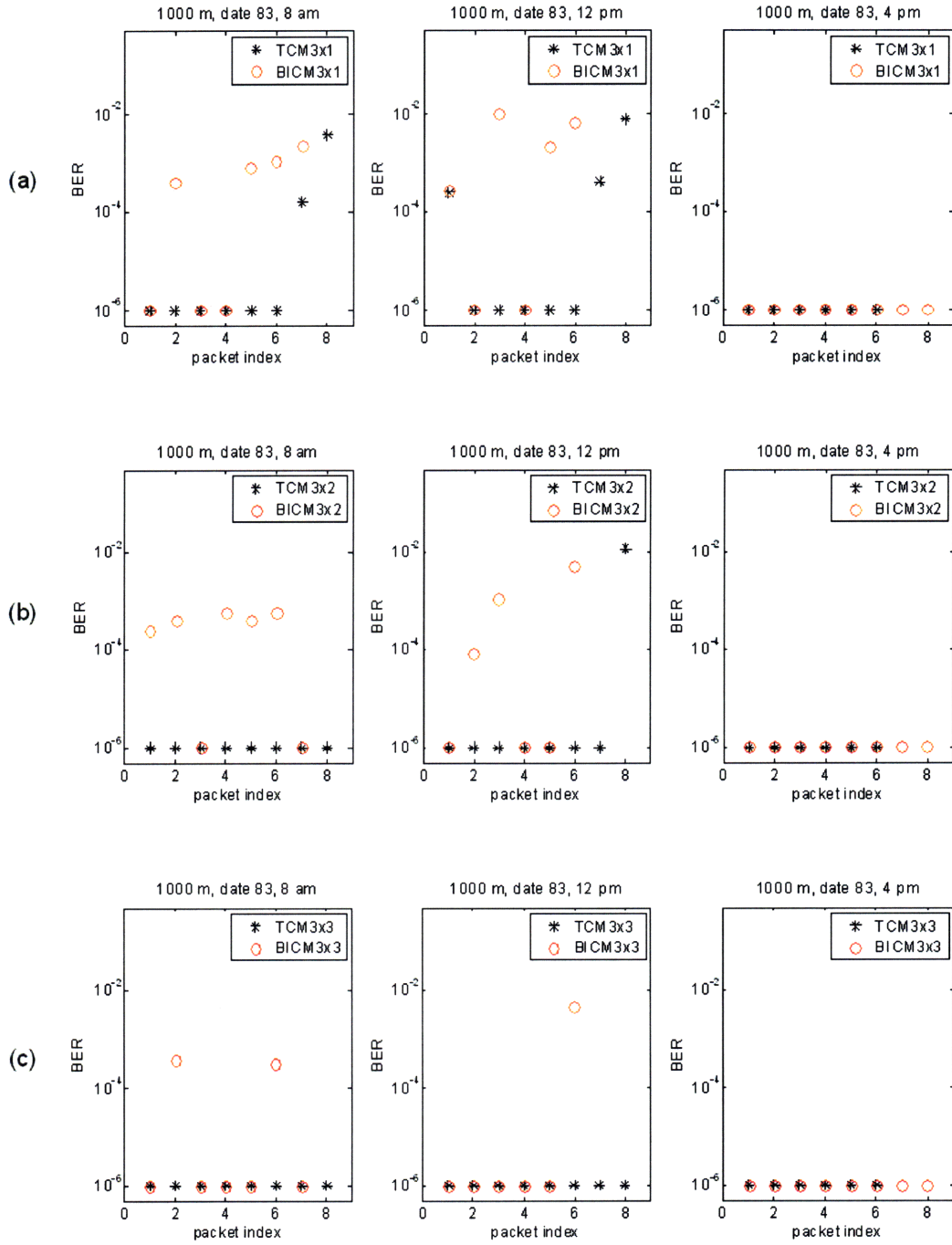
Figure 5-31: BER plots corresponding to date 83, 1000 m range station; (a) TCM/BICM systems with three transmit and one receive hydrophone (3x1); (b) TCM/BICM systems with three transmit and two receive hydrophones (3x2); (c) TCM/BICM systems with three transmit and three receive hydrophones (3x3).

160
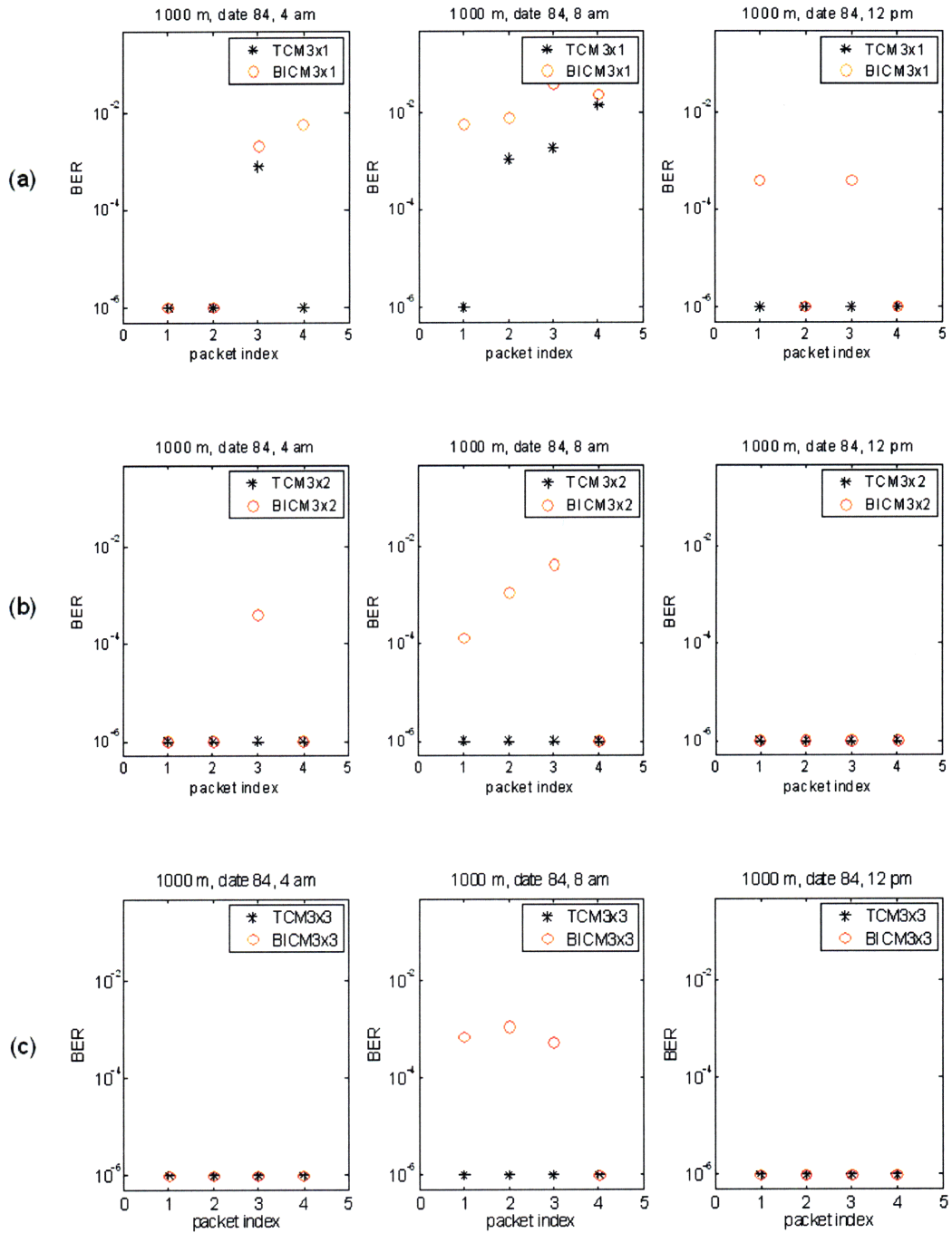
Figure 5-32: BER plots corresponding to date 84, 1000 m range station; (a) TCM/BICM systems with three transmit and one receive hydrophone (3x1); (b) TCM/BICM systems with three transmit and two receive hydrophones (3x2); (c) TCM/BICM systems with three transmit and three receive hydrophones (3x3).

Chapter 6

Conclusions

6.1 Thesis contributions

The main goal of this thesis was to the design a low-complexity, high data-rate acoustic communications system with robust performance under various channel conditions. The need for robust performance emerges from the fact that UWA channels have time-varying statistics, thus a coded modulation scheme optimally designed for a specific channel model will be suboptimal when the channel statistics change. To accomplish this goal, state-of-the art techniques which combine coded modulation with diversity, were employed. In particular, two systems with same bit-rate and decoding complexity were designed and compared. The first system combined Trellis Coded Modulation (TCM) based on an 8-PSK signal set, symbol interleaving, and orthogonal frequency-division multiplexing (OFDM). The second system combined bit-interleaved coded modulation (BICM) [42], based on a convolutional code and a 16-QAM signal set, with OFDM. Both systems were coupled with space-time block codes (STBC) [48] when two or three projectors were used. Testing the aforementioned systems using both simulated and experimental data from RACE'08, the following result was obtained: the BICM scheme achieves a lower BER when the UWA channel exhibits a low diversity order (that is usually the case when spatial diversity is very limited). This is because BICM has a higher code diversity (Hamming distance of the code), which is a key parameter towards achieving robust performance in fading channels. The TCM scheme, on the other hand, becomes a better choice when the UWA channel demonstrates a high diversity order (that is usually the case when spa-

162

tial diversity is sufficient). The reason is twofold: (1) diversity averages out the channel fade, and therefore the effective channel seen by the receiver is an AWGN-like channel; (2) TCM has a higher free Euclidean distance, which is the key parameter to achieve better performance in AWGN channels.

In addition to the result above, the following unique achievements are attributed to this thesis:

1. Identification of the conditions that allow to achieve robust performance using channel coding with relatively small blocklength: codes emphasizing larger Hamming distance should be preferred when there is no option for many transmit/receive hydrophones. In contrast, codes emphasizing larger free Euclidean distance should be preferred when many transmit and/or receive hydrophones are available.

2. Integration of coded OFDM and STBC such that maximum time-frequency-space diversity is exploited for underwater acoustic communications. That was achieved by distributing a codeword across different coherent bands and transmit antennas [65]. In addition, BICM was experimentally validated as an alternative coded modulation scheme for the first time.

6.2 Future work

There are three alluring directions for future research:

1. The experimental results of this thesis were obtained by using a fixed transmitter and receiver, however investigating the proposed systems in a mobile scenario makes the problem more interesting since the time variability of the channel becomes a limiting factor for mobile UWA communications.

2. We have shown that high-data-rate, reliable UWA communications can be achieved by using low-complexity OFDM modulation. Although ICI was ignored to reduce the system complexity, mobile systems operating in environments characterized by rapid fluctuations suffer from high levels of ICI, resulting in sever degradation of the system BER performance. While suppression of the carrier frequency offset-induced ICI has been addressed

[83], it is more challenging to compensate for the ICI caused by the Doppler spread of the time-varying fading channel.

3. A form of diversity, which is not addressed in this thesis, is *modulation* or *signal-space diversity* [38]. Modulation diversity refers to the design of multi-dimensional constellations aiming to maximize the distinct components between any two constellation points. By using component interleaving, these constellation yield diversity gains even without requiring channel coding. An easy way to construct such constellation is by applying a certain rotation to a conventional signal constellation.

Appendix A

Frequency Diversity via Linear and Decision Feedback Equalization

Here, we address how frequency diversity is exploited by using equalization. We consider two types of equalizers, which are widely used in UWA communications: the linear equalizer and the Decision Feedback Equalizer (DFE).

A sequence of channel symbols $x[1], x[2], \ldots$ is transmitted over an L -tap channel. For convenience, we assume that the channel taps are i.i.d. complex Gaussian random variables. Recall that the discrete-time, received signal can be expressed as

$$y[m] = \sum_{\ell=0}^{L-1} x[m - \ell] h_\ell[m] + w[m], \ m = 1, \ldots \tag{A.1}$$

Clearly, we need to observe the received symbols up to time $D + L - 1$ if we want to achieve full diversity of the symbol $x[D]$. Without loss of generality, we assume that the channel remains invariant over these symbol times. The received signal is written in matrix form as follows:

$$\mathbf{y} = \mathbf{H}\mathbf{x} + \mathbf{w} \tag{A.2}$$

where $\mathbf{y}^{\mathsf{T}} = [y[1], \ldots, y[D + L - 1]]$, $\mathbf{x}^{\mathsf{T}} = [x[1], \ldots, x[D + L - 1]]$, $\mathbf{w}^{\mathsf{T}} = [w[1], \ldots, w[D + L - 1]]$

and

$$\mathbf{H} = \begin{bmatrix} h_0 & 0 & \cdots & & & & & 0 \\ h_1 & h_0 & 0 & & & & & \\ \vdots & h_1 & \ddots & \ddots & & & & \\ h_{L-1} & \vdots & \ddots & \ddots & \ddots & & & \\ 0 & h_{L-1} & & \ddots & \ddots & \ddots & \vdots & \\ \vdots & & \ddots & & & \ddots & \ddots & 0 \\ 0 & \cdots & 0 & h_{L-1} & \cdots & h_1 & h_0 \end{bmatrix} \qquad (A.3)$$

is a $D + L - 1 \times D + L - 1$ lower triangular matrix. If we express $\mathbf{H}$ in its column form, i.e., $\mathbf{H} = [\mathbf{h}_1, \mathbf{h}_2, \ldots, \mathbf{h}_{D+L-1}]$, where for example, $\mathbf{h}_1^\mathsf{T} = [h_0, h_1, \ldots, h_{L-1}, \ldots, 0]$, then we can write the received vector in terms of the columns of $\mathbf{H}$ as:

$$\mathbf{y} = \mathbf{h}_k x[k] + \sum_{i \neq k} \mathbf{h}_i x[i] + \mathbf{w}. \qquad (A.4)$$

Assuming perfect channel knowledge at the receiver, a linear equalizer (also known as zero forcing receiver or decorator) extracts $x[k]$ by projecting $\mathbf{y}$ onto the subspace orthogonal to $\Gamma_k = \{\mathbf{h}_1, \ldots, \mathbf{h}_{k-1}, \mathbf{h}_{k+1}, \ldots \mathbf{h}_{D+L-1}\}$. Clearly, $\mathbf{H}$ has full rank if $h_0 \neq 0$ $\left(\det(\mathbf{H}) = h_0^{D+L-1}\right)$, hence the dimension of Γ_k is $D + L - 2$, implying that the dimension of the orthogonal sub-space is 1. Let us denote the orthogonal sub-space to Γ_k as a vector $\mathbf{q}_k$. After projecting $\mathbf{y}$ onto $\mathbf{q}_k$ we get

$$r_k = \mathbf{q}_k^\mathsf{T} \mathbf{y} = \underbrace{\mathbf{q}_k^\mathsf{T} \mathbf{h}_k}_{\tilde{h}_k} x[k] + \underbrace{\mathbf{q}_k^\mathsf{T} \mathbf{w}}_{\tilde{w}_k}, \quad k = 1, \ldots, D \qquad (A.5)$$

Under the assumption of independent fading, $\tilde{h}_k$ is a complex Gaussian random variable and $\tilde{w}_k$ is still white. Clearly, the resulting scalar channel of Eq. (A.5) is Rician faded with unit diversity order. Note that the channel model of Eq. (A.5) is analogous to the time diversity channel model of Eq. (3.45). We conclude that efficient exploiting of frequency diversity with linear equalization at the receiver is achieved only if channel coding and interleaving is employed at the transmitter.

The DFE is based on the following successive cancellation strategy: once a symbol is successfully detected, strip it off from the received signal so the interference is reduced for the

166

remaining symbols. In particular, if $x[1]$ is correctly detected then $\mathbf{h}_1 x[1]$ is subtracted from $\mathbf{y}$ resulting in the following signal

$$\mathbf{y}' = \mathbf{h}_2 x[2] + \sum_{i=3}^{D+L-2} \mathbf{h}_i x[i] + \mathbf{w}. \qquad (A.6)$$

Consequently, $x[2]$ has to deal with the remaining $x[3], \ldots, x[D+L-1]$ as interference. The orthogonal subspace to $\{\mathbf{h}_3, \ldots, \mathbf{h}_{D+L-1}\}$ is a $2 \times D + L - 1$ matrix, denoted as $\mathbf{Q}_2$. After projecting $\mathbf{y}'$ onto $\mathbf{Q}_2$ we have

$$\mathbf{r}_2 = \mathbf{Q}_2 \mathbf{y}' = \mathbf{Q}_2 \mathbf{h}_2 x[2] + \mathbf{Q}_2 \mathbf{w} \qquad (A.7)$$

where $\mathbf{Q}_2 \mathbf{h}_2$ is a 2×1 complex Gaussian vector and $\mathbf{Q}_2 \mathbf{w}$ is white since $\mathbf{Q}_2 \mathbf{Q}_2^\dagger = \mathbf{I}_2$. Obviously, the resulting channel of (A.7) is Rician faded with diversity order 2. Repeating the above operation $D-1$ times and assuming successful detection and subtraction, it is easy to see that the corresponding channel for $x[D]$ has Lth diversity order. Furthermore, if the columns of $\mathbf{H}$ are sequentially updated, all the channel symbols following $x[D]$ acquire Lth diversity order.

Appendix B

Scattering Function Estimation

In practice, the channel scattering function must be estimated by using probing signals. We start our analysis by assuming that the channel consists of a single scattering path, where the time derivative of the path length is u and R is the initial path length at the time the leading edge of the signal arrived at the receiver. The noiseless received signal is expressed as

$$y(t) = \mathrm{Re}\left\{ \sqrt{2}a\tilde{x}\left(t - \tau(t)\right) e^{j2\pi f_c(t-\tau(t))} \right\}, \tag{B.1}$$

where a represents the complex scattering path gain, $\tilde{x}(t)$ is the baseband probe signal of duration T and bandwidth W and $\tau(t)$ is the time-varying path delay. Note that

$$\tau(t) = \frac{R - ut}{c} = \tau - \delta t, \tag{B.2}$$

so the received waveform can be rewritten as

$$y(t) = \mathrm{Re}\left\{ \sqrt{2}a\tilde{x}\left((1 + \delta)t - \tau\right) e^{j2\pi f_c\delta t} e^{j2\pi f_c t} \right\} \tag{B.3}$$

where $e^{-j2\pi f_c\tau}$ has been absorbed by the phase of a. We see that the time-varying path length induces two distortions on the transmitted signal: (1) compression/dilation of the time axis by $1 + \delta$; (2) a Doppler shift $f_c\delta$.

To see when we can neglect time scaling, consider the error plotting $x(t)$ instead of $x((1 + \delta)t)$. The biggest error happens at the end of the signal, where the difference in the arguments is δT.

If the following condition (termed as the "narrowband condition" [5]) holds:

$$\delta T \ll \frac{1}{W} \implies WT \ll \frac{1}{\delta} = \frac{c}{u}, \tag{B.4}$$

then the signal does not appreciably change within the interval δT. Hence, the channel may be characterized as narrowband and the received signal may be considered as a Doppler shifted version of the transmitted signal, namely,

$$y(t) = \text{Re}\left\{\sqrt{2}a\tilde{x}\left(t - \tau\right)e^{j2\pi f_c \delta t}e^{j2\pi f_c t}\right\}. \tag{B.5}$$

In many real-life experiments the narrowband condition of (B.4) is not satisfied [77]. Resampling the received signal by δ' we have

$$
\begin{aligned}
y\left(\frac{t}{1+\delta'}\right) &= \text{Re}\left\{\sqrt{2}\alpha\tilde{x}\left(\frac{1+\delta}{1+\delta'}t - \tau\right)e^{j2\pi f_c \frac{\delta}{1+\delta'}t}e^{j2\pi f_c \frac{t}{1+\delta'}}\right\} \\
&= \text{Re}\left\{\sqrt{2}\alpha\tilde{x}\left(\frac{1+\delta}{1+\delta'}t - \tau\right)e^{j2\pi f_c \frac{\delta-\delta'}{1+\delta'}t}e^{j2\pi f_c t}\right\}. \tag{B.6}
\end{aligned}
$$

Observe that as δ approaches δ', we can neglect the residual time scaling effect, i.e., $\tilde{x}\left(\frac{1+\delta}{1+\delta'}t\right) \simeq \tilde{x}(t)$ but we cannot neglect the residual Doppler shift because the rate of change of the phase term $2\pi f_c \frac{\delta-\delta'}{1+\delta'}t$ is inversely proportional to $f_c\left(\delta - \delta'\right)$, which is a relatively large number (f_c is on the order of 10^4 Hz). Consequently, the received signal may be simplified to

$$y\left(\frac{t}{1+\delta'}\right) \simeq \text{Re}\left\{\sqrt{2}\alpha\tilde{x}\left(t - \tau\right)e^{j2\pi f_c \frac{\delta-\delta'}{1+\delta'}t}e^{j2\pi f_c t}\right\}. \tag{B.7}$$

We conclude that by appropriate resampling, the wideband received signal is degenerated to a narrowband one and the "effective" Doppler shift becomes $f_c\frac{\delta-\delta'}{1+\delta'} \triangleq v$.

If we assume an additive white noise process at the receiver, the ML estimates of delay τ and Doppler v are obtained at the maximum of the cross-ambiguity function (2-D surface) [5]

$$\Theta(\hat{\tau}, \hat{v}) = \left|\int_0^T y\left(t\right) x^*(t - \hat{\tau})e^{-j2\pi\hat{v}t}dt\right|^2, \tag{B.8}$$

where $\tilde{y}(t)$ is the resampled baseband signal, i.e.,

$$\tilde{y}(t) = \alpha\tilde{x}\,(t-\tau)\,e^{j2\pi vt}. \tag{B.9}$$

$\Theta(\hat{\tau}, \hat{v})$ is computed by cross-correlating the resampled received signal with frequency and delay shifted versions of the transmitted signal ($\hat{\tau}, \hat{v}$ are hypothesized values) followed by a square-law envelope detector. Modeling the UWA channel as a linear, time-varying system and using the delay-Doppler spread function to describe the input/output relation we have [2]:

$$\tilde{y}(t) = \int\int \tilde{x}(t-\tau)\tilde{U}(\tau,v)e^{j2\pi vt}d\tau dv + \tilde{w}(t) \tag{B.10}$$

where $\tilde{U}(\tau,v)$ is the complex gain introduced by all the scatterers within delay $(\tau, \tau + \Delta\tau)$ and Doppler $(v, v+\Delta v)$ and $\tilde{w}(t)$ denotes the additive, white, zero-mean complex Gaussian random process. Note that $\tilde{U}(\tau,v)$ is not time varying itself but time variability enters implicitly into the model by the mobility of the scatterers. Due to the WSSUS assumption, the autocorrelation of $\tilde{U}(\tau, f_d)$ degenerates in a simple form :

$$E\left[\tilde{U}(\tau+\Delta\tau, v+\Delta v)\tilde{U}^*(\tau,v)\right] = S(\tau,v)\delta(\Delta\tau)\delta(\Delta v) \tag{B.11}$$

where $S(\tau,v)$ stands for the channel scattering function. Substituting (B.10) into (B.8) and taking the expectation for $\tau = \hat{\tau}, v = \hat{v}$ we conclude to the fundamental result [5]:

$$E(\Theta(\tau,v)) = \int\int S(\xi,\sigma)\Theta_o(\tau+\xi, v+\sigma)d\xi d\sigma, \tag{B.12}$$

where

$$\Theta_o(\tau,v) = \left|\int_0^T x(t)x^*(t-\tau)e^{-j2\pi vt}dt\right|^2 \tag{B.13}$$

is the transmitted signal ambiguity function. From (B.12), we understand that by computing the mean of the cross ambiguity function, we view the true channel scattering function via its convolution with the signal ambiguity function. Consequently, the signal ambiguity function should be impulsive in both delay and Doppler in order to get the best possible estimate of the scattering function. A representative class of a signals with impulsive ambiguity functions are

170

the maximal-length pseudonoise (PN) sequences.

Bibliography

[1] R. Price, P. E. Green, "A communication technique for multipath channels," *Proc. IRE*, vol. 46, pp. 555–570, 1958.

[2] P. A. Bello, "Characterization of randomly time-variant linear channels," *IEEE Trans. Inform. Theory*, pp. 360-393, 1963.

[3] R. S. Kennedy, *Fading Dispersive Communication Channels*, New York, NY: Wiley, 1969.

[4] K. Abend, B. D. Fritchman, "Statistical detection for communication channels with inter-symbol interference," *Proc. IEEE*, pp. 779-785, 1970.

[5] H. Van Trees, *Detection, estimation and modulation theory, part III*, New York: Wiley, 1971.

[6] L.R. Bahl, J. Cocke, F. Jelinek, and J. Raviv, "Optimal decoding of linear codes for minimizing symbol error rate," *IEEE Trans. Inf. Theory*, vol. 20, no.2, pp.284–287, 1974.

[7] K. V. Mackenzie, "Nine-term equation for sound speed in the oceans, " *J. Acoust. Soc. Amer.*, 70(3), 807-812, 1981.

[8] G. Ungerboeck, "Channel coding with multilevel/phase signals," IEEE Trans. Inform. Theory, vol. IT-28, pp. 56-67, 1982.

[9] L. Brekhovskikh, Y. Lysanov, *Fundamentals of Ocean Acoustics*, New York: Springer, 1982.

[10] L. E. Kinsler, A. R. Frey, A. B. Coppens and J. V. Sanders, *Fundamentals of Acoustics*, 3rd ed., John Wiley & Sons cop., NY, 1982.

[11] S. Flatte, "Wave propagation through random media: Contribution from Ocean Acoustics," *in Proc. IEEE*, vol. 71, pp. 1267-1294, 1983.

[12] A. B. Baggeroer, "Acoustic telemetry - An overview," *IEEE J. Oceanic Eng.*, vol. OE-9, pp. 229–235, 1984.

[13] J. Catipovic, A. B. Baggeroer, K. Von Der Heydt, and D. Koelsch, "Design and performance analysis of a digital acoustic telemetry system for the short range underwater channel," *IEEE J. Oceanic Eng.*, vol. OE-9, pp. 242–252, 1984.

[14] D. Divsalar, M. K. Simon, "The design of trellis coded MPSK for fading channels: Set partitioning for optimum code design," *IEEE Trans. Commun.*, vol. 36, pp. 1013-1021, 1988.

[15] C. Schlegel, D. Costello, "Bandwidth efficient coding for fading channels: Code construction and performance analysis," *IEEE J. Sel. Areas Commun.*, vol. 7, pp. 1356-1368, 1989.

[16] J. G. Proakis, "Coded modulation for digital communications over Rayleigh fading channels," *IEEE J. Oceanic Eng.*, vol. 16, pp. 66-73, 1991.

[17] J. A. Catipovic and L. E. Freitag, "Spatial diversity processing for underwater acoustic telemetry," *IEEE J. Oceanic Eng.*, vol. 16, pp. 86–97, 1991.

[18] W. S. Burdic, *Underwater Acoustic System Analysis*, 2nd ed., Prentice-Hall, 1991.

[19] E. Zehavi, "8-PSK trellis codes for a Rayleigh channel," *IEEE Trans. Commun.*, vol. 40, pp. 873-884, 1992.

[20] C. Berrou, A. Glavieux, and P. Thitimajshima, "Near Shannon limit error-correcting coding and decoding: turbo-codes," *in Proc. ICC'93*, pp. 1064-1070, Geneve, Switzerland, 1993.

[21] M. Stojanovic, J. A. Catipovic and J. G. Proakis, "Adaptive multichannel combining and equalization for underwater acoustic communications," *J. Acoust. Soc. Amer.*, 94(3): Pt. 1, 1621-1631, 1993.

[22] S. Coatelan and A. Glavieux, "Design and test of a multi-carrier transmission system on the shallow water acoustic channel", in *Proc. OCEANS'94*, pp. 472-477, Sep. 1994.

[23] G. B. Henderson *et al*, "Investigation of adaptive beamformer performance and experimental verification of applications in high data rate digital underwater communications," in *Proc. OCEANS'94*, pp.296-300, 1994.

[24] M. Stojanovic, J. A. Catipovic and J. G. Proakis, "Phase-coherent digital communications for underwater acoustic channels," *IEEE J. Oceanic Eng.*, vol. 19, pp. 100–111, 1994.

[25] D. R. Dowling, "Acoustic pulse-compression using passive phase-conjugate processing," *J. Acoust. Soc. Amer.*, vol. 95, no. 3, pp. 1450-1458, 1994.

[26] S. H. Jamali, T. Le-Ngoc, *Coded Modulation Techniques for Fading Channels*, New York: Kluwer, 1994.

[27] W. H. Munk, R. C. Spindel, A. B. Baggeroer and T. G. Birdsall, "The Heard Island Feasibility Test," *J. Acoust. Soc. Amer.*, vol. 96, pp. 2330-2342, 1994.

[28] M. Stojanovic, J. G. Proakis and J. A. Catipovic, "Analysis of the impact of channel estimation errors on the performance of a decision-feedback equalizer in fading multipath channels," *IEEE Transactions Commun.*, vol. COM-43, No. 21314, pp. 877-886, 1995.

[29] W. Zou, Y. Wu, "COFDM: An overview", *IEEE Trans. Broadcasting*, vol. 41, pp. 1-8, 1995.

[30] Elie Bejjani and Jean-Claude Belfiore, "Multi-carrier Coherent Communications for the Underwater Acoustic Channel", in *Proc. MTS/IEEE OCEANS'96*, pp. 1125-1130, Sep. 1996,

[31] J. G. Bellingham, H. Schmidt and M. Deffenbaugh, "Acoustically focused oceanographic sampling the Haro Strait experiment," *J. Acoust. Soc. Amer.*, vol. 100, no. 4, p. 2612, 1996.

[32] M. Stojanovic, "Recent advances in high rate underwater acoustic communications," *IEEE J. Oceanic Eng.*, vol. , pp. 125–136, 1996.

[33] G. J. Foschini, "Layered space-time architecture for wireless communication in a fading environment when using multi-element antennas," Bell Labs Tech. J., vol. 1, pp. 41, 1996.

[34] W. K. Lam, R. F. Ormondroyd, "A broadband UWA communications system based on COFDM modulation," *in Proc. IEEE OCEANS'97 Conf.*, vol. , pp. 862-869, 1997.

[35] J. Ventura-Traveset, G. Caire, E. Biglieri, and G. Taricco, "Impact of diversity reception on fading channels with coded modulation–part I: coherent detection," *IEEE Trans. Commun.*, vol. 45, pp. 676-686, 1997.

[36] P. Höher, S. Kaiser and P. Robertson, "Two-dimensional pilot-symbol-aided channel estimation by Wiener filtering," *in Proc. ICASSP'97*, vol. 3, pp. 1845-1848, 1997.

[37] T. H. Eggen, "Underwater acoustic communication over doppler spread channels," Ph.D. thesis, MIT, 1997.

[38] E. Biglieri, J. Proakis and S. Shamai, "Fading channels: Information theoretic and communications aspects," *IEEE Tran. Inform. Theory*, vol. 44, no. 6, pp. 2619-2692, 1998.

[39] L. V. Subramaniam, B. S. Rajan, and R. Bahl, "Trellis coded modulation schemes for underwater acoustic communications," *in Proc. IEEE OCEANS'98 Conf.*, pp. , 1998.

[40] V. Tarokh , N. Seshadri and A. Calderbank, "Space-time codes for high data rate wireless communications: Performance criterion and code construction," *IEEE Trans. Inf. Theory*, vol. 44, pp. 744-765, 1998.

[41] D. Agrawal, V. Tarokh, A. Naguib and N. Seshadri, "Space–time coded OFDM for high data-rate wireless communication over wideband channels," *in Proc. IEEE VTC'98*, pp. 2232-2236, 1998.

[42] G. Caire, G. Taricco and E. Biglieri, "Bit-interleaved coded modulation," *IEEE Trans. Inform. Theory*, vol. 44, pp. 927-946, 1998.

[43] D. Brady, J. C. Preisig, *Underwater acoustic communications*, in: H. Vincent Poor, G. W. Wornell (Eds.), *Wireless Communications: Signal Processing Perspectives*, Prentice Hall Signal Processing Series, 1998.

[44] Y. (G.) Li, L. J. Cimini, and N. R. Sollenberger, "Robust channel estimation for OFDM systems with rapid dispersive fading channels," *IEEE Trans. Commun.*, vol. 46, pp. 902-915, 1998.

[45] S. M. Alamouti, "A simple transmitter diveristy scheme for wireless communications", *IEEE Journal on Selected Areas in Communication*, vol. 16, pp. 1451-1458, 1998.

[46] A. V. Oppenheim, R. W. Schafer, J. R. Buck, Discrete-Time Signal Processing, 2nd Ed., Prentice-Hall Signal Processing Series, 1999.

[47] M.Stojanovic, "Underwater Acoustic Communications," entry in Encyclopedia of Electrical and Electronics Engineering, John G. Webster, Ed., John Wiley & Sons, vol.22, pp.688-698, 1999.

[48] V. Tarokh, H. Jafarkhani, and A. R. Calderbank, "Space-time block codes from orthogonal designs," *IEEE Trans. Inform. Theory*, vol. 45, pp. 1456-1467, 1999.

[49] V. Tarokh, H. Jafarkhani, and A. R. Calderbank, "Space–time block coding for wireless communications: Performance results," *IEEE J. Select. Areas Commun.*, vol. 17, pp. 451–460, 1999.

[50] U. Wachsmann, R. F. H. Fischer, and J. B. Huber, "Multilevel codes: Theoretical concepts and practical design rules," *IEEE Trans. Inform. Theory*, vol. 45, pp. 1361-1391, 1999.

[51] B. S. Sharif, J. A. Neasham, O. R. Hinton, and A. E. Adams, "A computationally efficient Doppler compensation system for underwater acoustic communications," *IEEE J. Oceanic Eng.*, vol. 25, pp. 52–61, 2000.

[52] Y. V. Zakharov, V. P. Kodanev, "Multipath-Doppler diversity of OFDM signals in an underwater acoustic channel," *in Proc. IEEE International Conference on Acoustics, Speech and Signal Processing, ICASSP'00*, vol. 5, pp. 2941 - 2944, 2000.

[53] D. B. Kilfoyle, A. B. Baggeroer, "The state of the art in underwater acoustic telemetry," *IEEE J. Oceanic Eng.*, vol. 25, pp. 4-27, 2000.

[54] L. R. LeBlanc, P.-P. J. Beaujean, "Spatio-temporal processing of coherent acoustic communication data in shallow water," *IEEE J. Oceanic Eng.*, vol. 25, pp. 40-51, 2000.

176

[55] J. G. Proakis, *Digital Communications*, 4th Ed., McGraw Hill, NY, 2000.

[56] F. B. Jensen, W. A. Kuperman, M. B. Porter and H. Schmidt, *Computational ocean acoustics*, Springer-Verlag, New York, 2000.

[57] H. Bölcskei, A. J. Paulraj, "Space-frequency coded broadband OFDM systems," *in Proc. IEEE WCNC'00*, pp. 1-6, 2000.

[58] B. Lu, X. Wang, "Space-time code design in OFDM systems," *in Proc. IEEE GLOBE-COM'00*, pp. 1000-1004, 2000.

[59] Y. (G.) Li, "Pilot-symbol-aided channel estimation for OFDM in wireless systems," *IEEE Trans. Veh. Technol.*, vol. 49, pp. 1207-1215, 2000.

[60] J. Gomes, V. Barroso, "Equalization and coding for coherent communication in the ASI-MOV vertical link", *in Proc. MTS/IEEE OCEANS'01*, vol. 4, pp. 2170-2176, 2001.

[61] R. Gray, *Toeplitz and Circulant Matrices: A Review.* Available on line at http://www-ee.stanford.edu/~gray/toeplitz.pdf, 2001.

[62] T. S. Rappaport, *Wireless Communications: Principles and Practice,* 2nd Ed., Prentice Hall, 2002.

[63] A. M. Sayeed, V. V. Veeravalli, "Essential degrees of freedom in time and frequency selective MIMO channels," *in Proc. 5th Int. Symp. Wireless Personal Multimedia Comm.*, vol. 1, pp. 107-111, 2002.

[64] J. G. Proakis, M. Salehi, *Communication systems engineering*, 2nd Ed., Prentice Hall, 2002.

[65] A. F. Molisch, M. Z. Win, and J. H. Winters, "Space-time-frequency (STF) coding for MIMO-OFDM systems," *IEEE Commun. Lett.*, vol. 6, no. 9, pp. 370-372, 2002.

[66] X. Li, A. Chindapol and J. Ritcey, "Bit-interleaved Coded Modulation With Iterative Decoding and 8 PSK Signaling," *IEEE Trans. Comm.*, vol. 50, pp. 1250-1257, 2002.

[67] H. L. Van Trees, *Optimum Array Processing (Detection, Estimation, and Modulation Theory, Part IV)*, 1st Ed., Wiley, 2002.

[68] L. Zheng, D. Tse, "Diversity and Multiplexing: A Fundamental Tradeoff in Multiple Antenna Channels", *IEEE Trans. Inform. Theory*, vol. 48(2), pp. 359-383, 2002.

[69] T. H. Liew, L. Hanzo, "Space-time codes and concatenated channel codes for wireless communications," Proc. IEEE, vol. 90, pp. 187-219, 2002.

[70] M. Stojanovic, *Underwater acoustic communications*, in: J. G. Proakis (Ed.), *Entry in Encyclopedia of Telecommunications*, John Wiley & Sons, 2003.

[71] D. B. Kilfoyle, J. C. Preisig, and A. B. Baggeroer, "Spatial modulation over partially coherent multiple-input/multiple-output channels," *IEEE Trans. Signal Process.*, vol. 51, no. 3, pp. 794-804, 2003.

[72] Y. Gong, K. B. Letaief, "An efficient space-frequency coded OFDM system for broadband wireless communications," *IEEE Trans. Commun.*, vol. 51, pp. 2019-2029, 2003.

[73] T. Yong, W. Junli, L. Tao and Y. Guangxin, "Concatenated space-time block code with trellis coded modulation in OFDM systems," *in Proc. ICCT'03*, vol. 2, pp. 1194-1197, 2003.

[74] A. Paulraj, R. Nabar and D. Gore, *Introduction to Space-Time Wireless Communications*, 1st Ed., Cambridge University Press, 2003.

[75] P.-P. J. Beaujean, L. R. LeBlanc, "Adaptive array processing for high-speed acoustic communication in shallow water," *IEEE J. Oceanic Eng.*, vol. 29, pp. 807-823, 2004.

[76] R. H. Stewart, *Introduction to physical oceanography*, http://oceanworld.tamu.edu/resources/ocng_textbook/contents.html.

[77] J. Preisig, "Performance analysis of adaptive equalization for coherent acoustic communications in the time-varying ocean environment", *J. Acoust. Soc. Amer.*, vol. 118, no. 1, pp.263-278, 2005.

[78] M. Chitre, S. H. Ong and J. Potter, "Performance of coded OFDM in very shallow water channels and snapping shrimp noise," *in Proc. IEEE OCEANS'05 Conf.*, vol. 2, pp. 996-1001, 2005.

[79] D. Tse, P. Viswanath, *Fundamentals of Wireless Communication*, 1st Ed., Cambridge University Press, 2005.

[80] L. Freitag *et al*, "Multi-band acoustic modem for the communications and navigation aid AUV," *in Proc. IEEE OCEANS'05 Conf.*, pp. 1080-1085, 2005.

[81] M.Stojanovic, L.Freitag, "Multichannel Detection for Wideband Underwater Acoustic CDMA Communications," *IEEE Journal of Oceanic Engineering*, vol.31, No.3, pp.685-695, 2006.

[82] H. C. Song *et al*, "Spatial diversity in passive time reversal communications," J. Acoust. Soc. Am. (120), pp. 2067–2076, 2006.

[83] M.Stojanovic, "Low Complexity OFDM Detector for Underwater Acoustic Channels," *in Proc. IEEE Oceans'06*, Boston, MA, September 2006.

[84] M.Stojanovic, "On the Relationship Between Capacity and Distance in an Underwater Acoustic Channel," *in Proc. First ACM International Workshop on Underwater Networks* (WUWNeT'06) / MobiCom 2006, Los Angeles, CA, September 2006.

[85] Z. Kun *et al*, "A real-time coded OFDM acoustic modem in very shallow underwater communications," *in Proc. IEEE OCEANS'06 Conf.*, pp. 1-6, 2006.

[86] E. Akay, E. Ayanoglu, "Achieving Full Frequency and Space Diversity in Wireless Systems via BICM, OFDM, STBC, and Viterbi Decoding," *IEEE Trans. Commun.*, vol. 54, pp. 2164-2172, 2006.

[87] Y. Li, G. Stuber, *Orthogonal frequency division multiplexing for wireless communications*, Springer, 2006.

[88] C. Wang *et al*, "An intercarrier interference suppression technique using time-domain windowing for OFDM systems," VTC 2006-Spring. IEEE 63rd, vol. 5, pp. 2518-2522, 2006.

[89] S. Roy, T. M. Duman, V. McDonald, and J. G. Proakis, "High rate communication for underwater acoustic channels using multiple transmitters and space-time coding: Receiver structures and experimental results," *IEEE J. Oceanic Eng.*, vol. 32, pp. 663-688, 2007.

179

[90] B.Li, S.Zhou, M.Stojanovic, L.Freitag and P.Willet, "MIMO OFDM over an Underwater Acoustic Channel," *in Proc. IEEE Oceans'07 Conf.*, Vancouver, Canada, October 2007.

[91] B.Li, S.Zhou, M.Stojanovic, L.Freitag and P.Willet, "Multicarrier Communication Over Underwater Acoustic Channels With Nonuniform Doppler Shifts," *IEEE Journal of Oceanic Engineering*, vol.33, No.2, pp.198-209, 2008.